

DEVELOPMENT OF MODULAR HIGH-RESOLUTION ION MOBILITY
ORBITRAP PLATFORMS FOR NATIVE MASS SPECTROMETRY

A Dissertation

by

JACOB WATSON MCCABE

Submitted to the Graduate and Professional School of
Texas A&M University
in partial fulfillment of the requirements for the degree of

DOCTOR OF PHILOSOPHY

Chair of Committee,	David H. Russell
Committee Members,	Arthur Laganowsky
	Simon W. North
	Hays S. Rye
Head of Department,	Simon W. North

December 2021

Major Subject: Chemistry

Copyright 2021 Jacob Watson McCabe

ABSTRACT

Native ion mobility-mass spectrometry (IM-MS) has evolved into a multifunctional tool for the characterization and analysis of native intact protein complexes. Structural information can be inferred by the rotationally-averaged collision cross-section (CCS) measurements. Native IM-MS is complementary to nuclear magnetic resonance (NMR) spectroscopy, X-Ray crystallography (XRD), cryogenic-electron microscopy (CryoEM), as well as surface plasmon resonance (SPR) and isothermal titration calorimetry (ITC). Commercial IM-MS platforms excel with proteomic workflows but are limited in resolution, sensitivity, and mass range for large biomolecules. Structural biology problems require developing and applying new instruments that excel in the sensitivity, resolution, and resolving power of large biological systems (MW > 100 kDa), e.g., proteins, protein complexes, antibodies, chaperonins, and virus capsids. The work described *vide infra* focuses on developing and implementing novel home-built instrumentation for native IM-MS to expand the capabilities of the biophysical toolbox in structural biology.

DEDICATION

For my wife, Lori S. McCabe, who has always pushed me to be all I can achieve even from 700 miles away while loving me unconditionally. My parents, Sharon and James McCabe, teaching me that I can do anything I want to do as long as I'm willing to pay the price.

ACKNOWLEDGEMENTS

I want to thank my research advisor, David H. Russell, for his mentorship throughout my Ph.D. career and for allowing me an opportunity to grow as a scientist. I especially enjoyed the discussions and troubleshooting advice while things weren't always going as anticipated. More specifically, if something isn't working, 99% of the time, it was a bad cable, or a poor connection. I would also like to thank my committee member, Dr. Laganowsky, for his hours of conversation regarding experimental design, coding, and anything I could think of while his door was open. He has been such an integral part of my graduate career by teaching me the importance of the biological aspects and how to start coding in Python. I would also like to thank Dr. North and Dr. Rye for their guidance and support throughout the research. In addition, I would like to thank my outstanding collaborators: Dr. Wysocki, Dr. Clowers, and Dr. Reilly, who helped push this project to where it is today.

I want to thank Dr. Michael Poltash for his friendship, mentoring, and influencing me during his time here and teaching me the ins and outs of instrument development to help build a solid foundation for this platform. In addition, I would like to thank three Russell group members for their friendship over the years: Thomas E. Walker for always being willing to lend a hand when needed, Dr. Christopher Mallis, who always let me bounce ideas off him, no matter how outlandish, and Dr. Mehdi Shirzadeh who taught me something new every time I spoke to him.

I don't think this project would be here today without the help and friendship of Benjamin J. Jones from Professor Wysocki's lab. Ben was always there to answer questions, teaching me something new, or struggling through learning digital waveforms together.

A development research lab is only as good as the support staff. More specifically, William Seward and Karl Yeager from the Texas A&M Department of Chemistry Machine shop for their years of friendship and teaching me the practicality of my SolidWorks designs. Whenever I was in doubt, I knew it would not work, so I might as well try it. I'd like to thank Greg Mathijetz, who retired from the group before I even arrived but would still always answer my phone calls about electronics and life in general. Finally, a big thank you to both the Russell and Laganowsky research groups for the help and support with the collaborative environment that always made me want to help.

And lastly, I would like to thank Dr. Kelly L. Stratton of the University of Oklahoma Stephenson Cancer Center and Dr. Kevin Courtney of the University of Texas Southwestern Simmons Cancer Center for their medical expertise and encouragement during treatment.

CONTRIBUTORS AND FUNDING SOURCES

Contributors

This work was supervised by a dissertation committee consisting of advisor Professor David H. Russell, Professor Simon North, and Professor Arthur Laganowsky of the Department of Chemistry, and Professor Hays Rye of the Department of Biophysics and Biochemistry.

Chapter 3 was co-authored with Jixing Lyu and Dr. Yang Liu, who expressed the protein and collected the data. Chapter 4 was co-authored with Dr. Mehdi Shirzadeh, who beta-tested the initial designs and gave critical feedback. Chapter 5 was co-authored by Thomas E. Walker and Benjamin J. Jones, who aided in the designing, building, testing, and collecting the data. All other work conducted for the dissertation was completed by the student independently.

Funding Sources

This work was also made possible in part by the National Institute of Health under Grant Number R01GM121751, P41GM128577, and R01GM138863, and the National Science Foundation under Grant Number CHE-1707675. Its contents are solely the responsibility of the authors and do not necessarily represent the official views of these funding agencies.

NOMENCLATURE

ATD	arrival time distribution
CA	collisional activation
CD	Circular dichroism
CCS	rotationally averaged collision cross section
CID / CIU	Collision induced dissociation/unfolding
CSD	charge state distribution
CryoEM	cryogenic-electron microscopy
Cryo-IM-MS	cryogenic ion mobility – mass spectrometry
DC	direct current
DT	Drift Tube
DESI	desorption electrospray ionization
DT-IM	drift tube ion mobility
DT-IMS	drift tube ion mobility spectrometry
ECD	electron capture dissociation
EMR	extended mass range
ESI	electrospray ionization
ETD	electron transfer dissociation
FT	Fourier Transform
FT-IM-PF-DT	fourier-transform periodic-focusing ion-mobility
HCD	High-energy C-trap dissociation
ICR	Ion cyclotron resonance

ID	inner diameter
IM	ion mobility
IMS	ion mobility spectrometry
IM-MS	Ion mobility- mass spectrometry
ITC	isothermal titration calorimetry
K	mobility of an ion
MALDI	matrix assisted laser desorption ionization
MD	Molecular dynamic simulations
MS	mass spectrometry
MSMS	tandem mass spectrometry
m/z	mass-to-charge ratio
NMR	Nuclear magnetic resonance
PF-DT	periodic-focusing drift tube
PTMs	Post-Translational Modifications
QqQ	triple quadrupole
qQ-PF-DT-FT-IM	dual-quadrupole periodic-focusing fourier-transform ion-mobility
R	Resolution
REIS	Reverse entry ion source
RF	radio frequency voltage
RP	Resolving power
SASA	solvent acceswsible surface area
SAXS	small angle X-ray scattering

SID	surface-induced dissociation
SPR	surface plasmon resonance
ToF	time of flight
TIMS	trapped ion mobility spectrometry
TTR	Transthyretin
TWIMS	traveling wave ion mobility spectrometry
UF	uniform field
UF-DT	uniform field drift tube
UHMR	Thermo Ultra-High Mass Range Hybrid Quadrupole Orbitrap
UVPD	ultra-violet photodissociation
VT-ESI	Variable-temperature electrospray ionization
XRD	x-ray crystallography

TABLE OF CONTENTS

	Page
ABSTRACT	ii
DEDICATION	iii
ACKNOWLEDGEMENTS	iv
CONTRIBUTORS AND FUNDING SOURCES.....	vi
NOMENCLATURE.....	vii
TABLE OF CONTENTS	x
LIST OF FIGURES.....	xiii
LIST OF TABLES	xix
CHAPTER I INTRODUCTION	1
Native State of Biological Systems.....	1
Drift Tube Ion Mobility Spectrometry (DT-IMS).....	7
First Principles Collision Cross Section Derivation.....	8
Combating Radial Diffusion of UF-DT	10
Implementation of Magnetic Fields	10
Development of the Reverse Entry Ion Source.....	14
Reverse Entry Ion Source coupled to an Exactive Plus Orbitrap with Extended Mass Range	14
Development of FT-IM-PF-DT Orbitrap	16
Limitations of Commercial Instrumentation	16
Overcoming the Duty-Cycle Mismatch	17
Digital Waveform Technology.....	20
CHAPTER II FIRST-PRINCIPLES COLLISION CROSS SECTION MEASUREMENTS OF LARGE PROTEINS AND PROTEIN COMPLEXES	23
Introduction	23
Experimental	25
Chemicals and Materials	25
Instrumentation.....	26

Data Processing	26
Ion Trajectory Simulations	27
Collision-Cross Section Determination from PDB Files	28
Results and Discussion.....	29
First-Principles Determination of CCS	34
Benchmarking CCS to Other Methods.....	36
Conclusion.....	41
Supporting Information.....	42
CHAPTER III DISCOVERY OF POTENT CHARGE=REDUCTION MOLECULES FOR NATIVE ION MOBILITY MASS SPECTROMETRY STUDIES.....	52
Introduction	52
Experimental Section	54
Protein expression and purification.....	54
Preparation of charge reducing reagents	55
Native mass spectrometry (MS) analysis of AmtB	55
Native MS analysis of soluble proteins.....	56
Ion-Mobility Mass spectrometry	57
Determination of half maximal effective concentration (EC50).....	57
Results and discussion.....	58
Conclusion.....	71
Supporting Information.....	72
CHAPTER IV VARIABLE-TEMPERATURE-ELECTROSPRAY IONIZATION FOR TEMPERATURE-DEPENDENT FOLDING/REFOLDING REACTIONS OF PROTEINS AND LIGAND BINDING	84
Introduction	84
Experimental	87
Design of VT ESI Source	87
Sample Preparation.....	89
Mass Spectrometry and Ion Mobility Mass Spectrometry	89
Results and Discussion.....	90
Conclusions	97
Supporting Information	98
Expression and preparation of fraxatin	98
Analysis of experimental data	99
Custom Power Supply Fabrication.....	100
CHAPTER V IMPLEMENTING DIGITAL WAVEFORM TECHNOLOGY FOR EXTENDED M/Z RANGE OPERATION ON NATIVE DUAL-QUADRUPOLE FT-IM-ORBITRAP MASS SPECTROMETER.....	104
Introduction	104

Experimental Section	107
Methods	107
Instrumentation.....	107
Data Processing	110
Results and Discussion.....	111
Complex-down characterization of a protein complex (C-reactive protein (CRP))	116
Conclusions:	118
CHAPTER VI CONCLUSIONS	120
REFERENCES	122
APPENDIX A SOLIDWORKS DRAWINGS OF QQ-PF-DT-FT-IM ORBITRAP	169
APPENDIX B VARIABLE TEMPERATURE ELECTROSPRAY IONIZATION SOLIDWORKS DRAWINGS	244

LIST OF FIGURES

	Page
Figure 1: Comparison of traditional biophysical techniques to Native IM-MS. Reprinted with permission from <i>Mass Spec. Rev.</i> 40, 3, 280-305. Copyright 2020 Wiley Publishing.....	2
Figure 2: A schematic proposed by Russell, Williams, and Clemmer in 2012 illustrating the transition of a protein from the solution to the gas phase. Reprinted with permission from <i>Acc. Chem. Res.</i> 2017, 50, 3, 556–560. Copyright 2017 American Chemical Society.....	4
Figure 3: Summary of the significant developments in the field of native MS over the past ~20 years according to Heck and coworkers (black text) with major instrument development (right) and biological application (left). Reprinted with permission from <i>J. Am. Soc. Mass Spectrom.</i> 2017, 28, 1, 5–13. Copyright 2016 American Chemical Society.....	5
Figure 4: (A) Illustrates the resolving power of the Synapt G1 versus the Exactive Plus EMR as a function of m/z . (B) Apparent resolution for AmtB 127 kDa membrane protein with three heterolipids bound. Reprinted with permission from <i>J. Am. Soc. Mass Spectrom.</i> 2019, 30, 1, 192–198. Copyright 2018 American Chemical Society.....	7
Figure 5 Schematic of an UF-DT adapted from ref ³⁰ . Reprinted with permission from <i>J. Am. Soc. Mass Spectrom.</i> 2016, 27, 12, 2054–2063. Copyright 2016 American Chemical Society.....	8
Figure 6 SIMION trajectories of C_{60}^+ ion in 1 torr of He for (A) UF-DT and (B) PF-DT. ³⁹ Reprinted with permission from <i>Int. J. Mass. Spec.</i> 2004, 239, 1, 43-49. Copyright 2004 Elsevier.....	12
Figure 7. SIMION trajectories show position-dependent displacement of ions and demonstrate the periodic focusing nature of PF-DT. Reprinted with permission from <i>Int. J. Mass. Spec.</i> 2010, 296, 1-3, 36-42. Copyright 2010 Elsevier.....	14
Figure 8. A reverse entry ionization source (REIS) mounted to the HCD cell of a Thermo Fisher Scientific Exactive Plus Orbitrap with Extended Mass Range. Briefly, ions are generated via a nano-ESI source (not shown) into the heated capillary inlet. The ions are subsequently focused by the RF-IF designed by Jeon in 2013, prior to being guided by an RF-only multiple into the HCD cell of the EMR. Reprinted with permission from <i>J. Am. Soc.</i>	

Mass Spectrom. 2019, 30, 1, 192–198. Copyright 2018 American Chemical Society. 16

Figure 9 (A) The frequency sweep applied to the drift tube gives rise to local maximum and minimum in the signal as shown in the total ion chromatograph (TIC). A selected m/z of interest is isolated from the mass spectrum to give the resulting extracted ion chromatograph (EIC) of each individual ion. (B) This EIC can be FT into the frequency domain and can subsequently be converted to arrival time by dividing by the sweep rate (Δ frequency/acquisition time). The pulse pattern sweep applied to the DT over an 8 minute acquisition to create a frequency dependent drift tube. 19

Figure 10 Solidworks schematic of 1st generation Fourier-transform (FT) ion-mobility(IM) periodic-focusing (PF) drift-tube (DT) (FT-IM-PF-DT) coupled to a Thermo Scientific Exactive Plus Orbitrap MS with Extended Mass Range (EMR) that was used for the following section of experimentation Briefly, ions are generated via static-spray nano-ESI into a heated capillary at ~ 100 °C. Ions are then transmitted into a RF Ion funnel at (250V_{pp}). Ion beam is modulated at both the Gate 1 and Gate 2 by a linear frequency chip of 5 to 5005 Hz over 8 min to overcome the duty-cycle mismatch of IM separation and MS analysis. Reprinted with permission from *Anal. Chem.* 2018, 90, 17, 10472–10478. Copyright 2018 American Chemical Society. 20

Figure 11 Mathieu stability diagram modified for digital waveforms illustrating the effect of the duty cycle (δ) on the excitation for digital waveforms. Reprinted with permission from *Int. J. Mass. Spec.* 1973, 12, 4, 317-339. Copyright 1973 Elsevier. 21

Figure 12 Calculated α values obtained for ubiquitin (red square, ~ 8 kDa), transthyretin (blue triangles, ~ 56 kDa tetramer), and pyruvate kinase (green circles, ~ 257 kDa tetramer) versus the reduced electric field (E/N). These plots illustrate the dependence of α on the pressure and electric field. Note that larger proteins exhibit less radial motion than low molecular weight proteins at higher He pressure, leading to increasing α values with increasing molecular weight. By correlating α as a function of pressure, α can now be estimated over a range of electric fields and pressures. 31

Figure 13 Native mass spectra and CCS profiles for β -lactoglobulin (PDB: 1BEB) (A, B), bovine serum albumin (PDB: 4F5S) (C, D), and pyruvate kinase (PDB: 1F3W) (E, F).¹³⁵⁻¹³⁷ The peaks in the mass spectrum of BLG denoted by * correspond to a bound disaccharide (+325.2 Da). The widths of the peaks in the mass spectrum of BSA are broadened owing to some unknown impurities. Similarly, the peaks in the CCS profiles are also broadened

either owing to sample impurities and/or conformational heterogeneity. Peaks denoted by † in the pyruvate kinase sample is an impurity in the sample with an average mass of 154 kDa.....34

Figure 14 Percent difference of $\alpha_{E/N}$ corrected PF-DT CCS values vs literature experimental values and calculated CCS values from IMPACT, PSA, and Collidoscope for soluble proteins that span a range of molecular weights from 8.6 – 810 kDa. The CCS obtained using $\alpha_{E/N}$ corrected from Figure 2, using the lowest charge state of each protein in 200 mM ammonium acetate to be able to benchmark to previous literature values^{96, 138, 140, 153, 154}37

Figure 15 (A) mass spectra, (B) ATD vs mass plots, and (C) CCS vs CSD (n=6 replicate measurements) of native GroEL 14-mer complex with comparisons to PF-DT, TWIMS, RF-UF, Collidoscope, and IMPACT using both CryoEM (PDB: 5W0S) and XRD (PDB: 1SS8) structures.^{142, 143} CCS of each charge state for 14 mer GroEL as compared to IMPACT, Collidoscope (for both XRD and CryoEM), as well as TWIMS (Heck and coworkers 2009) and RF-UF (Bush and coworkers. 2010).^{138, 140}39

Figure 16 Natural compounds are potent charge-reducing molecules. A-C) Representative mass spectra of AmtB in C₈E₄ doped with 100 mM of (A) TMAO, (B) histamine, or (C) spermidine. Data was acquired on an ultra-high mass range (UHMR) Orbitrap mass spectrometer under gentle instrument conditions. Structures of molecules are shown in the inset. D) Total number of charge states for AmtB in the presence of compounds at different concentrations. E) Plot of average charge states (Z_{avg} , dots) as function of concentration of charge-reducing molecules. A modified form of Hill equation was fit to the data (solid lines) to determine the half maximal effective concentration (EC₅₀). F) Mass spectra of AmtB doped with different concentrations of spermine ranging from 0 to 250 mM.60

Figure 17 Charge reduction of AmtB by piperazine and amine derivatives thereof. A-C) Representative mass spectra of AmtB in C₈E₄ doped with 100 mM of (A) piperazine, (B) AEP, and (C) APP. Structures of molecules are shown in the inset. D) Plot of Z_{avg} (dots) as function of concentration of charge-reducing molecules and regression of a modified Hill equation (solid lines). .63

Figure 18 Charge-reduction of AmtB by synthetic polyamines. A-E) Representative mass spectra of AmtB in C₈E₄ doped with 100 mM of (A) B2A (B) B3A (C) DMP (D) T2A (E) T3A. Structures of molecules are shown in the inset. F) Plot of Z_{avg} (dots) as function of concentration of charge-reducing molecules and regression of a modified Hill equation (solid lines).65

Figure 19 Native IM-MS of trimeric AmtB on a FT-IM-PF-DT Orbitrap platform. A-B) Ion mobility mass spectra of AmtB in (A) C₈E₄ and in the presence of

(B) 50 mM Spermine. (C) Collision cross section (CCS) profiles for the most abundant charge states. A Gaussian function was fitted (solid lines) to the data (dashed lines) to determine the centroid CCS. (D) Plot of CCS for different charge states from AmtB in the presence of different charge reducing molecules.66

Figure 20 Effects of Capillary temperature and backing pressure on charge-reduction of AmtB . A-B) Z_{avg} of AmtB in the presence of 100mM (A) spermine or (B) TMAO acquired at different capillary temperatures. C-D) Mass spectra of AmtB charge reduced by 100 mM TMAO (C) without and (D) with application of backing pressure to the nanoESI emitter.69

Figure 21 (A) Solidworks rendering of the vT-ESI assembly with labels to identify the significant components. The fan mounted to the top of the device prevents overheating and reduces atmospheric moisture condensation for experiments performed below $\sim 15^\circ\text{C}$. The top stage of the thermoelectric chip (TEC) makes direct contact with a 40 mm x 40 mm x 13 mm heatsink (CTS Electronic Components APF40-40-13CB); a 40 mm x 15 mm 24 VDC fan with 14.83 CFM rated airflow (Delta Electronics AFB0424SHB) is used to dissipate the heat off of the heatsink. The vT-ESI assembly uses custom machined PEEK components that mount directly to a commercial Thermo Nanospray Flex source. Additional details about the electronics control system are contained in the Supporting Information. (B) Temperature calibration of the vT-ESI emitter solution is performed using thermocouples inserted into the static spray capillary and the SS heat exchanger (as shown in inset). The temperature variation ranged from $\sim \pm 5^\circ\text{C}$ at the highest and lowest temperature and $\sim \pm 2$ in the range of $5 - 98^\circ\text{C}$87

Figure 22 (A) Mass spectra of ubiquitin collected at 8°C , 69°C , and 98°C ; (B) Plot of average charge state (Z_{ave}) of ubiquitin (PDB: 1UBQ²⁵⁰) versus temperature of the solution contained in the ESI capillary. Melting temperature (T_M) is defined as the midpoint of the sigmoidal curve. (C and D) Plots of the temperature-dependent average charge states (Z_{ave}) of the partially-unfolded A-state ubiquitin observed in acidic water/methanol solutions (49:49:2 MeOH:H₂O:Acetic Acid (pH 2.3)). At temperatures above $\sim 50^\circ\text{C}$, the signal is attenuated due to the rapid evaporation of the solution. Inset shows the proposed A-state structure from Vajpai, N. *et al.*²⁵¹ 92

Figure 23 (A) Structure of human frataxin (PDB:1EKG)²⁶³ and (B) plot of the average charge state (Z_{avg}) of frataxin as a function of solution temperature in the ESI emitter. The ESI signal is unstable at $T > 82^\circ\text{C}$, presumably owing to decomposition and/or aggregation at higher temperatures. A parabolic fit (Sigmaplot 10.0, solid line) was added to the data. vT-IM-

Orbitrap CCS profiles and (C) Extract MS of the (D) 7⁺ charge state, (E) 6⁺ charge state of FXN at 5 °C, 37 °C, and 80 °C. The red line is a Gaussian function fitted to the raw CCS experimental data (grey). CCS values for the 5⁺ monomer are not shown due to the overlap with the 10⁺ dimer.95

Figure 24 Temperature dependence of 1µM GroEL in 200 mM ammonium acetate containing 125 µM ATP. (PDB: 1SS8).97

Figure 25 SolidWorks rendering of the nano-ESI dual-quadrupole FT-IM-PF-DT coupled to the HCD cell of a Thermo Exactive Plus Orbitrap with Extended Mass Range (qQ-FT-IM-PF-DT-HCD Orbitrap) with the major components labeled and the applied DC potential gradient across the instrument. The length of DT is not to scale in the rendering, i.e., the vacuum box and qQ are enlarged to better illustrate this device; the DT, 8-pole etc. have been described previously.109

Figure 26 (A) Total ion current (TIC) detected as the frequency of Q2 (85/15 duty cycle with a ±10V DC bias applied on rod pairs at 300V_{pp}) is increased from ~75 kHz to 125 kHz. Frequency stepped in 1 kHz steps at the rate of ~1 kHz per second in panel A to produce an *m/z* selection chromatogram of quadrupole 2 (Q2). (B) extracted MS for the given frequency range shown in panel 29A. Full-ion transmission and isolation of a single charge state for CRP (Panel C), AmtB (Panel D), and GroEL (Panel E).113

Figure 27 Illustrates how mild collisional activation in the q of the qQ-FT-IM-PF-DT Orbitrap can be used to remove adducted species (salts, endogenous lipids and other small molecules) from (A) trimeric ammonia transport channel (AmtB, 127kDa) and (B) GroEL (802 kDa, 14mer). The collision voltages indicated refer to the potential applied from the entrance lense of q1 to the DC offset bias on the q1 rods. It is possible that CA in q1 may produce non-native state ions; whether this occurs or not can be assessed by using ion mobility as shown in panels B and C of Figure 28. Resolution (centroid / Δ*m/z* @ FWHM) of the primary charge state is listed in each panel.114

Figure 28 Illustrates complex-down characterization of the CRP. (A) The native MS spectrum of CPR is shown in the top panel, and each of the panels below contain mass spectra resulting from collisional activation (at the indicated voltage) of the ion populations in the panel above. Panel (B) contains the same mass spectrum shown in (A) and the 2-D plots for arrival-time vs *m/z* for the 5-mer and 10-mer CRP ions. Panel (C) contains the mass spectrum acquired following mass-selection of the CRP 5-mer ions using DWT as described above. Panel (D) contain the mass spectrum obtained by using DWT to mass select the CRP monomer (24+ 5 mer ion), and panel (E) contains the top-down mass spectrum of the mass selected ion shown in

panel (D). The amino acid sequence of CRP is shown and the sequence
informative fragment ion are label accordingly..... 116

LIST OF TABLES

Page

Table 1 Summary of CCS values for replicate measurements ($n = 6$) as compared to other methods using the $\alpha_{E/N}$ mobility dampening term <i>vide supra</i> . ^{96, 138, 153-155} Experimental CCS values are highlighted in red font for easier comparison between. Masses listed are experimentally determined values. A more complete list of references for sources of experimental CCS values is noted in Table S1.	38
--	----

CHAPTER I

INTRODUCTION

Native mass spectrometry (MS) sits at the epicenter of the biophysical toolbox for protein characterization. Native MS tries to resemble the cellular environment in terms of ionic strength, pH, concentration, and temperature to maintain proper folding throughout the analysis; more specifically, by preserving non-covalent interactions (e.g., H-bonds, salt bridges, hydrophobic patches) of the protein from solution to the gas phase.^{1,2} Native IM-MS can also be coupled with sequencing³⁻⁷, individual ligand binding analysis⁸⁻¹⁷, and structural information studies^{15, 18-26}. Ion mobility-MS (IM-MS) is a multidimensional analysis technique where ions are separated based on their respective size, shape, and charge and thusly allowing the separation of isobaric species. IM-MS allows for the determination of ion-neutral collision cross-sections (CCS) for comparison with available protein structures^{27, 28}. In the following subsections, the past ~20 years of instrument development will be presented as a prelude to designing and constructing a high-resolution ion mobility-mass spectrometer.

Native State of Biological Systems

Anfinsen's hypothesis considers that the thermodynamic minimum corresponds to the native state of the protein. This native state is system/environment dependent that allows for tracking protein folding.²⁹ However, due to the vast degrees of freedom that a protein has, the total time to fold a single protein would take longer than the existence of the universe. The paradox can be resolved if protein folding follows a given path and is

influenced by the local amino acid sequence. The intermediates along the folding pathway can be detected and plotted in a folding funnel, where the deepest well illustrates the most stable native conformation.

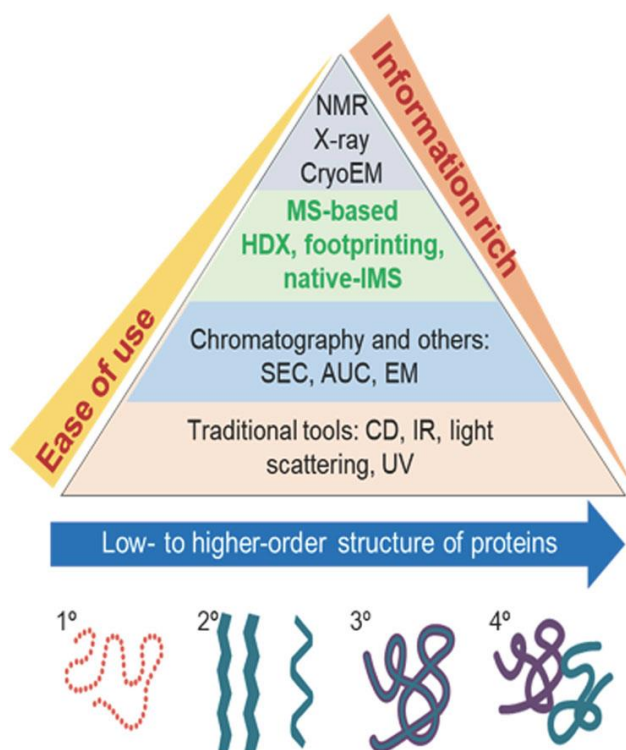


Figure 1: Comparison of traditional biophysical techniques to Native IM-MS. Reprinted with permission from Mass Spec. Rev. 40, 3, 280-305. Copyright 2020 Wiley Publishing.

Traditional tools in structural biology, such as NMR, XRD, CryoEM, and various optical spectroscopy techniques, have various degrees of structural information as shown in **Figure 1**, but measure sample-averaged populations. **Figure 1** shows the current biophysical toolbox for structural characterization plotted as “ease of use “ and “richness of information”. MS is the *only* technique that can obtain structural information of *individual* ion population. Coupling Native IM-MS to additional structural techniques

such as CIU³⁰, CID³¹, UVPD³², IRMPD^{33,34}, unprecedented advantage in the biophysical toolbox.

The “native” states of a biological system are defined by the primary (1°, amino acid sequence), secondary (2°, hydrogen-bond network), tertiary (3, conformation/3D structure), and quaternary (4°, topology and stoichiometry) structure of a protein or protein complex *in vivo*. The protein structure defines the activity and function of the protein in the native state, and non-native states or protein misfolding can be implicated in diseases such as Alzheimer's³⁵⁻³⁷, cancer^{38,39}, and Parkinson's^{35,37}.

Native MS aims to preserve the “native” protein structure following the transition from solution-phase molecules to solvent-free, gas-phase ions, as illustrated in **Figure 1**. Typically, proteins are ionized from a solution of near-neutral pH, low μM analyte concentration, and using instrument conditions to preserve the non-covalent adducts and subunit interfaces. Standard ionization methods for protein analysis electrospray ionization (ESI) and desorption ESI (DESI). In order to retain native conformations, a “soft” ionization technique where little energy is added to the complex is required. In these experiments, the ionization method employed is nano-electrospray ionization.

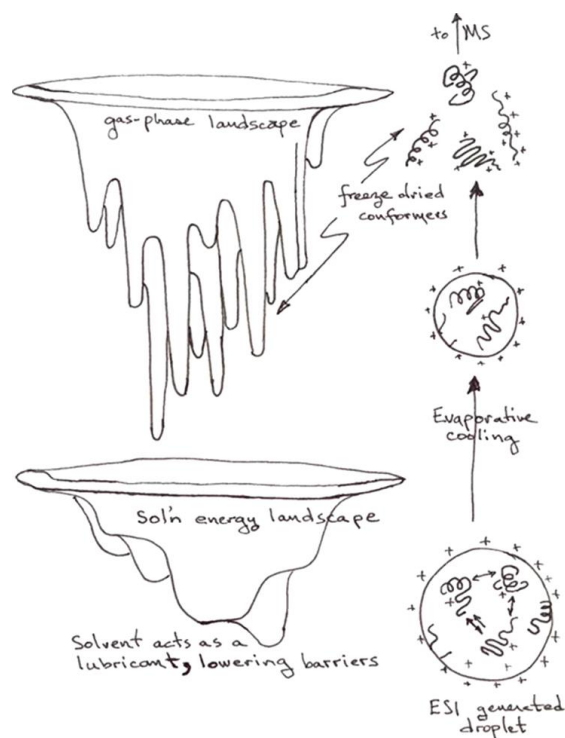


Figure 2: A schematic proposed by Russell, Williams, and Clemmer in 2012 illustrating the transition of a protein from the solution to the gas phase. Reprinted with permission from Acc. Chem. Res. 2017, 50, 3, 556–560. Copyright 2017 American Chemical Society.

Previous studies have shown that states of protein folding can be observed by monitoring the average charge state distribution (CSD) of the protein. Unfolded proteins typically have a larger solvent-accessible surface area (SASA) with a greater number of exposed charge-carrying sidechains. However, changes in CSD do not always indicate a transition between native and unfolded states; more specifically, a system that has multiple conformations at the same m/z cannot be detected by MS alone. Therefore, IMS serves as a complimentary technique to separates ions based on the size, shape, and charge. Further investigation on the Gibbs Energy Landscape will be explored in **Chapter 4**. Development Timeline for Native Mass Spectrometry

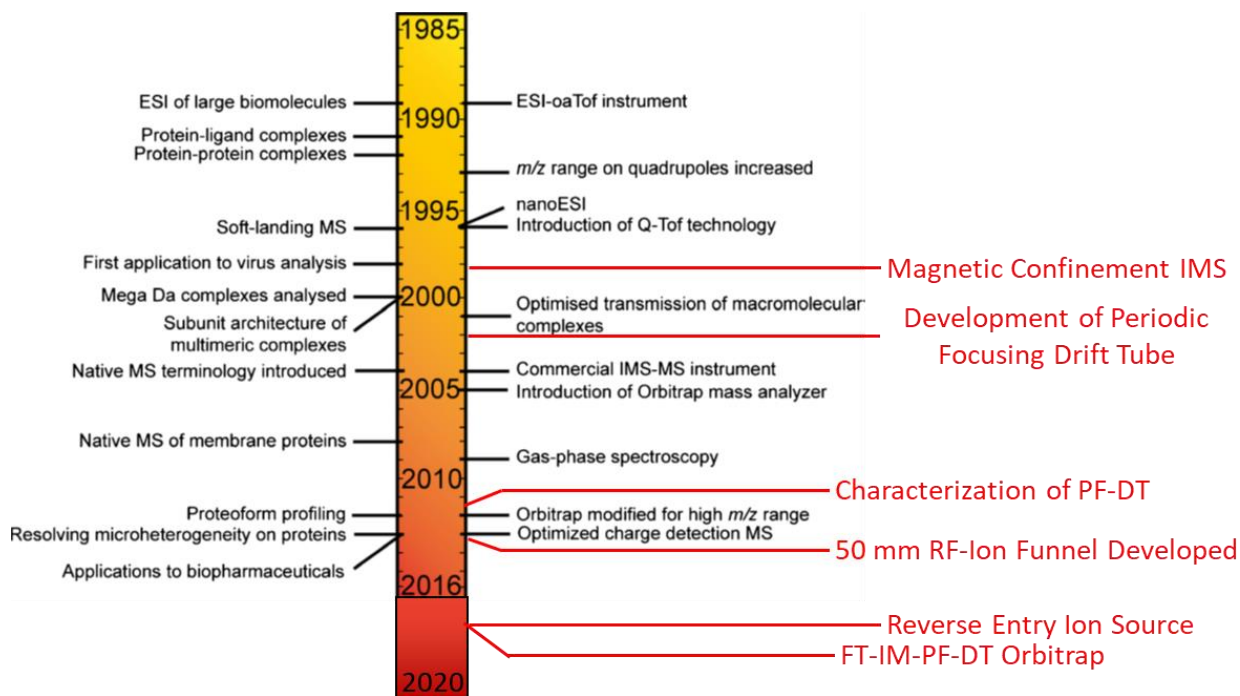


Figure 3: Summary of the significant developments in the field of native MS over the past ~20 years according to Heck and coworkers (black text) with major instrument development (right) and biological application (left). Reprinted with permission from J. Am. Soc. Mass Spectrom. 2017, 28, 1, 5–13. Copyright 2016 American Chemical Society.

Prior to developing soft-ionization techniques such as ESI, native protein complex analysis was almost impossible. The development of ESI enabled access to the study of a range of biomolecules by adding multiple charges during the ionization process. The added charge reduces the analyte mass-to-charge ratio (m/z) to where standard instruments can be used for native protein complex analysis. As the demands for biomolecule characterization grow, the need for higher resolution and higher resolution power instrumentation is also increased. Native mass spectrometry began on time-of-flight (TOF) systems primarily due to their theoretical unlimited mass range and modest resolving power. As the complexity of the studied system increases through the addition

of ligands or metal co-factors, the required mass resolution to detect these species increases as well. Time-of-flight instrument resolution can be increased by increasing the flight length, reducing the pressure in the analyzer to increase the mean free path, and adding reflectron(s) to reduce the kinetic energy spread of the ion packet, in addition to pulsing the ions orthogonally into the TOF to reduce the initial kinetic energy distribution. As instruments progressed, the introduction of the SYNAPT HDMS platform in 2006 by Waters Corporation (Manchester, UK) brought the first commercial hybrid-Q TOF IM-MS instrument to market. In 2012 Thermo Fisher Scientific introduced the first high-mass Orbitrap platform (Exactive Plus Series with Extended Mass Range (EMR) which is based on a modified Kingdon trap. Ions m/z is determined based on the axial oscillation frequency between two electrodes around a spindle and the use of FT. The oscillation frequency of ions is related to 1 divided by the square root of m/z ; this implication is a shallower decay in resolving power with m/z compared with ICR. High-resolution Orbitrap analysis allows the study of ligand additions to a membrane protein complex of interest, as shown in Figure 3.

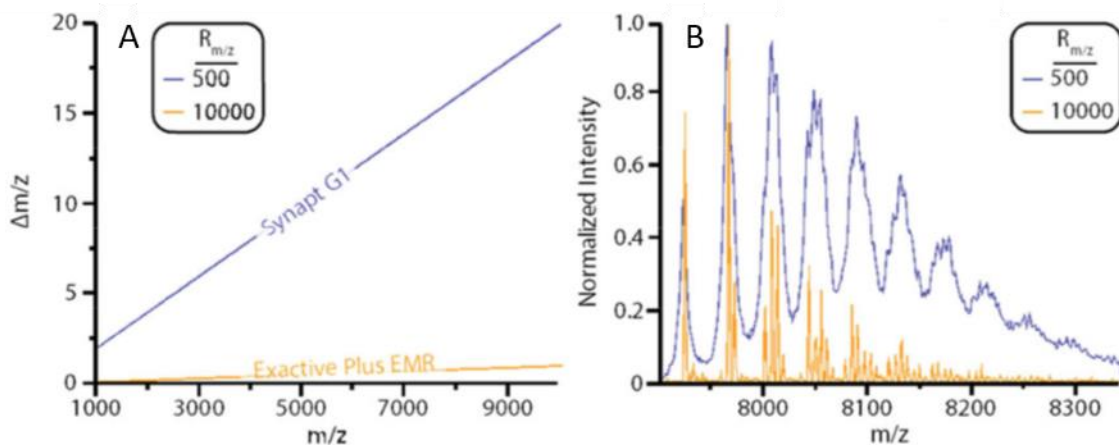


Figure 4: (A) Illustrates the resolving power of the Synapt G1 versus the Exactive Plus EMR as a function of m/z . (B) Apparent resolution for AmtB 127 kDa membrane protein with three heterolipids bound. Reprinted with permission from *J. Am. Soc. Mass Spectrom.* 2019, 30, 1, 192–198. Copyright 2018 American Chemical Society.

Drift Tube Ion Mobility Spectrometry (DT-IMS)

Ions in drift tube ion mobility devices are subject to numerous low-energy, thermal collisions with neutral background gas with a static applied electric potential drop across the drift region. The field applied in drift tube ion mobility (**Figure 4**) is maintained such that ion mobility is independent of the applied drift field (i.e., within the low-field limit typically on the order of 15 Townsend (Td) or less). Ions are pulsed into the drift region and separate based on differences in the influence of the electric field and drag forces from collisions with the background gas. The ion mobility is then determined by the time an ion takes to traverse the drift region and the applied electric field. Drift tube ion mobility allows for direct mobility measurement without the need for calibration, unlike the other techniques discussed here. Drift tube ion mobility does suffer the drawback of having lower resolution than traveling wave ion mobility or trapped ion mobility devices.

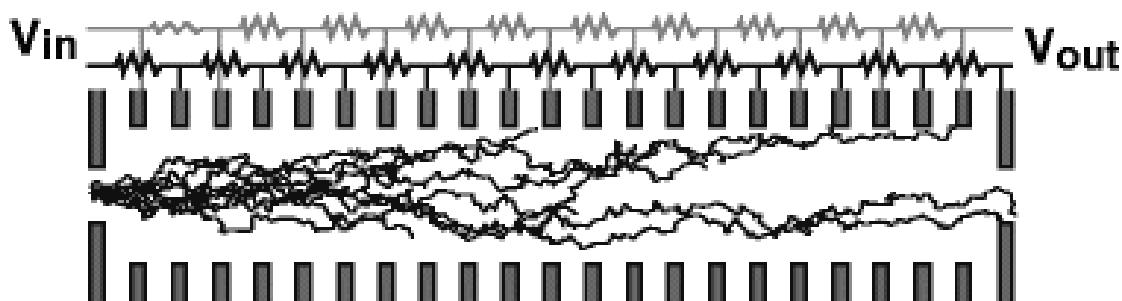


Figure 5 Schematic of an UF-DT adapted from ref ⁴⁰. Reprinted with permission from *J. Am. Soc. Mass Spectrom.* 2016, 27, 12, 2054–2063. Copyright 2016 American Chemical Society.

First Principles Collision Cross Section Derivation

Of all the available IM separation techniques, only drift-tube IM (DT-IM) can calculate first-principles CCS values and is described in more detail in **Chapter 3**. Known CCS values of analytes is needed to calibrate other techniques such as traveling wave ion mobility, trapped ion mobility, differential ion mobility, and field-asymmetric ion mobility. In DT-IM, the separation occurs based on the mobility of the ion, K , by applying a weak electric field gradient that pulls ions down the drift tube while there is a drag force applied via the buffer gas (typically He or N₂), slowing ion motion. The low-field limit is when K is *independent* of the field strength applied. The average drift velocity (v_{drift}) of the ions is determined by the DT length and the drift time defined as the following for uniform field (UF) drift tubes:

$$v_{Drift} = K E \quad (1)$$

where E is the voltage gradient applied across the drift tube. Solving for v_{drift} can be achieved by knowing the detection time of the ion and the initial inject time:

$$v_{Drift} = \frac{L}{t_{drift}} = K E \quad (2)$$

where L is the length of the drift tube (on-axis) and t_{drift} is the time the ion takes to traverse the length of the drift tube, L . The reduced mobility for a given analyte, normalized to standard temperature and pressure of 1 atm at 273.15 K, is defined by:⁴¹

$$K_o = \frac{3ze}{16N_o} \left(\frac{2\pi}{\mu k_b T} \right)^{1/2} \frac{1}{\Omega} \quad (3)$$

where e is the elementary charge, z is the charge of the analyte ion, N_o is the buffer gas number density, μ is the reduced mass of the buffer gas and ion, T is the temperature of the buffer gas, k_b is the Boltzmann constant, and Ω is the rotationally averaged collision cross-section.

The ion's respective mobility can be related directly back to size based on the rotationally averaged CCS (Ω) via the Mason-Schamp equation:⁴²

$$\Omega = \left(\frac{3ze}{16N_o} \right) \left(\frac{2\pi}{\mu k_b T} \right)^{1/2} \left(\frac{t_{drift} E}{L} \right) \left(\frac{P_o}{P} \right) \left(\frac{T}{T_o} \right)$$

(4)

where e , z , N_o , μ , T , k_b , t_{drift} , L , and Ω have been previously defined. **Equation 4** provides a first-principles measurement of the CCS as all of the variables can be directly measured in a UF-DT.

While DT-IMS allows for first principles CCS, the main challenge is poor transmission while still operating under the low-field limit. Longer drift tube lengths are needed for higher resolution IM, but the additional separation time increases diffusional broadening of an ion beam. The radial diffusion of ions as they transverse the DT leads to decreased sensitivity, poor resolution / resolving power due to poor peak definition, and

signal loss at the conductance-limiting aperture. Several ways to circumvent the radial diffusion have been developed some examples are as follows; the use of post-IM ion funnels (IF) to refocus the ion beam prior to the conductance limit, RF-confinement and magnetic confinement, which both limit radial diffusion of the ion beam, and periodic focusing (PF) DT which continually refocuses the beam to the drift axis at each electrode to limit the spread of the ion beam during the IMS experiment.

Combating Radial Diffusion of UF-DT

Implementation of Magnetic Fields

The Russell research group has developed several methods to circumvent radial diffusion. In 2000, Bluhm *et al.*, performed IM-MS inside of a 7T magnetic field.^{43,44} The magnetic field confines ions inward to the central drift axis. This additional magnet field increases the transmission and sensitivity of ions through the exit aperture needed to differentially pump the ion cyclotron resonance cell to a minimum of 10^{-6} torr. While the magnetic confinement was shown to increase ion transmission by reducing radial diffusion, problems arise due to the need to generate a large magnetic field and a large pressure differential for IM and subsequent MS analysis.

Periodic Focusing Drift Tube

The addition of a radio-frequency (RF) superimposed on top of ion optics was introduced by Javahery *et al.* in 1997 for obtaining CCS values on a triple quadrupole mass spectrometer.⁴⁵ The applied RF field minimized losses to diffusion by radially focusing and confining ions as they traversed the quadrupole. However, generating an RF field on the top of a DC gradient is difficult and can induce ion heating which may create

non-native states unintentionally. In 2004, an alternative design of DT, called periodic-focusing drift tube (PF-DT), was developed by Gillig *et al.* This approach achieves ion focusing as they traverse the DT without the need of additional voltages aside from the applied DC. The focusing is achieved by creating a distance-dependent electric field resulting in radial confinement of ions at every electrode. This distance-dependent electric field is generated due to the inherent design of the electrodes (6.25 mm thickness x 6.25 mm spacing x 8.0 mm inner diameter) where the ID is substantially smaller than the traditional UF lenses (>50 mm). **Figure 6** illustrates the effective focusing of PF-DT (B) as compared to the UF-DT (A) for C_{60}^+ under the low-field limit, as well as the intermediate-field limit. An experiment resolution of 120 was achieved using a 45 cm PF-DT at 1 Torr He, whereas the max resolution obtained via simulations for a UF is 60. Similarly, Verbeck *et al.* solved equations for estimating the resolution of IM at a high-field limit and postulated that there are no consequences for operating at the high-field

limit for a given set of analytes.⁴⁶

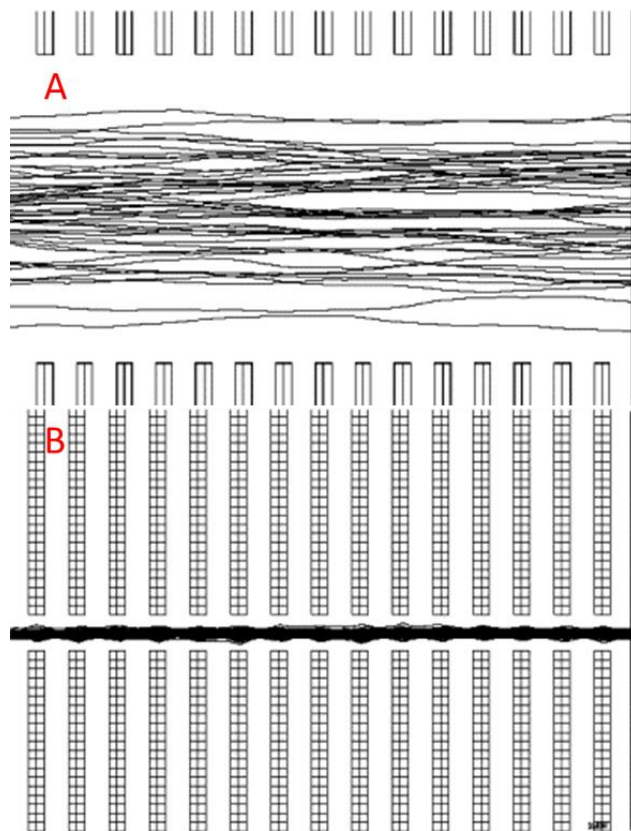


Figure 6 SIMION trajectories of C_{60}^+ ion in 1 torr of He for (A) UF-DT and (B) PF-DT.⁴⁷ Reprinted with permission from *Int. J. Mass. Spec.* 2004, 239, 1, 43-49. Copyright 2004 Elsevier.

During the initial development of the PF-DT, the reason for the increased resolution and focusing relative to UF-DT was attributed to the different lens geometry. The altered geometry of the ring electrodes induces a distance-dependent pseudo-RF electric field (operating in \sim kHz) as the ions traverse the length of the drift tube. Blase probed the effects of the inner diameter of the electrodes, length of the drift tube, and electric field strength of ions in PF-DT to optimize sensitivity and transmission of ions.⁴⁸ The ions follow an oscillating path which confines them along the radial axis of the drift

tube during periods of focusing and defocusing, shown in **Figure 7** regions A and C, respectively. Previously, longer arrival times obtained via PF were corrected to uniform field (UF) measurements with the inclusion of an alpha term (α) in the Mason-Schamp equation.⁴⁹ This α factor helps correct for the rippling motion and displacement of the ions from the center axis of the DT along its length; previous work using SIMION 8.1 to simulate ion trajectories through the PF-DT demonstrated that the value of α is dependent on the mass and charge of the ion, with more recent work suggesting that larger ions exhibit less oscillatory motion. Further detail is provided in **Chapter 2** to probe the effect of α for large native protein complexes.⁴⁹

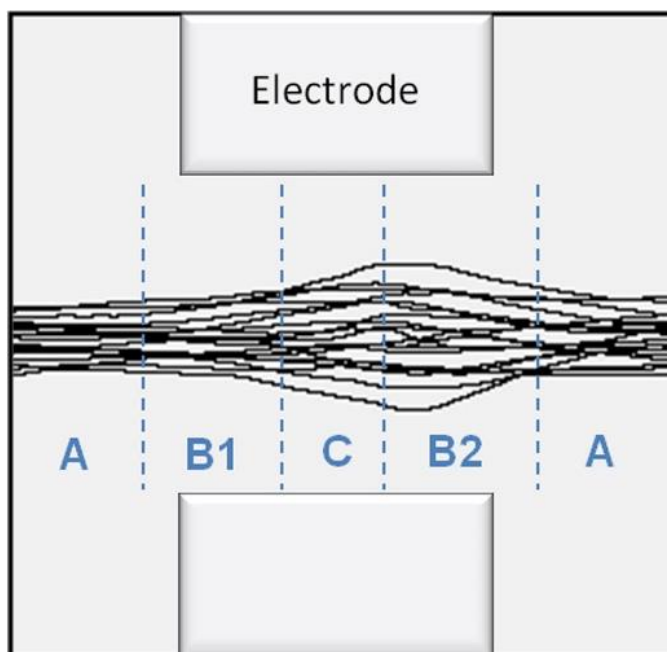


Figure 7. SIMION trajectories show position-dependent displacement of ions and demonstrate the periodic focusing nature of PF-DT. Reprinted with permission from *Int. J. Mass. Spec.* 2010, 296, 1-3, 36-42. Copyright 2010 Elsevier.

Development of the Reverse Entry Ion Source

Reverse Entry Ion Source coupled to an Exactive Plus Orbitrap with Extended Mass

Range

In 2013, Jeon designed a novel ESI source that coupled a long heated capillary into a short RF ion funnel to confine the ions⁵⁰, based on the initial design by the Richard Smith Lab⁵¹ and the Jarrold Group.⁵² This increases the efficiency, transmission, and sensitivity of an ion source by orders of magnitude over a simple skimmer cone type design due to reductions in ion loss through an aperture.

The initial ionization source designed by Jeon produces “cold” native-like ions under similar instrument tune conditions for Substance P and AmtB, as reported by Poltash

*et al.*⁹ The ionization source is coupled to the HCD cell versus modifying the commercial ionization source, thusly named “Reverse Entry Ionization Source”(REIS). The REIS configuration was implemented via the HCD cell of the Orbitrap for two main reasons: 1) as a building block for IM, careful tuning on the ion optics is critical to preserve native conformations of analytes, and the tuning space of commercial ion optics is minimal; and 2) during and after the development process, the standard ESI source is unaffected to allow use by other users and direct comparison of standard front- and homebuilt rear-entry ion optics. A Solidworks rendering of the REIS-EMR Orbitrap is shown in **Figure 8**. The performance of the REIS Orbitrap was comparable to the commercial ionization source for ubiquitin and ammonia transport channel, AmtB, for both average charge state as well as sensitivity.⁹

Membrane proteins are especially challenging to analyze via MS due to the need to solubilize the protein in a detergent.^{8, 10, 11, 53-56} This detergent solubilizes the protein in solution and can be removed by sufficient collisional activation (via CID).⁵³ Desired native MS of membrane proteins will have bare proteins that transition from the solution-phase to the gas phase without perturbing endogenous lipids and detergent such as DDM, as shown previously.⁸ Without enough energy added during the desolvation process, membrane proteins will retain the non-specific adducts used to solubilize the protein (e.g., detergents). In addition, from a complex mixture of membrane protein AmtB and native, endogenous lipids, 45 unique combinations of lipids were identified.⁹ Further investigation of membrane protein, AmtB, are discussed in **Chapters 4 and 5**.

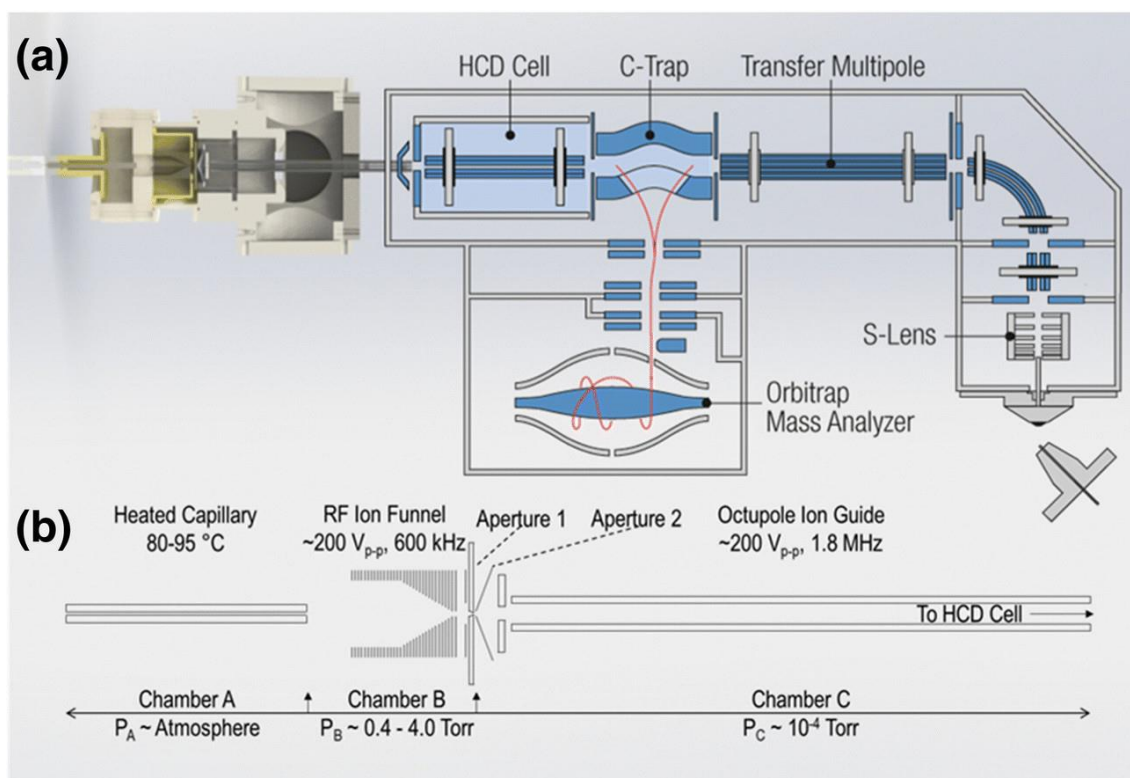


Figure 8. A reverse entry ionization source (REIS) mounted to the HCD cell of a Thermo Fisher Scientific Exactive Plus Orbitrap with Extended Mass Range. Briefly, ions are generated via a nano-ESI source (not shown) into the heated capillary inlet. The ions are subsequently focused by the RF-IF designed by Jeon in 2013, prior to being guided by an RF-only multiple into the HCD cell of the EMR. Reprinted with permission from J. Am. Soc. Mass Spectrom. 2019, 30, 1, 192–198. Copyright 2018 American Chemical Society.

Development of FT-IM-PF-DT Orbitrap

Limitations of Commercial Instrumentation

Commercial developments of MS and IM-MS instrument platforms over the past 30 years have focused primarily on “omics” applications, where the need for high throughput and sensitivity drives the instrument development. As instrument development improves, the complexity of biological systems that can be studied is increased by new methods to probe previously hidden interactions. Orbitrap platforms are perfect matches

for structural biology applications due to their footprint, resolution, and sensitivity.⁵⁷ The apparent resolution is much higher than what is achievable with traditional “omics”-era ToF-MS platforms. This increase in apparent resolution of the Orbitrap compared to TOF instruments is partial because of increased analyzer resolution and sensitivity, but also the enhanced desolvation of the ionization source that is required for large complexes. However, in the last few years, commercial vendors have begun to develop a new era of “native” instruments that excel in the detection and analysis of large biomolecules, *e.g.*, Waters SELECT Series Cyclic IMS, Agilent 6560 and 6545XT, and Thermo Fisher Q Exactive UHMR Hybrid Quadrupole-Orbitrap.

Overcoming the Duty-Cycle Mismatch

While the performance metrics of commercial instrumentation are evolving, the current generation still falls short of the need mass spectrometers capable of analysis kDa to Mda sized molecules. In 2012, the Russell Research Group initiated the effort to combine DT-IM with an Orbitrap platform. allows for both the high-resolution needed in the MS and IM domain to resolve solvent effects, protein-protein interactions, and protein-ligand interactions. However, the inherent coupling of these two techniques introduces a duty-cycle mismatch between the IM separation (tens of ms) and mass analysis (hundreds to thousands of ms), where a second IM gate is needed to select an individual arrival time for mass analysis and then is repeated over the entire drift-time window. Typically, IMS is coupled to mass analyzer with fast (microsecond acquisition) analysis, such as time-of-flight (TOF) MS, where as the IM separation is slow (tens to hundreds of milliseconds). This arrangement of the MS being after the IM results in nested MS analysis

of ions as they exit the DT.

Typically, in a pulse and wait experiment, “signal-averaged” IM experiment, the IM gate is pulsed at ~1% duty cycle (defined as the time the pulse is “on”), where the gate width influences the resolution. Because of the low duty cycle, 99% of the ion signal is terminated by the IM gate leading to long acquisition times. When this “signal-averaged” approach is implemented on a system with two gates, the resulting ion transmission is reduced even further to 0.01% of relative transmission with an abysmal signal-to-noise ratio (S/N) and acquisition times of hours.

Alternatives to a low relative ion transmission are to trap and accumulate an ion population prior to injection to bolster the sensitivity or multiplex the gate by pulsing multiple packets of ions into the DT for mobility analysis instead of just a single packet. While there are numerous multiplexing methods (*e.g.*, Hadamard and correlation), Fourier Transform IM (FT-IMS) was implemented due to the ease of use, the high relative transmission of 25%, and fast acquisition times. Briefly, FT-IMS converts the DT-IM from separation in the time domain into the frequency domain by linearly sweeping both gates (*e.g.*, 5-5005 Hz) with acquisition times ranging from 2 to 32 minutes.

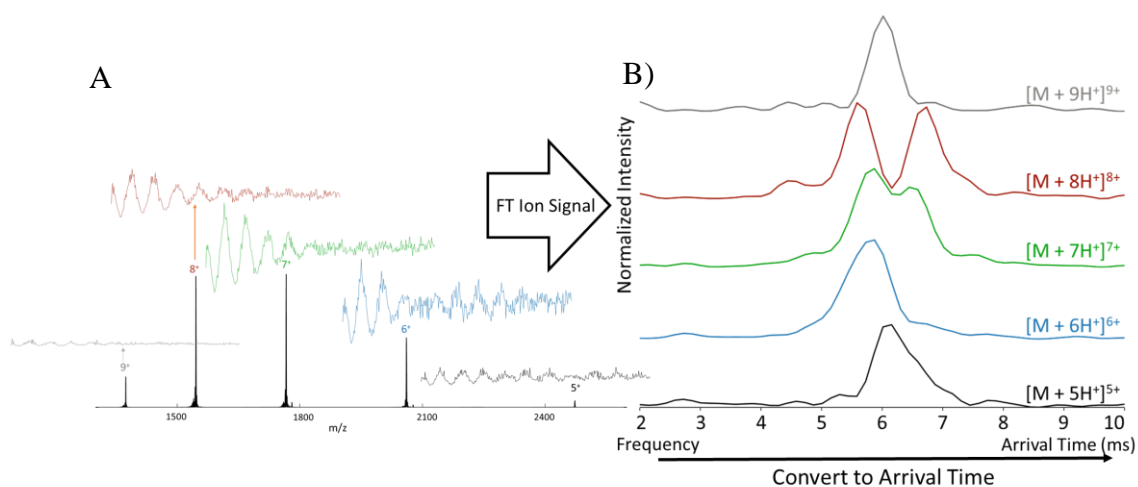


Figure 9 (A) The frequency sweep applied to the drift tube gives rise to local maximum and minimum in the signal as shown in the total ion chromatograph (TIC). A selected m/z of interest is isolated from the mass spectrum to give the resulting extracted ion chromatograph (EIC) of each individual ion. **(B)** This EIC can be FT into the frequency domain and can subsequently converted to arrival time by dividing by the sweep rate (Δ frequency/acquisition time). The pulse pattern sweep applied to the DT over an 8 minute acquisition to create a frequency dependent drift tube.

Figure 9 illustrates an example workflow of a protein analyzed by the FT-IM-PF-DT Orbitrap. The frequency of modulation the ions experience via the FT-IM mode is encoded into the respective m/z information (extracted ion chromatogram, **Figure 9A**) and thusly deconvoluted into an arrival-time distribution (ATD, **Figure 9B**).

A schematic of the instrumentation with the PF-DT added between the REIS-IF and the skimmer cone is shown in **Figure 10**, as described by Poltash *et al.*¹⁵. The high-resolution afforded by the FT-IM-PF-DT in both the IM and MS domains has probed biological details that were previously hidden. For example, the FT-IM-PF-DT was able to probe native transthyretin (TTR) conformation with a distribution of 0, 1, and 2 thyroxine bound. The increased number of thyroxines bound to TTR increases the ATD

of the complex, indicating a conformational change upon binding. However, the high-resolution and thusly resolving power provided by the Orbitrap revealed Zn(II) ions bound to TTR that caused a destabilization in conformation that had not been reported before via native MS.¹⁵ Further TTR investigation revealed that metal-induced oxidation rapidly occurs on Cys₁₀ that causes fragmentation and cleavage of a peptide bond.¹³ This platform was used as a starting point for additional development described *vide infra*.

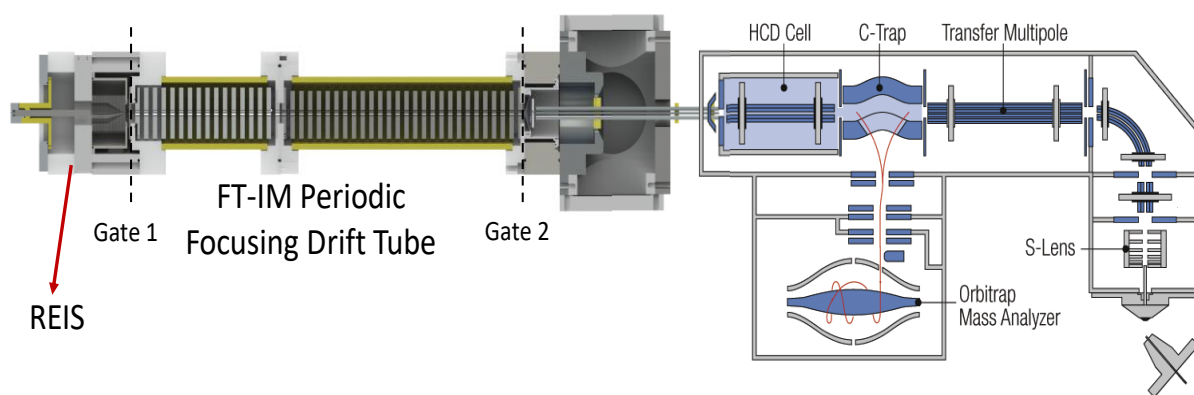


Figure 10 Solidworks schematic of 1st generation Fourier-transform (FT) ion-mobility(IM) periodic-focusing (PF) drift-tube (DT) (FT-IM-PF-DT) coupled to a Thermo Scientific Exactive Plus Orbitrap MS with Extended Mass Range (EMR) that was used for the following section of experimentation Briefly, ion are generated via static-spray nano-ESI into a heated capillary at ~100 °C. Ions are then transmitted into a RF Ion funnel at (250V_{pp}). Ion beam is modulated at both the Gate 1 and Gate 2 by a linear frequency chip of 5 to 5005 Hz over 8 min to overcome the duty-cycle mismatch of IM separation and MS analysis. Reprinted with permission from *Anal. Chem.* 2018, 90, 17, 10472–10478. Copyright 2018 American Chemical Society.

Digital Waveform Technology

Quadrupoles are routinely used as low-cost LC-MS instruments or triple quadrupole (QqQ) mass spectrometers in the MS community^{58,59} using the first quadrupole for mass isolation (denoted Q), the second quadrupole for activation/fragmentation (q),

and the final quadrupole for mass analysis (Q). In addition, quadrupoles have been used extensively in the past as a means to clean up samples, which can be used to add energy to remove detergent on membrane proteins.^{60, 61}

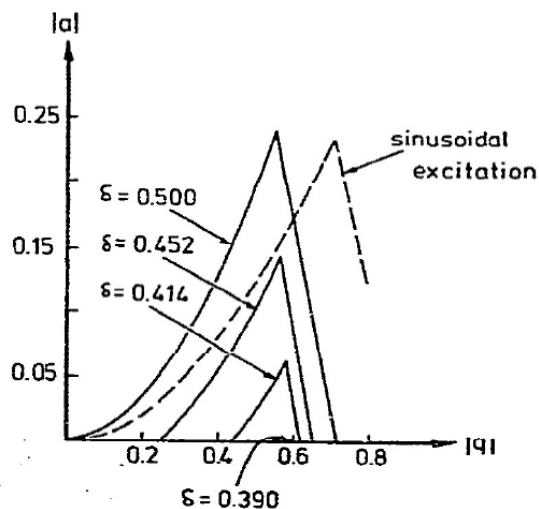


Figure 11 Mathieu stability diagram modified for digital waveforms illustrating the effect of the duty cycle (δ) on the excitation for digital waveforms. Reprinted with permission from *Int. J. Mass. Spec.* 1973, 12, 4, 317-339. Copyright 1973 Elsevier.

Typically, quadrupoles operate using a superimposed DC and an RF potential to either stabilize or destabilize ion trajectories through the quadrupole (denoted now as RF-Quad). Because of these RF and DC potentials, mass filter stability diagrams can be obtained by solving the Mathieu equation using Paul and Steinwedel's scalar potential.⁶² However, the RF frequency on the RF-Quad can be replaced with a simpler digital waveform that uses two square wave pulses of various duty cycles (δ) to solve the Mathieu equation.⁶³ By modulating δ of each wave, the constructive and destructive properties of waves allow for ion trapping (q), isolation (Q), and activation in a single quadrupole.⁶³

Figure 11 illustrates a Mathieu stability diagram based on the δ of the digital wave compared to the dashed line of sinusoidal excitation, showing similar results. When δ is low, ions are axially trapped inside of the quadrupole, whereas when δ is high, ions are axially ejected from the quadrupole.⁶³ It is apparent that as δ decreases, ions are destabilized in the quadrupole allowing for isolation of individual ions based solely on square waves.⁶³

Pulsing of square waves with precision and accuracy for quadrupoles, when eventually coupled to the FT-IM-PF-DT Orbitrap, is possible without the egregious cost and safety concerns of floating RF-Quad drivers to high DC potentials. In addition, the pulsing of similar square waves is already being implemented on the current instrumentation to drive the FT-IM gates. Professor Peter Reilly's research group at Washington State University has been leading the development of digital waveform technology for the past decade.⁶⁴⁻⁷¹ Recently, they have shown that digital waveform technology (DWT) can be used to collisionally trap and then subsequently activate ions to remove non-covalent adducts and oligomeric states.⁷⁰ The implementation of DWT to mass selection quadrupoles will be discussed in more detail in **Chapter 5**, as well as the next generation of IM-MS instrumentation.

CHAPTER II

FIRST-PRINCIPLES COLLISION CROSS SECTION MEASUREMENTS OF LARGE PROTEINS AND PROTEIN COMPLEXES*

Introduction

The arsenal of techniques currently used for studies of biomolecular structure, *viz.* circular dichroism (CD) spectroscopy,⁷² nuclear magnetic resonance (NMR) spectroscopy,^{73, 74} X-ray crystallography (XRD),^{75, 76} and cryogenic-electron microscopy (CryoEM)^{77, 78} have undergone major advancements over the past few decades. These advances are complemented by parallel advances in mass spectrometry (MS) based methods, including hydrogen/deuterium exchange (HDX),^{25, 26} hydroxyl radical footprinting (FPOP),^{79, 80} and increased numbers of covalent-labeling strategies.⁸¹ Rapid progress has also been realized in the development of top-down protein sequencing strategies,^{4, 82} and similar approaches incorporating surface-induced dissociation (SID) make possible complex-down approaches for determination of the stoichiometry and topology of protein complexes.²⁰⁻²² These latter MS-based approaches have occurred in parallel with the increased adoption of native MS, which aims to preserve the non-covalent interactions in the gas phase.^{1, 2}

*Reprinted with permission from McCabe, J.W.; Mallis, C.S.; Kocurek, K.I.; et al. First-Principles Collision Cross Section Measurements of Large Proteins and Protein Complexes. *Analytical Chemistry* **2020** 92 (16), 11155-11163. Copyright 2020 American Chemical Society.

Native MS,^{1, 2} a rapid and exquisitely sensitive technique, is now capable of providing information on protein complex subunit stoichiometry,^{24, 83-85} topology,⁸⁶⁻⁸⁸ assembly pathways,^{89, 90} and individual ligand binding events.⁹¹ Possibly of even greater significance for native MS is the ability to assess protein purity over traditional gel-based approaches.⁹² Native ion mobility-mass spectrometry (IM-MS) makes possible studies of protein structure^{93, 94} as well as how interactions with metal ions,^{12, 14} small molecules,^{13, 18} protein tags,⁹⁵ proteins,⁹¹ and nucleic acids⁹⁶ alter protein structure(s). An important feature of IM-MS is the ability to directly measure individual conformers that may comprise a population of gas-phase structures and the rotationally-averaged collision cross sections (CCS) that can be related to conformation and structural dynamics.⁹⁷⁻⁹⁹ Software deconvolution of IM-MS data can allow for previously unresolved isomeric mixtures to be exposed using automated ion mobility deconvolution (AIMD).^{5, 100, 101} When combined with collision-induced unfolding (CIU)¹⁰² and variable-temperature electrospray ionization (vT-ESI),^{103, 104} it is possible to accurately determine gas- and solution-phase stabilities of the ions, respectively, along with conformational changes that occur upon ligand binding and/or changes of the local environment.^{10, 103-106}

Although IM-MS instrumentation developed during the proteomics era represent major technological advances, these instruments impose significant limitations on studies of large (*i.e.* >100 kDa), intact biological assemblies.^{9, 15, 18} To circumvent these limitations, new IM-MS technologies with increased ion mobility and mass resolution are being developed, specifically, the Waters SELECT SERIES Cyclic IMS¹⁰⁷ and the native

ESI-Fourier transform (FT) IM-Orbitrap MS possess the unique potential for high-resolution structural characterization of large biomolecules.^{8, 9, 15, 18, 95, 108-110}

Because the operation of the PF-DT-FT-IM Orbitrap instrument differs from typical commercial IM-MS instruments, a brief description of the instrument operation is included here. The instrument employs a dual-gate configuration to overcome the inherent duty-cycle mismatch for the PF-DT (tens of milliseconds) and the Orbitrap (hundreds of milliseconds).^{15, 109, 111} Ion gates positioned at the entrance and exits of the DT are used to synchronously modulate the ion beam, which allows for operation of the DT as a frequency dispersive device. Ion drift frequencies of 5 Hz to 5 kHz correspond to ion drift times of 200 ms to 200 μ s, respectively. In the FT-IMS mode, it is possible to acquire arrival time distributions (ATDs) and CCS for *every* ion present in a given mass spectrum in a single eight-minute linear frequency sweep.

Here, the capabilities of a homebuilt PF-DT-FT-IM coupled to an Orbitrap mass spectrometer are critically evaluated with respect to the determination of CCS of soluble proteins and protein complexes ranging in size from 8.6 to 810 kDa. The reported CCS values are determined from first-principles using the modified Mason-Schamp equation,⁴² and these values are compared with those previously reported and calculated from X-ray and CryoEM structures using Ion Mobility Projection Approximation Calculation Tool (IMPACT),¹¹² projected superposition approximation (PSA),¹¹³⁻¹¹⁶ and Collidoscope.¹¹⁷

Experimental

Chemicals and Materials

Soluble protein samples were purchased from Sigma-Aldrich or Fisher Scientific in lyophilized form and diluted to 1 mg/mL in 18.2 M Ω -cm water (**Supplemental Table S1**). TTR and GroEL were expressed and purified as previously described.^{19, 118} The proteins were buffer exchanged using Micro Bio-Spin P-6 Gel Columns (Bio-Rad) into 200 mM ammonium acetate and working concentrations adjusted to 1 to 5 μ M. Several microliters of protein solution were backloaded into pulled borosilicate tips prepared in-house from borosilicate capillaries (Sutter Instruments, BF150-86-10) using a micropipette puller (Sutter Instruments, P1000).

Instrumentation

Here, we describe modifications to the previously developed PF-DT-FT-IM^{15, 18} Orbitrap that increase our capabilities for native IM-MS, especially for studies of large protein complexes. Specifically, the 58 cm PF-DT has been extended to 1.5 m thereby increasing the IM resolution. Increasing the DT length requires floating the ESI source an additional 1 kV higher and to minimize the effects of Paschen breakdown, all source housing components were fabricated from Delrin® acetal polymer. In addition, a second calibrated manometer was added to the end of the 1.5 m PF-DT to ensure carrier gas pressure (He, 99.999% purity) is constant throughout the length of the PF-DT.

Data Processing

Data files were processed as previously described.^{15, 18} In brief, custom in-house Python scripts utilized *multiplierz*¹¹⁹ to extract from Thermo RAW files mass spectral data from each scan over the entire acquisition. Ion mobility data were obtained by extracting intensity information for m/z values over acquisition time followed by Fourier transform

to convert from frequency to drift time domains using Scipy¹²⁰ and Numpy¹²¹ packages. The resulting data can then be imported into UniDec¹²² or PULSAR⁵⁵ for additional processing.

Ion Trajectory Simulations

SIMION (v8.1) ion trajectory simulations for ubiquitin (Ubq), transthyretin (TTR), and pyruvate kinase (PK) were performed under the low field limit, where the energy gained between collisions is less than the thermal energy of the collision gas for Ubq.⁴⁶ The simulations were limited to the specific design of the current PF-DT, where the lens thickness, spacing, and diameter are 6.35, 6.35, and 8.00 mm, respectively.^{49, 123, 124} These dimensions give rise to fringing E-fields that radially confine ions as they traverse the PF-DT. The details and potential deleterious effects of collisional heating of the ions by the radial focusing have been described previously.^{125, 126}

Calculation of Collision Cross Section

First-principles CCS (Ω) were calculated using the Mason-Schamp equation⁴² (**Eq. 1**) along with ion mobility dampening term, α , proposed previously⁴⁹ and described further in the main text;

$$\Omega = \alpha \left(\frac{3q}{16N_o} \right) \left(\frac{2\pi}{\mu k_b T} \right)^{1/2} \left(\frac{t_d E}{L} \right) \left(\frac{P_o T}{P T_o} \right)$$

[1]

q is the charge of the ion, N_o is the standard particle density of the buffer gas, μ is the reduced mass of the ion and the buffer gas, k_b is Boltzmann's constant, T is the temperature in the drift tube, t_d is the drift time of the ion, E is the electric field strength, L is the length of the drift tube set herein as the distance between the two ion gates, and P_o/T_o are the

standard pressure and temperature, respectively. Ions with equivalent CCS will have longer drift times in PF-DT than those in UF-DT due to the distance-dependent oscillations and focusing throughout the IM separation. Therefore, without accounting for the mobility dampening term (α), the CCS for PF-DT would be systematically larger than those acquired using a UF-DT.

Ion ATDs obtained by the dual-gate setup used in **Eq 1** are an *exact* measure of the drift time of the ions between the two gates, thus eliminating the need for a multi-electric field calibration ($1/V$ plots)¹²⁷⁻¹²⁹ to correct the measured ATD that ions spend outside of the drift tube. In addition, as long as the ions sampled by the second gate do not undergo dissociation or fragmentation, any post-mobility changes in conformation will not impact the measured ATDs.

Uncertainties in CCS measurements obtained using the PF-DT were calculated based on the standard deviation of 6 replicates for each protein or protein complex as recommended by Gabelica *et al.*¹²⁹ Day-to-day reproducibility of CCS was tested using transthyretin and was found to differ by less than 3% (data not shown). The temperature of the laboratory where these measurements were performed is maintained at ~21 °C (70 +/- 2°F).

Collision-Cross Section Determination from PDB Files

Atomic coordinates were downloaded from the PDB (www.rcsb.org) and visualized using PyMOL.^{130, 131} Biological assemblies were generated, if necessary, using crystallographic symmetry operators in PyMOL. Reference PDB codes for each protein and protein complex can be found in **Table 1**. PDB files were prepared for CCS

calculations using PyMOL by removing water molecules and other co-solutes with explicit hydrogens added before exporting the structures for CCS determination. Heme cofactors were not removed from the structures.

Correction factors proposed by Hall *et al.* were originally implemented to correct for underestimation of projection approximation (PA) CCS values obtained from MOBCAL, by scaling the PA CCS output values to the ratio of experimental and PDB molecular weights.¹³² Each of the CCS calculation tools utilized herein provides CCSs that are closely correlated to experimental CCSs and do not suggest scaling factors for missing atom coordinated in the published methods.

For IMPACT¹¹² and Collidoscope¹¹⁷, atomic coordinates were exported from PyMOL as .PDB files. For PSA¹¹³⁻¹¹⁶, structures were exported as .xyz files. Default parameters were used for IMPACT, and the TJM* results of six trials were averaged. Default parameters were used for Collidoscope using 10 energy states and a temperature of 298 K. The input charge states for Collidoscope were the lowest observed charge states from the MS experiments. Default parameters were used for PSA with an input temperature of 298 K. PSA calculations were performed on the PSA WebServer (v0.5.1, psa.chem.fsu.edu).

Results and Discussion

The Fourier transform IM-MS instrument used for this study incorporates several novel features, *viz.* a periodic-focusing IM drift tube (PF-DT) coupled to an extended mass range (EMR) Orbitrap mass spectrometer. The instrument and its operation as an FT-IM-MS platform have been described previously.^{15,18} Originally developed by Gillig *et al.* in

2004, the PF-DT has increased ion transmission owing to radial focusing of the ions during the IM separation, and this has proved especially impactful for studies of large, multiply-charged ions ($> 100\text{kDa}$).⁴⁷ That is, as the ions drift through the PF-DT they experience a position-dependent E-field with an effective time-dependent field that is determined by the velocity and charge of the ion.^{125, 133, 134} The radial focusing characteristics of the PF-DT are similar to both TWIMS¹³⁵ and RF-confining uniform-field DT (RF-UF).^{47, 134} Gamage *et al.* were able to explicitly derive an effective potential model for the PF-DT that describes changes in the electric fields as a function of distance, which were then used to determine deviations from the uniform field (UF) trajectories owing to the oscillatory (non-linear) trajectories of ions in the PF drift field.¹³³ Silveira *et al.* derived an ion drift time damping term (α) that accounts for deviations in the drift times for ions in PF-DT as compared to UF-DT, which can be directly applied to the Mason-Schamp equation to calculate first-principles CCS.^{42, 49, 125, 133}

The mobility damping term (α) applies to all classes of analytes, as shown previously with C_{60}^+ , peptides, and denatured proteins,^{49, 134} Poltash *et al.* previously showed the utility of PF-DT for analysis of protein complexes, *i.e.*, TTR (MW 55.75 kDa).^{15, 18} CCSs were not reported in that study because the effects of α on the ATDs of native proteins or protein complexes ions had not been completed.¹³⁶ SIMION 8.1 simulations were performed to probe the relationship between α and reduced electric fields (E/N), denoted as $\alpha_{E/N}$, allowing for the calculation of first-principles CCS of native proteins and protein complexes. Trajectories for ubiquitin, transthyretin, and pyruvate kinase were simulated using *collision_hs1.lua*¹³⁷ (**Figure S1**) to probe native protein and

protein complexes over a range of molecular weights, charge states, and pressures (1.00 to 2.30 Torr) to obtain the ATDs for both PF-DT and UF-DT.⁴⁹ The simulated CCS/ATDs can be used to determine α as shown in **Equation 2**:¹³³

$$\alpha \approx \frac{CCS_{PF-DT}}{CCS_{UF-DT}} \approx \frac{ATD_{UF-DT}}{ATD_{PF-DT}}$$

[2]

Where CCS is the CCS obtained via **Eq. 1** for both PF-DT and UF-DT, and ATD is the arrival time distribution (s) of the ion packet in both the PF-DT and UF-DT.

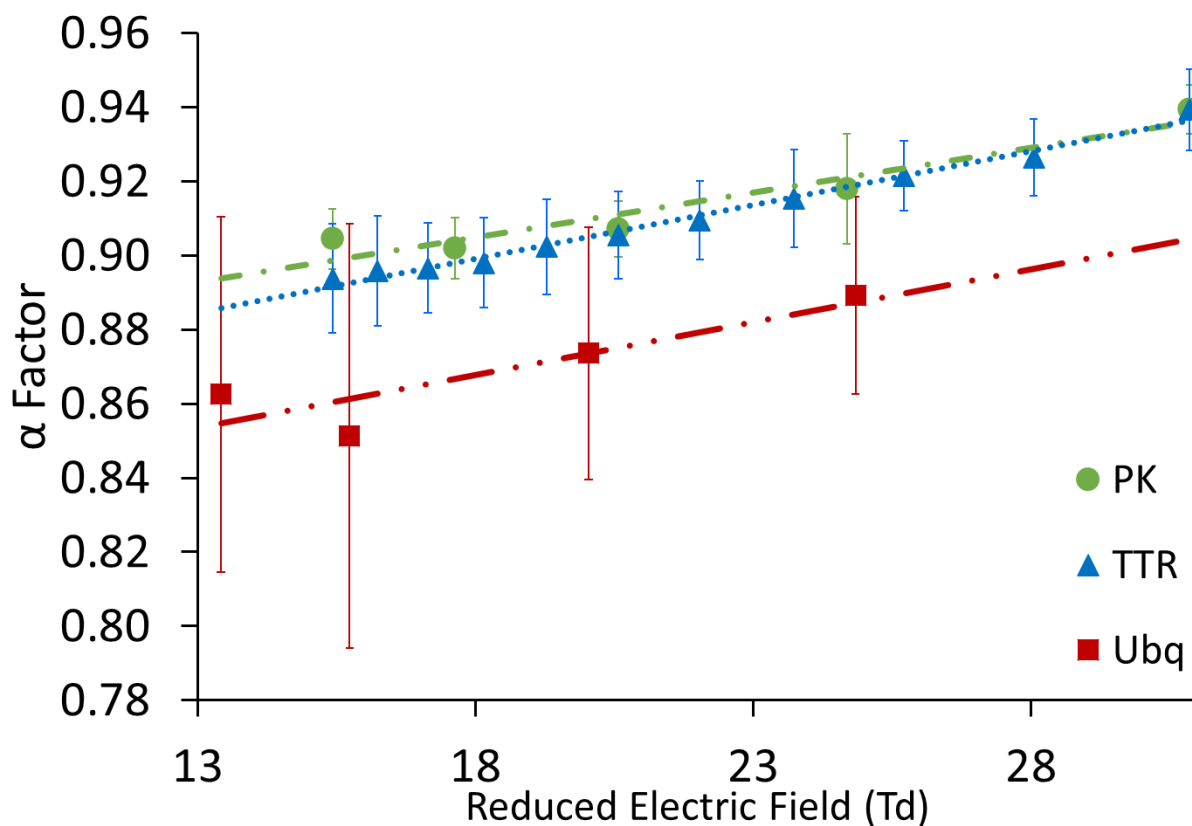


Figure 12 Calculated α values obtained for ubiquitin (red square, ~8kDa), transthyretin (blue triangles, ~56 kDa tetramer), and pyruvate kinase (green circles, ~86 kDa dimer), as a function of reduced electric field.

~257 kDa tetramer) versus the reduced electric field (E/N). These plots illustrate the dependence of α on the pressure and electric field. Note that larger proteins exhibit less radial motion than low molecular weight proteins at higher He pressure, leading to increasing α values with increasing molecular weight. By correlating α as a function of pressure, α can now be estimated over a range of electric fields and pressures.

Figure 12 contains plots of α versus reduced electric field (E/N) for simulated ion trajectories for proteins varying in molecular weight and charge. Generally, all three ions exhibit less radial motion (α approaches 1) with increasing E/N ; however, as E/N decreases, the ions experience a linear decrease in α owing to the change in pressure. Deviations from linearity at lower E/N is attributed to ions spending more time between the electrodes, leading to increased numbers of collisions.^{125, 133, 134} Error bars, shown in **Figure 12**, represent the propagated error ($\pm 1\sigma$) in the simulated ion arrival time distribution from both PF-DT and UF-DT.

The magnitude of the error bars of $\alpha_{E/N}$ for ubiquitin increases as E/N decreases (**Figure 12**) and is directly correlated to the amplitude of the oscillatory motion (X-Y plane, where Z is the direction of the applied E-field) of the ions in the PF-DT, which can lead to broadening of the ATD (see **Figure S1**). Simulations of both TTR and PK show a linear decrease that approaches an α value of approximately 0.89 and 0.91, respectively, at E/N of 15 Td. Proteins having similar size generally have similar charge state distributions, thus resulting in similar α values;²³ however, ion shapes, *i.e.*, prolate, spherical, and oblate (*vide infra*), are also a contributor to ion ATDs.¹³⁸⁻¹⁴² Silveria *et al.* described the effect that charge has on the expected α , where higher charge ions have less radial motion and increased focusing of ions.⁴⁹ However, SIMION simulations show that

when the charge state of a protein approaches 15^+ , (*e.g.* TTR and heavier), α approaches unity and increasing the charge of the protein does not significantly impact α . For example, the effects of the distance-dependent pseudo-RF E-field on heavy, multiply-charged ions, *viz.* pyruvate kinase (MW 233.4kDa), is diminished shown by the ion trajectories having less radial motion and increased ion focusing. This effect is similar to the stabilities of ion trajectories in an RF quadrupole where heavier complexes are more strongly influenced by the DC bias than by the applied RF potential, and the inverse is true for lower mass ions.^{125, 133} Ion trajectory simulations clearly demonstrate: (1) efficient radial focusing between each electrode, consistent with previous results for peptides and denatured proteins,^{18, 49, 125, 133, 134} (2) increased ion transmission for PF compared to UF (data not shown), and (3) amplified radial focusing and increased transmission for large protein systems carrying large numbers of charges.

First-Principles Determination of CCS

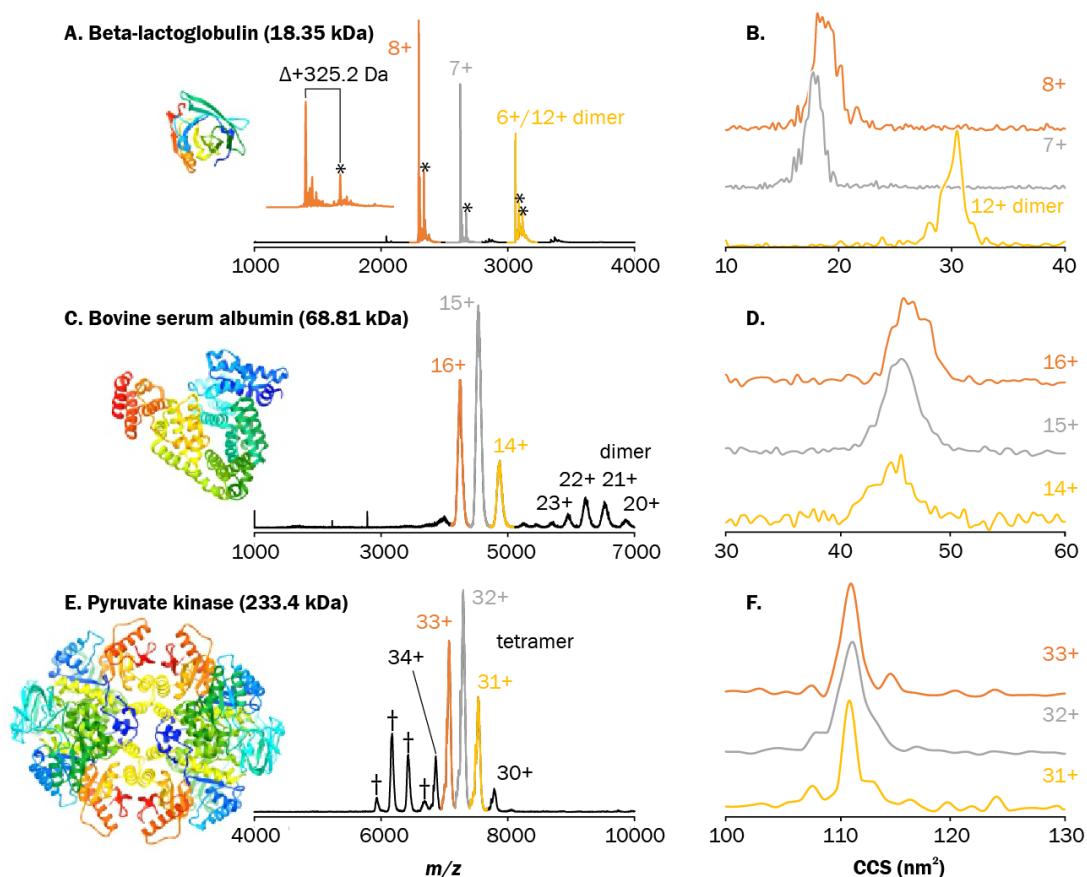


Figure 13 Native mass spectra and CCS profiles for β -lactoglobulin (PDB: 1BEB) (A, B), bovine serum albumin (PDB: 4F5S) (C, D), and pyruvate kinase (PDB: 1F3W) (E, F).¹⁴³⁻¹⁴⁵ The peaks in the mass spectrum of BLG denoted by * correspond to a bound disaccharide (+325.2 Da). The widths of the peaks in the mass spectrum of BSA are broadened owing to some unknown impurities. Similarly, the peaks in the CCS profiles are also broadened either owing to sample impurities and/or conformational heterogeneity. Peaks denoted by † in the pyruvate kinase sample is an impurity in the sample with an average mass of 154 kDa.

Experimental ATDs were used to calculate CCS values using **Eq. 1** and the $\alpha_{E/N}$ values derived from SIMION 8.1 (**Figure 13**). The $\alpha_{E/N}$ is applied as a function of MW of the protein, by categorizing proteins as small (<20 kDa), medium (<70 kDa), and large (>100 kDa) in a similar fashion to the $\alpha(z)$ previously reported by Silveria *et al.*⁴⁹

Figure 13 contains structures, mass spectra, and CCS profiles for β -lactoglobulin A monomer (BLG, 18.35 kDa), bovine serum albumin (BSA, 68.81 kDa), and pyruvate kinase (PK, 233.4 kDa). BLG, BSA, and PK are used as examples of small (<20 kDa), medium (<70 kDa), and large (>100 kDa) molecular weight proteins, respectively, that have been used as model proteins in previous studies and are listed in various reference CCS databases.¹⁴⁶ The mass resolving power of the Orbitrap allows for baseline separation of intact BLG as well as BLG bound to an endogenous ligand¹⁴⁷ with a mass of 325.2 Da (**Figure 13A**). Notably, using low resolving power instruments previously employed, the ligated form of BLG may not be sufficiently resolved to obtain a clean CCS profile(s).¹⁴⁸ Note also that signals for BLG⁶⁺ and 2BLG¹²⁺ ions are isobaric, and orthogonal separations using IM, are needed to confidently assign these signals. Based on the calculated CCS for the 2BLG¹²⁺ ions (**Figure 13B**), this signal is assigned to the dimer. The CCS for BLG monomer is 17.8 nm² as compared to 29.5 nm² for 2BLG¹²⁺, and both are in excellent agreement (1.9%) with previously reported RF-UF values.¹⁴⁶

The importance of mass resolving power is further illustrated by the analysis of BSA. Close inspection of MS signals of BSA suggests that they are significantly broadened compared to the expected isotope distribution (**Figure 13C**), possibly owing to unresolved protein-adduct ions. Note also that the CCS profiles for BSA 14⁺ and 16⁺ charge states are quite broad (**Figure 13D**). Possible sources for peak broadening are: (i) in the m/z domain unresolved adduct ions as observed for BLG and/or (ii) heterogeneity of the structure of the ion that is further complicated by these observed adducts in the mass

domain. To address this issue, several BSA samples were analyzed using a UHMR Orbitrap instrument.¹⁴⁹ The high-resolution mass spectra contained abundant signals for Cu-adducted BSA ions, whereas many as 10 Cu were observed (see **Figure S2-S4**).

The mass spectrum of PK (**Figure 13E**) contains abundant signals for the intact tetramer (with charge states of 30-34⁺). Low abundance, partially resolved signals from contaminants are also observed on the EMR platform. While the resolving power of the EMR Orbitrap is not sufficient to resolve these ions, they are fully resolved on the UHMR Orbitrap (see **Figure S5**). The deconvolution of the UHMR data shows contamination in the sample with a mass of ~154 kDa. CCS values obtained for the three most abundant tetrameric ions (PK³¹⁺ to PK³³⁺) were $109.7 \pm 1.7 \text{ nm}^2$, $109.9 \pm 0.1 \text{ nm}^2$, $110.0 \pm 0.6 \text{ nm}^2$, respectively (**Figure 13F**). These CCS were obtained by extracting the ATDs for the regions of the m/z peak that do not overlap with the partially resolved signals.

Collectively, the data contained in **Figure 13** demonstrate the capabilities of the FT-IMS-Orbitrap instrument for studies of small to large biomolecular ions. **Figure 13** also demonstrates similar sensitivity for a 1.5 m PF-DT when compared to the shorter, 58 cm PF-DT.¹⁵ In addition to being able to analyze higher MW complexes, an ion mobility resolution (centroid divided by CCS FWHM) of ~60 for PK was obtained due to this increased length of the DT, which to our knowledge is the highest DT-IM resolution reported for a large, intact native protein complex.

Benchmarking CCS to Other Methods

Figure 14 contains the comparison of α_{EN} corrected CCS values obtained by using the PF-DT to previously published CCS first-principles and CCS values computationally

calculated from atomic coordinates obtained from XRD using PSA, IMPACT, and Collidoscope.^{143-146, 150-160} The positive/negative percent differences correspond to a *larger/smaller* percent difference in the CCS of the respective methods from the PF-DT calculated CCS. As an example, the CCS of BSA calculated via IMPACT is 5.7% larger than the PF-DT CCS value. A complete listing of CCS values and PDB codes reported in **Figure 14** are listed in **Table 1**, and CCS for all the detected charge states of these proteins can be found in the supplemental information (**Table S2**). In general, the $\alpha_{E/N}$ corrected PF-DT CCS values are on average 5.5% larger than experimental CCS values obtained using RF-confining uniform-field (RF-UF), with increased deviation as the MW of the proteins increases. On average, PF-DT and calculated CCS differed by +8.3%, -2.3%, and +8.0% than those calculated using IMPACT, PSA, and Collidoscope, respectively.

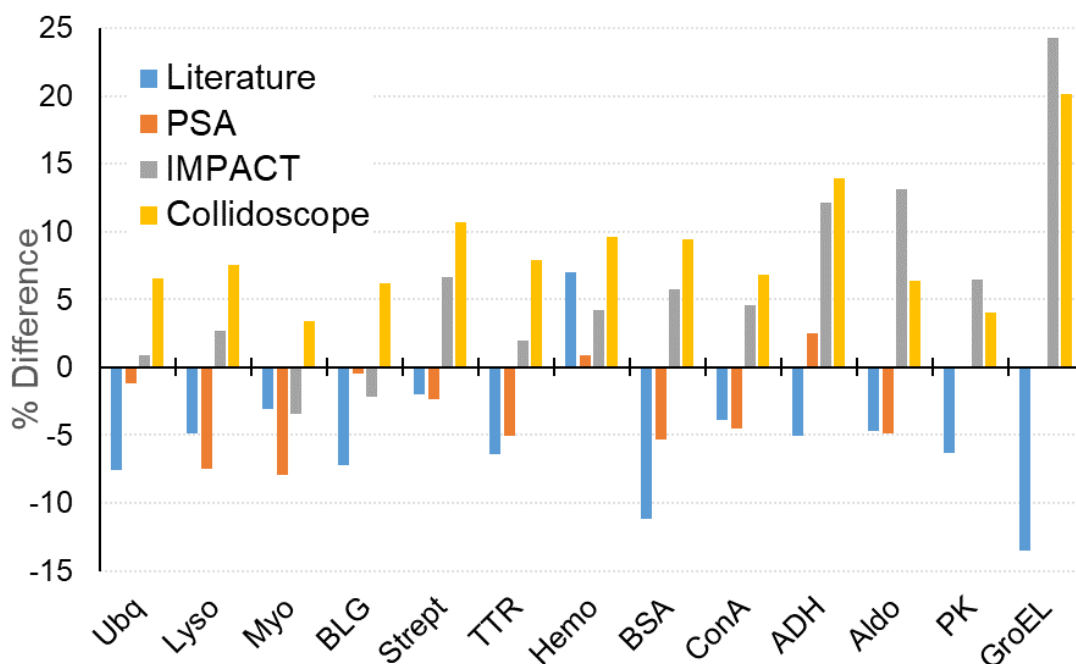


Figure 14 Percent difference of $\alpha_{E/N}$ corrected PF-DT CCS values vs literature experimental values and calculated CCS values from IMPACT, PSA, and Collidoscope for soluble proteins that span a range of molecular weights from 8.6 –

810 kDa. The CCS obtained using $\alpha_{E/N}$ corrected from Figure 2, using the lowest charge state of each protein in 200 mM ammonium acetate to be able to benchmark to previous literature values^{104, 146, 148, 161, 162}

Table 1 Summary of CCS values for replicate measurements ($n = 6$) as compared to other methods using the $\alpha_{E/N}$ mobility dampening term *vide supra*.^{104, 146, 161-163} Experimental CCS values are highlighted in red font for easier comparison between. Masses listed are experimentally determined values. A more complete list of references for sources of experimental CCS values is noted in Table S1.

Protein Name	Mass (kDa)	z(+)	PF-DT CCS (nm ²)	u(CCS) (%)	K ₀ (cm ² /V·s)	K ₀ /z	CCS Lit (nm ²)	IMPACT (nm ²)	PSA (nm ²)	Collidoscope (nm ²)	PDB Code
Ubiquitin	8.558	4	10.8	3.04	1.73	4.32E-01	10.0	10.9	10.7	11.2	1UBQ
Lysozyme	14.30	6	14.2	1.94	1.97	3.28E-01	13.6	14.6	13.2	13.6	1AKI
Myoglobin	17.56	7	17.7	2.57	1.83	2.61E-01	17.2	17.1	16.3	17.9	1WLA
β -Lactoglobulin	18.35	7	17.8	1.90	1.83	2.62E-01	16.6	17.4	17.8	18.2	1BEB
2 β -Lactoglobulin	36.71	12	29.5	1.20	1.83	3.06E-01	29.0	31.2	27.9	31.8	2Q2M
Strep	51.88	13	34.9	1.03	1.78	1.37E-01	33.4	37.0	34.3	38.1	4Y5D
TTR	55.75	14	36.3	0.53	1.83	1.30E-01	34.1	36.9	34.6	37.8	1F41
Hemoglobin	64.48	16	40.3	1.04	1.91	1.19E-01	43.2	42.0	40.6	43.5	2QSS
BSA	68.81	14	45.7	1.88	1.49	1.06E-01	40.9	51.2	44.2	51.8	3V03
Concanvalin A	102.9	18	57.7	0.20	1.50	8.35E-02	0.0	61.1	56.3	62.9	3QLQ
ADH	148.2	23	73.6	0.52	1.51	6.29E-02	69.4	82.9	74.9	83.9	4W6Z
Aldolase	157.1	23	79.8	0.80	1.39	6.04E-02	76.1	88.6	79.1	89.1	6ALD
Pyruvate Kinase	233.4	31	109.7	1.70	1.38	4.46E-02	103.0	115.3	-	116.2	1F3W
GroEL	810.1	63	239.8	2.01	1.41	2.24E-02	209.0	305.3	-	292.7	1SS8

GroEL, an homotetradecameric protein complex ($n=14$), was used to critically evaluate the performance of the IM-Orbitrap for the analysis of larger protein complexes. The charge states of GroEL vary depending on the solution/buffer conditions, and it is unclear as to whether these changes altered the structure of the GroEL complex.^{148, 162} The MS data collected of GroEL via the PF-DT show a higher experimental mass than the theoretical mass (802.1 kDa, UniProt: P0A6F5)¹⁶⁴ that may be attributed to water, salts, or other adducts trapped inside the GroEL cavity. Zero-charge MS data was compiled for various instrument configurations and activating conditions in supplemental **Table S3**. Previously reported CCS for GroEL were obtained from ammonium acetate solutions and the CCSs (210 to 270 nm²), are significantly smaller than the calculated CCS (~300 nm²).¹⁴⁶ **Figure 15** contains native MS and IM-MS data for GroEL showing: (A) mass

spectra (charge states centered at 65⁺), (B) ATD vs. *m/z* plot, and (C) a plot of experimental PF-DT CCS values (*n* = 6 replicate measurements) for the most abundant charge states versus previous reported experimental (TWIMS and RF-UF). Also shown in this figure are the calculated CCS values (Collidoscope and IMPACT) for GroEL structures obtained from cryo-EM (PDB: 5W0S) and XRD (PDB: 1SS8) structures.^{150, 151}

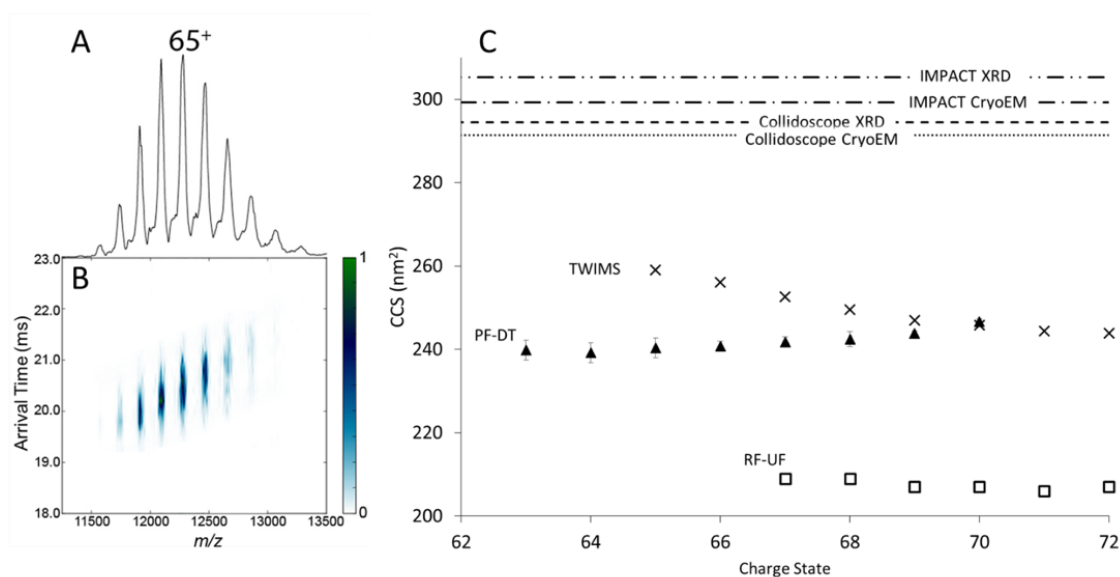


Figure 15 (A) mass spectra, (B) ATD vs mass plots, and (C) CCS vs CSD (n=6 replicate measurements) of native GroEL 14-mer complex with comparisons to PF-DT, TWIMS, RF-UF, Collidoscope, and IMPACT using both CryoEM (PDB: 5W0S) and XRD (PDB: 1SS8) structures.^{150, 151} CCS of each charge state for 14 mer GroEL as compared to IMPACT, Collidoscope (for both XRD and CryoEM), as well as TWIMS (Heck and coworkers 2009) and RF-UF (Bush and coworkers. 2010).^{146, 148}

The CCS obtained using PF-DT of $240 \pm 5 \text{ nm}^2$ for the 63⁺ charge state of GroEL is 24% and 20% smaller than that calculated by IMPACT using structures obtained by XRD and cryo-EM, respectively. These differences are also smaller (20% and 19%, respectively) than the Collidoscope calculated CCS. In both cases, the calculated values are considerably larger than the CCS obtained using PF-DT. There appears to be a small

increase in the CCS obtained by using PF-DT as the charge state increases; however, the CCS obtained by TWIMS decreases as the charge state increases.¹⁴⁸ It is generally observed that CCS increases with increasing charge, but to our knowledge, neither trend for CCS vs. charge state has been broadly applicable for protein complexes.

The smaller experimental CCS suggests that the gas-phase ions have significantly different shapes from GroEL molecules that are trapped in virtuous ice or a rigid crystal lattice. Previous studies have shown that apical domain of GroEL is highly flexible, and this flexibility is what allows ATP-dependent binding of the GroES to GroEL (group 1 chaperonins) resulting the transition from a “barrel” to a prolated “football” like structure.^{141, 142, 165-167} Similar flexibility of apical domain is found for Group 2 chaperonins that do not require GroES for function or formation of prolate “football” shapes.¹¹⁴ Thus, we attribute the differences between experimental and calculated CCS to differences in shapes of these ions. Ewing *et al.* explained these differences by invoking formation of collapsed conformers during the transition from solution to the gas phase;¹¹⁷ however, we estimate that a “closed” (prolate) conformation formed by changes in the orientation of the apical domain would have a smaller CCS than would an “open” conformation.^{141, 142} In fact, the GroEL ions sampled here are not fully dehydrated. For example, the mass of the GroEL ions we observed differs from the theoretical molecular weight by ~8,000 Da, *viz.* 810.1 kDa vs. 802.1 kDa., a mass difference that Heck and coworkers attributed to “...trapping water molecules, buffer molecules and salt within the protein complex”.⁹³ Preliminary results suggest that the water, buffer molecules, and salts present do not have a structural role. For example, mild collisional heating of the GroEL

65⁺ ions can be used to remove these adducted species from the 810.1 kDa GroEL ions, and the resulting 802.1 kDa GroEL ions also have a CCS of ~240 nm². Thus, the disparity between the experimental and calculated CCS for gas-phase ions and structures of condensed phase structures (cryo-EM and XRD)^{117,118} warrant more extensive experimental and computational investigations.

Conclusion

The PF-DT-FT-IMS-Orbitrap instrument takes advantage of radial focusing by the PF-DT, which increases the transmission of high charge state ions, and multiplexed data acquisition to overcome the duty-cycle mismatch of DT-IM and Orbitrap MS. Multiplexed acquisition also yields increased sensitivity owing to the inherent gains afforded by the Fellgett's or multiplexed advantage, *viz.* "more signal more of the time."¹⁶⁸ While traditional commercial IM time-of-flight (IM-ToF) instruments have made possible rapid developments in omics-related research, these instruments, unfortunately, fall short of the needs for the growing field of structural biology, *viz.* first-principles determinations of CCS combined with high-resolution MS measurements of native, intact proteins and protein complexes.

First-principles determinations of CCS of varying MW proteins and protein complexes (8.6 – 810 kDa) have been determined on a high-resolution PF-DT FT-IM-Orbitrap MS. The CCS values corrected for the mobility damping term, α , fall within 6% of previously published RF-UF values, and within 2-8% of CCS values calculated from crystal structures using different methods. Transmission for large biomolecules is increased by using the PF-DT, in agreement with trajectory simulations obtained by using

SIMON 8.1, thereby increasing the sensitivity of the PF-DT FT-IM-Orbitrap instrument. With smaller systems, sample complexity is not the limiting factor and the mass resolution of IM-ToF instruments is more than adequate for identification of charge states, low MW adducts, and/or truncations, which has been extensively demonstrated.^{9, 15, 18} The increased resolution offered on the PF-DT FT-IM-Orbitrap MS over traditional IM-ToF provides modern means to ascertain the purity of proteins (vis-à-vis fewer PTMs, noncovalent adducts, truncations, metalation, etc.) that can impact the conformational dynamics of the proteins. With the technological advancements achieved with the PF-DT FT-IM-Orbitrap platform, the rigor for pure samples for IM standards to be used as calibrants is brought to the fore.

Supporting Information

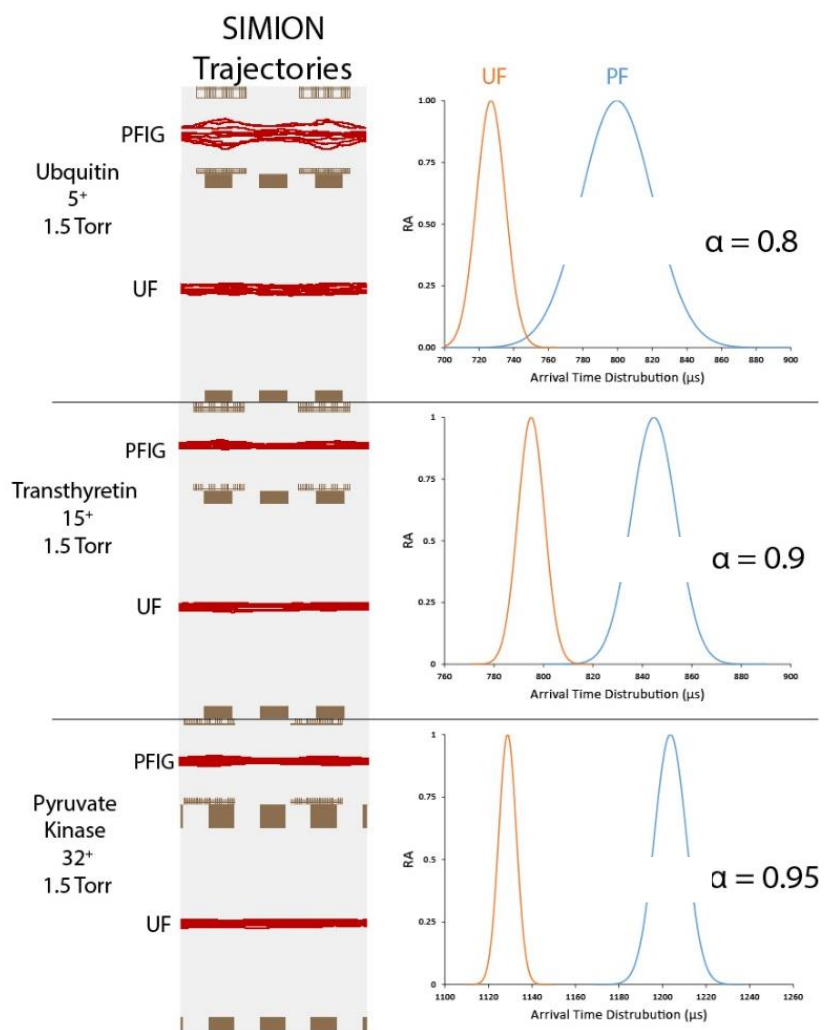


Figure S1: α factor determination via SIMION 8.1. 30 ions of different mass and CCS are simulated in a 10 cm uniform field (UF) and periodic focusing (DT). The average and standard deviation of the arrival time for the ions are fitted to a Gaussian peak. The ratio of the arrival times of UF vs PF gives rise to the calculated α value. The respective simulations were performed at multiple pressures to determine $\alpha_{E/N}$.

Table S1: Proteins and sources with abbreviations.

Protein	Abbrev	n	Molecular Weight (kDa)	Source	Manufacture	Product Number
Ubiquitin	Ubq	1	8.558	bovine erythrocytes	Sigma	U6253
Lysozyme	Lyso	1	14.30	Chicken Egg White	Fisher	BP535
Myoglobin	Myo	1	17.56	equine skeletal muscle	Sigma	M0630
β -Lactoglobulin A	BLG	1, 2	18.35, 36.71	bovine milk	Sigma	L7880
Streptavidin	Strept	4	51.88	<i>S. avidinii</i>	ThermoFisher	434301
Transthyretin	TTR	4	55.75	Recombinant	Ref ¹⁹	---
Hemoglobin	Hemo	4	64.48	Horse Heart	Sigma	H4632
Bovine Serum Albumin	BSA	1	68.81	Bovine	Sigma	05470
Concanavalin A	ConA	4	102.9	<i>Canavalia ensiformis</i>	Sigma	C2010
Alcohol Dehydrogenase	ADH	4	148.2	<i>S. cerevisiae</i>	Sigma	A7011
Aldolase	Aldo	4	157.1	rabbit muscle	Sigma	A2714
Pyruvate Kinase	PK	4	233.4	rabbit muscle	Sigma	P9136
GroEL	GroEL	14	810.1	Recombinant	Ref ¹¹⁸	---

Table S2: CCS and K_0 values calculated via PF-DT in helium (99.999%) for all experimental charge states. * denotes partially unfolded conformation.

Protein	Mass (kDa)	Pressure	z(+)	$\alpha_{E/N}$	PF-DT			
					CCS (nm ²)	u(CCS) (%)	K_0 (cm ² /V·s)	K_0/z
Ubq	8.558	1.725	4	0.87	10.8	3.04	1.73	4.32E-01
			5		11.4	3.17	2.06	4.11E-01
			6*		16.3	2.55	1.73	2.88E-01
Lyso	14.30	1.725	6	0.87	14.2	1.94	1.97	3.28E-01
			7		15.1	2.56	2.16	3.09E-01
			8*		19.2	4.37	1.94	2.43E-01
Myo	17.56	1.725	7	0.87	17.7	2.57	1.83	2.61E-01
			8		20.7	2.07	1.89	2.37E-01
BLG	18.35	1.725	7	0.87	17.8	1.90	1.83	2.62E-01
			8		18.2	2.72	2.06	2.57E-01
2 BLG	36.71	1.725	12	0.87	29.5	1.20	1.83	3.06E-01
Strept	51.88	2.085	13	0.89	34.9	1.03	1.78	1.37E-01
			14		36.9	1.38	1.81	1.30E-01
			15		37.5	0.82	1.91	1.27E-01
			16		37.1	2.02	2.06	1.29E-01
TTR	55.75	2.085	14	0.89	36.3	0.53	1.83	1.30E-01
			15		36.2	0.50	1.96	1.31E-01
			16		36.3	0.50	2.08	1.30E-01
Hemo	64.48	2.085	16	0.89	40.3	1.04	1.91	1.19E-01
			17		40.6	0.63	2.01	1.18E-01
BSA	68.81	1.786	14	0.90	45.7	1.88	1.49	1.06E-01
			15		45.8	0.76	1.60	1.06E-01
			16		45.9	1.25	1.70	1.06E-01
ConA	102.9	2.085	18	0.90	57.7	0.50	1.50	8.35E-02
			19		57.9	0.50	1.58	8.32E-02
			20		57.8	0.41	1.67	8.33E-02
			21		57.9	0.39	1.75	8.31E-02
ADH	148.2	2.085	23	0.90	73.6	0.52	1.51	6.29E-02
			24		73.0	0.54	1.57	6.29E-02
			25		73.6	0.50	1.63	6.27E-02
			26		73.7	0.50	1.69	6.26E-02

Table S2 (continued)

Aldo	157.1	2.085	23	0.90	79.8	0.80	1.39	6.04E-02
			24		80.1	0.41	1.44	6.02E-02
			25		80.1	0.54	1.50	6.01E-02
			26		81.3	1.97	1.54	5.93E-02
PK	233.4	1.558	31	0.91	109.7	1.70	1.38	4.46E-02
			32		109.9	0.50	1.42	4.45E-02
			33		110.0	0.60	1.47	4.45E-02
			34		110.1	0.85	1.52	4.46E-02
GroEL	810.1	1.645	61	1.00	231.1	2.10	1.42	2.33E-02
			62		237.6	2.04	1.40	2.26E-02
			63		239.8	2.01	1.41	2.24E-02
			64		239.2	0.95	1.44	2.25E-02
			65		240.4	0.96	1.45	2.24E-02
			66		240.8	1.49	1.47	2.23E-02
			67		241.8	0.50	1.49	2.22E-02
			68		242.5	0.58	1.51	2.22E-02
			69		243.8	0.50	1.52	2.20E-02
70	246.7	1.16	1.53	2.18E-02				

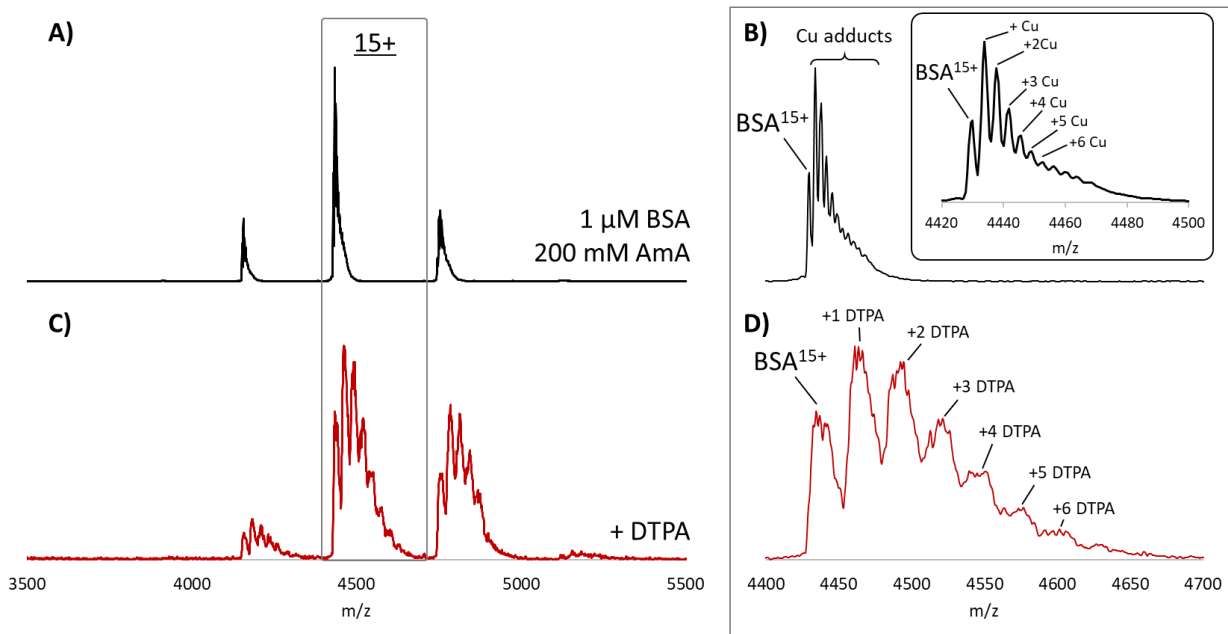


Figure S2. A) Resulting high-resolution MS spectra of native BSA results in charge state distributions centered on 15^+ . B) Expansion of the 15^+ mass distributions reveal a host of adducts with an average molecular weight of *ca.* 60 Da, identified as possible Cu adducts (inset). C) Addition of a known Cu chelator (DTPA, diethylenetriamine pentaacetic acid), results in a slight shift towards lower average charge and a host of adducts. D) Expansion of the BSA^{15+} distribution reveals up to 6 DTPA adducts.

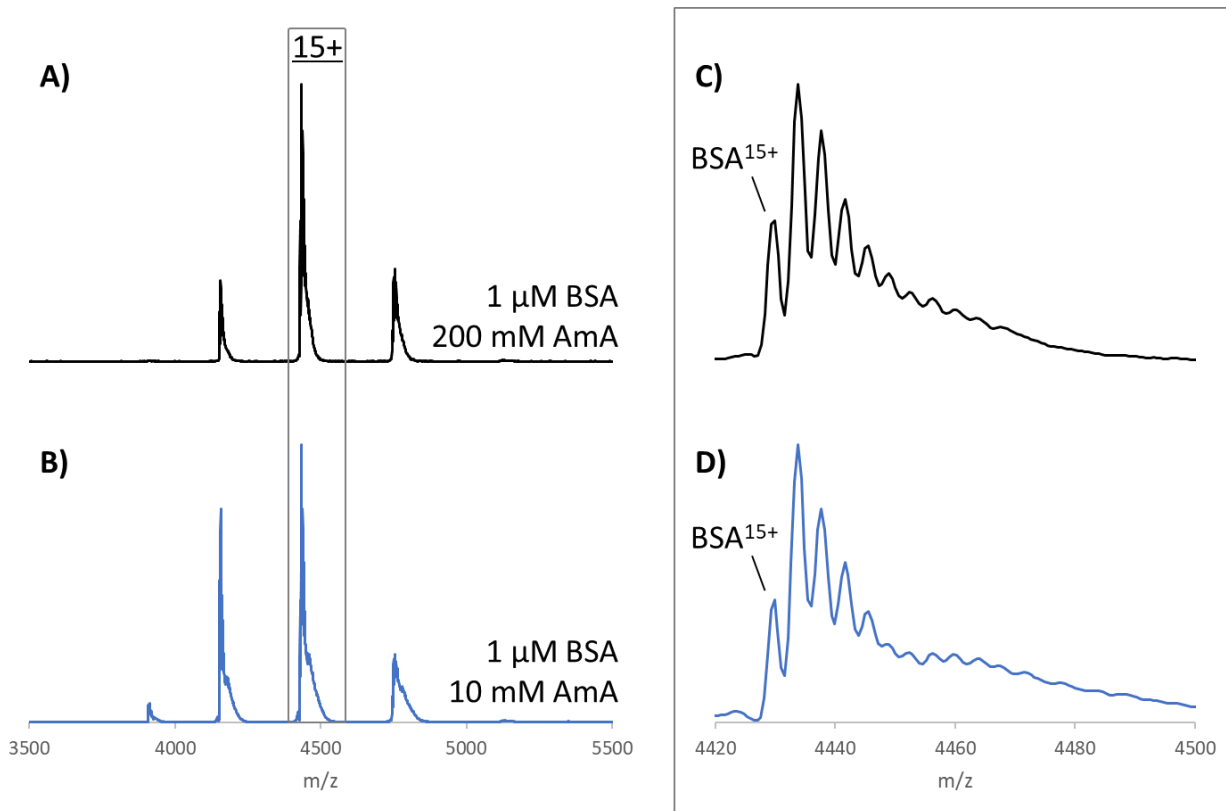


Figure S3. A) Resulting high-resolution MS spectra of native BSA in 200 mM ammonium acetate (AmA) results in charge state distributions centered on 15⁺. B) Decreasing the AmA concentration to 10 mM results in a slight shift towards higher average charge state. Expansion of the BSA¹⁵⁺ ion distributions from (C) 200 mM and (D) 10 mM AmA show qualitatively similar relative abundances of Cu adduction.

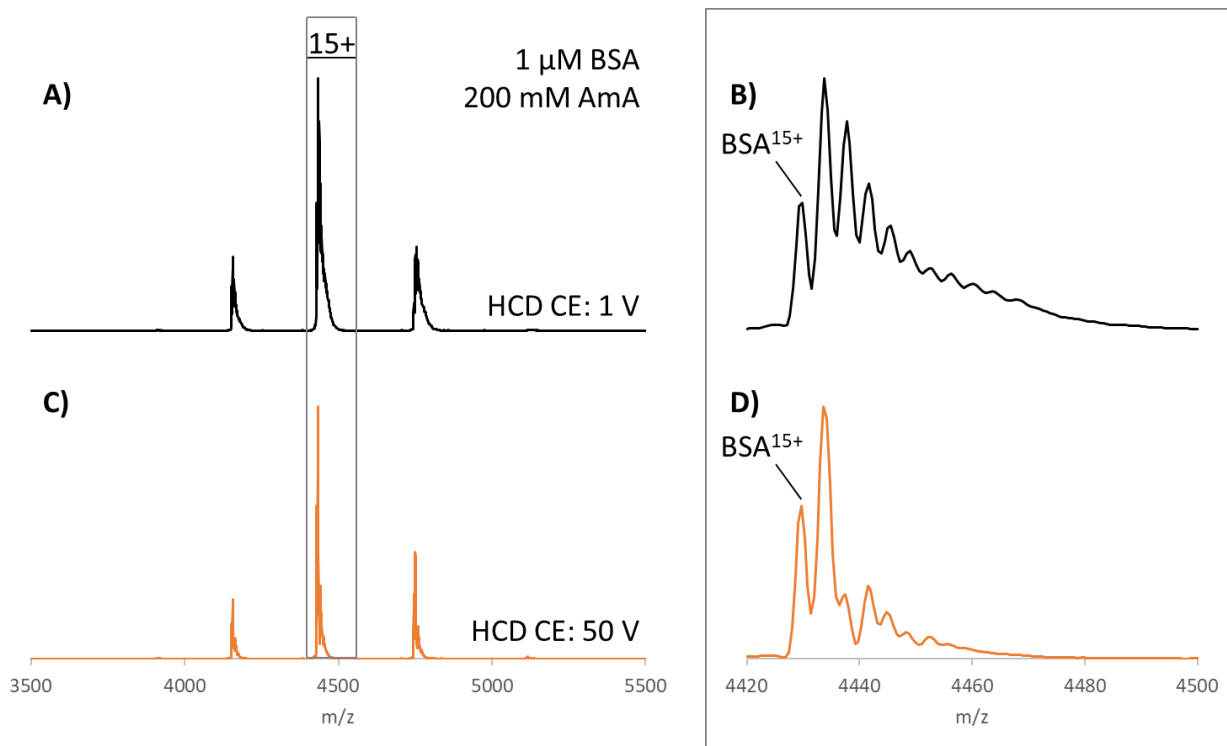


Figure S4. A) Resulting high resolution MS spectra of native BSA in 200 mM ammonium acetate (AmA) results in charge state distributions centered on 15+. B) Expansion of the BSA¹⁵⁺ spectra reveals several *ca.* 60 Da adducts. C) Increasing the HCD collision energy to 50 V does not significantly affect the observed charge state distribution. D) Expansion of the collisionally activated BSA¹⁵⁺ signal reveals fewer adducts.

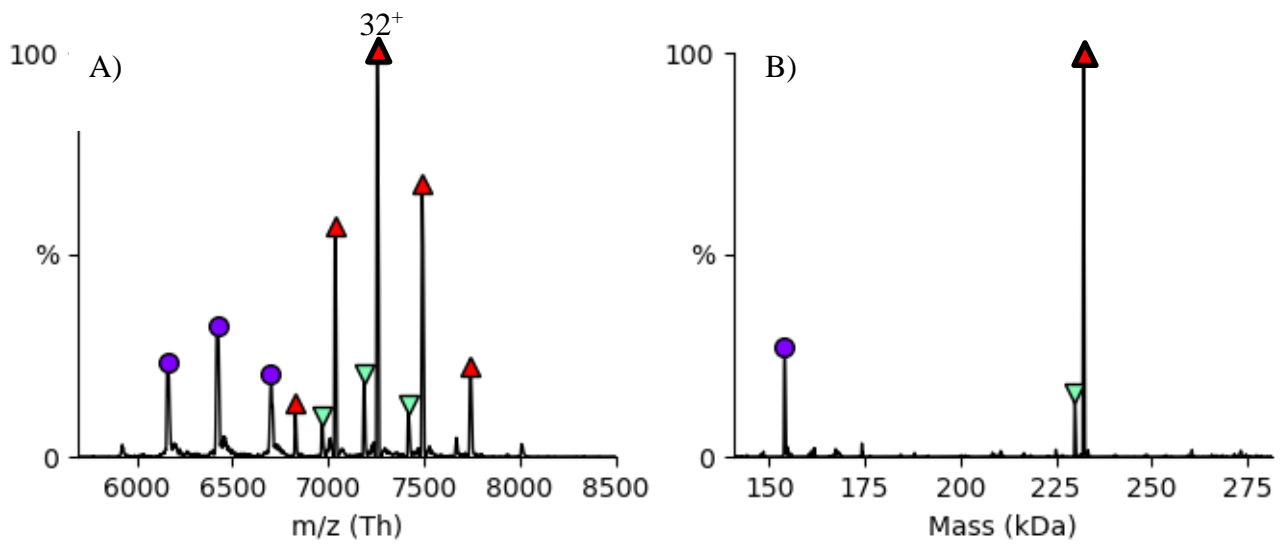


Figure S5. A) Resulting high resolution MS spectra of native pyruvate kinase in 200 mM ammonium acetate (AmA) results in charge state distributions centered on 32+. B) Deconvoluted MS of PK with the resulting masses: 154.1, 229.9, 232.2 kDa showing dirty samples that can be resolved by higher MS resolution.

Table S3: MS data for 1 μ M GroEL in 200 mM ammonium acetate (AmA) obtained on different instruments.

Charge State	GroEL Observed Mass			
	UHMR*	UHMR REIS†	IM EMR‡	EMR REIS†
75		801993.0		
74		802046.8		
73	800917.3	802001.4		
72	800904.2	802005.8		804825.4
71	800917.6	802060.7		804930.6
70	800926.7	802068.1	810649.7	805072.8
69	800921.0	802133.3	809940.6	805538.4
68	800933.2	802193.3	809914.7	805577.6
67	800940.1	802272.1	810259.1	805502.1
66	800950.9	802567.3	810454.3	805729.3
65	800953.4	802595.3	810432.4	805684.8
64	800955.5		810046.7	806036.5
63			809965.2	806665.9
62			810059.1	806290.8
61			810315.5	
60			810570.6	
Average Mass (Da)	800932.0	802176.1	810237.1	805623.1
Std.Dev	16.7	207.8	253.5	536.1
%RSD	0.0021	0.0259	0.0313	0.0665

* UHMR MS data were collected under the default GroEL tune file via the commercial ionization source.

† Both the UHMR and the EMR were modified in a similar fashion as previously described to optimize tuning and sensitivity while having gentle tune conditions.⁹

‡ IM-EMR data is collected via the optimized conditions with minimal heating to preserve native-like conformations.

CHAPTER III

DISCOVERY OF POTENT CHARGE=REDUCTION MOLECULES FOR NATIVE ION MOBILITY MASS SPECTROMETRY STUDIES*

Introduction

Native mass spectrometry (MS) is an emerging biophysical approach for characterizing the structure and function of biomolecular assemblies, especially for membrane protein complexes.¹⁶⁹⁻¹⁷² Under tuned conditions that minimize perturbation to protein structure, native MS can maintain non-covalent interactions in the gas phase that enables quantitative studies of ligand binding,^{10, 173, 174} subunits stoichiometry^{175, 176} and lipid-protein interactions.^{173, 177-179} Ion-mobility (IM) spectrometry in conjunction with MS provides means for the separation of ions by their size and charge along with determination of the rotationally-averaged collision cross section (CCS). IM-MS approaches have also been developed to characterize the resistance of membrane proteins and their complexes with ligands to unfolding in the gas-phase.^{174, 178, 180} Of late, native MS has uncovered that specific protein-lipid interactions can allosterically modulate other interactions with protein,^{173, 179} lipid,¹⁷⁷ and drug¹⁸¹⁻¹⁸³ molecules.

*Reprinted with permission from Lyu, J; Liu, Y.; McCabe, J.W.; *et al.* Discovery of Potent Charge-Reducing Molecules for Native Ion Mobility Mass Spectrometry Studies. *Analytical Chemistry*. **2020** 92 (16), 11242–11249. Copyright 2020 American Chemical Society.

Membrane proteins are typically encapsulated in detergent micelles for native MS studies. The detergent solubilized complexes are ionized using nano-electrospray ionization followed by application of minimal collisional activation to release the protein complex from the detergent micelle.^{184, 185} In general, the mass spectrometer is tuned to preserve the structure and non-covalent interactions of protein complexes.¹⁸⁶ However, even under carefully tuned instrument conditions, protein structure and function can inadvertently be disrupted, resulting in measurements that deviate from those obtained by other biophysical techniques. An attractive approach to preserve the non-covalent interactions is reducing the charges carried by protein molecules to reduce their internal energy and minimize coulombic repulsion thereby lowering the propensity for unfolding or activation.¹⁸⁷⁻¹⁸⁹ It has been well-established that detergents play an important role in the number of charge states acquired by membrane proteins.^{178, 184} N-Dodecyl- β -D-Maltopyranoside (DDM), a commonly used detergent for purifying and solubilizing membrane proteins, results in charges states that are difficult to minimize activation energy resulting in partial unfolding of membrane proteins.^{178, 181, 184} The discovery of charge-reducing detergents, such as tetraethylene glycol mono-octyl ether (C₈E₄) and n-dodecyl-N,N-dimethylamine-N-oxide (LDAO), has revolutionized the native MS field by enabling IM measurements of compact, native-like complexes with collision cross section (CCS) values that are in direct agreement with those calculated from atomic coordinates.¹⁷⁸ In addition to aiding the preservation of native-like states of protein complexes and increased spacing between bound adducts, which has been shown to be beneficial for observing more lipid bound states of membrane proteins.¹⁹⁰

Numerous studies have reported methods to achieve lower charge states of proteins for MS measurements.^{188, 190-194} Adding charge reducing chemicals to protein samples, such as the abundant naturally occurring osmolyte¹⁹⁵⁻¹⁹⁷ trimethylamine N-oxide (TMAO), has been shown to significantly lower the average charge state (Z_{avg}) of protein complexes.^{190, 198, 199} Imidazole and derivatives thereof have shown marginal charge reduction for membrane protein complexes (by about ~2-3 charge states), especially in cases when non-charge-reducing detergents are used.^{188, 200} Besides the addition of small molecules, synthetic oligoglycerol detergents have been developed for membrane protein complexes that exhibit varying charge-reducing properties.¹⁹¹ Despite recent advances in manipulation of charge, these charge reducing modalities have a number of limitations. Some charge-reducing molecules require high concentration to be effective and/or an undesirable tendency to adduct to protein complexes leading to broadened mass spectral peaks. There is a need to further investigate charge-reducing approaches that are not only effective, but also applicable to a wide range of proteins.

Experimental Section

Protein expression and purification. AmtB was expressed and purified as previously described¹⁷⁸ with the exception of a modified expression plasmid was used. The AmtB gene from *Escherichia coli* with N-terminal TEV protease cleavable His₁₀ and MBP (described in previous study¹⁷⁸) was amplified by polymerase chain reaction (PCR) and cloned into pCOLA backbone which also co-expresses GlnK with Y51F mutation

(removes possible heterogeneity arising from uridylation²⁰¹) as a TEV protease cleavable N-terminal fusion to Strep-tag II as described before¹⁰. The AmtB used in this study contains the C312T mutation that retains the ability to couple to GlnK (manuscript in preparation). For soluble proteins, streptavidin was purchased from Sigma, and egg white lysozyme was purchased from Amresco. GlnK was expressed and purified as previously described.¹⁰

Preparation of charge reducing reagents. Trimethylamine N-oxide was purchased from Cayman Chemical. Spermidine was purchased from Beantown Chemical. Spermine was purchased from Alfa Aesar. Histamine, bis(2-aminoethyl)amine, bis(3-aminopropyl)amine, tris(2-aminoethyl)amine, 3,3'-Diamino-N-methyldipropylamine, tris(3-aminopropyl)amine, piperazine, 1-(2-Aminoethyl)piperazine, 1,4-Bis(3-aminopropyl)piperazine were purchased from Sigma-Aldrich. Protein was buffer exchanged to 200mM ammonium acetate (supplemented with 0.5% C₈E₄ for membrane protein). Charge reducing reagents stocks were made by dissolved into the same buffer as the protein, and were mixed with protein to obtain desired final concentrations of charge reducing reagent.

Native mass spectrometry (MS) analysis of AmtB Native MS was performed on a Q Exactive Ultra-High Mass Range (UHMR) from ThermoFisher Scientific, modified with a custom reverse entry ion source (REIS) and 1.5 m drift tube. A Synapt G1 HDMS instrument with a 32-k RF generator from Waters Corporation was also used for

membrane and soluble protein measurements. Nono-electrospray ionization was performed as previously described¹⁸⁶. UHMR parameters applied for AmtB included 250 °C capillary temperature, 1.40kV spray voltage, 200 maximum inject time, resolution set to 6250 with 1 no averaging, 50eV in-source CID, 40 CE, trapping gas pressure of 5. Ion transfer is set to High m/z mode, with in-source desolvation voltage set to -180V.

Native MS analysis of soluble proteins. Measurements for soluble proteins were collected on a Synapt G1 HDMS from Waters. For GlnK, source temperature was lowered to 80 °C, and trap and transfer collision energy was set to 40 and 25, respectively. Trap wave velocity and height set to 300 m/s and 1V, respectively. IMS wave velocity and height set to 300 m/s and 18V, respectively. For streptavidin, source temperature was set to 80 °C, and trap and transfer collision energy was set to 20 and 10, respectively. Trap wave and velocity and height set to 300 m/s and 1V, respectively. IMS wave velocity and height set to 300 m/s and 18V, respectively. For lysozyme, capillary voltage was set to 1.5kV. Source temperature was set to 50 °C, with 50V and 2V on sampling and extraction cone, respectively. Trap and transfer CE were set to 30 and 15, respectively. Trap gas flow rate was set to 5mL/min. Trap wave and velocity and height set to 100 m/s and 0.4V, respectively. IMS wave velocity and height set to 100 m/s and 4V, respectively. Soluble protein spectra were collected from 1000 to 10000 m/z. All mass spectra were deconvoluted using Unidec²⁰².

Ion-Mobility Mass spectrometry. Ion-Mobility Mass Spectrometry (IM-MS) was performed on a homebuilt periodic focusing drift-tube (PF-DT) Fourier-transform IM (FT-IM) orbitrap platform, as described previously.^{9, 13, 18, 203} Briefly, ions are generated via a nano-ESI source before entering a heated capillary transfer tube at 155 °C, which are then focused into a RF-ion funnel (~3 Torr) before being differentially pumped into a DC only periodic focusing funnel with a field strength of 50V/cm. Ions are then gated using a modified Bradbury-Nelson gate that pulses ions into the 1.5 m PF-DT for mobility separation, with a second gate post-IM to allow for implementation of FT-IM. Two MKS calibrated manometers were placed on both ends of the PF-DT to ensure steady-state of He (99.999% purity). Ions are then transferred via a multipole into the HCD cell of the Thermo Scientific Exactive Series platform. FT-IM-PF-DT data is processed into ATDs and subsequently to CCS using custom Python 3.7 codes utilizing Scipy¹²⁰ and multiplierz¹¹⁹.

Determination of half maximal effective concentration (EC50). Native mass spectra of AmtB solubilized in 2x CMC C₈E₄ were processed with UniDec²⁰² to determine the weighted average charge state (Z_{avg}). The half maximal effective concentration (EC₅₀) or potency of charge-reducing compounds was calculated using a modified form of the Hill equation:²⁰⁴

$$Y = \frac{b}{1 + \left(\frac{EC_{50}}{X}\right)^{n_H}}$$

where n_H is the Hill coefficient, b is the value of the upper asymptote, and X is the concentration of charge-reducing molecule. Z_{avg} data was essentially inverted to enable the equation above to be fitted to the experimental data as follows:

$$Z' = \left(\frac{100}{Z_{avg}} \right) - \left(\frac{100}{Z_{avg,max}} \right)$$

where $Z_{avg,max}$ is the maximum average charge state measured without any charge reducing molecule added. Equation 1 was fitted to the inverted data using Python (version 3.7) scripts making use of NumPy and SciPy modules.^{121, 205} The resulting fits had an R^2 value of 0.98 or better. Z' and b were converted back to units of charge:

$$Z_{avg} = \frac{100}{Z' + \frac{100}{Z_{avg,max}}}$$

Plots were generated using Python and the Matplotlib module.²⁰⁶

Results and discussion

Inspired by recent reports of TMAO and imidazole derivatives' effectiveness for charge-reducing protein complexes,^{188, 190, 198, 199} we explored the potential of other small molecules found in biology and characterized their impact on the trimeric ammonia channel (AmtB), a model integral membrane protein (Fig. 16). The first molecule we investigated was histamine, an amine-functionalized imidazole involved in the immune response and plays important roles in the nervous system²⁰⁷. The addition of 100 mM histamine, which the charge-reducing properties have not been studied before, to AmtB solubilized in C_8E_4 resulted in a reduction of the Z_{avg} by four compared to the mass

spectrum acquired in the absence of histamine (Z_{avg} of 16.2) (Fig. 16B and Fig. S1). For reference, the addition of 100 mM TMAO results in a broad charge state distribution with a Z_{avg} of 10.9 (Fig. 16A). We next explored spermidine and spermine, natural polyamines found in cells and involved in many cellular functions, such as promoting cellular proliferation and required for replication of many viruses.²⁰⁸⁻²¹¹ Compared to histamine, spermidine and spermine at 100mM displayed pronounced charge-reducing properties with Z_{avg} of 10.9 and 10.0, respectively (Fig. 16C). Unlike TMAO, histamine, spermidine and spermine resulted in narrow charge state distributions (Fig. 16D). More specifically, the total number of charge states (Z_{tot}) for 10 and 250 mM TMAO was 13 and 6, respectively. The Z_{tot} for histamine, spermidine and spermine at the highest concentration investigated are 3, 4, and 3, respectively (Fig. 16D). Moreover, the quality of the mass spectra for these molecules did not diminish, unlike previous reports showing the various degree of adduction to soluble proteins.²¹²

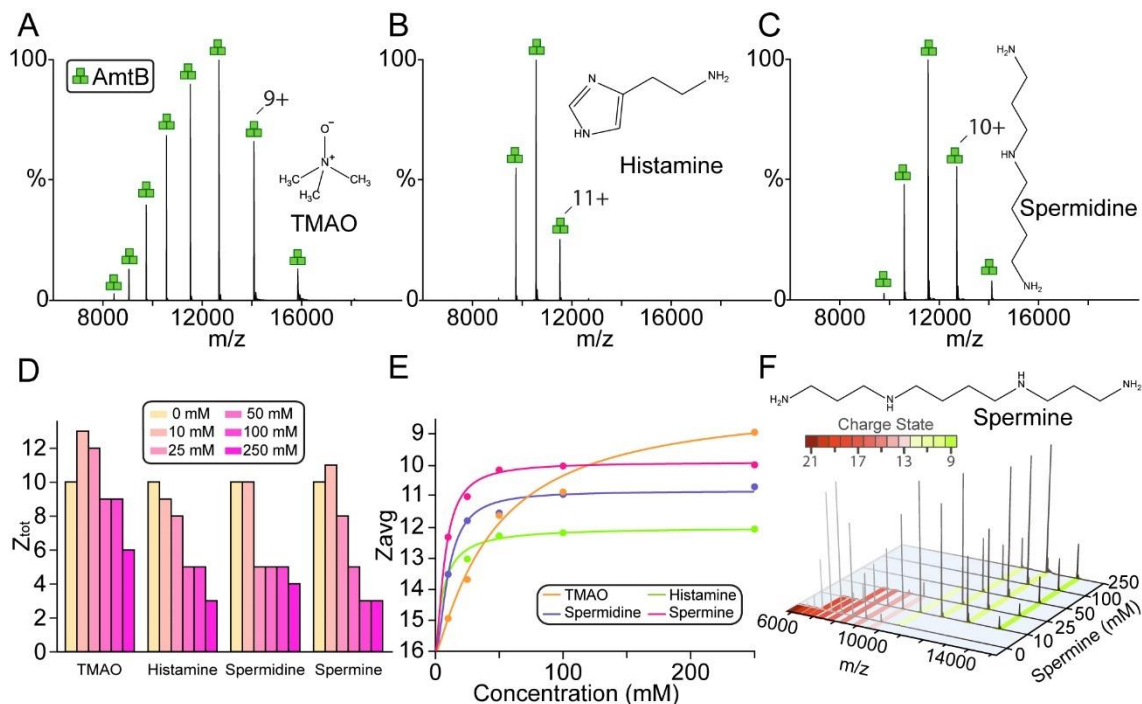


Figure 16 Natural compounds are potent charge-reducing molecules. A-C) Representative mass spectra of AmtB in C₈E₄ doped with 100 mM of (A) TMAO, (B) histamine, or (C) spermidine. Data was acquired on an ultra-high mass range (UHMR) Orbitrap mass spectrometer under gentle instrument conditions. Structures of molecules are shown in the inset. D) Total number of charge states for AmtB in the presence of compounds at different concentrations. E) Plot of average charge states (Z_{avg} , dots) as function of concentration of charge-reducing molecules. A modified form of Hill equation was fit to the data (solid lines) to determine the half maximal effective concentration (EC_{50}). F) Mass spectra of AmtB doped with different concentrations of spermine ranging from 0 to 250 mM.

We next titrated AmtB with different charge-reducing molecules to better understand the potency of these compounds. For example, AmtB in the presence of increasing concentrations of spermine progressively reduced charge on the protein complex (Fig. 16F). At low concentrations of spermine the charge state distribution was broad and asymmetric. Interestingly, at higher spermine concentrations the charge-reducing effect

was diminished and Z_{avg} reached a plateau around 10 (Fig. 16E). In a similar fashion to spermine, histamine and spermidine displayed a rapid decrease in Z_{avg} at lower concentrations and reached a plateau at higher concentrations, over 100 mM (Fig. 16E). The trend for TMAO differed from other compounds where Z_{avg} gradually decrease with increasing concentrations (Fig. 16E). To quantify the potency of these compounds, a modified form of the Hill equation was fit to the Z_{avg} data to determine the half maximal effective concentration (EC_{50}) and the minimum Z_{avg} value (or upper asymptote). With the exception of TMAO, the charge-reducing molecules had an $EC_{50} \sim 10$ mM whereas the value for minimum Z_{avg} ($Z_{avg,min}$) was the lowest for spermine (Table S1). In contrast, TMAO with an EC_{50} of 87 mM for the range of concentrations screened is nearly nine-fold greater than the other molecules. Lastly, it is worth noting that 10mM spermine achieved the same degree of charge reduction for AmtB as 250 mM histamine, underscoring the potency of this class of compounds.

Given the results for amine-functionalized linear molecules, cyclic amines such as piperazine and piperazine derivatives were investigated for their ability to charge-reduce AmtB in C_8E_4 (Fig. 17 and Table S1, S2). Titration of piperazine revealed a shallow change in Z_{avg} with increasing concentration and reaching $Z_{avg,min}$ of 14. Piperazine derivatives with one aminoethyl (AEP, 1-(2-Aminoethyl)piperazine) or two aminopropyl (APP, 1,4-Bis(3-aminopropyl)piperazine) substituents increased the amount charge-reduction with $Z_{avg,min}$ of 13 and 10, respectively (Fig. 17B-C). Piperazine and derivatives have a range of EC_{50} values (7-12 mM) and, like other amine containing molecules, the

charge-reducing effect reached a plateau at higher concentrations. Interestingly, substitution of piperazine with amine containing substituents not only increased the ability to charge-reduce but also resulted in narrowing of the charge state distribution where Z_{tot} decreased from 7 to 5 at the highest concentration studied (Table S3). However, APP, the best piperazine derivative, was not as potent in regards to charge-reduction compared to spermine. Taken together, these results suggest that aliphatic polyamines represent promising candidates as charge-reducing agents.

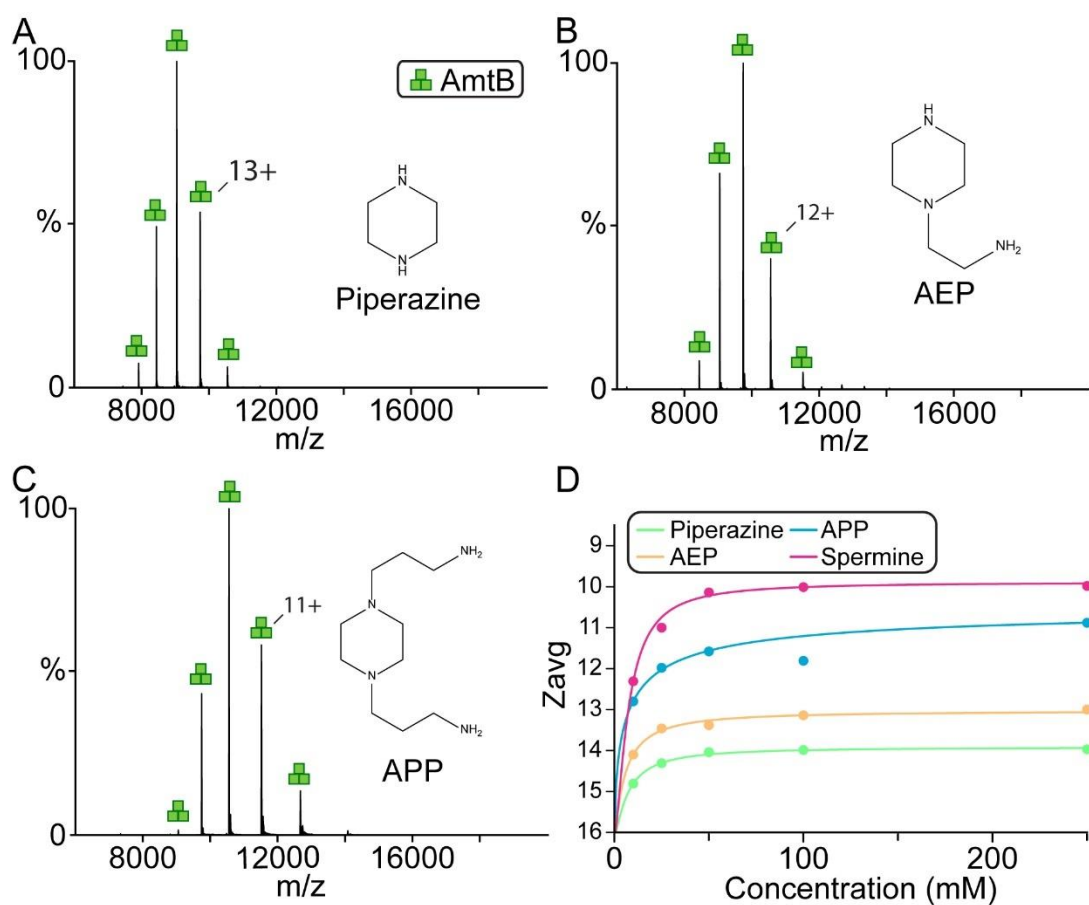


Figure 17 Charge reduction of AmtB by piperazine and amine derivatives thereof. A-C) Representative mass spectra of AmtB in C8E4 doped with 100 mM of (A) piperazine, (B) AEP, and (C) APP. Structures of molecules are shown in the inset. D) Plot of Z_{avg} (dots) as function of concentration of charge-reducing molecules and regression of a modified Hill equation (solid lines).

The results for spermine and other natural polyamines prompted us to investigate analogues of polyamines. Bis(2-aminoethyl)amine (B2A) and bis(3-aminopropyl)amine (B3A) are symmetric variants of spermidine (contains aminopropyl and aminobutyl groups) and addition of these compounds resulted in charge-reduction of AmtB (Fig. 18A-B). However, B2A and B3A were not as potent compared to spermine with a Z_{avg} of 11. A marginal increase in charge-reducing properties (Z_{avg} decrease by ~ 1) was observed for 3,3-Diamino-N-methyldipropylamine (DMP), which differs from B3A by a methyl group (Fig. 18C). Tris(2-aminoethyl)amine (T2A) and Tris(3-aminopropyl)amine (T3A) are molecules with four amines and showed increase charge-reducing properties compared to their counterparts B2A and B3A, respectively. T3A at the highest concentration reduced charge at comparable levels to that of spermine and spermidine. Notably, the addition of amine resulted in a reduction of both Z_{tot} and $Z_{avg,min}$. No correlation is observed for EC_{50} and $Z_{avg,min}$ of these molecules.

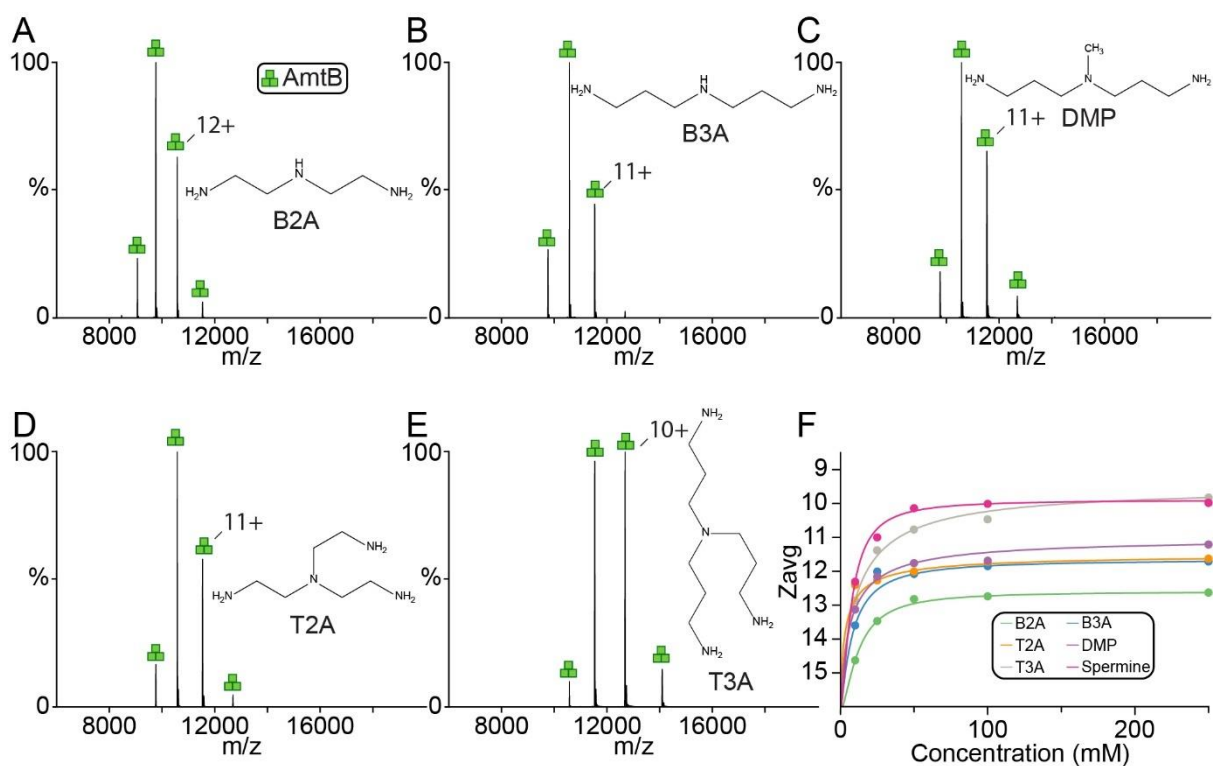


Figure 18 Charge-reduction of AmtB by synthetic polyamines. A-E) Representative mass spectra of AmtB in C_8E_4 doped with 100 mM of (A) B2A (B) B3A (C) DMP (D) T2A (E) T3A. Structures of molecules are shown in the inset. F) Plot of Z_{avg} (dots) as function of concentration of charge-reducing molecules and regression of a modified Hill equation (solid lines).

We next evaluated the performance of charge-reducing molecules for native ion mobility mass spectrometry (IM-MS) studies. Native IM-MS data was collected for a subset of molecules at 50mM concentration on a high-resolution Fourier-transform ion-mobility (FT-IM) PF-DT Orbitrap platform²⁰³ (Fig. 19). The mass spectrum of AmtB in C_8E_4 acquired on the FT-IM-PF-DT Orbitrap is comparable to that obtained using the commercial ionization source (Fig. 19 and S1). However, lower charge states for AmtB in the presence of spermine was observed on the FT-IM-PF-DT, consistent with previous results.^{203, 213} The collision cross section (CCS) profiles for the lowest (C_8E_4) and most

charge reducing (addition of Spermine) show a 0.4% difference with a slightly decreased in the R_{IM} of spermine (Fig. 19C). Here, CCS values for AmtB in the absence and presence of different charge-reducing molecules show, at most, a 3% difference (Fig. 19D).

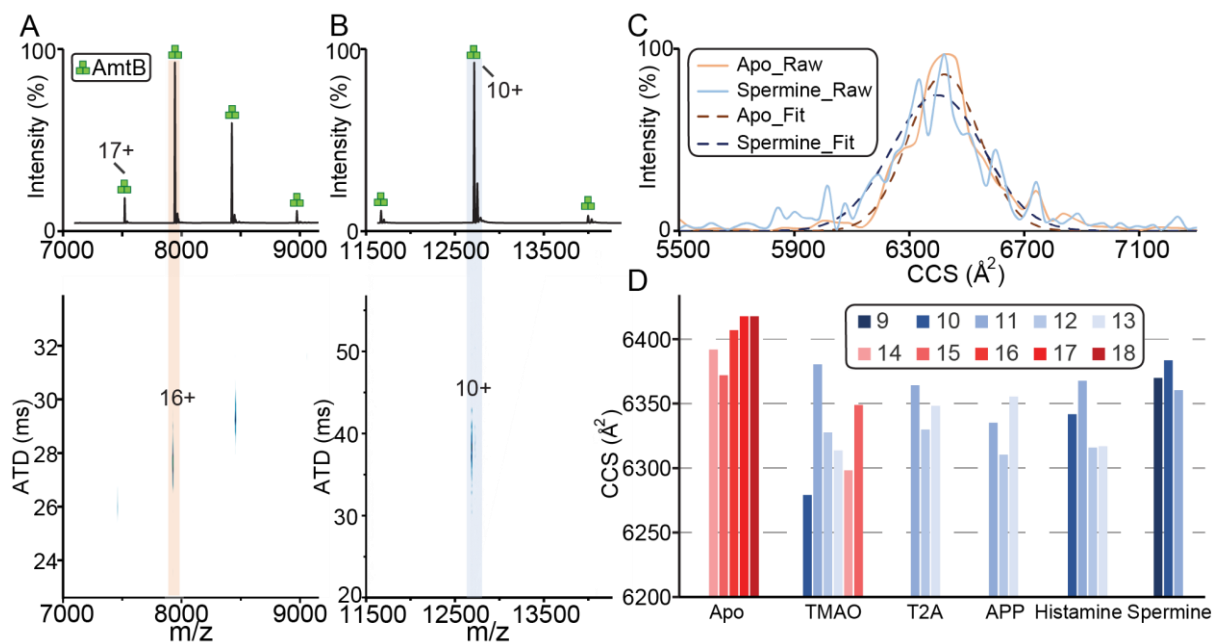


Figure 19 Native IM-MS of trimeric AmtB on a FT-IM-PF-DT Orbitrap platform. A-B) Ion mobility mass spectra of AmtB in (A) C_8E_4 and in the presence of (B) 50 mM Spermine. (C) Collision cross section (CCS) profiles for the most abundant charge states. A Gaussian function was fitted (solid lines) to the data (dashed lines) to determine the centroid CCS. (D) Plot of CCS for different charge states from AmtB in the presence of different charge reducing molecules.

We also explored the charge-reducing effect of these reagents on AmtB solubilized in the non-charge-reducing detergent DDM. Mixtures of AmtB in DDM with different charge-reducing molecules and at various concentrations could not generate interpretable mass spectra (Fig. S2). This finding is consistent with a recent study that reports charge-reduction of membrane proteins with alkali metal acetate is dependent on detergent.¹⁹³ However, the mechanism behind this phenomenon is not clear but a plausible explanation is that DDM may directly compete with these molecules interacting with the membrane protein. Alternatively, the larger micelle size of DDM may prevent meaningful contacts between these molecules and the protein. Nevertheless, C₈E₄ exhibits charge-reducing properties that are amplified (mutually or inclusive) with charge-reducing molecules, such polyamines. These results highlight the fact that there is an urgent need for detergents engineered for native MS applications that have desirable attributes, such as charge-reducing properties, ease of release from the protein complex, and the ability to stabilize membrane proteins.

The ability of these molecules to charge-reduce soluble proteins was also investigated. The monomeric lysozyme, trimeric GlnK, and tetrameric streptavidin were mixed with a charge-reducing reagent at equimolar ratios (Fig. S3). Some of the charge-reducing molecules adducted to the protein giving rise to an uninterpretable mass spectrum. This adduction behavior indicates that they interact strongly with proteins. Charged-reduced mass spectra for the three soluble proteins were observed for T3A, while the others were

largely protein-dependent. For example, lysozyme in the presence of B2A was poorly resolved whereas spermine, APP and B3A resulted in resolved mass spectra. Data quality and charge reduction patterns differed for GlnK and Streptavidin. It is interesting to note that TMAO's ability to charge-reduce does not prevent the gas-phase dissociation of oligomeric proteins tested. Recently, charge reduction of soluble proteins by TMAO has been reported to be dependent on collisional activation.¹⁹⁸ We next investigated the impact of increasing collision energy and cone voltage for soluble proteins. Activation of lysozyme in the presence of 50 mM spermine using either collision energy or cone voltage did not result enhanced charge reduction (Fig. S6-7). In summary, polyamines can charge-reduce soluble proteins but their efficacy appears to be protein-dependent.

To better understand the mechanism of charge reduction for membrane proteins, we conducted studies of AmtB in C₈E₄ with either 100mM spermine or TMAO at different solution or capillary temperatures. Native mass spectra of AmtB in the presence of spermine or TMAO acquired under different solution temperatures (32.0 to 37.0°C) showed similar results (Fig. S8). AmtB with either charge reducing additive was introduced into the mass spectrometer with the capillary temperature ranging from 100 to 430°C. For spermine, a capillary temperature below 200°C resulted in severe adduction, presumably spermine molecules, and a resolved mass spectrum was not obtained. For both additives, increasing the capillary temperature resulted in reduction of Z_{avg} (Fig. 20). The Z_{avg} of AmtB with spermine marginally decreased from 9.8 to 9.5 at 430°C (Fig. 20A). For TMAO, Z_{avg} significantly decreased from 12.0 to 9.3 at the highest capillary

temperature (Fig. 20B). We also noticed that application of backing pressure to nanoESI emitter for AmtB with TMAO resulted in significant reduction in charge (Fig. 20C-D). This observation can be rationalized the production of larger droplets results in a higher concentration of TMAO in the final droplets formed in the electrospray process. Taken together, our findings are in good agreement with previous reports^{212, 214} and indicate that charge reduction occurs in the final stages of the desolvation process.

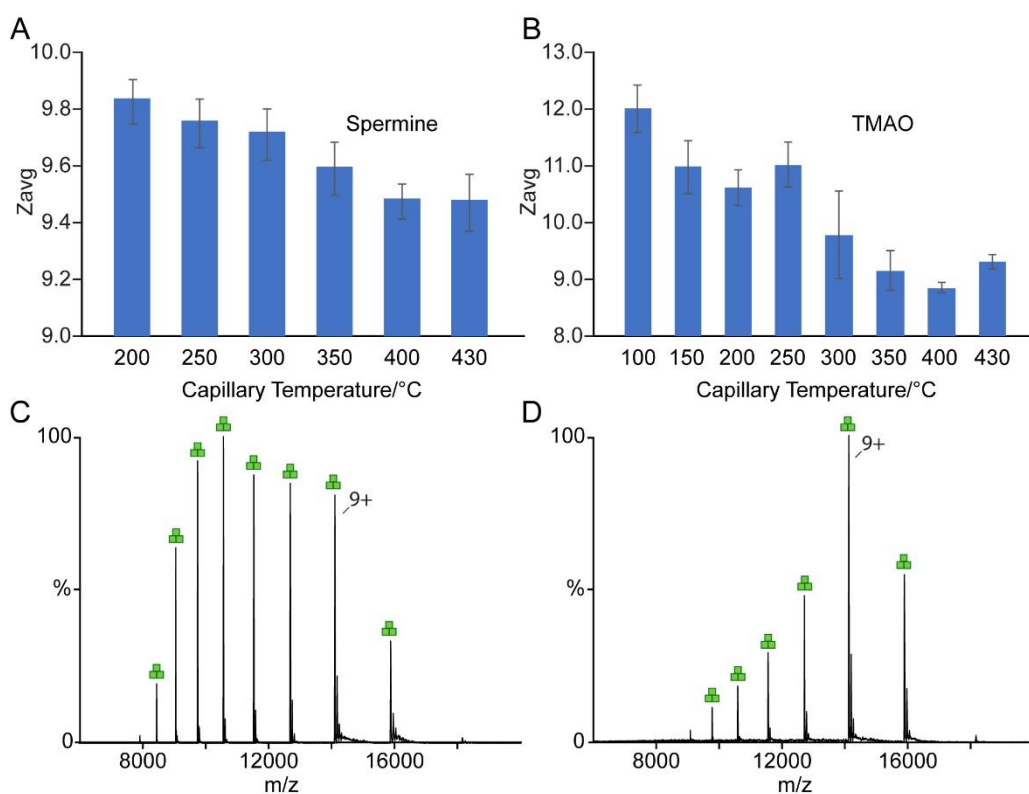


Figure 20 Effects of Capillary temperature and backing pressure on charge-reduction of AmtB . A-B) Z_{avg} of AmtB in the presence of 100mM (A) spermine or (B) TMAO acquired at different capillary temperatures. C-D) Mass spectra of AmtB charge reduced by 100 mM TMAO (C) without and (D) with application of backing pressure to the nanoESI emitter.

Figure 5.

By comparison of the chemical structures and their potency of charge reduction, a plausible explanation is that potency is correlated with their gas-phase basicity. Heck and co-workers have shown using soluble proteins a linear relationship between the additive gas-phase basicity (or proton affinity) and average charge state.²¹⁴ For polyamines, it has been reported that increasing either the number of nitrogen or carbon atoms results in higher gas-phase basicity.²¹⁵ Following on this generalization, the installation of a methyl group at the secondary amine of B3A makes DMP more basic that in turn improves its charge-reduction potency. Moreover, increasing the number of amino groups within the molecule, which increase gas-phase basicity, also leads to better charge-reducing molecule as seen for piperazine and derivatives thereof. Our observation of the potency of these charge reduction chemicals reveals there is a correlation with EC₅₀ and empirically measured gas-phase basicity, which agrees with the previous reports.^{212, 214-216} Another contributing feature of the charge-reducing molecule is the number of carbons, which would increase gas-phase basicity.²¹⁵⁻²¹⁸ Polyamines with more carbons generally show greater degree of charge reduction.²¹⁵ Among these charge reduction chemicals, TMAO appears to be outlier due to the significant difference in the Hill plot compared to other polyamines, which could be explained by the difference of charge reduction mechanism of TMAO. It has been proposed that TMAO reduces charge of proteins by proton transfer from gas-phase collision.¹⁹⁸ However, it remains difficult to discern if this process is result of (i) additive ligand dissociating from the protein either taking a proton with it or leaves the proton on the protein,^{212, 214} (ii) gas-phase collision of the additive with protein resulting in proton transfer to the additive,¹⁹⁸ or (iii) a combination of both processes.

The results of this study also point to an additional feature that implicates the direct interaction of charge-reducing molecules and protein. For example, there are marked differences when comparing spermidine and B3A, which differ by $Z_{\text{avg,tot}}$ by one charge. In addition, longer alkyl chains may interact more strongly with membrane proteins and/or detergent micelles. Different detergent environments may have different degrees of accessible protein surface area due to potential changes in droplet size and/or detergent micelle size. Taken together, the varied effects of polyamines on soluble proteins may be due to the hydrophobicity of the molecules in combination with their basicity. In short, the system composed of detergent encapsulated membrane proteins with charge reducing molecules is complex and further studies are warranted to better understand the dependence of detergent on charge reduction.

Conclusion

In summary, this study reports a set of potent charge-reducing molecules for native IM-MS studies. The reported molecules do not adduct nor impede the analysis membrane proteins for native MS studies. We also demonstrate improved charge-reduction potency; spermidine requires nearly 10-fold less in concentration compared to TMAO to achieve the same degree of charge reduction. Moreover, the polyamines are advantageous over TMAO as a narrower charge state distribution is observed improving the signal-to-noise ratio. Polyamines provide new approaches to manipulate charge in efforts to preserve non-covalent interactions and minimize perturbation and over-activation.

Supporting Information

Table S1. EC₅₀ and other fitting parameters for different charge-reducing molecules.

	n _H	EC ₅₀ (mM)	b	Z _{avg,min}
<i>Trimethylamine N-oxide</i>	1.1	87.3	6.5	7.9
<i>Histamine</i>	1.1	8	2.1	12
<i>Spermidine</i>	1.7	12.9	3.1	10.8
<i>Spermine</i>	1.5	10.2	3.9	9.9
<i>Piperazine</i>	1.3	8.2	1	13.9
<i>1-(2-Aminoethyl)piperazine</i>	1.1	6.8	1.5	13
<i>1,4-Bis(3-aminopropyl)piperazine</i>	0.6	11.6	3.4	10.4
<i>Bis(2-aminoethyl)amine</i>	1.5	14.2	1.7	12.6
<i>Bis(3-aminopropyl)amine</i>	1.2	10.5	2.4	11.6
<i>3,3-Diamino-N-methyldipropylamine</i>	0.9	10.4	2.9	11
<i>Tris(2-aminoethyl)amine</i>	0.8	5	2.5	11.5
<i>Tris(3-aminopropyl)amine</i>	0.9	18.6	4.4	9.5

Table S2. Name abbreviation of charge reducing chemicals.

Chemicals	Abbreviation
Trimethylamine N-oxide	TMAO
1-(2-Aminoethyl)piperazine	AEP
1,4-Bis(3-aminopropyl)piperazine	APP
Bis(2-aminoethyl)amine	B2A
Bis(3-aminopropyl)amine	B3A
3,3-Diamino-N-methyldipropylamine	DMP
Tris(2-aminoethyl)amine	T2A
Tris(3-aminopropyl)amine	T3A

Table S3. Total number of charge states (Z_{tot}) of AmtB mixed with charge reducing agents at various concentrations.

	0 mM	10 mM	25 mM	50 mM	100 mM	250 mM
TMAO	10	13	12	9	9	6
Histamine	10	9	8	5	5	3
Spermidine	10	10	5	5	5	4
Spermine	10	11	8	5	3	3
Piperazine	10	9	8	7	7	7
AEP	10	7	7	7	7	8
APP	10	7	7	6	6	5
B2A	10	9	7	6	5	5
B3A	10	9	6	5	4	4
DMP	10	9	6	6	5	5
T2A	10	9	6	5	4	4
T3A	10	11	7	5	4	4

Supplementary Figures

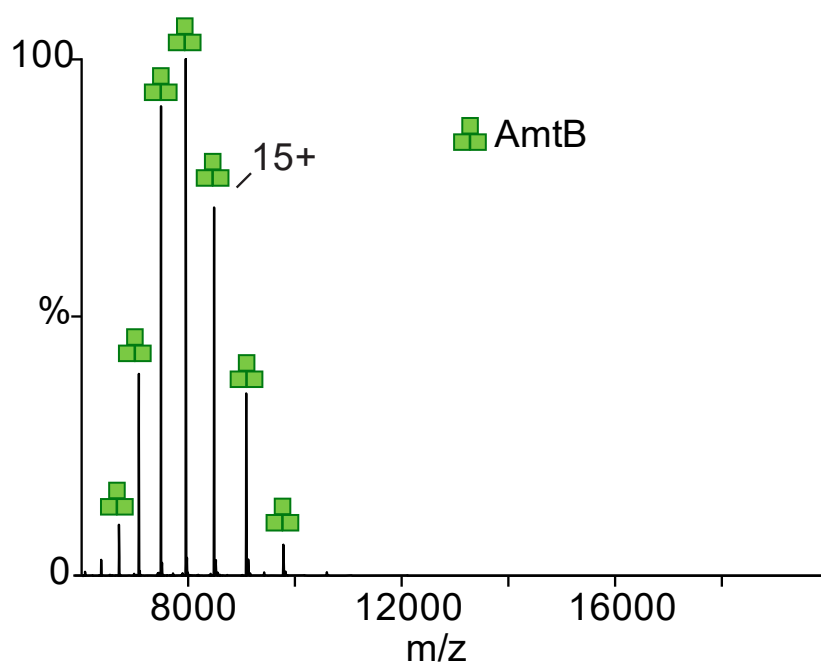


Figure S1. Native mass spectrum of AmtB in 200 mM AA with 0.5% (v/v) C₈E₄ collected on the UHMR, no additional charge reducing reagent added.

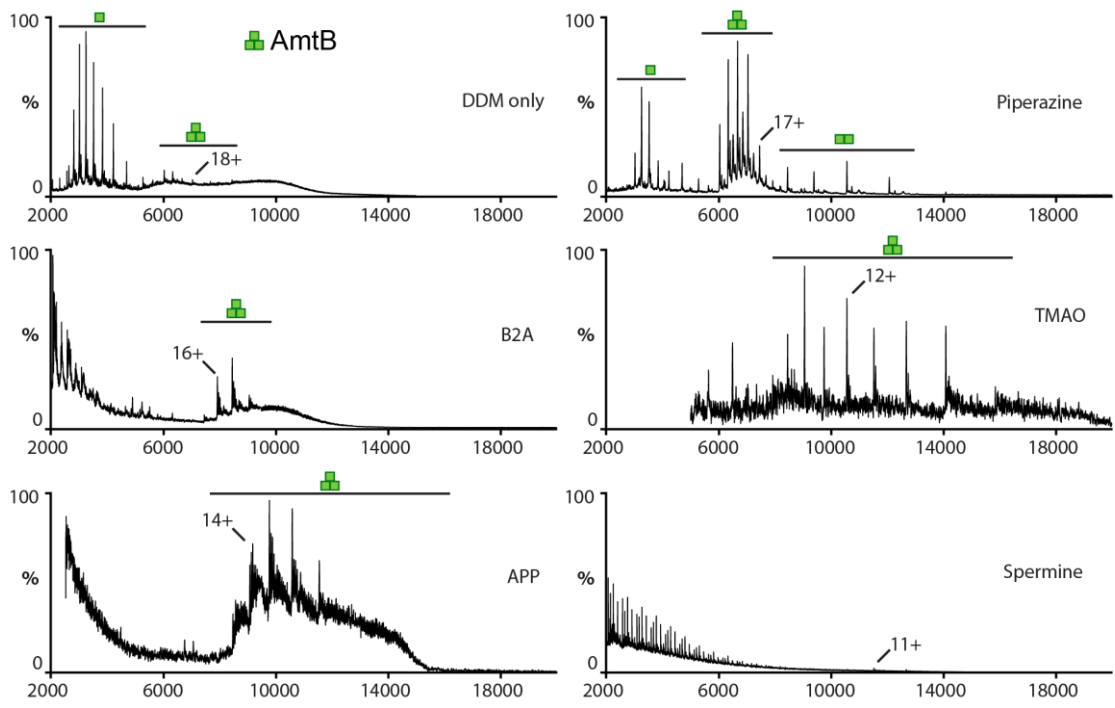


Figure S2. Native mass spectrum of AmtB solubilized by DDM with added charge reducing agents. Shown are the mixtures that generated interpretable mass spectra. Other agents used in this study causes poorly resolved peaks when mixed with AmtB in DDM and are not shown. Note that AmtB trimers readily falls apart with insufficient charge reduction.

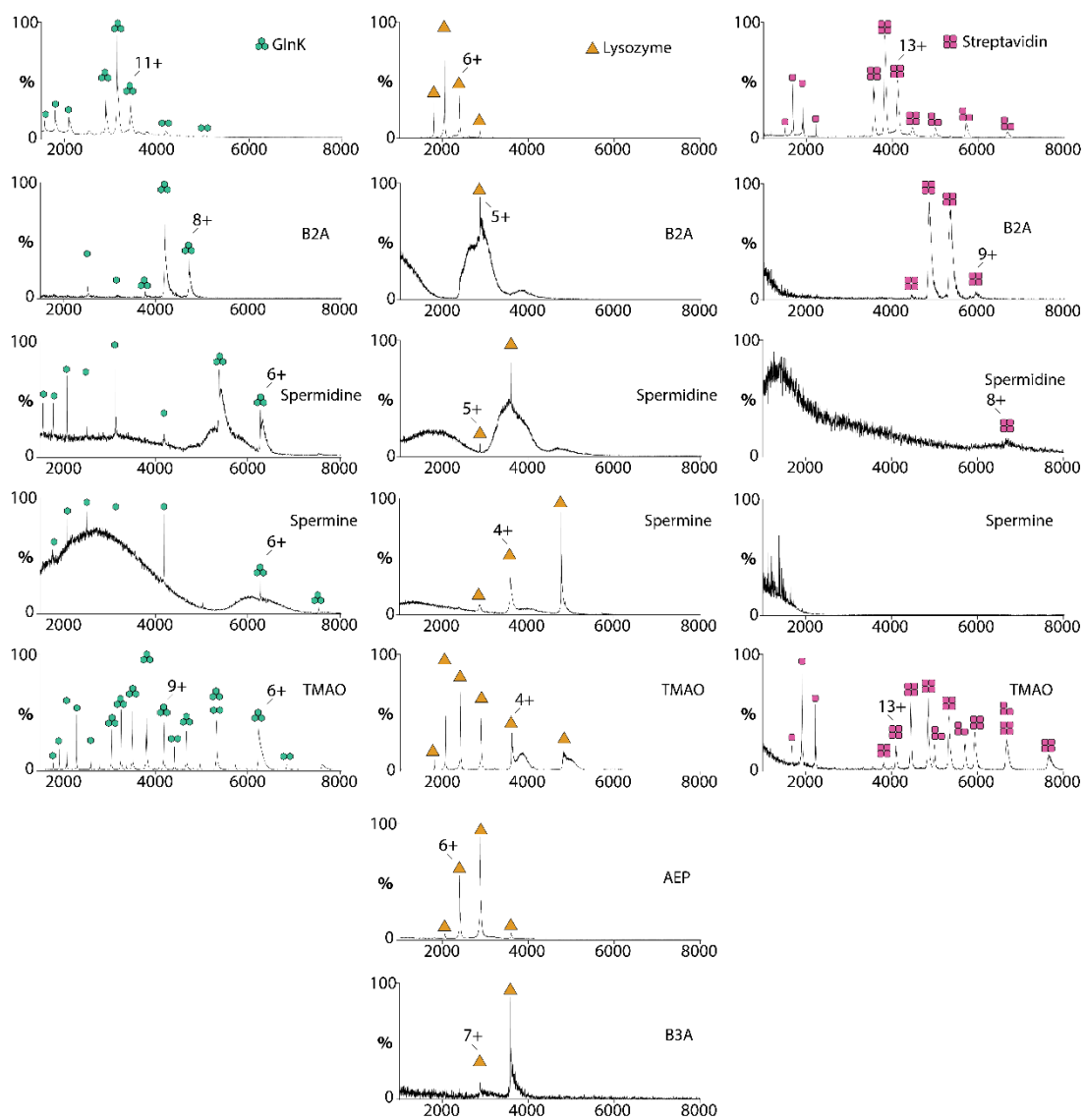


Figure S3. Native mass spectra showing variable charge reduction effects on soluble proteins. GlnK (Left column), Lysozyme (middle column) and Streptavidin (right column) show representative spectra with decipherable mass species. Top row show representative spectra for respective soluble proteins in 200 mM ammonium acetate, pH 7.4.

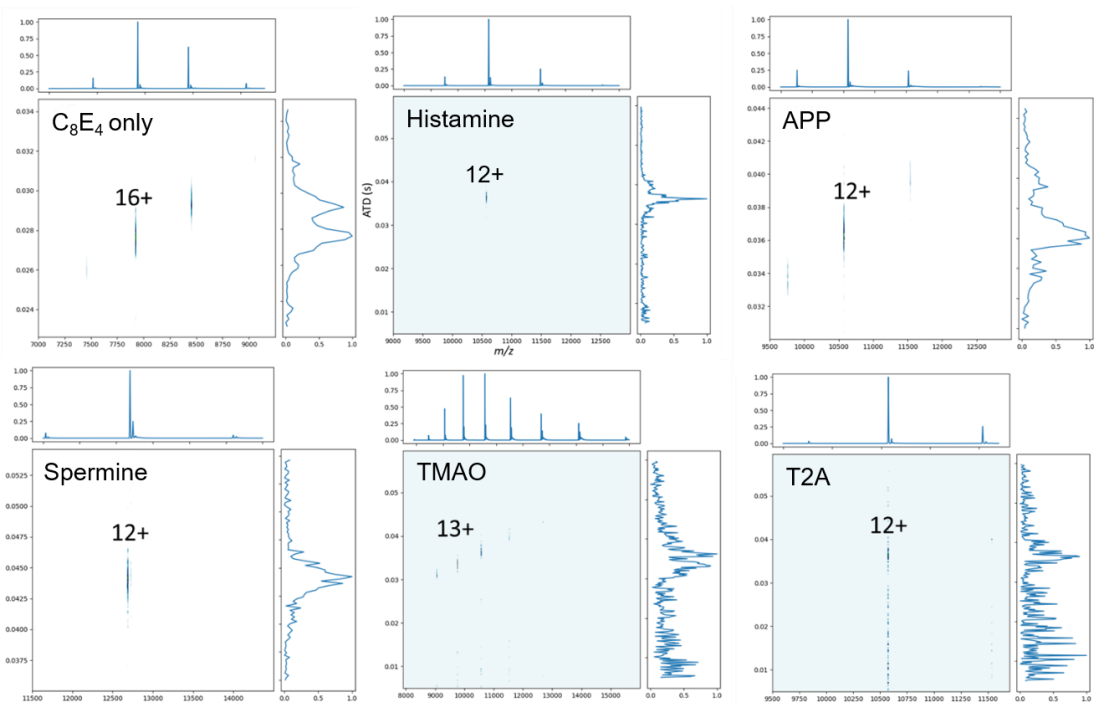


Figure S4: MS, 2D ATD(s) vs m/z , and ATD plots for all molecules analyzed via the FT-IM-PF-DT Orbitrap Platform.

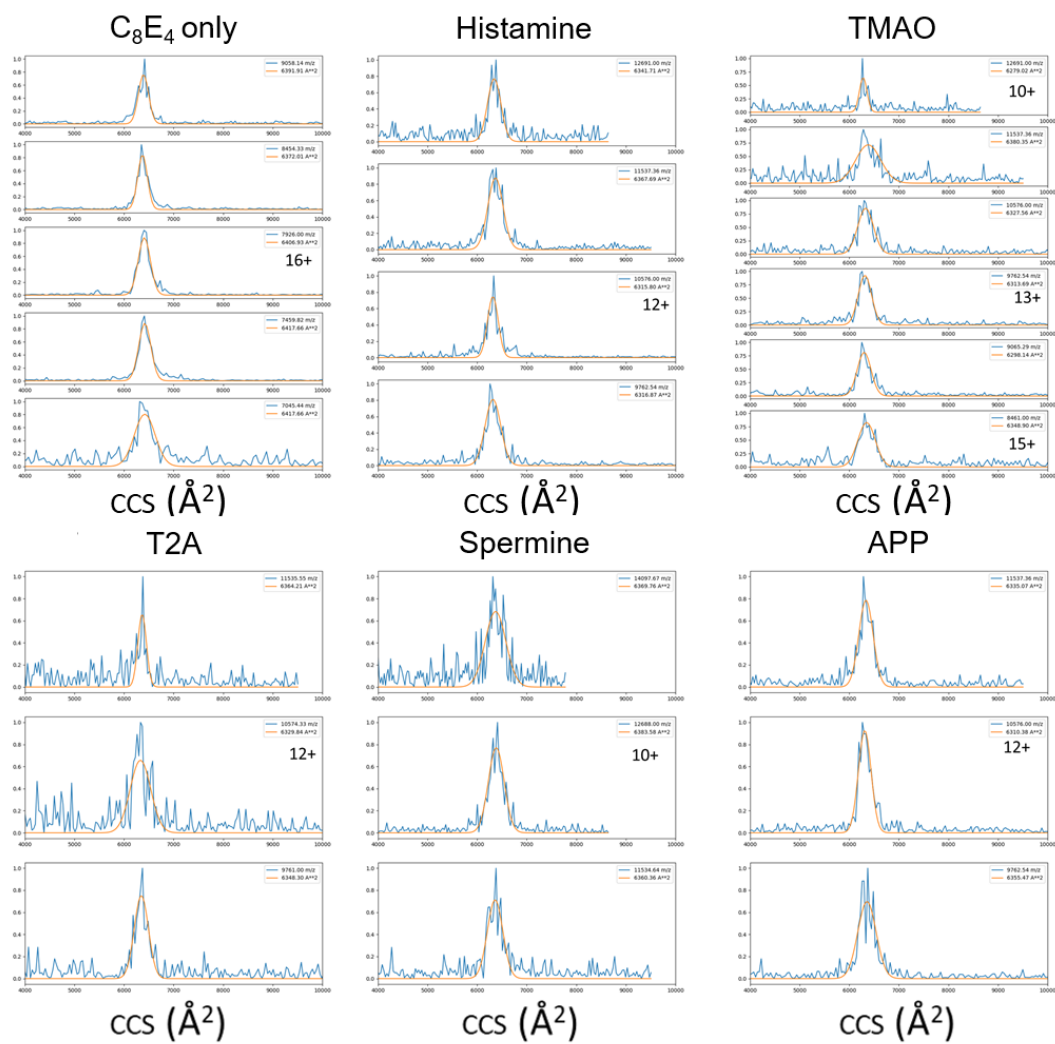


Figure S5: Raw data and Gaussian fitted CCS peaks for all molecules analyzed via the FT-IM-PF-DT Orbitrap Platform

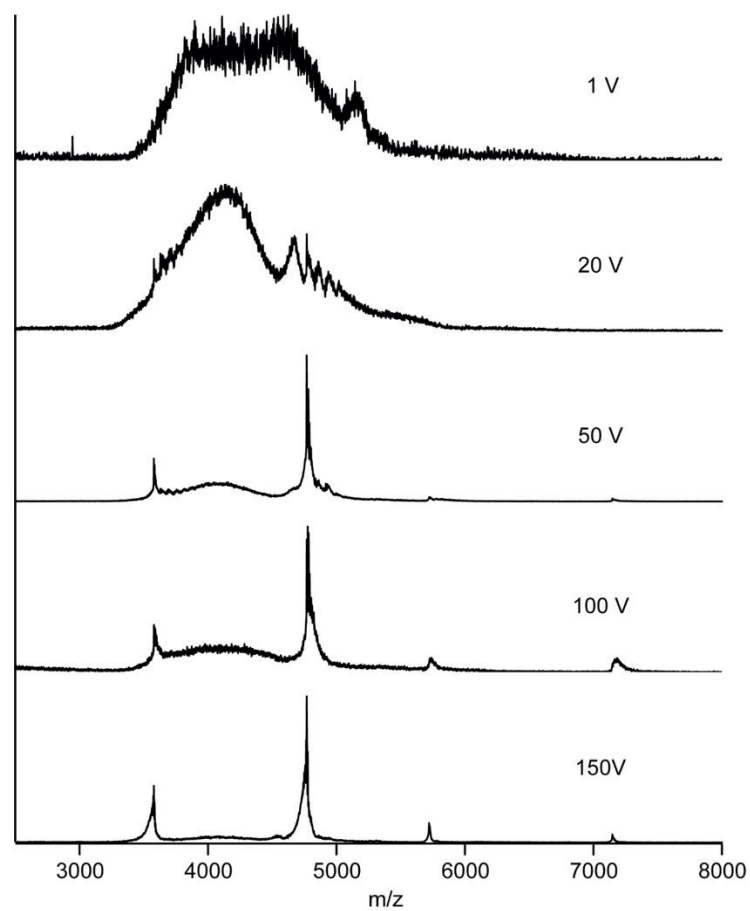


Figure S6: Mass spectra of charge-reduction of lysozyme by 50mM spermine with increasing collision energy.

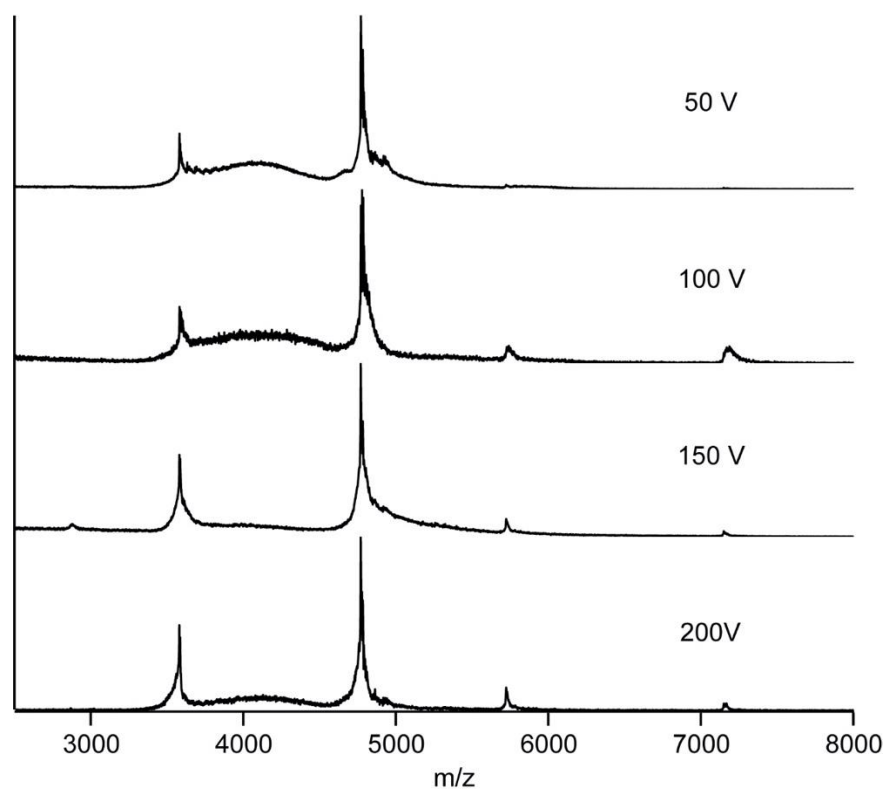


Figure S7: Mass spectra of charge-reduction of lysozyme by 50mM spermine with increasing cone voltage.

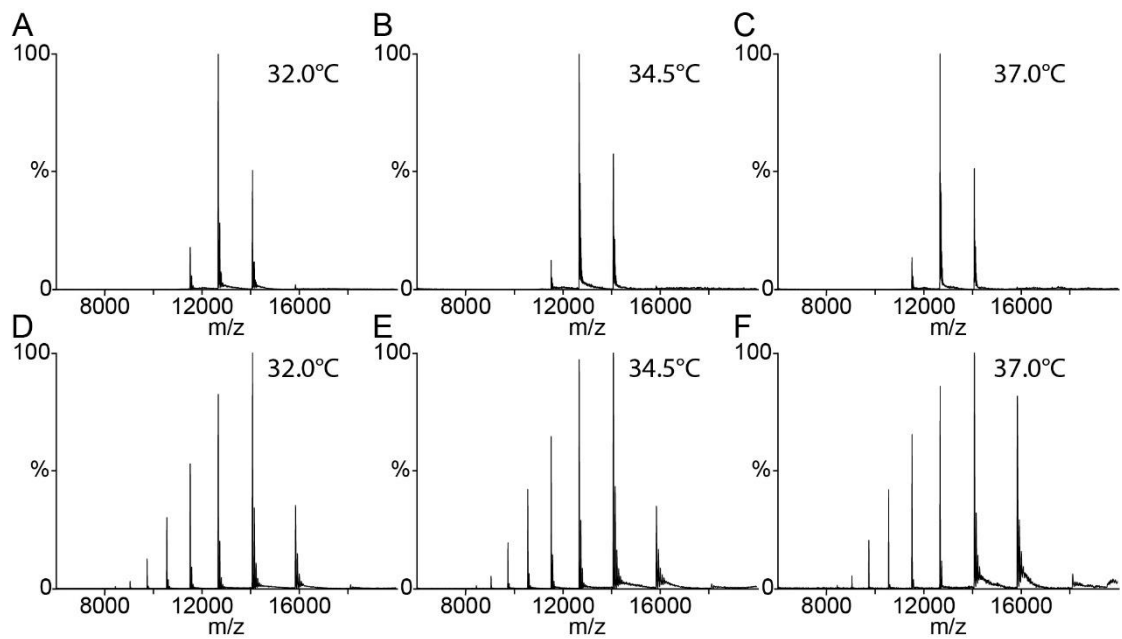


Figure S8: A-C) Mass spectra of AmtB charge reduced by 100mM spermine with solution temperature at (A) 32.0°C (B) 34.5°C (C) 37.0°C. D-F) Mass spectra of AmtB charge reduced by 100mM TMAO with solution temperature at (D) 32.0°C (E) 34.5°C (F) 37.0°C.

CHAPTER IV
VARIABLE-TEMPERATURE-ELECTROSPRAY IONIZATION FOR
TEMPERATURE-DEPENDENT FOLDING/REFOLDING REACTIONS OF
PROTEINS AND LIGAND BINDING*

Introduction

Since Hopkin's 1930 report on the temperature-dependent denaturation of ovalbumin,²¹⁹ the influence of temperature on protein stability, structure, and self-assembly has captivated scientists' interest. Privalov²²⁰ and Ben-Naim,²²¹ emphasize in their reviews the importance of the local environment (Gibbs free energy landscape (GEL)) on the stabilities, structures, and folding/denaturation of proteins. While Anfinsen's hypothesis considers the native state as being a thermodynamic minimum,²⁹ the native state is, in fact, unique to the local environment as defined by temperature, pressure, and concentration of the protein, *viz.* GEL. While solvent effects are known as determinants for charge state distributions observed by ESI MS, very little is known about how they affect the structure/conformations of gas-phase ions.²²²⁻²²⁵ Despite the importance of temperature on peptide and protein structure, careful studies aimed at understanding these effects have only been implemented recently.^{89, 106, 163, 226-233}

*Reprinted with permission from McCabe, J.W.; Shirzadeh, M.; Walker, T.E.; *et al.* Variable-Temperature Electrospray Ionization for Temperature-Dependent Folding/Refolding Reactions of Proteins and Ligand Binding. *Anal. Chem.* **2021**, 93 (18), 6924–6931. Copyright 2021 American Chemical Society.

Here, we describe a variable-temperature electrospray ionization (vT-ESI) source that can be used to study both cold- and heat-induced solution-phase reactions of peptides and proteins at temperatures of $\sim 5 - 98$ °C. vT-ESI-MS is not new; Cong *et al.* developed a vT-ESI-MS source to study lipid binding of membrane protein complexes,²³⁴⁻²³⁶ El-Baba *et al.* developed a vT-ESI to study heat-induced protein denaturation (ambient to > 90 °C),²³⁷ Köhler *et al.* developed a vT-ESI source that operates between 15- 85 °C,²³⁸ and Marchand *et al.* developed a dual-block vT-ESI capable of temperature-jump mass spectrometry.²³⁹ These vT-ESI-MS devices afford an exquisite approach for studies of solution-phase thermochemistry. For example, using this approach, it is possible to directly measure temperature dependence of the formation of specific products by monitoring the masses of the products.^{9, 103, 104, 237, 240-245} Using vT-ESI-IM-MS, which reports the masses and sizes/shapes (rotationally-averaged collision cross-sections) of products, folding/unfolding and self-assembly reactions can be investigated.^{18, 246} All of the above-mentioned studies illustrate the unique capabilities of vT-ESI MS and vT-ESI IM-MS to directly measure individual peptide/protein conformers that comprise a conformationally heterogeneous population,¹⁰³ while simultaneously measuring the thermodynamics, *viz.* ΔG , ΔH , and $T\Delta S$, of the chemical reactions.

While different strategies for implementing vT-ESI have been reported,²³⁴⁻²³⁹ the present work aims to develop a vT-ESI device compatible with static ESI and capabilities for investigating both cold- and heat-induced folding and self-assembly reactions using mass spectrometry and ion mobility-mass spectrometry. Most importantly, the device needs to be compatible with static nanospray ESI, allowing for small volumes ($< 10\mu\text{L}$)

of protein solutions and measurement of temperature-dependent product profiles between 5–98 °C.

Experimental

Design of VT ESI Source

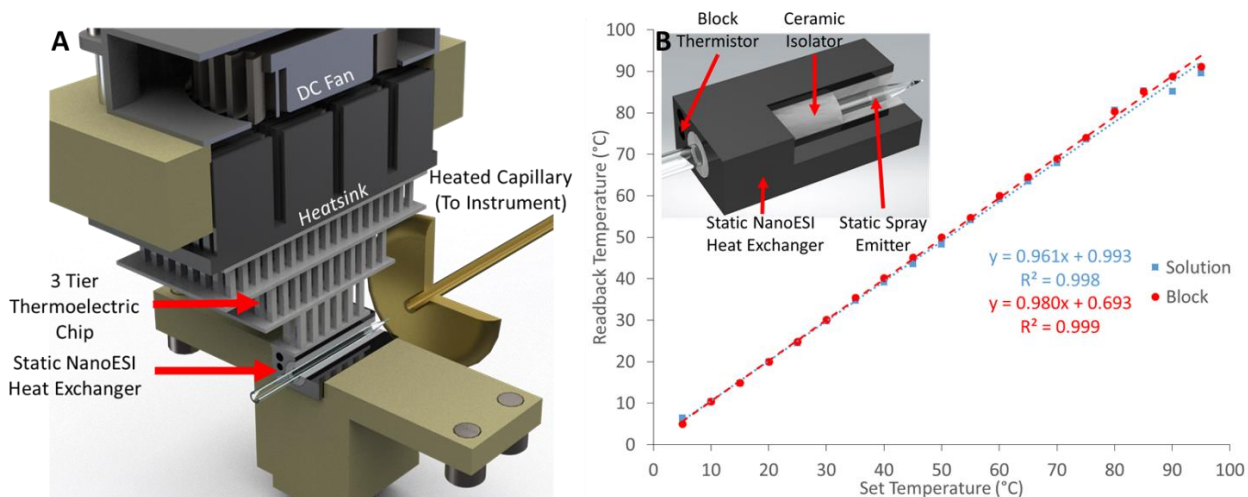


Figure 21 (A) Solidworks rendering of the vT-ESI assembly with labels to identify the significant components. The fan mounted to the top of the device prevents overheating and reduces atmospheric moisture condensation for experiments performed below ~ 15 °C. The top stage of the thermoelectric chip (TEC) makes direct contact with a 40 mm x 40 mm x 13 mm heatsink (CTS Electronic Components APF40-40-13CB); a 40 mm x 15 mm 24 VDC fan with 14.83 CFM rated airflow (Delta Electronics AFB0424SHB) is used to dissipate the heat off of the heatsink. The vT-ESI assembly uses custom machined PEEK components that mount directly to a commercial Thermo Nanospray Flex source. Additional details about the electronics control system are contained in the Supporting Information. **(B)** Temperature calibration of the vT-ESI emitter solution is performed using thermocouples inserted into the static spray capillary and the SS heat exchanger (as shown in inset). The temperature variation ranged from $\sim \pm 5$ °C at the highest and lowest temperature and $\sim \pm 2$ in the range of 5 – 98 °C.

Figure 21A contains a Solidworks rendering of the TEC vT-ESI assembly using static nano ESI emitters. The ESI emitter is positioned inside a ceramic sleeve (Kimball Physics (AL2O3-TU-C-500) and cut to length in-house) that serves as an electrical insulator from an aluminum heat exchanger. The heat exchanger makes direct contact with a 3-stage TEC (Peltier chip) (Laird Thermal Systems 9360001-301 3-tier). The TEC is

used to maintain the temperature of the heat exchanger and the solution contained in the ESI emitter at the desired temperature, ranging from $\sim 5 - 98$ °C. The vT-ESI capillary temperature was calibrated across the range of temperatures by simultaneously monitoring the static-spray (SS) heat exchanger temperature and the solution contained in the ESI emitter (**Figure 21B**). The solution temperature was measured using a calibrated T-Type thermocouple (Physitemp Clifton, NJ) paired to a thermocouple (National Instruments USB-TC01) positioned inside the borosilicate pulled glass capillary filled with a 200 mM ammonium acetate solution. The ESI SS capillary was placed inside an alumina silicate ceramic isolator that covered the entire length of the block to ensure the TEC is isolated from ESI voltage (typically between 1.2-1.6 kV) applied via a Pt wire (Alfa Aesar, $\geq 99.9\%$ 0.3048 mm diameter). The block temperature was set to the desired temperature using a temperature controller that utilizes pulse width modulation (TE Technology TC-720); the temperature was monitored for ~ 2 min to ensure the system had reached equilibrium. The custom power supply developed for the operation of the vT-ESI device is described in the Supporting Information.

It is important to note that airflow around the vT-ESI heat exchanger/emitter is essential for reducing condensation at cold temperatures, especially at temperatures below 15 °C, while minimizing air turbulence with deleterious effects for the stability of ionization. We have found that the fan assembly employed here, with controlled fan speed, is essential for both cold and heated operations. The 3-tier Peltier TEC provides much-improved performance over a single-tier design. The temperature ramps obtained using the 3-tier design are steeper and allow for reliable operation at much lower temperatures.

Sample Preparation

Ubiquitin (U6253, Sigma Aldrich) samples were prepared from a stock solution to have a final concentration of 1 μM in 1% acetic acid, pH of 2.8, which is similar to those used previously by El-Baba et al.²³⁷ The A state ubiquitin solutions were prepared by dilution of a 1 mg/mL ubiquitin stock solution to a working concentration of 1 μM in 49:49:2 methanol:water:glacial acetic acid (pH 2).²⁴⁷⁻²⁴⁹ GroEL¹¹⁸ were expressed in-house as described previously. Frataxin (FXN) was expressed and prepared in-house; a detailed protocol is given in Supporting Information. Before MS analysis, the sample was bio-spun in 200 mM ammonium acetate and diluted to a working concentration of 5 μM for FXN and 1 μM for GroEL.

Mass Spectrometry and Ion Mobility Mass Spectrometry

The vT-ESI-MS measurements were performed on an Exactive Plus-Extended Mass Range (Thermo Fisher, Bremen, Germany) mass spectrometer. Approximately 7.5 μL of protein solution was loaded into the borosilicate glass capillary (Sutter Instruments, B150-86-10, and P-1000). ESI voltage (~ 1 kV) was applied by a platinum wire inserted into the solution. The protein solution was equilibrated for 3 min at each temperature prior to each MS acquisition. Data were converted to .txt files using custom python code and imported into UniDec¹²² and ProteinMetrics.²⁵⁰ Melting temperatures (T_M) were estimated from the inflection point of a 4-parameter sigmoidal fit using SigmaPlot version 10.0 from Systat Software, Inc., (San Jose, California). Additional information on the data processing can be found in the Supporting Information. The IM-MS data were collected

using a 1.5 m drift-tube Fourier-transform ion mobility-UHMR Orbitrap, as described previously.^{9, 15, 251-254} A-state ubiquitin IM-MS data were collected on a Waters SYNAPT G2 modified with the newly designed vT-ESI source. CCS calibration was performed using the method described by Ruotolo et al.²⁵⁵

Results and Discussion

Here, we describe vT-ESI-MS and IM-MS studies using cold- and heat-induced folding reactions for single-domain proteins, *viz.* ubiquitin and frataxin, and temperature-dependent ligand binding for the chaperonin GroEL. For purposes of this study, we are interested in comparing and contrasting cold- and heat-induced folding for proteins containing similar 2^o structure motifs (helices and β -sheets) similar to ubiquitin.

Ubiquitin has been extensively used in variable temperature studies using both MS and IMMS. Thus, it was selected for the initial testing of our vT-ESI device.^{237, 242} The initial experiments employed conditions that preserve native-like, low-charge state ubiquitin.²³⁷ **Figure 22A** contains mass spectra of ubiquitin acquired at different solution temperatures (8 °C, 69 °C, and 98 °C). As expected at these temperatures, changes in the charge state distributions are consistent with temperature-dependent unfolding transitions reported by El-Baba *et al.*²³⁷ However, when the ubiquitin solution conditions were altered to a native buffer system of 200 mM ammonium acetate, no thermal unfolding was observed, indicating the buffer system plays a crucial role in the GEL (data not shown). **Figure 22B** contains a plot of the average charge state (Z_{avg}) as a function of temperature from 8 °C to 98 °C; within this range, Z_{avg} changes from 7.25 to 10.07. It is interesting to

note that changes in Z_{avg} obtained by reversing the temperature profile (T scans from high- to low-temperature) yield very similar melting profiles.

While the general appearance of the melting curve is in good agreement (within $\pm 0.25 Z_{\text{avg}}$) with that reported by El-Baba *et al.*,²³⁷ the T_M value of 65.2 ± 0.8 °C is lower than their reported value of 71 °C. These differences in T_M are attributed to the differences in pH of the solutions. Previous studies reported that the T_M of ubiquitin are pH-dependent; a change in pH from 3.0 to 2.75 shifts T_M from 74.1 °C to 66.3 °C.²⁵⁶ It is also possible that T_M values may depend on the size of the ESI emitter owing formation of different droplet sizes. Effects of droplet size on the melting of ubiquitin were noted in experiments using 10.6 μm IR heating of the nanodroplets.²⁴²

Prior vT-ESI IMMS studies revealed a complex distribution of intermediate states of ubiquitin using heat-induced melting, including the well-characterized A-state, a partially unfolded conformation consisting of mostly α -helices (structure shown in Figure 22D).^{237, 242, 257} **Figure 22D** contains a plot of Z_{avg} charge state versus temperature plots obtained using acidic water/methanol solutions (49:49:2 MeOH:H₂O:Acetic Acid (pH 2.3); solutions conditions that have been shown to promote the formation of A-state ubiquitin. Note that Z_{avg} for temperatures greater than ~ 20 °C are higher than that for the “native-like” ubiquitin (see **Figure 22A**). Note the marked increase in the abundance of 7⁺ ions that is characteristic of native-like ubiquitin ions; however, the CCS profiles for these 7⁺ ions (shown in Figure S2) reveal that only a small fraction of the ion population are native-like in terms of the measured CCS 1028 Å². The CCS profiles obtained under

these conditions are very similar to those reported by El Baba *et al.* at elevated, denaturing conditions, *viz.* CCS values of 1264 Å², 1327 Å², and 1517 Å².²³

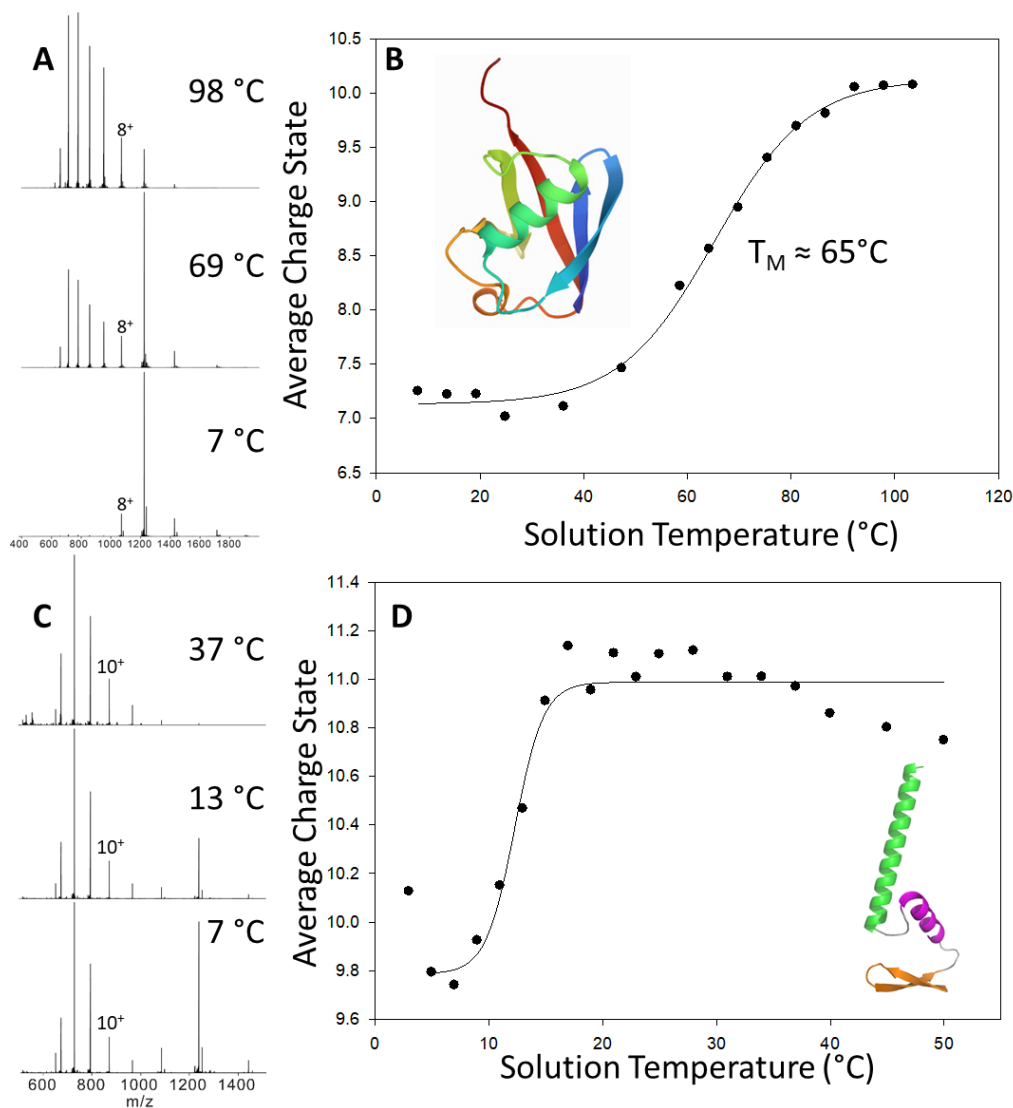


Figure 22 (A) Mass spectra of ubiquitin collected at 8 °C, 69 °C, and 98 °C; **(B)** Plot of average charge state (Z_{ave}) of ubiquitin (PDB: 1UBQ²⁵⁸) versus temperature of the solution contained in the ESI capillary. Melting temperature (T_M) is defined as the midpoint of the sigmoidal curve. **(C and D)** Plots of the temperature-dependent average charge states (Z_{ave}) of the partially-unfolded A-state ubiquitin observed in acidic water/methanol solutions (49:49:2 MeOH:H₂O:Acetic Acid (pH 2.3)). At temperatures above ~50 °C, the signal is attenuated due to the rapid evaporation of the solution. Inset shows the proposed A-state structure from Vajpai, N. *et al.*²⁵⁹

Additional vT-ESI studies were performed using human frataxin (FXN), a 14.237 kDa protein (Uniprot Q16595) allosteric activator of the Fe-S cluster biosynthesis in mitochondria²⁶⁰⁻²⁶⁴ that has been linked to the neurodegenerative disease Friedreich's ataxia.²⁶⁵ The vT-ESI data for mature, FXN (residues 81-210) over the temperature range of 5 – 98 °C. **Figure 23B** contains a T-dependent Z_{avg} plot for FXN. At 3 °C, the Z_{avg} is 6.57, decreases to a minimum of 6.4 at 39 °C, then increases to 6.57 at 81 °C. The parabolic fit is similar to T-dependent stability reported for yeast frataxin (Yfh1) using CD or NMR spectroscopy.^{266, 267} The changes in the relative abundances of the 7⁺, 6⁺, and 5⁺ FXN charge states (**Figure 23C**) are consistent with changes in the solvent-accessible surface area (SASA) of the protein. While the collision cross sections (CCS) (**Figure 23D** and **23E**) for cold- (5 °C) and heat-induced (80 °C) unfolding are similar to that obtained at physiological temperature (37 °C) (see Supporting Information **Table S1**), the T-dependent CCS differences for the 6⁺ charge state of FXN are statistically significant ($p > 0.05$) using an unpaired t-test. However, the changes in CCS for 7⁺ charge state are not statistically significant.²⁶⁸ More importantly, the peak widths (FWHM) for the CCS profiles are larger for the 6⁺ ions than for the 7⁺, which may reflect differences (conformational or dynamics) for the lower charge state ions. For example, the observed differences for cold-unfolding may be attributed to differences in the 3^o structure, *e.g.* differences in the alignment of the helices and or sheet motifs; prior CD studies suggests that the 2^o is retained at cold-induced conditions.⁷² Conversely, the CD spectra suggests that heat-induced unfolding CD promote changes of the 2^o structure.⁷² The CD studies were performed using very different buffers and ionic strengths than those used for vt-ESI

(20 mM HEPES vs. 200 mM ammonium acetate) where solution parameters are known to strongly affect structure and stability.²⁶⁹ Owing to the expected effects of buffers and ionic strengths on cold- and heat-induced folding,²²⁰ further investigations of these effects are warranted.

Previously reported studies suggest different mechanisms for cold- and heat-induced folding for Yfh1, which is directly amenable to vT-IM-MS.^{266, 267, 270} The FXN (PDB:1EKG)²⁷¹ and Yfh1 share a high degree of sequence overlap but differ in terms of the flexibility of the N-terminal residues. The N-terminal of FXN is highly dynamic with little to no 2° structure,^{272, 273} whereas Yfh1 has a defined 2° structure.²⁷⁴ The C-terminus length of frataxin orthologues also influences their thermodynamic stability, where FXN has a longer sequence compared to Yfh1.²⁷⁵ Owing to these differences, CD results have shown Yfh1 has unstable 2° structures under cold conditions while FXN is relatively stable. The observation of FXN cold-denaturation by vT-IM-MS in this study highlights the capability of the new device to resolve subtle structural changes that were previously hidden via traditional biophysical techniques.²⁵⁴

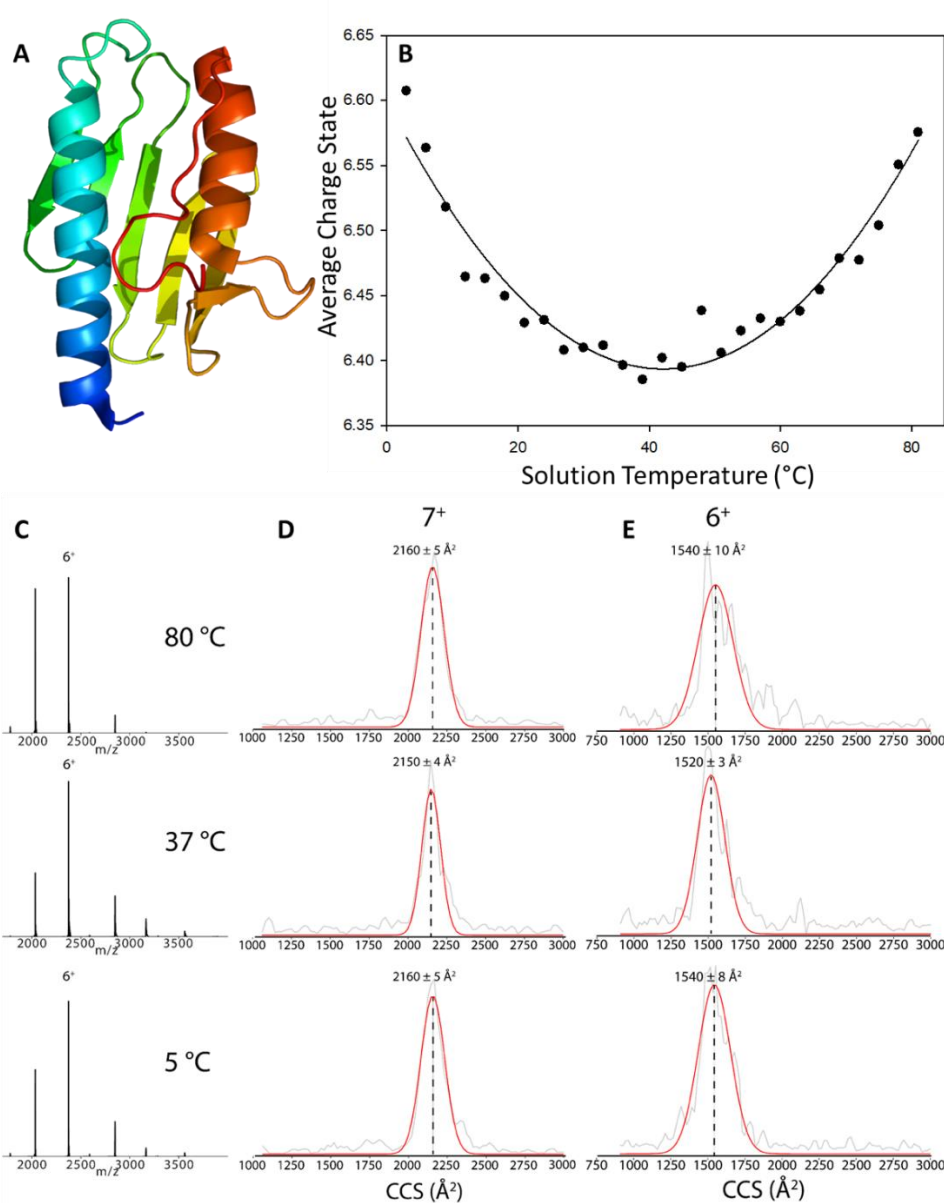


Figure 23 (A) Structure of human frataxin (PDB:1EKG)²⁷¹ and (B) plot of the average charge state (Z_{avg}) of frataxin as a function of solution temperature in the ESI emitter. The ESI signal is unstable at $T > 82$ °C, presumably owing to decomposition and/or aggregation at higher temperatures. A parabolic fit (Sigmaplot 10.0, solid line) was added to the data. vT-IM-Orbitrap CCS profiles and (C) Extract MS of the (D) 7⁺ charge state, (E) 6⁺ charge state of FXN at 5 °C, 37 °C, and 80 °C. The red line is a Gaussian function fitted to the raw CCS experimental data (grey). CCS values for the 5⁺ monomer are not shown due to the overlap with the 10⁺ dimer.

The activities of ion channels and chaperones are highly regulated by conformational (“open” and “closed”) changes that are induced or stabilized by ligand binding that are subject to both enthalpic and entropic barriers.²³⁴ GroEL (HSP60, 800 kDa), a 14-mer complex of the HSP10 monomers that are arranged as two stacked heptamers (see **Figure 24**), forms a large central cavity in which non-native proteins bind via hydrophobic interactions.^{276, 277} The mechanical action GroEL/GroES complex, is an example of ATP-dependent movement of the apical domain regulating substrate binding and release.²⁷⁶ Here, vT-ESI is used to investigate the T-dependent ATP binding to GroEL. **Figure 24** contains a plot of Z_{avg} for GroEL between 8 – 38 °C and the products formed upon binding ATP (GroEL(ATP)_n); mass spectra are shown in Supporting Information (**Figure S3**). Z_{avg} for apo GroEL (solid black data points) decreases from 65 to ~ 64.5 at temperatures between 8 °C and 24 °C and then increases to > 66 at temperatures above 24 °C. It is interesting to note that significant changes in ATP binding are observed over this same range of temperatures. While the Z_{avg} obtained for GroEL binding to 1 - 4 ATPs are mostly similar, a sharp decrease in Z_{avg} is observed for binding the fifth ATP, and there are no detectable signals for binding 6 - 9 ATPs at T greater than 24 °C. The T-dependent changes in Z_{avg} and ATP binding are interpreted as evidence of changes in the conformation of the architecture of the GroEL complex, as well as altering the entropic barrier. These data were acquired using ammonium acetate (AmA) buffer, and it is interesting to note that such behavior is not observed when using ethylene diammonium diacetate (EDDA) buffer, which produces lower Z_{avg} charge states of GroEL. However, the change in ATP binding occurs in the same range of temperatures for both buffers

(manuscript in preparation). For example, at temperatures below 24 °C for GroEL in AmA, bindings of up to 9 ATPs are observed, but at temperatures greater than 24 °C, the maximum number of ATPs bound is 5.

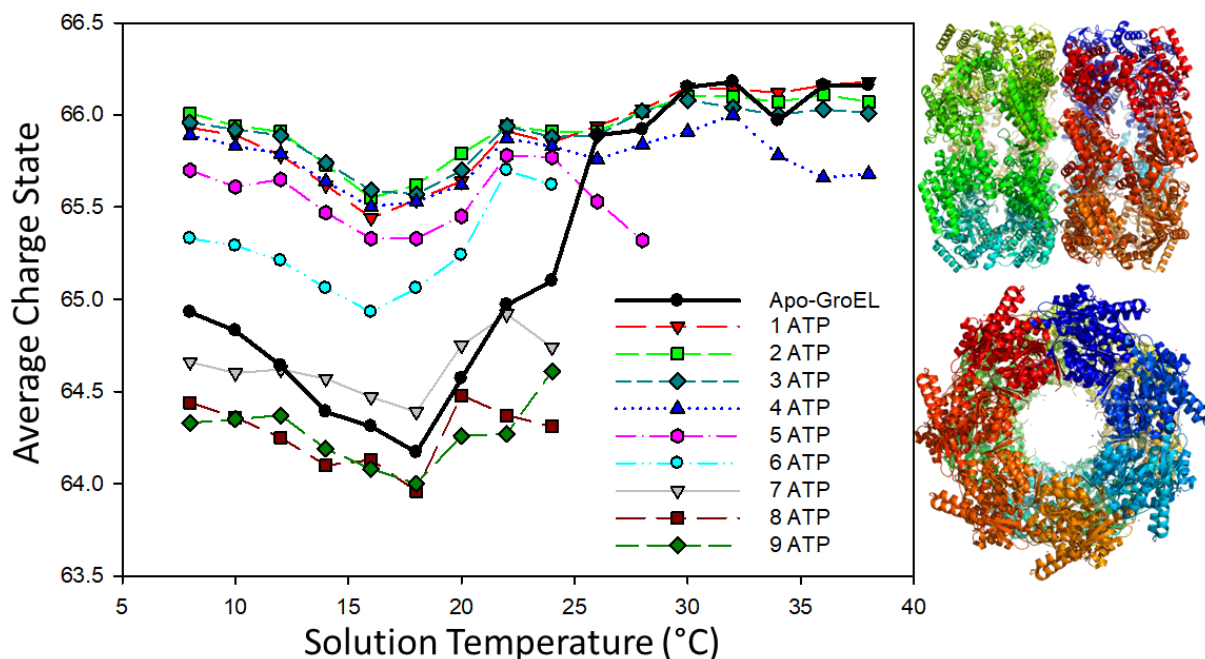


Figure 24 Temperature dependence of 1µM GroEL in 200 mM ammonium acetate containing 125 µM ATP. (PDB: 1SS8).

Conclusions

The TEC (Peltier) vT-ESI source was designed for easy implementation on different MS platforms. These include a number of mass spectrometers – the ThermoFisher Orbitraps, including those equipped with REIS and FT-IMS capabilities,^{9, 15, 236, 251-254} the Agilent 6560 IM-QTOF and 6545 XT, and the Waters SYNAPT instruments equipped with TWIMS. The performance metrics of the 3-stage TEC vT-ESI

device make it possible to rapidly acquire reproducible melting curves for static spray capillaries over the temperature range of 5 – 98 °C. The cold- and heat-folding studies on ubiquitin and frataxin clearly illustrate new applications for vT-ESI-MS. While both ubiquitin and frataxin are monomeric proteins, their respective thermal unfolding curves are significantly different, a sigmoidal vs. a parabolic curve, respectively. Changes in the Gibbs energy landscape owing to changes in pH, buffers, and/or ligand binding gives rise to drastic differences in thermal unfolding curves and may impact the future definition of “native-MS”. The results reported on temperature-dependence of ATP binding to GroEL bodes well for future studies on the stabilities and dynamics of protein complexes extending into the mega-dalton molecular weight range. Combining vT-ESI with recent developments in next-generation high-performance IM-MS instrumentation opens new opportunities for studies of intact soluble and membrane protein complexes and other non-denaturing studies.^{107, 251, 254, 278}

Supporting Information

Expression and preparation of fraxatin

A *His₆-GST-TEV-FXN* construct was generated by subcloning the FXN (Δ 1-81) gene into a pET-28a(+) vector containing *His₆-GST-TEV-CyaY*²⁷⁹ using the MEGAWHOP²⁸⁰ protocol, and was transformed into the *E. coli* strain BL21(DE3) for expression. After growing at 37 °C to an OD₆₀₀ of 0.5, 0.1 mM isopropyl β -D-1-thiogalactopyranoside (IPTG) was added into the cell culture to induce protein expression at 18 °C. Cells were harvested by centrifugation the following morning, and stored in a -80 °C freezer until

use. The cell pellet from a 3 L culture was thawed and resuspended in GST buffer A (50 mM Hepes, 150 mM NaCl, pH = 7.8). The cells were lysed by 2 cycles of French press at 18,500 psi, followed by centrifugation at 16,420 RCF for 30 min. The clarified lysate was loaded onto a manually packed GST-column (Prometheus) at 4 °C and bound proteins were eluted with GST buffer B (50 mM Hepes, 150 mM NaCl, 10 mM glutathione, pH = 7.8). The GST tag was cut by an overnight TEV digestion at 4 °C, and the products were loaded onto a Ni-NTA column (5 mL; GE Healthcare) to remove the TEV protease. The flow-through from the Ni-NTA column was concentrated to 20 mL, diluted to 150 mL with size exclusion buffer (50 mM Hepes, 250 mM NaCl, pH = 7.5), and loaded onto a HiPrep 26/60 Sephacryl S100 HR column. Fractions containing FXN were pooled, concentrated, frozen in liquid nitrogen, and stored at -80 °C until use. Concentration was determined using an extinction coefficient of 26,930 M⁻¹ cm⁻¹ at 280 nm as estimated by ExPASy ProtParam.

Analysis of experimental data

MS data were collected at a determined heat exchanger temperature based on a solution temperature determined from prior calibration. The average charge state (Z_{avg}) was calculated following the method of El-Baba et al.²³⁷,

$$Z_{avg} = \frac{\sum_j^n z_j i_j}{\sum_j^n i_j}$$

where Z_{avg} is the average charge state, j is a single temperature, i is the normalized intensity of the ion signal. To determine the melting temp (T_{melt}), the inflection point was calculated

by fitting the experimental data with a sigmoidal curve generated in SigmaPlot 10 using a sigmoid, 4 parameter fit,

$$Z_{avg}(T) = \frac{a}{1 + e^{-\left(\frac{T-T_{melt}}{b}\right)}}$$

where Z_{avg} is the average charge state and T_{melt} is the temperature of melting, and a and b are fitting parameters.

Custom Power Supply Fabrication

The TEC controller and additional electronics are housed in a small aluminum enclosure (22.86 cm L x 17.78 cm W x 5.08 cm H). An AC/DC power supply (Meanwell LRS-100 24) provides 24 VDC to the TEC controller, 24 VDC fans, and the DC/DC converter (Texas Instruments PTN78020WAH). The DC/DC converter is mounted on a custom PCB, designed using EAGLE 9.6.2 (Autodesk), and fabricated by OSHPark (www.oshpark.com). The DC/DC converter steps down the 24V DC from the power supply to the max voltage of the TEC of 5.3V at 6A. The DC/DC converter allows for the TEC to operate at the optimal voltage and current to quickly and efficiently change the temperature. In addition, the voltage output of the DC/DC converter can be changed by changing the resistance value if a different TEC is ever selected. The small footprint and preset output voltage allow users who are not familiar with the system to operate the VT-ESI device using included software safely and quickly with the TC-720 (TE Technology). A wiring schematic of the power supply can be found in **Figure S1**.

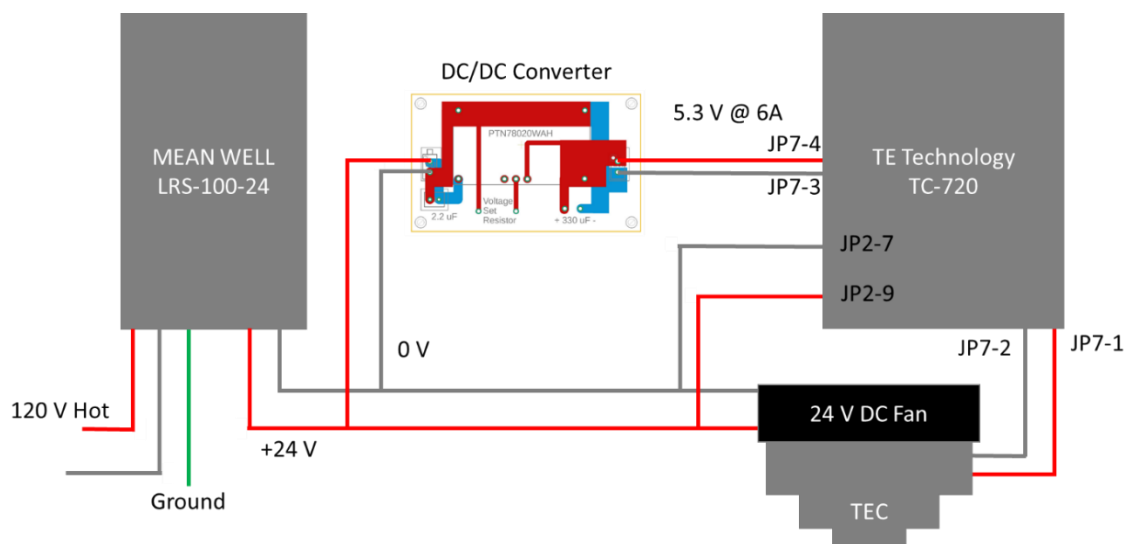


Figure S1. Wiring schematic of the Peltier TEC.

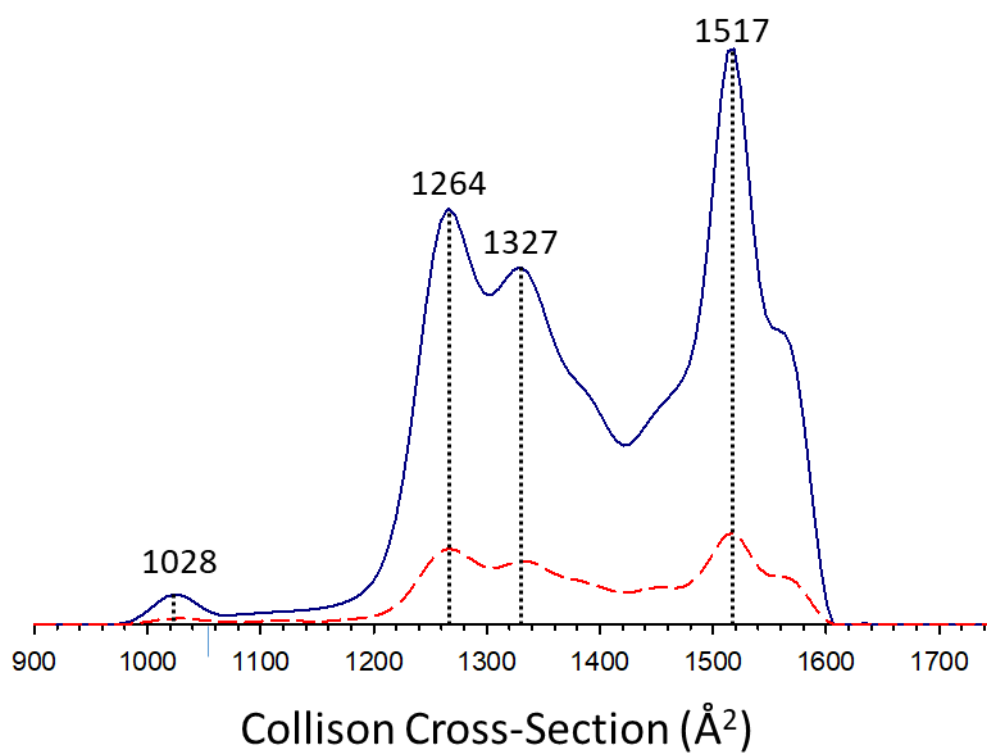


Figure S2. CCS profiles for the A state of ubiquitin from a 49:49:2 MeOH:H₂O:acetic acid solution. Data acquired using the Waters SYNAPT G2 TWIMS and vT-ESI at 5 °C (blue) and 25 °C (red).²⁵⁵

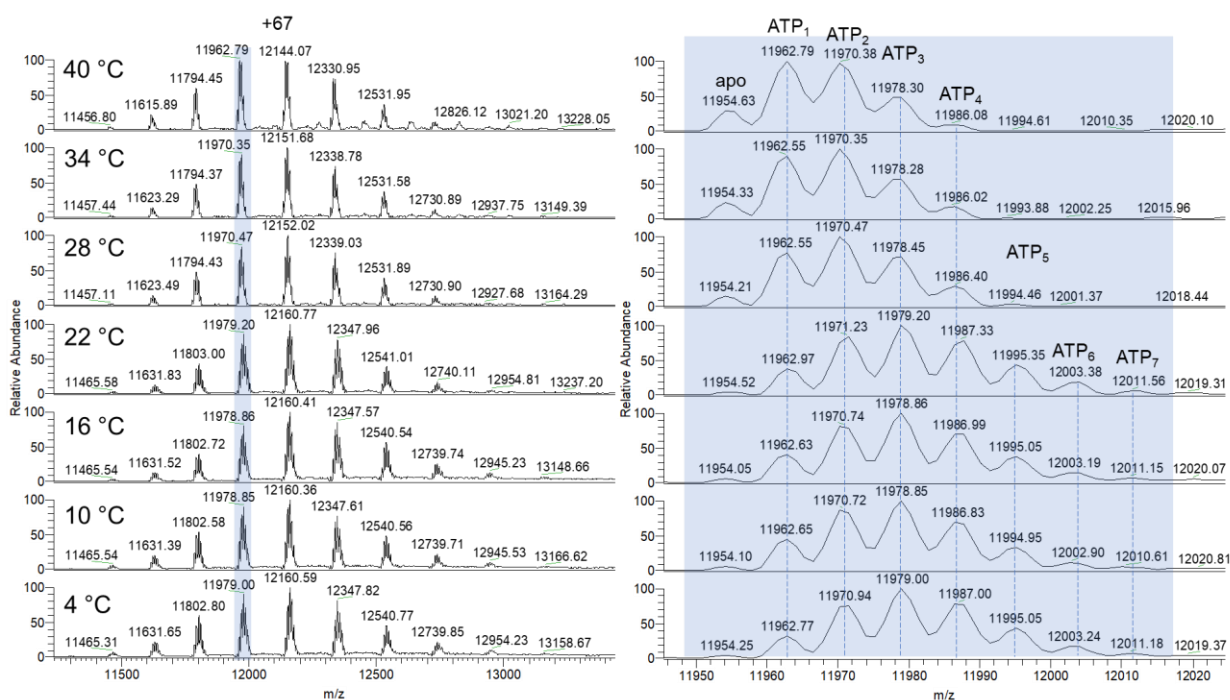


Figure S3. Temperature-dependent MS of 1 μ M GroEL with ATP (125 μ M) in 200 mM ammonium acetate.

Temperature	Z (+)	Average CCS (\AA^2)	Standard Deviation of CCS	FWHM	R_{IM}
5 °C	6	1540	8	257	6.0
	7	2160	5	176	12.3
37 °C	6	1520	3	220	6.9
	7	2150	4	142	15.1
80 °C	6	1540	10	275	5.6
	7	2160	5	180	12.0

Table S1: Calculated CCS values for acquisitions of FXN at 5 °C, 37 °C, and 80 °C with the peak fitting parameters (n=3). Where R_{IM} is the $CCS/\Delta CCS_{FWHM}$

CHAPTER V
IMPLEMENTING DIGITAL WAVEFORM TECHNOLOGY FOR EXTENDED M/Z
RANGE OPERATION ON NATIVE DUAL-QUADRUPOLE FT-IM-ORBITRAP
MASS SPECTROMETER

Introduction

Studies of proteins, protein complexes and non-covalent protein-ligand interactions using native mass spectrometry have expanded the structural biology toolbox. Often quoted attributes ascribed to native MS are sensitivity and dynamic range, which makes possible studies of reaction products, including intermediates on pathway from initial reactant to final products.^{106, 252} is highly complementary to the traditional structural biology techniques, *i.e.*, cryogenic electron microscopy^{77, 78}, X-ray crystallography^{75, 76}, and NMR spectroscopy^{73, 74}. While the working mass range, mass resolution and mass measurement accuracy for large 100 kDa and even MDa protein complexes have increased greatly over the past decade, there remain significant challenges to development of advanced technologies for structure-based MS studies. Ion mobility-mass spectrometry analysis allows for the calculation of an ions mobility which can be related to collision cross-section (CCS) which is representative of structure and size. We previously described a “next generation” IM-MS instrument consisting of a periodic focusing drift tube (PF-DT) IM and Orbitrap mass analyzer specifically designed for studies of large proteins and protein complexes.^{13, 15, 236, 251, 254} The PF-DT IM system affords 1st principles determinations of rotationally-averaged ion-neutral CCS^{49, 251}, and the Orbitrap ultra-high

mass range (UHMR) mass analyzer affords high mass resolution detection of ions having m/z up to 80,000. The addition of a variable-temperature (vT)-ESI (T variable from ~5 - 95 °C) source to the IM-UHMR, allowed for detailed studies of the thermodynamics (ΔG , ΔH and ΔS) of protein/protein complex, folding/unfolding, as well as ligand-protein and ligand-protein complex interactions.²⁸¹ Here, we describe an additional modification to the PF-DT-FT-IMS-Orbitrap, that further enhances our capabilities for structural characterization of large proteins and protein complexes *viz.*, incorporation of a dual quadrupole (qQ) mass analyzer that is positioned between the vT-ESI source and the IM drift tube. The first quadrupole is operated in an RF-only mode and can also be used for mild collisional activation of the ions to remove unwanted adducted species (H_2O , salts, detergents and charge reducing reagents). The second quadrupole (denoted Q) is used for mass selection and is operated using digital-waveform technology (DWT) developed in the Reilly laboratory.^{64-67, 69-71, 282-289} Although not yet implemented, the modular design of the instrument allows for the installation of a surface-induced dissociation (SID) region, the method of choice for determinations of stoichiometry and topology of protein complexes.^{19-22, 290} Collectively, the (vT)-nESI-qQ-PF-DT-FT-IM-Orbitrap marks a significant advance in our research capabilities for native mass spectrometry-guided structural biology. Below we describe the advantages of this (vT)-nESI-qQ-PF-DT-FT-IM-Orbitrap and its ability to analyze difficult samples such as membrane proteins by activating ions in quadrupole 1 (q1), removing non-specific adducts such as lipids and salts.⁷⁰ Also, we demonstrate the capability of the DWT in Q2 to select individual charge states of protein complexes up to 12500 m/z .^{64, 69, 287} Lastly, we show IM data and the

ability to perform complex-down sequencing and analysis of proteins. The capabilities of this instrument demonstrate its ability to analyze complex systems with its plethora of analysis methods stemming from the modularity of the design.

Experimental Section

Methods

Human recombinant C-Reactive Protein (CRP, Product number 236608) was purchased from Milpore Sigma lyophilized solution at a 1 mg/mL in 140mM NaCl, 20mM Tris-HCl, 2mM CaCl₂, 0.05% NaN₃ at a pH of 7.5. Ammonium transport channel, AmtB, and GroEL were expressed and purified as previously described.^{10, 53, 56, 118, 236} The proteins were buffer exchanged using Micro Bio-Spin P-6 Gel Columns (Bio-Rad) into 200 mM ammonium acetate and working concentrations adjusted to 1 to 5 μ M. Several microliters of protein solution were backloaded into pulled borosilicate tips prepared in-house from borosilicate capillaries (Sutter Instruments, BF150-86-10) using a micropipette puller (Sutter Instruments, P1000).

Instrumentation

The PF-DT-FT-IM Orbitrap has been described previously,^{15, 236, 251, 254, 281} and the latest version of the instrument, including the qQ module, is shown in **Figure 25**. The qQ-PF-DT-FT-IM-Orbitrap configuration consists of a reverse-entry ion source (REIS) that has been previously described.⁹ The REIS source is mounted onto an aluminum vacuum chamber (designed and fabricated in-house). The vacuum chamber is divided in two differentially pumped regions and pumped by a two-stage, split flow turbomolecular vacuum pump (Pfeiffer TMH 261-250-010 P3P). The first vacuum chamber (maintained at $\sim 10^{-3}$ torr) houses a 250 mm hyperbolic quadrupole (q) that is operated in a transmission/focusing mode and can also be tuned for collisional activation (CA). Collisional activation is achieved by raising the potentials on all optics up to and including

the conductance limit into the q1 chamber, activation voltage is defined as the potential difference between the previous aperture and the quadrupole 1 DC bias. The ions exiting q are guided to the second chamber by an octupole ion guide constructed from 3.175 mm rods with 4.75 mm r_0 measuring 47 mm in length and enter a 250 mm hyperbolic quadrupole (Q2) that is maintained at 10^{-4} - 10^{-5} torr). Q2 is used for mass selection of the ions by digital waveform technologies (DWT) as described and developed by the Reilly laboratory.^{64-67, 69-71, 282-289} Both quadrupoles are identical Thermo Fisher 4 mm r_0 hyperbolic rods with pre and post filters (Part Number 80100-60109) quadrupole pre and post filters were wired directly to the main rods prior to use. All the experiments described below employ DWT operation of the Q MS. Ions exiting Q2 enter an octupole ion guide (47mm) and are then transferred to a 55 cm PF-DT analyzer that is maintained at pressures of 1-2 torr of He. The DT-IMS is operated in the FT-IMS mode as described previously.^{15, 108, 109, 291-294} The ions exiting the DT enter a final octupole ion guide (xx mm) and are transferred the HCD cell of the Orbitrap mass spectrometer.

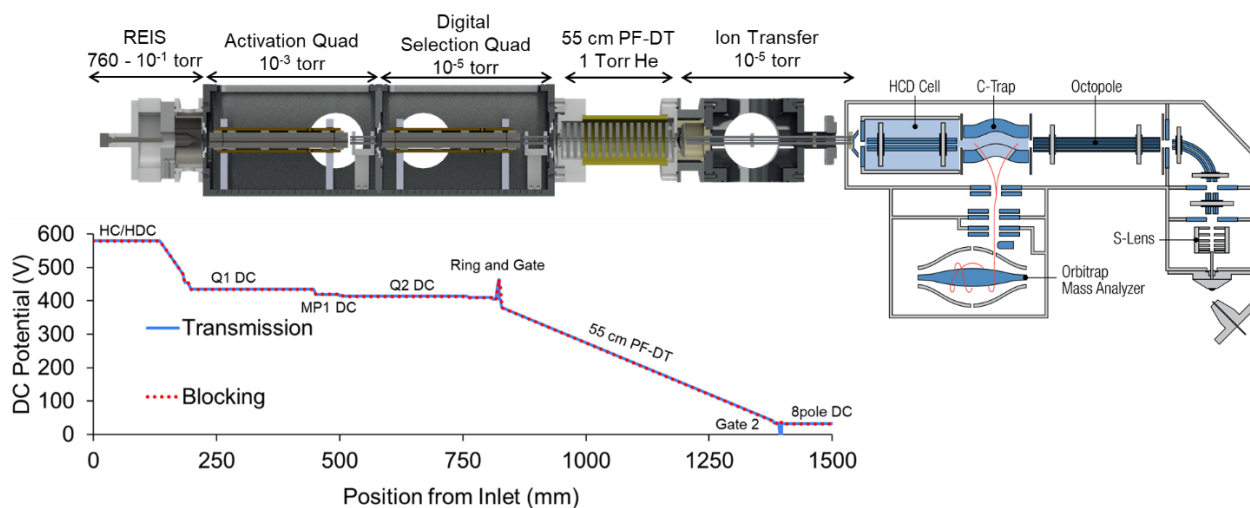


Figure 25 SolidWorks rendering of the nano-ESI dual-quadrupole FT-IM-PF-DT coupled to the HCD cell of a Thermo Exactive Plus Orbitrap with Extended Mass Range (qQ-FT-IM-PF-DT-HCD Orbitrap) with the major components labeled and the applied DC potential gradient across the instrument. The length of DT is not to scale in the rendering, i.e., the vacuum box and qQ are enlarged to better illustrate this device; the DT, 8-pole etc. have been described previously.

The DC voltages used in this work are provided by a Modular Intelligent Power Sources (MIPS) system (GAA Custom Engineering Kennewick, WA) and Ortec 710 Quad 1 kV power supply. Confining RF voltages for the ion funnel, octupoles in the dual-quad system, and transfer octupole are driven using MIPS RF High Q Heads at 200 Vpp 440 kHz, 200, Vpp 650 kHz, 250 Vpp 700 kHz, respectively. The transmission quadrupole “q1” in the activation region is driven by a MIPS Ultra RF head ~1.15 MHz 150-350 Vpp tuned for each system. The mass-selection quadrupole (denoted “Q2”) utilizes an custom built comparison-based control system capable of a high-resolution duty cycle control designed by the Reilly Group,⁶⁷ fabricated by PCBPrime (Aurora, CO), and assembled at Texas A&M University. Briefly, Digital waveform technology (DWT) utilizes two

rectangular waves with a varying duty cycle (defined as the percent in a given period that the wave spends in the “High” versus “Low” state) to manipulate ions on the Mathieu stability diagram. Isolation is obtained by tuning the duty cycle to vary the resolution and access higher stability zones and then sweeping the frequency of the waveforms by making an ion of interest stable in both the X and Y plane. This mode of mass selection has been demonstrated by Opačić et al. for lysozyme (14.3 kDa monomeric protein) by applying a 75% duty cycle to the X-waveform and a 25% duty cycle to the Y-waveform (i.e. a 75/25 duty cycle).⁷⁰ This waveform allows mass analysis in stability zone B.²⁸⁷ DWT was implemented due the high-electric fields pre-IM where there DC bias of Q2 is elevated ~500V above ground, without the added cost or complexity of using a traditional high mass sinusoidal quadrupole driver.²⁹⁵ The DC voltage is applied to the quadrupole using a set of DC-RF coupling circuits designed and fabricated by Gordon Anderson (GAA Custom Electronics).

Data Processing

IM data files were processed as previously described.^{13, 15, 18} In brief, custom in-house Python scripts utilized *multiplierz*¹¹⁹ to extract from Thermo RAW files mass spectral data from each scan over the entire acquisition. Ion mobility data were obtained by extracting intensity information for m/z values over acquisition time followed by Fourier transform to convert from frequency to drift time domains using Scipy¹²⁰ and Numpy¹²¹ packages. The resulting data can then be imported into UniDec¹²² or PULSAR⁵⁵ for additional processing.

Results and Discussion

Previously, mass selection with DWT has only been experimentally achieved for small, non-native proteins⁷⁰, but has been simulated for complexes approaching MDa masses.^{64, 65, 71, 285, 286} In this work, the mass selection of individual charge states for large protein complexes (>100 kDa) has been effectuated. The overall performance of DWT for isolation of single charge states of C-reactive protein (CRP), membrane protein ammonium transport channel (AmtB), and type 1 chaperonin GroEL is illustrated by data shown in **Figure 26**. This data was collected using a highly asymmetric duty cycle of 85/15 to generate the waveform in Q2. Transmission for all ions is generally achieved at a 50/50 duty cycle; more asymmetric duty cycles (such as 60/40, 75/25, 85/15) produce a narrowing window of stability in the m/z dimension. The positioning of this selection window in the m/z dimension is controlled by the DWT frequency that is applied to Q2, as reported previously.⁶⁹ Thus, scanning the frequency of a requisitely narrow stability window should give rise to individual charge states as a function DWT frequency. **Figure 26A** exhibits this frequency scanning procedure for a sample of CRP scanned from 75kHz to 125kHz. Note the low abundance of the TIC at low frequencies (~75kHz), which indicates the low-mass cut-off (LMCO) is above the lowest charge state of the 10mer resulting in no ion transmission. As the frequency increases, stability zones are reached to allow for the transmission of the CRP 10-mer charge state distribution. These signals then dissipate as the frequency increases, signifying that the frequencies in the middle of the plot do not stabilize any of the observed species. Around 100kHz in Q2, the first signals for the CRP 5mer begin to arise; each of the subsequent peaks in **Figure 28A** are a result

of stabilizing individual charge states for the CRP 5-mer (m/z 5008 (23^+), m/z 4779 (24^+), m/z 4609 (25^+) respectively). The TIC peaks are extracted and displayed as mass spectral plots in **Figures 26B** demonstrating the selection of individual charge states in Q2.

Isolation of other model protein complexes is executed by repeating the frequency sweep for selecting a single CRP charge state. **Figure 26C**, **26D**, and **26E** demonstrate the selection capabilities of Q2 using model protein systems for CRP, AmtB, and GroEL, respectively, at a fixed frequency and duty cycle. CRP 115 kDa full MS and isolated 24^+ charge state at m/z 4800 shown in panels C. AmtB 127 kDa with 155 V desolvation applied in q1 full MS and isolation of the 16^+ charge state at m/z 7935 shown in panel D. GroEL 801 kDa full MS and isolated 64^+ charge state at 12514 m/z with some contamination of the 63^+ charge state in panel E. Collectively, the data shown in **Figure 26** illustrates isolation a single charge state of native protein complexes with molecular weights ranging from ~100 kDa to approaching 1 MDa, thereby making it possible to perform more detailed experiments, IMS, CID, both top-down and complex-down, on specific charge states of proteins and protein complex.

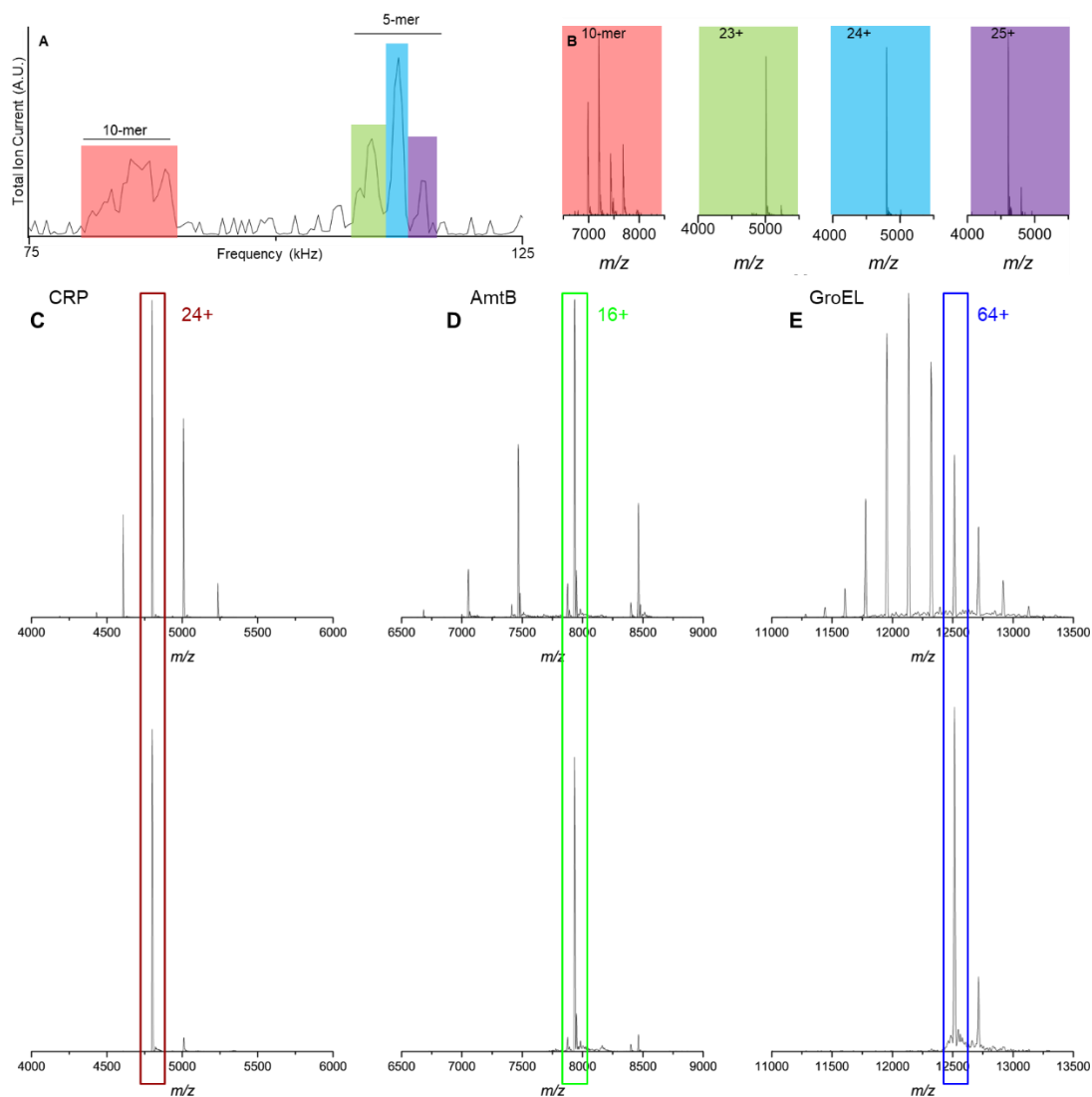


Figure 26 (A) Total ion current (TIC) detected as the frequency of Q2 (85/15 duty cycle with a $\pm 10V$ DC bias applied on rod pairs at $300V_{pp}$) is increased from ~ 75 kHz to 125 kHz. Frequency stepped in 1 kHz steps at the rate of ~ 1 kHz per second in panel A to produce an m/z selection chromatogram of quadrupole 2 (Q2). (B) extracted MS for the given frequency range shown in panel 29A. Full-ion transmission and isolation of a single charge state for CRP (Panel C), AmtB (Panel D), and GroEL (Panel E).

The performance of the qQ-FT-IMS-Orbitrap mass spectrometer was evaluated using protein complexes that illustrate specific requirements for a variety of native MS research projects. The following experiments were carried out: (i) MS analysis of C-reactive protein complex using a range of collisional activation (CA) conditions, (ii) mild CA to remove adducted species (salts, solvent, detergents) from a membrane protein complex (AmtB), (iii) demonstrate capabilities of the instrument for the analysis of a very large protein complex (801 kDa. complex of GroEL).

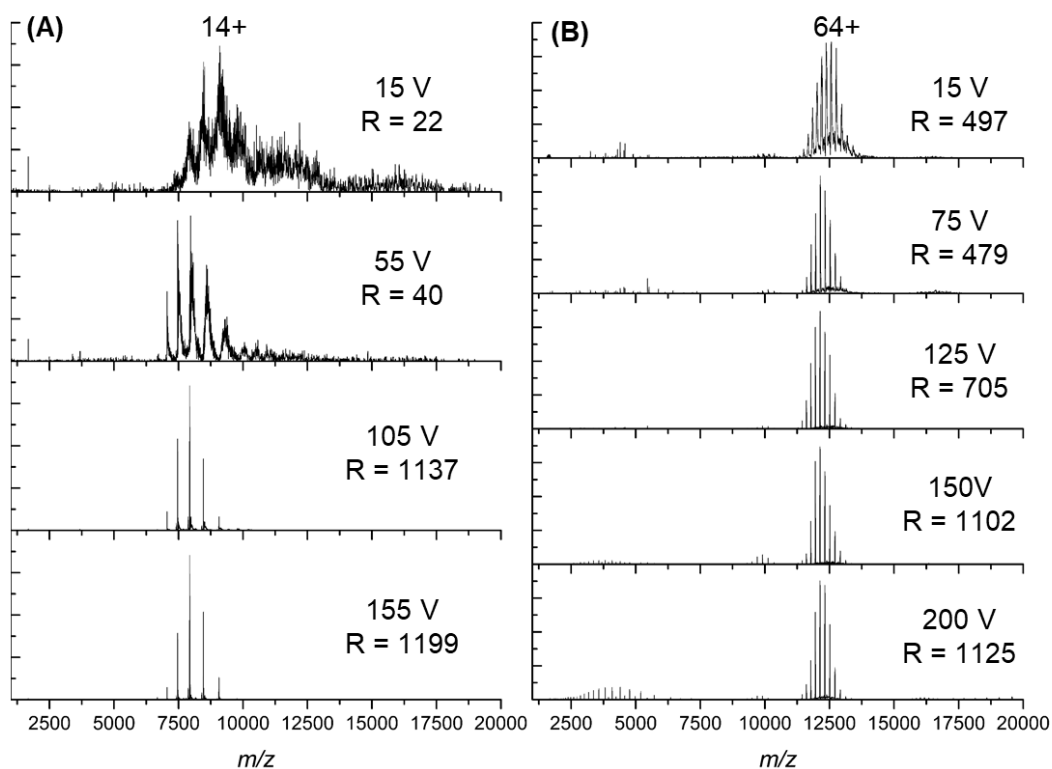


Figure 27 Illustrates how mild collisional activation in the q of the qQ-FT-IM-PF-DT Orbitrap can be used to remove adducted species (salts, endogenous lipids and other small molecules) from (A) trimeric ammonia transport channel (AmtB, 127kDa) and (B) GroEL (802 kDa, 14mer). The collision voltages indicated refer to the potential applied from the entrance lense of q1 to the DC offset bias on the q1 rods. It is possible that CA in q1 may produce non-native state ions; whether this occurs or not can be assessed by using ion mobility as shown in panels B and C of

Figure 28. Resolution (centroid / $\Delta m/z$ @ FWHM) of the primary charge state is listed in each panel.

Native mass spectra of membrane protein complexes contain abundant signals that arise from non-specific adducts, *i.e.*, detergents, and/or salts on the protein that are carried over during the ESI process. The qQ quadrupole system was specifically designed in order to implement mild-collisional activation of complexes to remove these adducted species. AmtB is a membrane protein that requires solubilization in detergent micelles for MS compatibility;^{10, 11, 53, 54, 180, 190, 235} the detergent micelle containing the membrane protein is transferred into the gas phase and subsequently disrupted by collisional activation to yield a native protein complex. **Figure 27A** shows the activation of AmtB as a function of the DC potential between aperture 1 and DC bias of q1. At 15 V potential drop, AmtB has C₈E₄ detergent adducted that needs to be removed via mild-activation or by elevating the source pressure to expose the bare protein.²⁹⁶ As the collision energy of AmtB is elevated to 155 V, the detergent is collisionally removed as observed by the increase in the resolution (defined as the m/z centroid / $\Delta m/z$ at full width) half maximum (FWHM)), consistent with previously reported results. Similar effects of mild activation are observed for GroEL (**Figure 27B**), where initially endogenous adducts are bound to GroEL at low activation voltages (15V).²⁵¹ As the activation voltage is increased to 125 V for GroEL, the non-specific adducts are collisionally removed. The activation in q1 results in baseline resolved charge states shown by the resolution increase from 497 to 705 at 15 V to 125 V, respectively. However, as activation energy increases beyond 125 V, the GroEL 14-mer dissociates into monomer and 13-mer at low abundance.

Complex-down characterization of a protein complex (C-reactive protein (CRP))

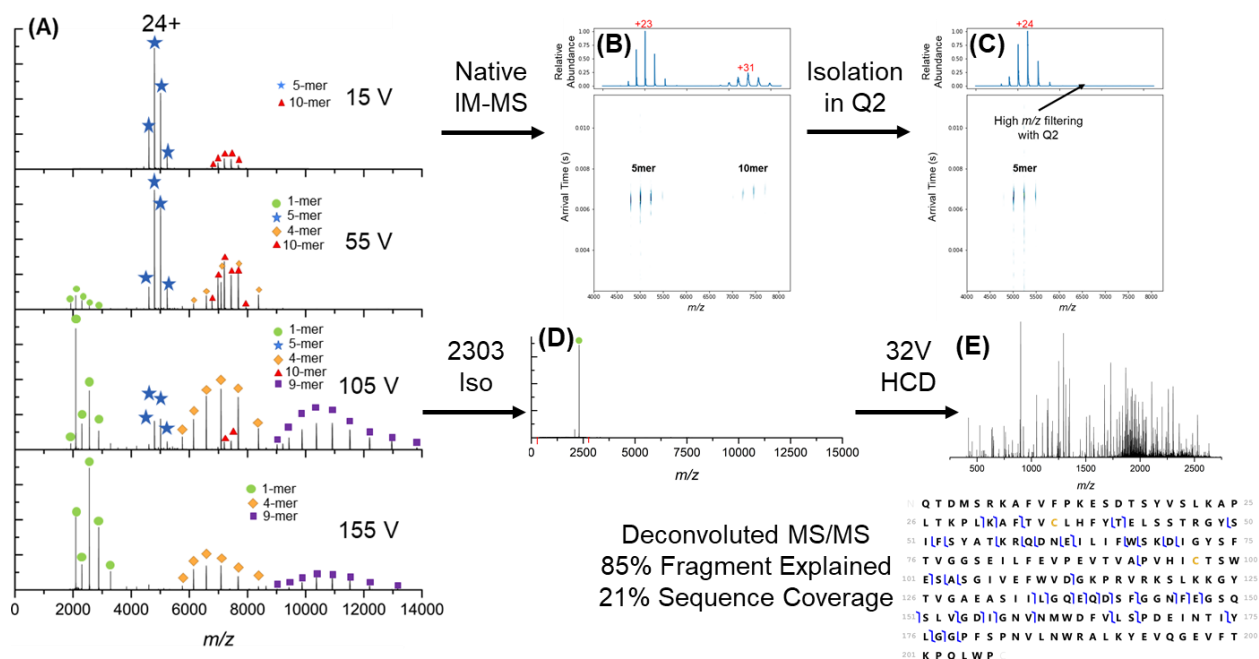


Figure 28 Illustrates complex-down characterization of the CRP. (A) The native MS spectrum of CPR is shown in the top panel, and each of the panels below contain mass spectra resulting from collisional activation (at the indicated voltage) of the ion populations in the panel above. Panel (B) contains the same mass spectrum shown in (A) and the 2-D plots for arrival-time vs m/z for the 5-mer and 10-mer CRP ions. Panel (C) contains the mass spectrum acquired following mass-selection of the CRP 5-mer ions using DWT as described above. Panel (D) contain the mass spectrum obtained by using DWT to mass select the CRP monomer (24+ 5 mer ion), and panel (E) contains the top-down mass spectrum of the mass selected ion shown in panel (D). The amino acid sequence of CRP is shown and the sequence informative fragment ion are label accordingly.

Activation in q1, in addition to enhanced desolvation for adducted protein complexes, can dissociate protein complexes to produce monomer and complementary n-1 mer for accurate mass analysis. **Figure 28A** illustrates the CID products obtained at different activation voltages in q1. Using mild activation energies (~15 V), the mass

spectrum of CRP contains abundant ions corresponding to the native, intact 5-mer of CRP (115 kDa) and low abundance signals for the non-specific 10-mer. Increasing the collision potential to 105 V promote dissociation of CRP 10-mer to form the 5-mer and also increases the formation of 1-mer, 4-mer, and 9-mer, possibly mixed fragment ions formed by dissociation of the 5-mer and 10-mer. Further increases in “energy” q_1 results in more substantial precursor depletion and CID product formation.

Ion-mobility measurements were achieved using a qQ-FT-IM-PF-DT with a DT length of 55 cm. The overall theory and operation of the PF-FT technology are described in previous publications.^{46, 47, 49, 125, 133, 134} The data shown in **Figure 28B** was collected at a field strength of $6.2 \text{ V/cm}^{-1} \text{ torr}^{-1}$. **Figure 28B** shows the 2-D plots of CRP arrival time vs. m/z for the 5-mer and 10-mer, where **Figure 28** only the 5-mer is selected using Q2 by destabilizing the 10-mer before IM-MS. Selection of the 5-mer, as illustrated in **Figure 28C**, was achieved by tuning the frequency of the digital waves in an 85/15 duty cycle. Note that the observed shift in the centroid of the CSD between 31B and 31C results from the selection window and not indicative of ion heating prior to mobility. By selecting an oligomeric state vs. full-ion transmission, the number of ions entering the DT decreases, diminishing the space charging that ions undergo. Additionally, the individual charge states are separated in the mobility domain, increasing the S/N ratio without the loss of ion signal. The selection of an entire oligomeric state vs. a single charge state allows for other forms of pre-IM activation to be used at higher throughput.

The qQ-FT-IM-PF-DT Orbitrap described allows for structural characterization of analytes of interest by selection and then activation prior to mass analysis via native

complex-down MS. Native ions (**Figure 28A**) are initially activated in q1 (**Figure 29A @ 105V**), where the resulting monomers produced by CID are isolated in DWT-driven Q2 using an 85/15 duty cycle (**Figure 28D**). Mass-selected 10^+ monomer ions were subsequently activated in the HCD cell prior to high-resolution mass analysis (**Figure 28E**). The resulting pseudo-MS³ fragments were deconvoluted via UniDec¹²², ProteinMetrics²⁵⁰, and ProSite Lite²⁹⁷ to get top-down sequencing of the protein, resulting in ~21% sequence coverage for the 10^+ monomer where 80% of the detected fragments are assignable. The sequence coverage increased to 31%, with 85% assigned fragments, when the 12^+ monomer ion was selected in Q2 and fragmented in the HCD cell (data not shown). The mass resolution of the Orbitrap platform increases the number of assignable high-charge fragments due to isotopic resolution.²⁹⁸

Conclusions:

A novel dual-quadrupole FT-IM orbitrap has been developed, creating the next generation of high-resolution IM-MS platforms. This platform allows for activation, mass selection, and IM-MS analysis, and complex down analysis of protein complexes. Additional activation techniques (e.g., CID, and SID) can be added to this platform to expand the biophysical toolbox in structural biology. A collisional activation region has been designed prior to mass filtering to clean up intrinsically dirty proteins, as shown with AmtB and GroEL, and allow for dissociation of complexes. Most notably, without digital waveform technology, floating a selection quadrupole is near-impossible with safety concerns and the high cost of RF drivers. For the first time, DWT has been shown to

transmit, isolate, and filter large protein complexes (approaching the mega-Dalton size) that support the previously described theory.

CHAPTER VI

CONCLUSIONS

The technology of IM-MS is constantly improving to facilitate new techniques, applications, designs, and analyte types. Each new development in technology loops through a “Tick – Tock” cycle between the development of instrumentation and increasing sample complexity, where previously hidden details are revealed. New commercial developments in native MS or IM-MS have come from the adaptation/commercialization of academic research projects.

CCS determinations of native proteins and protein complexes using Fourier-transform periodic-focusing ion mobility (PF-DT-FT-IM) Orbitrap was shown in **Chapter 2**. SIMION 8.1 was used to calculate the mobility dampening term, α , for native proteins and protein complexes. The calculated α value was used for the determination of first-principles CCS of 13 proteins and protein complexes spanning a molecular weight range of 8 to 800 kDa.

Technology transfer of novel instrumentation from the Thermo Scientific Exactive Plus Orbitrap with Extended Mass Range to the Thermo Scientific Q Exactive UHMR Hybrid Quadrupole-Orbitrap was performed. A PF-DT-FT-IM was coupled to a state-of-the-art Orbitrap MS capable of sampling up to 80,000 m/z . Native IM-MS-Orbitrap data was collected on soluble protein complexes ranging from ~50 to 800 kDa, as well as a trimeric membrane protein complex, the ammonia transport channel (AmtB, ~127 kDa) with novel charge reduction agents was shown in **Chapter 3**.

A home-built vT-nESI source was developed to control the solution temperature of samples contained within static nESI capillaries in **Chapter 4**. The new vT-nESI consists of an aluminum heat exchanger interfaced to a three-stage thermoelectric chip (TEC) with a DC-fan coupled to a heatsink to dissipate heat generated by the device. The TEC maintains the temperature of the heat exchanger and the solution contained in the static-nESI capillaries at the desired temperatures ranging from 5 to 98°C. The vT-nESI source showed, for the first time by mass spectrometry analysis, both cold- and heat-induced folding changes of model proteins, detection of low-temperature endotherms, and ligand binding of the protein folding chaperonin GroEL.

While the instrumentation developed for the IM-UHMR acquires high-resolution IM-MS data, there are limitations to the number of pre-IM activation methods to probe primary, secondary, tertiary, and quaternary structures of proteins. Furthermore, by not activating ions, the achievable maximum resolution is diminished in both the mass and IM domains. The development described in **Chapter 5** shows a modular platform allowing for activation using the first quadrupole region and a quadrupole mass filter utilizing digital waveform technology. These additional capabilities allow for studying a broader range of protein complex systems, which require desolvation energy previously unavailable on the IM-UHMR platform. Ultimately, the (vT)-nESI-qQ-PF-DT-FT-IM-Orbitrap platform described in **Chapter 5** allows for numerous pre-mobility activation techniques and high-resolution IM-MS to be implemented after ion clean-up and mass selection.

REFERENCES

1. Leney, A. C.; Heck, A. J. R., Native Mass Spectrometry: What is in the Name? *Journal of the American Society for Mass Spectrometry* **2017**, *28* (1), 5-13.
2. Chandler, S. A.; Benesch, J. L. P., Mass spectrometry beyond the native state. *Current Opinion in Chemical Biology* **2018**, *42*, 130-137.
3. Zhurov, K. O.; Fornelli, L.; Wodrich, M. D.; Laskay, Ü. A.; Tsybin, Y. O., Principles of electron capture and transfer dissociation mass spectrometry applied to peptide and protein structure analysis. *Chemical Society Reviews* **2013**, *42* (12), 5014-5030.
4. Catherman, A. D.; Skinner, O. S.; Kelleher, N. L., Top Down proteomics: facts and perspectives. *Biochem Biophys Res Commun* **2014**, *445* (4), 683-693.
5. Harper, B.; Neumann, E. K.; Stow, S. M.; May, J. C.; McLean, J. A.; Solouki, T., Determination of ion mobility collision cross sections for unresolved isomeric mixtures using tandem mass spectrometry and chemometric deconvolution. *Analytica Chimica Acta* **2016**, *939*, 64-72.
6. Fornelli, L.; Srzentić, K.; Toby, T. K.; Doubleday, P. F.; Huguet, R.; Mullen, C.; Melani, R. D.; dos Santos Seckler, H.; DeHart, C. J.; Weisbrod, C. R.; Durbin, K. R.; Greer, J. B.; Early, B. P.; Fellers, R. T.; Zabrouskov, V.; Thomas, P.; Compton, P. D.; Kelleher, N. L., Thorough performance evaluation of 213 nm ultraviolet

photodissociation for top-down proteomics. *Molecular & Cellular Proteomics* **2019**, mcp.TIR119.001638.

7. Brodbelt, J. S., Photodissociation mass spectrometry: new tools for characterization of biological molecules. *Chemical Society Reviews* **2014**, *43* (8), 2757-2783.

8. Liu, Y.; LoCaste, C. E.; Liu, W.; Poltash, M. L.; Russell, D. H.; Laganowsky, A., Selective binding of a toxin and phosphatidylinositides to a mammalian potassium channel. *Nature Communications* **2019**, *10* (1), 1352.

9. Poltash, M. L.; McCabe, J. W.; Patrick, J. W.; Laganowsky, A.; Russell, D. H., Development and Evaluation of a Reverse-Entry Ion Source Orbitrap Mass Spectrometer. *Journal of the American Society for Mass Spectrometry* **2019**, *30* (1), 192-198.

10. Cong, X.; Liu, Y.; Liu, W.; Liang, X.; Russell, D. H.; Laganowsky, A., Determining Membrane Protein-Lipid Binding Thermodynamics Using Native Mass Spectrometry. *J Am Chem Soc* **2016**, *138* (13), 4346-9.

11. Liu, Y.; Cong, X.; Liu, W.; Laganowsky, A., Characterization of Membrane Protein-Lipid Interactions by Mass Spectrometry Ion Mobility Mass Spectrometry. *Journal of the American Society for Mass Spectrometry* **2017**, *28* (4), 579-586.

12. Chen, S.-H.; Russell, D. H., Reaction of Human Cd7metallothionein and N-Ethylmaleimide: Kinetic and Structural Insights from Electrospray Ionization Mass Spectrometry. *Biochemistry* **2015**, *54* (39), 6021-6028.

13. Poltash, M. L.; Shirzadeh, M.; McCabe, J. W.; Moghadamchargari, Z.; Laganowsky, A.; Russell, D. H., New insights into the metal-induced oxidative degradation pathways of transthyretin. *Chemical Communications* **2019**, *55* (28), 4091-4094.
14. Chen, S.-H.; Chen, L.; Russell, D. H., Metal-Induced Conformational Changes of Human Metallothionein-2A: A Combined Theoretical and Experimental Study of Metal-Free and Partially Metalated Intermediates. *Journal of the American Chemical Society* **2014**, *136* (26), 9499-9508.
15. Poltash, M. L.; McCabe, J. W.; Shirzadeh, M.; Laganowsky, A.; Clowers, B. H.; Russell, D. H., Fourier Transform-Ion Mobility-Orbitrap Mass Spectrometer: A Next-Generation Instrument for Native Mass Spectrometry. *Analytical Chemistry* **2018**, *90* (17), 10472-10478.
16. Moghadamchargari, Z.; Huddleston, J.; Shirzadeh, M.; Zheng, X.; Clemmer, D. E.; M. Raushel, F.; Russell, D. H.; Laganowsky, A., Intrinsic GTPase Activity of K-RAS Monitored by Native Mass Spectrometry. *Biochemistry* **2019**, *58* (31), 3396-3405.
17. Holmquist, M. L.; Ihms, E. C.; Gollnick, P.; Wysocki, V. H.; Foster, M. P., Population Distributions from Native Mass Spectrometry Titrations Reveal Nearest-Neighbor Cooperativity in the Ring-Shaped Oligomeric Protein TRAP. *Biochemistry* **2020**, *59* (27), 2518-2527.

18. Poltash, M. L.; McCabe, J. W.; Shirzadeh, M.; Laganowsky, A.; Russell, D. H., Native IM-Orbitrap MS: Resolving what was hidden. *TrAC Trends in Analytical Chemistry* **2019**.
19. Shirzadeh, M.; Boone, C. D.; Laganowsky, A.; Russell, D. H., Topological Analysis of Transthyretin Disassembly Mechanism: Surface-Induced Dissociation Reveals Hidden Reaction Pathways. *Analytical Chemistry* **2019**, *91* (3), 2345-2351.
20. Stiving, A. Q.; VanAernum, Z. L.; Busch, F.; Harvey, S. R.; Sarni, S. H.; Wysocki, V. H., Surface-Induced Dissociation: An Effective Method for Characterization of Protein Quaternary Structure. *Analytical Chemistry* **2019**, *91* (1), 190-209.
21. VanAernum, Z. L.; Gilbert, J. D.; Belov, M. E.; Makarov, A. A.; Horning, S. R.; Wysocki, V. H., Surface-Induced Dissociation of Noncovalent Protein Complexes in an Extended Mass Range Orbitrap Mass Spectrometer. *Analytical Chemistry* **2019**, *91* (5), 3611-3618.
22. Zhou, M.; Wysocki, V. H., Surface Induced Dissociation: Dissecting Noncovalent Protein Complexes in the Gas phase. *Accounts of Chemical Research* **2014**, *47* (4), 1010-1018.
23. Kaltashov, I. A.; Mohimen, A., Estimates of Protein Surface Areas in Solution by Electrospray Ionization Mass Spectrometry. *Analytical Chemistry* **2005**, *77* (16), 5370-5379.
24. Rajabi, K.; Ashcroft, A. E.; Radford, S. E., Mass spectrometric methods to analyze the structural organization of macromolecular complexes. *Methods* **2015**, *89*, 13-21.

25. Konermann, L.; Pan, J.; Liu, Y.-H., Hydrogen exchange mass spectrometry for studying protein structure and dynamics. *Chemical Society Reviews* **2011**, *40* (3), 1224-1234.
26. Masson, G. R.; Burke, J. E.; Ahn, N. G.; Anand, G. S.; Borchers, C.; Brier, S.; Bou-Assaf, G. M.; Engen, J. R.; Englander, S. W.; Faber, J.; Garlish, R.; Griffin, P. R.; Gross, M. L.; Guttman, M.; Hamuro, Y.; Heck, A. J. R.; Houde, D.; Iacob, R. E.; Jørgensen, T. J. D.; Kaltashov, I. A.; Klinman, J. P.; Konermann, L.; Man, P.; Mayne, L.; Pascal, B. D.; Reichmann, D.; Skehel, M.; Snijder, J.; Strutzenberg, T. S.; Underbakke, E. S.; Wagner, C.; Wales, T. E.; Walters, B. T.; Weis, D. D.; Wilson, D. J.; Wintrode, P. L.; Zhang, Z.; Zheng, J.; Schriemer, D. C.; Rand, K. D., Recommendations for performing, interpreting and reporting hydrogen deuterium exchange mass spectrometry (HDX-MS) experiments. *Nature Methods* **2019**, *16* (7), 595-602.
27. Rolland, A. D.; Prell, J. S., Computational insights into compaction of gas-phase protein and protein complex ions in native ion mobility-mass spectrometry. *TrAC Trends in Analytical Chemistry* **2019**, *116*, 282-291.
28. Berman, H. M.; Westbrook, J.; Feng, Z.; Gilliland, G.; Bhat, T. N.; Weissig, H.; Shindyalov, I. N.; Bourne, P. E., The Protein Data Bank. *Nucleic Acids Research* **2000**, *28* (1), 235-242.
29. Anfinsen, C. B., Principles that Govern the Folding of Protein Chains. *Science* **1973**, *181* (4096), 223-230.

30. Polasky, D. A.; Dixit, S. M.; Fantin, S. M.; Ruotolo, B. T., CIUSuite 2: Next-Generation Software for the Analysis of Gas-Phase Protein Unfolding Data. *Analytical Chemistry* **2019**, *91* (4), 3147-3155.
31. Donor, M. T.; Shepherd, S. O.; Prell, J. S., Rapid Determination of Activation Energies for Gas-Phase Protein Unfolding and Dissociation in a Q-IM-ToF Mass Spectrometer. *Journal of the American Society for Mass Spectrometry* **2020**, *31* (3), 602-610.
32. Sipe, S. N.; Brodbelt, J. S., Impact of charge state on 193 nm ultraviolet photodissociation of protein complexes. *Physical Chemistry Chemical Physics* **2019**, *21* (18), 9265-9276.
33. Pagel, K.; Kupser, P.; Bierau, F.; Polfer, N. C.; Steill, J. D.; Oomens, J.; Meijer, G.; Kokscha, B.; von Helden, G., Gas-phase IR spectra of intact α -helical coiled coil protein complexes. *International Journal of Mass Spectrometry* **2009**, *283* (1), 161-168.
34. Seo, J.; Hoffmann, W.; Warnke, S.; Huang, X.; Gewinner, S.; Schöllkopf, W.; Bowers, M. T.; von Helden, G.; Pagel, K., An infrared spectroscopy approach to follow β -sheet formation in peptide amyloid assemblies. *Nature Chemistry* **2017**, *9* (1), 39-44.
35. Selkoe, D. J., Cell biology of protein misfolding: The examples of Alzheimer's and Parkinson's diseases. *Nature Cell Biology* **2004**, *6* (11), 1054-1061.
36. Zhang, Q.; Powers, E. T.; Nieva, J.; Huff, M. E.; Dendle, M. A.; Bieschke, J.; Glabe, C. G.; Eschenmoser, A.; Wentworth, P.; Lerner, R. A.; Kelly, J. W., Metabolite-

initiated protein misfolding may trigger Alzheimer's disease. *Proceedings of the National Academy of Sciences of the United States of America* **2004**, *101* (14), 4752-4757.

37. Forloni, G.; Terreni, L.; Bertani, I.; Fogliarino, S.; Invernizzi, R.; Assini, A.; Ribizzi, G.; Negro, A.; Calabrese, E.; Volonté, M. A.; Mariani, C.; Franceschi, M.; Tabaton, M.; Bertoli, A., Protein misfolding in Alzheimer's and Parkinson's disease: genetics and molecular mechanisms. *Neurobiology of Aging* **2002**, *23* (5), 957-976.

38. Silva, J. L.; Vieira, T. C. R. G.; Gomes, M. P. B.; Bom, A. P. A.; Lima, L. M. T. R.; Freitas, M. S.; Ishimaru, D.; Cordeiro, Y.; Foguel, D., Ligand Binding and Hydration in Protein Misfolding: Insights from Studies of Prion and p53 Tumor Suppressor Proteins. *Accounts of Chemical Research* **2010**, *43* (2), 271-279.

39. Wang, M.; Kaufman, R. J., The impact of the endoplasmic reticulum protein-folding environment on cancer development. *Nature Reviews Cancer* **2014**, *14* (9), 581-597.

40. Allen, S. J.; Bush, M. F., Radio-Frequency (rf) Confinement in Ion Mobility Spectrometry: Apparent Mobilities and Effective Temperatures. *Journal of The American Society for Mass Spectrometry* **2016**, *27* (12), 2054-2063.

41. Gabelica, V.; Shvartsburg, A. A.; Afonso, C.; Barran, P.; Benesch, J. L. P.; Bleiholder, C.; Bowers, M. T.; Bilbao, A.; Bush, M. F.; Campbell, J. L.; Campuzano, I. D. G.; Causon, T.; Clowers, B. H.; Creaser, C. S.; De Pauw, E.; Far, J.; Fernandez-Lima, F.; Fjeldsted, J. C.; Giles, K.; Groessl, M.; Hogan Jr, C. J.; Hann, S.; Kim, H. I.; Kurulugama, R. T.; May, J. C.; McLean, J. A.; Pagel, K.; Richardson, K.; Ridgeway,

- M. E.; Rosu, F.; Sobott, F.; Thalassinou, K.; Valentine, S. J.; Wyttenbach, T., Recommendations for reporting ion mobility Mass Spectrometry measurements. *Mass Spectrom Rev* **2019**, *38* (3), 291-320.
42. Mason, E. A.; McDaniel, E. W., Transport properties of ions in gases. *NASA STI/Recon Technical Report A* **1988**, *89*, 15174.
43. Bluhm, B. K.; Gillig, K. J.; Russell, D. H., Development of a Fourier-transform ion cyclotron resonance mass spectrometer-ion mobility spectrometer. *Review of Scientific Instruments* **2000**, *71* (11), 4078-4086.
44. Bluhm, B. K.; North, S. W.; Russell, D. H., Separation of spin-orbit coupled metastable states of Kr⁺ and Xe⁺ by ion mobility. *The Journal of Chemical Physics* **2001**, *114* (4), 1709-1715.
45. Javahery, G.; Thomson, B., A segmented radiofrequency-only quadrupole collision cell for measurements of ion collision cross section on a triple quadrupole mass spectrometer. *Journal of the American Society for Mass Spectrometry* **1997**, *8* (7), 697-702.
46. Verbeck, G. F.; Ruotolo, B. T.; Gillig, K. J.; Russell, D. H., Resolution equations for high-field ion mobility. *Journal of the American Society for Mass Spectrometry* **2004**, *15* (9), 1320-1324.
47. Gillig, K. J.; Ruotolo, B. T.; Stone, E. G.; Russell, D. H., An electrostatic focusing ion guide for ion mobility-mass spectrometry. *International Journal of Mass Spectrometry* **2004**, *239* (1), 43-49.

48. Blase, R. C.; Silveira, J. A.; Gillig, K. J.; Gamage, C. M.; Russell, D. H., Increased ion transmission in IMS: A high resolution, periodic-focusing DC ion guide ion mobility spectrometer. *International Journal of Mass Spectrometry* **2011**, *301* (1), 166-173.
49. Silveira, J. A.; Jeon, J.; Gamage, C. M.; Pai, P.-J.; Fort, K. L.; Russell, D. H., Damping Factor Links Periodic Focusing and Uniform Field Ion Mobility for Accurate Determination of Collision Cross Sections. *Analytical Chemistry* **2012**, *84* (6), 2818-2824.
50. Jeon, J. Development and Application of an Electrospray Ionization Ion Mobility-mass Spectrometer Using an RF Ion Funnel and Periodic-focusing Ion Guide. Texas A&M University, OAKTrust, 2013.
51. Kelly, R. T.; Tolmachev, A. V.; Page, J. S.; Tang, K.; Smith, R. D., The ion funnel: theory, implementations, and applications. *Mass Spectrom Rev* **2010**, *29* (2), 294-312.
52. Julian, R. R.; Mabbett, S. R.; Jarrold, M. F., Ion Funnels for the Masses: Experiments and Simulations with a Simplified Ion Funnel. *Journal of the American Society for Mass Spectrometry* **2005**, *16* (10), 1708-1712.
53. Laganowsky, A.; Reading, E.; Hopper, J. T. S.; Robinson, C. V., Mass spectrometry of intact membrane protein complexes. *Nature Protocols* **2013**, *8* (4), 639-651.

54. Laganowsky, A.; Reading, E.; Allison, T. M.; Ulmschneider, M. B.; Degiacomi, M. T.; Baldwin, A. J.; Robinson, C. V., Membrane proteins bind lipids selectively to modulate their structure and function. *Nature* **2014**, *510* (7503), 172-175.
55. Allison, T. M.; Reading, E.; Liko, I.; Baldwin, A. J.; Laganowsky, A.; Robinson, C. V., Quantifying the stabilizing effects of protein–ligand interactions in the gas phase. *Nature Communications* **2015**, *6* (1), 8551.
56. Patrick, J. W.; Boone, C. D.; Liu, W.; Conover, G. M.; Liu, Y.; Cong, X.; Laganowsky, A., Allostery revealed within lipid binding events to membrane proteins. **2018**, *115* (12), 2976-2981.
57. Hecht, E. S.; Scigelova, M.; Eliuk, S.; Makarov, A., Fundamentals and Advances of Orbitrap Mass Spectrometry. In *Encyclopedia of Analytical Chemistry*, pp 1-40.
58. Yost, R. A.; Enke, C. G., Triple Quadrupole Mass Spectrometry. *Analytical Chemistry* **1979**, *51* (12), 1251A-1264A.
59. Pitt, J. J., Principles and applications of liquid chromatography-mass spectrometry in clinical biochemistry. *Clin Biochem Rev* **2009**, *30* (1), 19-34.
60. Murrell, J.; Despeyroux, D.; Lammert, S. A.; Stephenson, J. L.; Goeringer, D. E., “Fast excitation” CID in a quadrupole ion trap mass spectrometer. *Journal of the American Society for Mass Spectrometry* **2003**, *14* (7), 785-789.
61. Ichou, F.; Lesage, D.; Machuron-Mandard, X.; Junot, C.; Cole, R. B.; Tabet, J.-C., Collision cell pressure effect on CID spectra pattern using triple quadrupole instruments: a RRKM modeling. **2013**, *48* (2), 179-186.

62. Paul, W.; Steinwedel, H., Notizen: Ein neues Massenspektrometer ohne Magnetfeld. **1953**, 8 (7), 448.
63. Richards, J. A.; Huey, R. M.; Hiller, J., A new operating mode for the quadrupole mass filter. *International Journal of Mass Spectrometry and Ion Physics* **1973**, 12 (4), 317-339.
64. Lee, J.; Marino, M. A.; Koizumi, H.; Reilly, P. T. A., Simulation of duty cycle-based trapping and ejection of massive ions using linear digital quadrupoles: The enabling technology for high resolution time-of-flight mass spectrometry in the ultra high mass range. *International Journal of Mass Spectrometry* **2011**, 304 (1), 36-40.
65. Reilly, P. T. A.; Brabeck, G. F., Mapping the pseudopotential well for all values of the Mathieu parameter q in digital and sinusoidal ion traps. *International Journal of Mass Spectrometry* **2015**, 392, 86-90.
66. Brabeck, G. F.; Reilly, P. T. A., Computational Analysis of Quadrupole Mass Filters Employing Nontraditional Waveforms. *Journal of The American Society for Mass Spectrometry* **2016**, 27 (6), 1122-1127.
67. Hoffman, N. M.; Opačić, B.; Reilly, P. T. A., Note: An inexpensive square waveform ion funnel driver. *Review of Scientific Instruments* **2017**, 88 (1), 016104.
68. Opačić, B.; Huntley, A. P.; Clowers, B. H.; Reilly, P. T. A., Digital mass filter analysis in stability zones A and B. **2018**, 53 (12), 1155-1168.
69. Hoffman, N. M.; Gotlib, Z. P.; Opačić, B.; Huntley, A. P.; Moon, A. M.; Donahoe, K. E. G.; Brabeck, G. F.; Reilly, P. T. A., Digital Waveform Technology and

the Next Generation of Mass Spectrometers. *Journal of The American Society for Mass Spectrometry* **2018**, *29* (2), 331-341.

70. Opačić, B.; Hoffman, N. M.; Gotlib, Z. P.; Clowers, B. H.; Reilly, P. T. A., Using Digital Waveforms to Mitigate Solvent Clustering During Mass Filter Analysis of Proteins. *Journal of the American Society for Mass Spectrometry* **2018**, *29* (10), 2081-2085.

71. Huntley, A. P.; Brabeck, G. F.; Reilly, P. T. A., Tutorial and comprehensive computational study of acceptance and transmission of sinusoidal and digital ion guides. *Journal of Mass Spectrometry* **2019**, *54* (11), 857-868.

72. Wallace, B. A., The role of circular dichroism spectroscopy in the era of integrative structural biology. *Current Opinion in Structural Biology* **2019**, *58*, 191-196.

73. Markwick, P. R. L.; Malliavin, T.; Nilges, M., Structural biology by NMR: structure, dynamics, and interactions. *PLoS Comput Biol* **2008**, *4* (9), e1000168-e1000168.

74. van der Wel, P. C. A., New applications of solid-state NMR in structural biology. *Emerg Top Life Sci* **2018**, *2* (1), 57-67.

75. Shi, Y., A Glimpse of Structural Biology through X-Ray Crystallography. *Cell* **2014**, *159* (5), 995-1014.

76. Zheng, H.; Handing, K. B.; Zimmerman, M. D.; Shabalin, I. G.; Almo, S. C.; Minor, W., X-ray crystallography over the past decade for novel drug discovery - where are we heading next? *Expert Opin Drug Discov* **2015**, *10* (9), 975-989.

77. Murata, K.; Wolf, M., Cryo-electron microscopy for structural analysis of dynamic biological macromolecules. *Biochimica et Biophysica Acta (BBA) - General Subjects* **2018**, *1862* (2), 324-334.
78. Bai, X.-c.; McMullan, G.; Scheres, S. H. W., How cryo-EM is revolutionizing structural biology. *Trends in Biochemical Sciences* **2015**, *40* (1), 49-57.
79. Kiselar, J.; Chance, M. R., High-Resolution Hydroxyl Radical Protein Footprinting: Biophysics Tool for Drug Discovery. *Annual Review of Biophysics* **2018**, *47* (1), 315-333.
80. Gau, B. C.; Sharp, J. S.; Rempel, D. L.; Gross, M. L., Fast Photochemical Oxidation of Protein Footprints Faster than Protein Unfolding. *Analytical Chemistry* **2009**, *81* (16), 6563-6571.
81. Mendoza, V. L.; Vachet, R. W., Probing protein structure by amino acid-specific covalent labeling and mass spectrometry. *Mass Spectrom Rev* **2009**, *28* (5), 785-815.
82. Donnelly, D. P.; Rawlins, C. M.; DeHart, C. J.; Fornelli, L.; Schachner, L. F.; Lin, Z.; Lippens, J. L.; Aluri, K. C.; Sarin, R.; Chen, B.; Lantz, C.; Jung, W.; Johnson, K. R.; Koller, A.; Wolff, J. J.; Campuzano, I. D. G.; Auclair, J. R.; Ivanov, A. R.; Whitelegge, J. P.; Paša-Tolić, L.; Chamot-Rooke, J.; Danis, P. O.; Smith, L. M.; Tsybin, Y. O.; Loo, J. A.; Ge, Y.; Kelleher, N. L.; Agar, J. N., Best practices and benchmarks for intact protein analysis for top-down mass spectrometry. *Nature Methods* **2019**, *16* (7), 587-594.

83. Benesch, J. L. P.; Aquilina, J. A.; Ruotolo, B. T.; Sobott, F.; Robinson, C. V., Tandem Mass Spectrometry Reveals the Quaternary Organization of Macromolecular Assemblies. *Chemistry & Biology* **2006**, *13* (6), 597-605.
84. Hernández, H.; Robinson, C. V., Determining the stoichiometry and interactions of macromolecular assemblies from mass spectrometry. *Nature Protocols* **2007**, *2* (3), 715-726.
85. Zilkenat, S.; Grin, I.; Wagner, S., Stoichiometry determination of macromolecular membrane protein complexes. In *Biological Chemistry*, 2017; Vol. 398, p 155.
86. Patterson, A.; Tokmina-Lukaszewska, M.; Bothner, B., Chapter Five - Probing Cascade complex composition and stability using native mass spectrometry techniques. In *Methods in Enzymology*, Bailey, S., Ed. Academic Press: 2019; Vol. 616, pp 87-116.
87. Sahasrabudde, A.; Hsia, Y.; Busch, F.; Sheffler, W.; King, N. P.; Baker, D.; Wysocki, V. H., Confirmation of intersubunit connectivity and topology of designed protein complexes by native MS. *Proceedings of the National Academy of Sciences* **2018**.
88. Taverner, T.; Hernández, H.; Sharon, M.; Ruotolo, B. T.; Matak-Vinković, D.; Devos, D.; Russell, R. B.; Robinson, C. V., Subunit Architecture of Intact Protein Complexes from Mass Spectrometry and Homology Modeling. *Accounts of Chemical Research* **2008**, *41* (5), 617-627.
89. Levy, E. D.; Erba, E. B.; Robinson, C. V.; Teichmann, S. A., Assembly reflects evolution of protein complexes. *Nature* **2008**, *453* (7199), 1262-1265.

90. Bleiholder, C.; Bowers, M. T., The Solution Assembly of Biological Molecules Using Ion Mobility Methods: From Amino Acids to Amyloid β -Protein. *Annual Review of Analytical Chemistry* **2017**, *10* (1), 365-386.
91. Hyung, S.-J.; Robinson, C. V.; Ruotolo, B. T., Gas-Phase Unfolding and Disassembly Reveals Stability Differences in Ligand-Bound Multiprotein Complexes. *Chemistry & Biology* **2009**, *16* (4), 382-390.
92. Laemmli, U. K., Cleavage of Structural Proteins during the Assembly of the Head of Bacteriophage T4. *Nature* **1970**, *227* (5259), 680-685.
93. Majuta, S. N.; Maleki, H.; Kiani Karanji, A.; Attanyake, K.; Loch, E.; Valentine, S. J., Magnifying ion mobility spectrometry–mass spectrometry measurements for biomolecular structure studies. *Current Opinion in Chemical Biology* **2018**, *42*, 101-110.
94. Ben-Nissan, G.; Sharon, M., The application of ion-mobility mass spectrometry for structure/function investigation of protein complexes. *Current Opinion in Chemical Biology* **2018**, *42*, 25-33.
95. Shirzadeh, M.; Poltash, M. L.; Laganowsky, A.; Russell, D. H., Structural Analysis of the Effect of a Dual-FLAG Tag on Transthyretin. *Biochemistry* **2020**.
96. Poltash, M. L.; Shirzadeh, M.; McCabe, J. W.; Moghadamchargari, Z.; Laganowsky, A.; Russell, D. H., New insights into the metal-induced oxidative degradation pathways of transthyretin. *Chem Commun (Camb)* **2019**, *55* (28), 4091-4094.

97. Wyttenbach, T.; von Helden, G.; Batka, J. J.; Carlat, D.; Bowers, M. T., Effect of the long-range potential on ion mobility measurements. *Journal of the American Society for Mass Spectrometry* **1997**, *8* (3), 275-282.
98. May, J. C.; Morris, C. B.; McLean, J. A., Ion Mobility Collision Cross Section Compendium. *Analytical Chemistry* **2017**, *89* (2), 1032-1044.
99. Paglia, G.; Angel, P.; Williams, J. P.; Richardson, K.; Olivos, H. J.; Thompson, J. W.; Menikarachchi, L.; Lai, S.; Walsh, C.; Moseley, A.; Plumb, R. S.; Grant, D. F.; Palsson, B. O.; Langridge, J.; Geromanos, S.; Astarita, G., Ion Mobility-Derived Collision Cross Section As an Additional Measure for Lipid Fingerprinting and Identification. *Analytical Chemistry* **2015**, *87* (2), 1137-1144.
100. Pettit, M. E.; Harper, B.; Brantley, M. R.; Solouki, T., Collision-energy resolved ion mobility characterization of isomeric mixtures. *Analyst* **2015**, *140* (20), 6886-6896.
101. Brantley, M.; Zekavat, B.; Harper, B.; Mason, R.; Solouki, T., Automated Deconvolution of Overlapped Ion Mobility Profiles. *Journal of The American Society for Mass Spectrometry* **2014**, *25* (10), 1810-1819.
102. Dixit, S. M.; Polasky, D. A.; Ruotolo, B. T., Collision induced unfolding of isolated proteins in the gas phase: past, present, and future. *Current Opinion in Chemical Biology* **2018**, *42*, 93-100.
103. El-Baba, T. J.; Clemmer, D. E., Solution thermochemistry of concanavalin A tetramer conformers measured by variable-temperature ESI-IMS-MS. *International Journal of Mass Spectrometry* **2019**, *443*, 93-100.

104. Woodall, D. W.; Brown, C. J.; Raab, S. A.; El-Baba, T. J.; Laganowsky, A.; Russell, D. H.; Clemmer, D. E., Melting of Hemoglobin in Native Solutions as measured by IMS-MS. *Analytical Chemistry* **2020**, *92* (4), 3440-3446.
105. Marchand, A.; Rosu, F.; Zenobi, R.; Gabelica, V., Thermal Denaturation of DNA G-Quadruplexes and their Complexes with Ligands: Thermodynamic Analysis of the Multiple States Revealed by Mass Spectrometry. *bioRxiv* **2018**, 370254.
106. Clemmer, D. E.; Russell, D. H.; Williams, E. R., Characterizing the Conformationome: Toward a Structural Understanding of the Proteome. *Accounts of Chemical Research* **2017**, *50* (3), 556-560.
107. Giles, K.; Ujma, J.; Wildgoose, J.; Pringle, S.; Richardson, K.; Langridge, D.; Green, M., A Cyclic Ion Mobility-Mass Spectrometry System. *Analytical Chemistry* **2019**, *91* (13), 8564-8573.
108. Knorr, F. J.; Eatherton, R. L.; Siems, W. F.; Hill, H. H., Fourier Transform Ion Mobility Spectrometry. *Analytical Chemistry* **1985**, *57* (2), 402-406.
109. Morrison, K. A.; Siems, W. F.; Clowers, B. H., Augmenting Ion Trap Mass Spectrometers Using a Frequency Modulated Drift Tube Ion Mobility Spectrometer. *Analytical Chemistry* **2016**, *88* (6), 3121-3129.
110. Clowers, B. H.; Ibrahim, Y.; Prior, D. C.; Danielson, W. F.; Belov, M.; Smith, R. D., Enhanced Ion Utilization Efficiency Using an Electrodynamic Ion Funnel Trap as an Injection Mechanism for Ion Mobility Spectrometry. *Analytical chemistry* **2008**, *80* (3), 612-623.

111. Clowers, B. H.; Hill, H. H., Mass Analysis of Mobility-Selected Ion Populations Using Dual Gate, Ion Mobility, Quadrupole Ion Trap Mass Spectrometry. *Analytical Chemistry* **2005**, *77* (18), 5877-5885.
112. Marklund, Erik G.; Degiacomi, Matteo T.; Robinson, Carol V.; Baldwin, Andrew J.; Benesch, Justin L. P., Collision Cross Sections for Structural Proteomics. *Structure* **2015**, *23* (4), 791-799.
113. Bleiholder, C.; Wyttenbach, T.; Bowers, M. T., A novel projection approximation algorithm for the fast and accurate computation of molecular collision cross sections (I). Method. *International Journal of Mass Spectrometry* **2011**, *308* (1), 1-10.
114. Bleiholder, C.; Contreras, S.; Do, T. D.; Bowers, M. T., A novel projection approximation algorithm for the fast and accurate computation of molecular collision cross sections (II). Model parameterization and definition of empirical shape factors for proteins. *International Journal of Mass Spectrometry* **2013**, *345-347*, 89-96.
115. Anderson, S. E.; Bleiholder, C.; Brocker, E. R.; Stang, P. J.; Bowers, M. T., A novel projection approximation algorithm for the fast and accurate computation of molecular collision cross sections (III): Application to supramolecular coordination-driven assemblies with complex shapes. *International Journal of Mass Spectrometry* **2012**, *330-332*, 78-84.
116. Bleiholder, C.; Contreras, S.; Bowers, M. T., A novel projection approximation algorithm for the fast and accurate computation of molecular collision cross sections (IV).

Application to polypeptides. *International Journal of Mass Spectrometry* **2013**, 354-355, 275-280.

117. Ewing, S. A.; Donor, M. T.; Wilson, J. W.; Prell, J. S., Collidoscope: An Improved Tool for Computing Collisional Cross-Sections with the Trajectory Method. *Journal of The American Society for Mass Spectrometry* **2017**, 28 (4), 587-596.

118. Weaver, J.; Jiang, M.; Roth, A.; Puchalla, J.; Zhang, J.; Rye, H. S., GroEL actively stimulates folding of the endogenous substrate protein PepQ. *Nature Communications* **2017**, 8 (1), 15934.

119. Alexander, W. M.; Ficarro, S. B.; Adelmant, G.; Marto, J. A., multipliez v2.0: A Python-based ecosystem for shared access and analysis of native mass spectrometry data. *Proteomics* **2017**, 17 (15-16), 1700091.

120. Virtanen, P.; Gommers, R.; Oliphant, T. E.; Haberland, M.; Reddy, T.; Cournapeau, D.; Burovski, E.; Peterson, P.; Weckesser, W.; Bright, J.; van der Walt, S. J.; Brett, M.; Wilson, J.; Millman, K. J.; Mayorov, N.; Nelson, A. R. J.; Jones, E.; Kern, R.; Larson, E.; Carey, C. J.; Polat, İ.; Feng, Y.; Moore, E. W.; VanderPlas, J.; Laxalde, D.; Perktold, J.; Cimrman, R.; Henriksen, I.; Quintero, E. A.; Harris, C. R.; Archibald, A. M.; Ribeiro, A. H.; Pedregosa, F.; van Mulbregt, P.; Vijaykumar, A.; Bardelli, A. P.; Rothberg, A.; Hilboll, A.; Kloeckner, A.; Scopatz, A.; Lee, A.; Rokem, A.; Woods, C. N.; Fulton, C.; Masson, C.; Häggström, C.; Fitzgerald, C.; Nicholson, D. A.; Hagen, D. R.; Pasechnik, D. V.; Olivetti, E.; Martin, E.; Wieser, E.; Silva, F.; Lenders, F.; Wilhelm, F.; Young, G.; Price, G. A.; Ingold, G.-L.; Allen, G. E.; Lee, G.

R.; Audren, H.; Probst, I.; Dietrich, J. P.; Silterra, J.; Webber, J. T.; Slavič, J.; Nothman, J.; Buchner, J.; Kulick, J.; Schönberger, J. L.; de Miranda Cardoso, J. V.; Reimer, J.; Harrington, J.; Rodríguez, J. L. C.; Nunez-Iglesias, J.; Kuczynski, J.; Tritz, K.; Thoma, M.; Newville, M.; Kümmerer, M.; Bolingbroke, M.; Tartre, M.; Pak, M.; Smith, N. J.; Nowaczyk, N.; Shebanov, N.; Pavlyk, O.; Brodtkorb, P. A.; Lee, P.; McGibbon, R. T.; Feldbauer, R.; Lewis, S.; Tygier, S.; Sievert, S.; Vigna, S.; Peterson, S.; More, S.; Pudlik, T.; Oshima, T.; Pingel, T. J.; Robitaille, T. P.; Spura, T.; Jones, T. R.; Cera, T.; Leslie, T.; Zito, T.; Krauss, T.; Upadhyay, U.; Halchenko, Y. O.; Vázquez-Baeza, Y.; SciPy, C., SciPy 1.0: fundamental algorithms for scientific computing in Python. *Nature Methods* **2020**, *17* (3), 261-272.

121. Walt, S. v. d.; Colbert, S. C.; Varoquaux, G., The NumPy Array: A Structure for Efficient Numerical Computation. *Computing in Science & Engineering* **2011**, *13* (2), 22-30.

122. Marty, M. T.; Baldwin, A. J.; Marklund, E. G.; Hochberg, G. K. A.; Benesch, J. L. P.; Robinson, C. V., Bayesian Deconvolution of Mass and Ion Mobility Spectra: From Binary Interactions to Polydisperse Ensembles. *Analytical Chemistry* **2015**, *87* (8), 4370-4376.

123. Silveira, J. A.; Gamage, C. M.; Blase, R. C.; Russell, D. H., Gas-phase ion dynamics in a periodic-focusing DC ion guide. **2010**, *296* (1-3), 36-42.

124. Gamage, C. M.; Silveira, J. A.; Blase, R. C.; Russell, D. H., Gas-phase ion dynamics in a periodic-focusing DC ion guide (Part II): Discrete transport modes. *International Journal of Mass Spectrometry* **2011**, *303* (2-3), 154-163.
125. Silveira, J. A.; Gamage, C. M.; Blase, R. C.; Russell, D. H., Gas-phase ion dynamics in a periodic-focusing DC ion guide. *International Journal of Mass Spectrometry* **2010**, *296* (1-3), 36-42.
126. Fort, K. L.; Silveira, J. A.; Russell, D. H., The Periodic Focusing Ion Funnel: Theory, Design, and Experimental Characterization by High-Resolution Ion Mobility-Mass Spectrometry. *Analytical Chemistry* **2013**, *85* (20), 9543-9548.
127. Stow, S. M.; Causon, T. J.; Zheng, X.; Kurulugama, R. T.; Mairinger, T.; May, J. C.; Rennie, E. E.; Baker, E. S.; Smith, R. D.; McLean, J. A.; Hann, S.; Fjeldsted, J. C., An Interlaboratory Evaluation of Drift Tube Ion Mobility–Mass Spectrometry Collision Cross Section Measurements. *Analytical Chemistry* **2017**, *89* (17), 9048-9055.
128. Cole, R. B., *Electrospray and MALDI mass spectrometry: fundamentals, instrumentation, practicalities, and biological applications*. John Wiley & Sons: 2011.
129. Gabelica, V.; Shvartsburg, A. A.; Afonso, C.; Barran, P.; Benesch, J. L. P.; Bleiholder, C.; Bowers, M. T.; Bilbao, A.; Bush, M. F.; Campbell, J. L.; Campuzano, I. D. G.; Causon, T.; Clowers, B. H.; Creaser, C. S.; De Pauw, E.; Far, J.; Fernandez-Lima, F.; Fjeldsted, J. C.; Giles, K.; Groessl, M.; Hogan Jr, C. J.; Hann, S.; Kim, H. I.; Kurulugama, R. T.; May, J. C.; McLean, J. A.; Pagel, K.; Richardson, K.; Ridgeway, M. E.; Rosu, F.; Sobott, F.; Thalassinou, K.; Valentine, S. J.; Wytenbach, T.,

Recommendations for reporting ion mobility Mass Spectrometry measurements. **2019**, *38* (3), 291-320.

130. Schrodinger, LLC, The AxPyMOL Molecular Graphics Plugin for Microsoft PowerPoint, Version 1.8. 2015.

131. Schrodinger, LLC, The JyMOL Molecular Graphics Development Component, Version 1.8. 2015.

132. Hall, Z.; Politis, A.; Robinson, Carol V., Structural Modeling of Heteromeric Protein Complexes from Disassembly Pathways and Ion Mobility-Mass Spectrometry. *Structure* **2012**, *20* (9), 1596-1609.

133. Gamage, C. M.; Silveira, J. A.; Blase, R. C.; Russell, D. H., Gas-phase ion dynamics in a periodic-focusing DC ion guide (Part II): Discrete transport modes. *International Journal of Mass Spectrometry* **2011**, *303* (2–3), 154-163.

134. Blase, R. C.; Silveira, J. A.; Gillig, K. J.; Gamage, C. M.; Russell, D. H., Increased ion transmission in IMS: A high resolution, periodic-focusing DC ion guide ion mobility spectrometer. *International Journal of Mass Spectrometry* **2011**, *301* (1–3), 166-173.

135. Dixit, S. M.; Richardson, K.; Langridge, D.; Giles, K.; Ruotolo, B. T., A novel ion pseudo-trapping phenomenon within travelling wave ion guides. *Journal of the American Society for Mass Spectrometry* **2020**.

136. Poltash, M. L.; McCabe, J. W.; Shirzadeh, M.; Laganowsky, A.; Clowers, B. H.; Russell, D. H., Fourier Transform-Ion Mobility-Orbitrap Mass Spectrometer: A Next-

Generation Instrument for Native Mass Spectrometry. *Anal Chem* **2018**, *90* (17), 10472-10478.

137. Manura, D.; Dahl, D., SIMION (R) 8.0 User Manual (Scientific Instrument Services, Inc. Ringoes, NJ 08551, <<http://simion.com>>, January 2008). **2008**.

138. Ruotolo, B. T.; Gillig, K. J.; Woods, A. S.; Egan, T. F.; Ugarov, M. V.; Schultz, J. A.; Russell, D. H., Analysis of Phosphorylated Peptides by Ion Mobility-Mass Spectrometry. *Analytical Chemistry* **2004**, *76* (22), 6727-6733.

139. McLean, J. A.; Ruotolo, B. T.; Gillig, K. J.; Russell, D. H., Ion mobility–mass spectrometry: a new paradigm for proteomics. *International Journal of Mass Spectrometry* **2005**, *240* (3), 301-315.

140. McLean, J. A., The mass-mobility correlation redux: The conformational landscape of anhydrous biomolecules. *Journal of the American Society for Mass Spectrometry* **2009**, *20* (10), 1775-1781.

141. Hewitt, D.; Marklund, E.; Scott, D. J.; Robinson, C. V.; Borysik, A. J., A Hydrodynamic Comparison of Solution and Gas Phase Proteins and Their Complexes. *J Phys Chem B* **2014**, *118* (29), 8489-8495.

142. Michael, L.; Cagla, S.; Joseph, G.; Samira, S.; Chester, L. D.; povilas, u.; David, D.; Timothy, A.; Matteo, D.; Erik, M., Predicting the Shapes of Protein Complexes Through Collision Cross Section Measurements and Database Searches. *ChemRxiv* **2020**.

143. Brownlow, S.; Cabral, J. H. M.; Cooper, R.; Flower, D. R.; Yewdall, S. J.; Polikarpov, I.; North, A. C. T.; Sawyer, L., Bovine β -lactoglobulin at 1.8 Å resolution — still an enigmatic lipocalin. *Structure* **1997**, *5* (4), 481-495.
144. Majorek, K. A.; Porebski, P. J.; Dayal, A.; Zimmerman, M. D.; Jablonska, K.; Stewart, A. J.; Chruszcz, M.; Minor, W., Structural and immunologic characterization of bovine, horse, and rabbit serum albumins. *Molecular Immunology* **2012**, *52* (3), 174-182.
145. Wooll, J. O.; Friesen, R. H. E.; White, M. A.; Watowich, S. J.; Fox, R. O.; Lee, J. C.; Czerwinski, E. W., Structural and Functional Linkages Between Subunit Interfaces in Mammalian Pyruvate Kinase. *Journal of Molecular Biology* **2001**, *312* (3), 525-540.
146. Bush, M. F.; Hall, Z.; Giles, K.; Hoyes, J.; Robinson, C. V.; Ruotolo, B. T., Collision Cross Sections of Proteins and Their Complexes: A Calibration Framework and Database for Gas-Phase Structural Biology. *Analytical Chemistry* **2010**, *82* (22), 9557-9565.
147. Fenaille, F.; Morgan, F.; Parisod, V.; Tabet, J.-C.; Guy, P. A., Solid-state glycation of β -lactoglobulin by lactose and galactose: localization of the modified amino acids using mass spectrometric techniques. *Journal of Mass Spectrometry* **2004**, *39* (1), 16-28.
148. Duijn, E. v.; Barendregt, A.; Synowsky, S.; Versluis, C.; Heck, A. J. R., Chaperonin Complexes Monitored by Ion Mobility Mass Spectrometry. *Journal of the American Chemical Society* **2009**, *131* (4), 1452-1459.

149. Fort, K. L.; van de Waterbeemd, M.; Boll, D.; Reinhardt-Szyba, M.; Belov, M. E.; Sasaki, E.; Zschoche, R.; Hilvert, D.; Makarov, A. A.; Heck, A. J. R., Expanding the structural analysis capabilities on an Orbitrap-based mass spectrometer for large macromolecular complexes. *Analyst* **2018**, *143* (1), 100-105.
150. Chaudhry, C.; Horwich, A. L.; Brunger, A. T.; Adams, P. D., Exploring the Structural Dynamics of the E.coli Chaperonin GroEL Using Translation-libration-screw Crystallographic Refinement of Intermediate States. *Journal of Molecular Biology* **2004**, *342* (1), 229-245.
151. Roh, S.-H.; Hryc, C. F.; Jeong, H.-H.; Fei, X.; Jakana, J.; Lorimer, G. H.; Chiu, W., Subunit conformational variation within individual GroEL oligomers resolved by Cryo-EM. *Proceedings of the National Academy of Sciences* **2017**, *114* (31), 8259-8264.
152. Terai, T.; Kohno, M.; Boncompain, G.; Sugiyama, S.; Saito, N.; Fujikake, R.; Ueno, T.; Komatsu, T.; Hanaoka, K.; Okabe, T.; Urano, Y.; Perez, F.; Nagano, T., Artificial Ligands of Streptavidin (ALiS): Discovery, Characterization, and Application for Reversible Control of Intracellular Protein Transport. *Journal of the American Chemical Society* **2015**, *137* (33), 10464-10467.
153. Choi, K. H.; Mazurkie, A. S.; Morris, A. J.; Utheza, D.; Tolan, D. R.; Allen, K. N., Structure of a Fructose-1,6-bis(phosphate) Aldolase Liganded to Its Natural Substrate in a Cleavage-Defective Mutant at 2.3 Å. *Biochemistry* **1999**, *38* (39), 12655-12664.
154. Raj, S. B.; Ramaswamy, S.; Plapp, B. V., Yeast Alcohol Dehydrogenase Structure and Catalysis. *Biochemistry* **2014**, *53* (36), 5791-5803.

155. Trastoy, B.; Bonsor, D. A.; Pérez-Ojeda, M. E.; Jimeno, M. L.; Méndez-Ardoy, A.; García Fernández, J. M.; Sundberg, E. J.; Chiara, J. L., Synthesis and Biophysical Study of Disassembling Nanohybrid Bioconjugates with a Cubic Octasilsesquioxane Core. *Advanced Functional Materials* **2012**, 22 (15), 3191-3201.
156. Aranda IV, R.; Cai, H.; Worley, C. E.; Levin, E. J.; Li, R.; Olson, J. S.; Phillips Jr, G. N.; Richards, M. P., Structural analysis of fish versus mammalian hemoglobins: Effect of the heme pocket environment on autooxidation and hemin loss. *Proteins: Structure, Function, and Bioinformatics* **2009**, 75 (1), 217-230.
157. Hörnberg, A.; Eneqvist, T.; Olofsson, A.; Lundgren, E.; Sauer-Eriksson, A. E., A comparative analysis of 23 structures of the amyloidogenic protein transthyretin. *J Mol Biol* **2000**, 302 (3), 649-669.
158. Maurus, R.; Overall, C. M.; Bogumil, R.; Luo, Y.; Mauk, A. G.; Smith, M.; Brayer, G. D., A myoglobin variant with a polar substitution in a conserved hydrophobic cluster in the heme binding pocket. *Biochimica et Biophysica Acta (BBA) - Protein Structure and Molecular Enzymology* **1997**, 1341 (1), 1-13.
159. Al-Karadaghi, S.; Hansson, M.; Nikonov, S.; Jönsson, B.; Hederstedt, L., Crystal structure of ferrochelatase: the terminal enzyme in heme biosynthesis. *Structure* **1997**, 5 (11), 1501-1510.
160. Vijay-Kumar, S.; Bugg, C. E.; Cook, W. J., Structure of ubiquitin refined at 1.8 Å resolution. *Journal of Molecular Biology* **1987**, 194 (3), 531-544.

161. May, J. C.; Jurneczko, E.; Stow, S. M.; Kratochvil, I.; Kalkhof, S.; McLean, J. A., Conformational Landscapes of Ubiquitin, Cytochrome c, and Myoglobin: Uniform Field Ion Mobility Measurements in Helium and Nitrogen Drift Gas. *International journal of mass spectrometry* **2018**, *427*, 79-90.
162. Stiving, A. Q.; Jones, B. J.; Ujma, J.; Giles, K.; Wysocki, V. H., Collision Cross Sections of Charge-Reduced Proteins and Protein Complexes: a Database for CCS Calibration. *Analytical Chemistry* **2020**.
163. Valentine, S. J.; Counterman, A. E.; Clemmer, D. E., Conformer-dependent proton-transfer reactions of ubiquitin ions. *Journal of the American Society for Mass Spectrometry* **1997**, *8* (9), 954-961.
164. Consortium, T. U., UniProt: a worldwide hub of protein knowledge. *Nucleic Acids Research* **2018**, *47* (D1), D506-D515.
165. Pereira, J. H.; Ralston, C. Y.; Douglas, N. R.; Meyer, D.; Knee, K. M.; Goulet, D. R.; King, J. A.; Frydman, J.; Adams, P. D., Crystal structures of a group II chaperonin reveal the open and closed states associated with the protein folding cycle. *J Biol Chem* **2010**, *285* (36), 27958-27966.
166. Koike-Takeshita, A.; Arakawa, T.; Taguchi, H.; Shimamura, T., Crystal Structure of a Symmetric Football-Shaped GroEL:GroES2-ATP14 Complex Determined at 3.8Å Reveals Rearrangement between Two GroEL Rings. *Journal of Molecular Biology* **2014**, *426* (21), 3634-3641.

167. Fei, X.; Ye, X.; LaRonde, N. A.; Lorimer, G. H., Formation and structures of GroEL:GroES₂ chaperonin footballs, the protein-folding functional form. *Proc Natl Acad Sci U S A* **2014**, *111* (35), 12775-12780.
168. Fellgett, P. B., On the Ultimate Sensitivity and Practical Performance of Radiation Detectors. *J. Opt. Soc. Am.* **1949**, *39* (11), 970-976.
169. Calabrese, A. N.; Radford, S. E., Mass spectrometry-enabled structural biology of membrane proteins. *Methods* **2018**, *147*, 187-205.
170. Hilton, G. R.; Benesch, J. L., Two decades of studying non-covalent biomolecular assemblies by means of electrospray ionization mass spectrometry. *J R Soc Interface* **2012**, *9* (70), 801-16.
171. Loo, J. A., Studying noncovalent protein complexes by electrospray ionization mass spectrometry. *Mass Spectrom Rev* **1997**, *16* (1), 1-23.
172. Gupta, K.; Donlan, J. A. C.; Hopper, J. T. S.; Uzdavinys, P.; Landreh, M.; Struwe, W. B.; Drew, D.; Baldwin, A. J.; Stansfeld, P. J.; Robinson, C. V., The role of interfacial lipids in stabilizing membrane protein oligomers. *Nature* **2017**, *541* (7637), 421-424.
173. Cong, X.; Liu, Y.; Liu, W.; Liang, X.; Laganowsky, A., Allosteric modulation of protein-protein interactions by individual lipid binding events. *Nat Commun* **2017**, *8* (1), 2203.
174. Fantin, S. M.; Parson, K. F.; Niu, S.; Liu, J.; Polasky, D. A.; Dixit, S. M.; Ferguson-Miller, S. M.; Ruotolo, B. T., Collision Induced Unfolding Classifies Ligands

Bound to the Integral Membrane Translocator Protein. *Anal Chem* **2019**, *91* (24), 15469-15476.

175. Wilson, J. W.; Rolland, A. D.; Klausen, G. M.; Prell, J. S., Ion Mobility-Mass Spectrometry Reveals That alpha-Hemolysin from *Staphylococcus aureus* Simultaneously Forms Hexameric and Heptameric Complexes in Detergent Micelle Solutions. *Anal Chem* **2019**, *91* (15), 10204-10211.

176. Barrera, N. P.; Isaacson, S. C.; Zhou, M.; Bavro, V. N.; Welch, A.; Schaedler, T. A.; Seeger, M. A.; Miguel, R. N.; Korkhov, V. M.; van Veen, H. W.; Venter, H.; Walmsley, A. R.; Tate, C. G.; Robinson, C. V., Mass spectrometry of membrane transporters reveals subunit stoichiometry and interactions. *Nat Methods* **2009**, *6* (8), 585-7.

177. Patrick, J. W.; Boone, C. D.; Liu, W.; Conover, G. M.; Liu, Y.; Cong, X.; Laganowsky, A., Allostery revealed within lipid binding events to membrane proteins. *Proc Natl Acad Sci U S A* **2018**, *115* (12), 2976-2981.

178. Laganowsky, A.; Reading, E.; Allison, T. M.; Ulmschneider, M. B.; Degiacomi, M. T.; Baldwin, A. J.; Robinson, C. V., Membrane proteins bind lipids selectively to modulate their structure and function. *Nature* **2014**, *510* (7503), 172-5.

179. Yen, H. Y.; Hoi, K. K.; Liko, I.; Hedger, G.; Horrell, M. R.; Song, W.; Wu, D.; Heine, P.; Warne, T.; Lee, Y.; Carpenter, B.; Pluckthun, A.; Tate, C. G.; Sansom, M. S. P.; Robinson, C. V., PtdIns(4,5)P₂ stabilizes active states of GPCRs and enhances selectivity of G-protein coupling. *Nature* **2018**, *559* (7714), 423-427.

180. Allison, T. M.; Reading, E.; Liko, I.; Baldwin, A. J.; Laganowsky, A.; Robinson, C. V., Quantifying the stabilizing effects of protein-ligand interactions in the gas phase. *Nat Commun* **2015**, in press.
181. Marcoux, J.; Wang, S. C.; Politis, A.; Reading, E.; Ma, J.; Biggin, P. C.; Zhou, M.; Tao, H.; Zhang, Q.; Chang, G.; Morgner, N.; Robinson, C. V., Mass spectrometry reveals synergistic effects of nucleotides, lipids, and drugs binding to a multidrug resistance efflux pump. *Proc Natl Acad Sci U S A* **2013**, *110* (24), 9704-9.
182. Bolla, J. R.; Sauer, J. B.; Wu, D.; Mehmood, S.; Allison, T. M.; Robinson, C. V., Direct observation of the influence of cardiolipin and antibiotics on lipid II binding to MurJ. *Nat Chem* **2018**, *10* (3), 363-371.
183. Gault, J.; Donlan, J. A.; Liko, I.; Hopper, J. T.; Gupta, K.; Housden, N. G.; Struwe, W. B.; Marty, M. T.; Mize, T.; Bechara, C.; Zhu, Y.; Wu, B.; Kleanthous, C.; Belov, M.; Damoc, E.; Makarov, A.; Robinson, C. V., High-resolution mass spectrometry of small molecules bound to membrane proteins. *Nat Methods* **2016**, *13* (4), 333-6.
184. Reading, E.; Liko, I.; Allison, T. M.; Benesch, J. L.; Laganowsky, A.; Robinson, C. V., The role of the detergent micelle in preserving the structure of membrane proteins in the gas phase. *Angew Chem Int Ed Engl* **2015**, *54* (15), 4577-81.
185. Borysik, A. J.; Hewitt, D. J.; Robinson, C. V., Detergent release prolongs the lifetime of native-like membrane protein conformations in the gas-phase. *J Am Chem Soc* **2013**, *135* (16), 6078-83.

186. Hopper, J. T. S.; Yu, Y. T.-C.; Li, D.; Raymond, A.; Bostock, M.; Liko, I.; Mikhailov, V.; Laganowsky, A.; Benesch, J. L. P.; Caffrey, M.; Nietlispach, D.; Robinson, C. V., Detergent-free mass spectrometry of membrane protein complexes. *Nature Methods* **2013**, *10* (12), 1206-1208.
187. Hall, Z.; Politis, A.; Bush, M. F.; Smith, L. J.; Robinson, C. V., Charge-state dependent compaction and dissociation of protein complexes: insights from ion mobility and molecular dynamics. *J Am Chem Soc* **2012**, *134* (7), 3429-38.
188. Townsend, J. A.; Keener, J. E.; Miller, Z. M.; Prell, J. S.; Marty, M. T., Imidazole Derivatives Improve Charge Reduction and Stabilization for Native Mass Spectrometry. *Anal Chem* **2019**, *91* (22), 14765-14772.
189. Lemaire, D.; Marie, G.; Serani, L.; Laprevote, O., Stabilization of gas-phase noncovalent macromolecular complexes in electrospray mass spectrometry using aqueous triethylammonium bicarbonate buffer. *Anal Chem* **2001**, *73* (8), 1699-706.
190. Patrick, J. W.; Laganowsky, A., Generation of Charge-Reduced Ions of Membrane Protein Complexes for Native Ion Mobility Mass Spectrometry Studies. *J Am Soc Mass Spectrom* **2019**.
191. Urner, L. H.; Liko, I.; Yen, H. Y.; Hoi, K. K.; Bolla, J. R.; Gault, J.; Almeida, F. G.; Schweder, M. P.; Shutin, D.; Ehrmann, S.; Haag, R.; Robinson, C. V.; Pagel, K., Modular detergents tailor the purification and structural analysis of membrane proteins including G-protein coupled receptors. *Nat Commun* **2020**, *11* (1), 564.

192. Scalf, M.; Westphall, M. S.; Smith, L. M., Charge reduction electrospray mass spectrometry. *Anal Chem* **2000**, *72* (1), 52-60.
193. Petroff, J. T., 2nd; Tong, A.; Chen, L. J.; Dekoster, G. T.; Khan, F.; Abramson, J.; Frieden, C.; Cheng, W. W. L., Charge Reduction of Membrane Proteins in Native Mass Spectrometry Using Alkali Metal Acetate Salts. *Anal Chem* **2020**.
194. Hopper, J. T.; Sokratous, K.; Oldham, N. J., Charge state and adduct reduction in electrospray ionization-mass spectrometry using solvent vapor exposure. *Anal Biochem* **2012**, *421* (2), 788-90.
195. Lidbury, I.; Murrell, J. C.; Chen, Y., Trimethylamine N-oxide metabolism by abundant marine heterotrophic bacteria. *Proc Natl Acad Sci U S A* **2014**, *111* (7), 2710-5.
196. Velasquez, M. T.; Ramezani, A.; Manal, A.; Raj, D. S., Trimethylamine N-Oxide: The Good, the Bad and the Unknown. *Toxins (Basel)* **2016**, *8* (11).
197. Yancey, P. H., Organic osmolytes as compatible, metabolic and counteracting cytoprotectants in high osmolarity and other stresses. *J Exp Biol* **2005**, *208* (Pt 15), 2819-30.
198. Kaldmae, M.; Osterlund, N.; Lianoudaki, D.; Sahin, C.; Bergman, P.; Nyman, T.; Kronqvist, N.; Ilag, L. L.; Allison, T. M.; Marklund, E. G.; Landreh, M., Gas-Phase Collisions with Trimethylamine-N-Oxide Enable Activation-Controlled Protein Ion Charge Reduction. *J Am Soc Mass Spectrom* **2019**, *30* (8), 1385-1388.
199. Gault, J.; Lianoudaki, D.; Kaldmae, M.; Kronqvist, N.; Rising, A.; Johansson, J.; Lohkamp, B.; Lain, S.; Allison, T. M.; Lane, D. P.; Marklund, E. G.; Landreh, M.,

- Mass Spectrometry Reveals the Direct Action of a Chemical Chaperone. *J Phys Chem Lett* **2018**, *9* (14), 4082-4086.
200. Mehmood, S.; Marcoux, J.; Hopper, J. T.; Allison, T. M.; Liko, I.; Borysik, A. J.; Robinson, C. V., Charge reduction stabilizes intact membrane protein complexes for mass spectrometry. *J Am Chem Soc* **2014**, *136* (49), 17010-2.
201. Gruswitz, F.; O'Connell, J., 3rd; Stroud, R. M., Inhibitory complex of the transmembrane ammonia channel, AmtB, and the cytosolic regulatory protein, GlnK, at 1.96 Å. *Proc Natl Acad Sci U S A* **2007**, *104* (1), 42-7.
202. Marty, M. T.; Baldwin, A. J.; Marklund, E. G.; Hochberg, G. K.; Benesch, J. L.; Robinson, C. V., Bayesian deconvolution of mass and ion mobility spectra: from binary interactions to polydisperse ensembles. *Anal Chem* **2015**, *87* (8), 4370-6.
203. Poltash, M. L.; McCabe, J. W.; Shirzadeh, M.; Laganowsky, A.; Clowers, B. H.; Russell, D. H., Fourier Transform-Ion Mobility-Orbitrap Mass Spectrometer: A Next-Generation Instrument for Native Mass Spectrometry. *Anal Chem* **2018**.
204. Hill, A. V., The possible effects of the aggregation of the molecules of haemoglobin on its dissociation curves. *Journal of Physiology* **1910**, *40*, iv-ii.
205. Millman, K. J.; Aivazis, M., Python for Scientists and Engineers. *Computing in Science & Engineering* **2011**, *13* (2), 9-12.
206. Hunter, J. D., Matplotlib: A 2D Graphics Environment. *Computing in Science & Engineering* **2007**, *9* (3), 90-95.

207. Nieto-Alamilla, G.; Marquez-Gomez, R.; Garcia-Galvez, A. M.; Morales-Figueroa, G. E.; Arias-Montano, J. A., The Histamine H3 Receptor: Structure, Pharmacology, and Function. *Mol Pharmacol* **2016**, *90* (5), 649-673.
208. Thomas, T.; Thomas, T. J., Selectivity of polyamines in triplex DNA stabilization. *Biochemistry* **1993**, *32* (50), 14068-74.
209. Li, M. M.; MacDonald, M. R., Polyamines: Small Molecules with a Big Role in Promoting Virus Infection. *Cell Host Microbe* **2016**, *20* (2), 123-4.
210. Mounce, B. C.; Olsen, M. E.; Vignuzzi, M.; Connor, J. H., Polyamines and Their Role in Virus Infection. *Microbiol Mol Biol Rev* **2017**, *81* (4).
211. Handa, A. K.; Fatima, T.; Mattoo, A. K., Polyamines: Bio-Molecules with Diverse Functions in Plant and Human Health and Disease. *Front Chem* **2018**, *6*, 10.
212. Verkerk, U. H.; Peschke, M.; Kebarle, P., Effect of buffer cations and of H₃O⁺ on the charge states of native proteins. Significance to determinations of stability constants of protein complexes. *J Mass Spectrom* **2003**, *38* (6), 618-31.
213. Poltash, M. L.; McCabe, J. W.; Patrick, J. W.; Laganowsky, A.; Russell, D. H., Development and Evaluation of a Reverse-Entry Ion Source Orbitrap Mass Spectrometer. *Journal of The American Society for Mass Spectrometry* **2018**.
214. Catalina, M. I.; van den Heuvel, R. H.; van Duijn, E.; Heck, A. J., Decharging of globular proteins and protein complexes in electrospray. *Chemistry* **2005**, *11* (3), 960-8.
215. Reyzer, M. L.; Brodbelt, J. S., Gas-phase basicities of polyamines. *Journal of the American Society for Mass Spectrometry* **1998**, *9* (10), 1043-1048.

216. Aue, D. H.; Webb, H. M.; Bowers, M. T., Quantitative relative gas-phase basicities of alkylamines. Correlation with solution basicity. *Journal of the American Chemical Society* **1972**, *94* (13), 4726-4728.
217. da Silva, E. F., Comparison of quantum mechanical and experimental gas-phase basicities of amines and alcohols. *J Phys Chem A* **2005**, *109* (8), 1603-7.
218. Brauman, J. I.; Riveros, J. M.; Blair, L. K., Gas-phase basicities of amines. *Journal of the American Chemical Society* **1971**, *93* (16), 3914-3916.
219. Hopkins, F. G., Denaturation of Proteins by Urea and Related Substances. *Nature* **1930**, *126* (3174), 328-330.
220. Privalov, P. L., Cold Denaturation of Protein. *Critical Reviews in Biochemistry and Molecular Biology* **1990**, *25* (4), 281-306.
221. Ben-Naim, A., Levinthal's question revisited, and answered. *Journal of Biomolecular Structure and Dynamics* **2012**, *30* (1), 113-124.
222. Konermann, L.; Douglas, D. J., Acid-Induced Unfolding of Cytochrome c at Different Methanol Concentrations: Electrospray Ionization Mass Spectrometry Specifically Monitors Changes in the Tertiary Structure. *Biochemistry* **1997**, *36* (40), 12296-12302.
223. Konermann, L.; Rosell, F. I.; Mauk, A. G.; Douglas, D. J., Acid-Induced Denaturation of Myoglobin Studied by Time-Resolved Electrospray Ionization Mass Spectrometry. *Biochemistry* **1997**, *36* (21), 6448-6454.

224. Konermann, L.; Collings, B. A.; Douglas, D. J., Cytochrome c folding kinetics studied by time-resolved electrospray ionization mass spectrometry. *Biochemistry* **1997**, *36* (18), 5554-9.
225. Wyttenbach, T.; Bowers, M. T., Intermolecular interactions in biomolecular systems examined by mass spectrometry. *Annual review of physical chemistry* **2007**, *58*, 511-33.
226. Lumry, R.; Eyring, H., Conformation Changes of Proteins. *The Journal of Physical Chemistry* **1954**, *58* (2), 110-120.
227. Shi, L.; Holliday, A. E.; Shi, H.; Zhu, F.; Ewing, M. A.; Russell, D. H.; Clemmer, D. E., Characterizing Intermediates Along the Transition from Polyproline I to Polyproline II Using Ion Mobility Spectrometry-Mass Spectrometry. *Journal of the American Chemical Society* **2014**, *136* (36), 12702-12711.
228. Fuller, D. R.; Glover, M. S.; Pierson, N. A.; Kim, D.; Russell, D. H.; Clemmer, D. E., Cis→Trans Isomerization of Pro7 in Oxytocin Regulates Zn²⁺ Binding. *Journal of the American Society for Mass Spectrometry* **2016**, *27* (8), 1376-1382.
229. Shi, L.; Holliday, A. E.; Khanal, N.; Russell, D. H.; Clemmer, D. E., Configurationally-Coupled Protonation of Polyproline-7. *Journal of the American Chemical Society* **2015**, *137* (27), 8680-8683.
230. Fuller, D. R.; Conant, C. R.; El-Baba, T. J.; Brown, C. J.; Woodall, D. W.; Russell, D. H.; Clemmer, D. E., Conformationally Regulated Peptide Bond Cleavage in Bradykinin. *Journal of the American Chemical Society* **2018**, *140* (30), 9357-9360.

231. El-Baba, T. J.; Kim, D.; Rogers, D. B.; Khan, F. A.; Hales, D. A.; Russell, D. H.; Clemmer, D. E., Long-Lived Intermediates in a Cooperative Two-State Folding Transition. *The Journal of Physical Chemistry B* **2016**, *120* (47), 12040-12046.
232. Conant, C. R.; Fuller, D. R.; Zhang, Z.; Woodall, D. W.; Russell, D. H.; Clemmer, D. E., Substance P in the Gas Phase: Conformational Changes and Dissociations Induced by Collisional Activation in a Drift Tube. *Journal of the American Society for Mass Spectrometry* **2019**, *30* (6), 932-945.
233. Shi, L.; Holliday, A. E.; Bohrer, B. C.; Kim, D.; Servage, K. A.; Russell, D. H.; Clemmer, D. E., “Wet” Versus “Dry” Folding of Polyproline. *Journal of the American Society for Mass Spectrometry* **2016**, *27* (6), 1037-1047.
234. Cong, X.; Liu, Y.; Liu, W.; Liang, X.; Russell, D. H.; Laganowsky, A., Determining Membrane Protein–Lipid Binding Thermodynamics Using Native Mass Spectrometry. *Journal of the American Chemical Society* **2016**, *138* (13), 4346-4349.
235. Patrick, J. W.; Laganowsky, A., Probing Heterogeneous Lipid Interactions with Membrane Proteins Using Mass Spectrometry. In *Lipid-Protein Interactions: Methods and Protocols*, Kleinschmidt, J. H., Ed. Springer New York: New York, NY, 2019; pp 175-190.
236. Lyu, J.; Liu, Y.; McCabe, J. W.; Schrecke, S.; Fang, L.; Russell, D. H.; Laganowsky, A., Discovery of Potent Charge-Reducing Molecules for Native Ion Mobility Mass Spectrometry Studies. *Analytical Chemistry* **2020**, *92* (16), 11242-11249.

237. El-Baba, T. J.; Woodall, D. W.; Raab, S. A.; Fuller, D. R.; Laganowsky, A.; Russell, D. H.; Clemmer, D. E., Melting Proteins: Evidence for Multiple Stable Structures upon Thermal Denaturation of Native Ubiquitin from Ion Mobility Spectrometry-Mass Spectrometry Measurements. *Journal of the American Chemical Society* **2017**, *139* (18), 6306-6309.
238. Köhler, M.; Marchand, A.; Hentzen, N. B.; Egli, J.; Begley, A. I.; Wennemers, H.; Zenobi, R., Temperature-controlled electrospray ionization mass spectrometry as a tool to study collagen homo- and heterotrimers. *Chemical Science* **2019**, *10* (42), 9829-9835.
239. Marchand, A.; Czar, M. F.; Eggel, E. N.; Kaeslin, J.; Zenobi, R., Studying biomolecular folding and binding using temperature-jump mass spectrometry. *Nature Communications* **2020**, *11* (1), 566.
240. Brown, C. J.; Woodall, D. W.; El-Baba, T. J.; Clemmer, D. E., Characterizing Thermal Transitions of IgG with Mass Spectrometry. *Journal of the American Society for Mass Spectrometry* **2019**, *30* (11), 2438-2445.
241. Raab, S. A.; El-Baba, T. J.; Woodall, D. W.; Liu, W.; Liu, Y.; Baird, Z.; Hales, D. A.; Laganowsky, A.; Russell, D. H.; Clemmer, D. E., Evidence for Many Unique Solution Structures for Chymotrypsin Inhibitor 2: A Thermodynamic Perspective Derived from vT-ESI-IMS-MS Measurements. *Journal of the American Chemical Society* **2020**, *142* (41), 17372-17383.

242. El-Baba, T. J.; Fuller, D. R.; Woodall, D. W.; Raab, S. A.; Conant, C. R.; Dilger, J. M.; Toker, Y.; Williams, E. R.; Russell, D. H.; Clemmer, D. E., Melting proteins confined in nanodroplets with 10.6 μm light provides clues about early steps of denaturation. *Chem Commun (Camb)* **2018**, 54 (26), 3270-3273.
243. Jakub, U.; Rosie, U.; Florian, B.; Bruno, B.; Perdita, B., *Protein Unfolding in Freeze Frames: Intermediates of Ubiquitin and Lysozyme Revealed by Variable Temperature Ion Mobility-Mass Spectrometry*. 2020.
244. Woodall, D. W.; Henderson, L. W.; Raab, S. A.; Honma, K.; Clemmer, D. E., Understanding the Thermal Denaturation of Myoglobin with IMS-MS: Evidence for Multiple Stable Structures and Trapped Pre-equilibrium States. *Journal of the American Society for Mass Spectrometry* **2021**, 32 (1), 64-72.
245. Woodall, D. W.; El-Baba, T. J.; Fuller, D. R.; Liu, W.; Brown, C. J.; Laganowsky, A.; Russell, D. H.; Clemmer, D. E., Variable-Temperature ESI-IMS-MS Analysis of Myohemerythrin Reveals Ligand Losses, Unfolding, and a Non-Native Disulfide Bond. *Analytical Chemistry* **2019**, 91 (10), 6808-6814.
246. Shirzadeh, M.; Poltash, M. L.; Laganowsky, A.; Russell, D. H., Structural Analysis of the Effect of a Dual-FLAG Tag on Transthyretin. *Biochemistry* **2020**, 59 (9), 1013-1022.
247. Hoerner, J. K.; Xiao, H.; Kaltashov, I. A., Structural and Dynamic Characteristics of a Partially Folded State of Ubiquitin Revealed by Hydrogen Exchange Mass Spectrometry. *Biochemistry* **2005**, 44 (33), 11286-11294.

248. Brutscher, B.; Brüschweiler, R.; Ernst, R. R., Backbone Dynamics and Structural Characterization of the Partially Folded A State of Ubiquitin by ^1H , ^{13}C , and ^{15}N Nuclear Magnetic Resonance Spectroscopy. *Biochemistry* **1997**, *36* (42), 13043-13053.
249. Pan, Y.; Briggs, M. S., Hydrogen exchange in native and alcohol forms of ubiquitin. *Biochemistry* **1992**, *31* (46), 11405-12.
250. Bern, M.; Caval, T.; Kil, Y. J.; Tang, W.; Becker, C.; Carlson, E.; Kletter, D.; Sen, K. I.; Galy, N.; Hagemans, D.; Franc, V.; Heck, A. J. R., Parsimonious Charge Deconvolution for Native Mass Spectrometry. *Journal of Proteome Research* **2018**, *17* (3), 1216-1226.
251. McCabe, J. W.; Mallis, C. S.; Kocurek, K. I.; Poltash, M. L.; Shirzadeh, M.; Hebert, M. J.; Fan, L.; Walker, T. E.; Zheng, X.; Jiang, T.; Dong, S.; Lin, C.-W.; Laganowsky, A.; Russell, D. H., First-Principles Collision Cross Section Measurements of Large Proteins and Protein Complexes. *Analytical Chemistry* **2020**, *92* (16), 11155-11163.
252. McCabe, J. W.; Hebert, M. J.; Shirzadeh, M.; Mallis, C. S.; Denton, J. K.; Walker, T. E.; Russell, D. H., THE IMS PARADOX: A PERSPECTIVE ON STRUCTURAL ION MOBILITY-MASS SPECTROMETRY. *Mass Spectrom Rev* **2020**, *40* (3), 280-305.
253. Lin, C.-W.; McCabe, J. W.; Russell, D. H.; Barondeau, D. P., Molecular Mechanism of ISC Iron–Sulfur Cluster Biogenesis Revealed by High-Resolution Native

Mass Spectrometry. *Journal of the American Chemical Society* **2020**, *142* (13), 6018-6029.

254. Poltash, M. L.; McCabe, J. W.; Shirzadeh, M.; Laganowsky, A.; Russell, D. H., Native IM-Orbitrap MS: Resolving what was hidden. *TrAC Trends in Analytical Chemistry* **2020**, *124*, 115533.

255. Ruotolo, B. T.; Benesch, J. L. P.; Sandercock, A. M.; Hyung, S.-J.; Robinson, C. V., Ion mobility–mass spectrometry analysis of large protein complexes. *Nature Protocols* **2008**, *3* (7), 1139-1152.

256. Wintrode, P. L.; Makhatadze, G. I.; Privalov, P. L., Thermodynamics of ubiquitin unfolding. *Proteins: Struct., Funct., Bioinf.* **1994**, *18* (3), 246-253.

257. Shi, H.; Pierson, N. A.; Valentine, S. J.; Clemmer, D. E., Conformation Types of Ubiquitin [M+8H]⁸⁺ Ions from Water:Methanol Solutions: Evidence for the N and A States in Aqueous Solution. *J Phys Chem B* **2012**, *116* (10), 3344-3352.

258. Vijay-Kumar, S.; Bugg, C. E.; Cook, W. J., Structure of ubiquitin refined at 1.8 Å resolution. *Journal of Molecular Biology* **1987**, *194* (3), 531-44.

259. Vajpai, N.; Nisius, L.; Wiktor, M.; Grzesiek, S., High-pressure NMR reveals close similarity between cold and alcohol protein denaturation in ubiquitin. *Proc. Natl. Acad. Sci. USA* **2013**, *110* (5), E368-E376.

260. Bridwell-Rabb, J.; Fox, N. G.; Tsai, C. L.; Winn, A. M.; Barondeau, D. P., Human frataxin activates Fe-S cluster biosynthesis by facilitating sulfur transfer chemistry. *Biochemistry* **2014**, *53* (30), 4904-13.

261. Patra, S.; Barondeau, D. P., Mechanism of activation of the human cysteine desulfurase complex by frataxin. *Proc. Natl. Acad. Sci. USA* **2019**, *116* (39), 19421.
262. Prischi, F.; Konarev, P. V.; Iannuzzi, C.; Pastore, C.; Adinolfi, S.; Martin, S. R.; Svergun, D. I.; Pastore, A., Structural bases for the interaction of frataxin with the central components of iron-sulphur cluster assembly. *Nat Commun* **2010**, *1*, 95.
263. Fox, N. G.; Yu, X.; Feng, X.; Bailey, H. J.; Martelli, A.; Nabhan, J. F.; Strain-Damerell, C.; Bulawa, C.; Yue, W. W.; Han, S., Structure of the human frataxin-bound iron-sulfur cluster assembly complex provides insight into its activation mechanism. *Nat. Commun.* **2019**, *10* (1), 2210.
264. Tsai, C.-L.; Barondeau, D. P., Human Frataxin Is an Allosteric Switch That Activates the Fe–S Cluster Biosynthetic Complex. *Biochemistry* **2010**, *49* (43), 9132-9139.
265. Campuzano, V.; Montermini, L.; Moltò, M. D.; Pianese, L.; Cossée, M.; Cavalcanti, F.; Monros, E.; Rodius, F.; Duclos, F.; Monticelli, A.; Zara, F.; Cañizares, J.; Koutnikova, H.; Bidichandani, S. I.; Gellera, C.; Brice, A.; Trouillas, P.; De Michele, G.; Filla, A.; De Frutos, R.; Palau, F.; Patel, P. I.; Di Donato, S.; Mandel, J.-L.; Coccozza, S.; Koenig, M.; Pandolfo, M., Friedreich's Ataxia: Autosomal Recessive Disease Caused by an Intronic GAA Triplet Repeat Expansion. *Science* **1996**, *271* (5254), 1423.

266. Sanfelice, D.; Morandi, E.; Pastore, A.; Niccolai, N.; Temussi, P. A., Cold Denaturation Unveiled: Molecular Mechanism of the Asymmetric Unfolding of Yeast Frataxin. *ChemPhysChem* **2015**, *16* (17), 3599-3602.
267. Pastore, A.; Martin, S. R.; Politou, A.; Kondapalli, K. C.; Stemmler, T.; Temussi, P. A., Unbiased Cold Denaturation: Low- and High-Temperature Unfolding of Yeast Frataxin under Physiological Conditions. *J. Am. Chem. Soc.* **2007**, *129* (17), 5374-5375.
268. Krzywinski, M.; Altman, N., Significance, P values and t-tests. *Nature Methods* **2013**, *10* (11), 1041-1042.
269. Xia, Z.; DeGrandchamp, J. B.; Williams, E. R., Native mass spectrometry beyond ammonium acetate: effects of nonvolatile salts on protein stability and structure. *Analyst* **2019**, *144* (8), 2565-2573.
270. Bonetti, D.; Toto, A.; Giri, R.; Morrone, A.; Sanfelice, D.; Pastore, A.; Temussi, P.; Gianni, S.; Brunori, M., The kinetics of folding of frataxin. *Phys. Chem. Chem. Phys.* **2014**, *16* (14), 6391-6397.
271. Dhe-Paganon, S.; Shigeta, R.; Chi, Y. I.; Ristow, M.; Shoelson, S. E., Crystal structure of human frataxin. *J. Biol. Chem.* **2000**, *275* (40), 30753-6.
272. Musco, G.; Stier, G.; Kolmerer, B.; Adinolfi, S.; Martin, S.; Frenkiel, T.; Gibson, T.; Pastore, A., Towards a structural understanding of Friedreich's ataxia: the solution structure of frataxin. *Structure* **2000**, *8* (7), 695-707.
273. Prischi, F.; Giannini, C.; Adinolfi, S.; Pastore, A., The N-terminus of mature human frataxin is intrinsically unfolded. *FEBS J* **2009**, *276* (22), 6669-6676.

274. Pastore, A.; Puccio, H., Frataxin: a protein in search for a function. *Journal of Neurochemistry* **2013**, *126* (s1), 43-52.
275. Adinolfi, S.; Nair, M.; Politou, A.; Bayer, E.; Martin, S.; Temussi, P.; Pastore, A., The factors governing the thermal stability of frataxin orthologues: how to increase a protein's stability. *Biochemistry* **2004**, *43* (21), 6511-8.
276. Lin, Z.; Rye, H. S., GroEL-mediated protein folding: making the impossible, possible. *Critical reviews in biochemistry and molecular biology* **2006**, *41* (4), 211-239.
277. Bukau, B.; Horwich, A. L., The Hsp70 and Hsp60 Chaperone Machines. *Cell* **1998**, *92* (3), 351-366.
278. Mallis, C. S.; Zheng, X.; Qiu, X.; McCabe, J. W.; Shirzadeh, M.; Lyu, J.; Laganowsky, A.; Russell, D. H., Development of Native MS Capabilities on an Extended Mass Range Q-TOF MS. *International Journal of Mass Spectrometry* **2020**, *458*.
279. Bridwell-Rabb, J.; Iannuzzi, C.; Pastore, A.; Barondeau, D. P., Effector role reversal during evolution: the case of frataxin in Fe-S cluster biosynthesis. *Biochemistry* **2012**, *51* (12), 2506-14.
280. Miyazaki, K., MEGAWHOP cloning: a method of creating random mutagenesis libraries via megaprimer PCR of whole plasmids. *Methods in enzymology* **2011**, *498*, 399-406.
281. McCabe, J. W.; Shirzadeh, M.; Walker, T. E.; Lin, C.-W.; Jones, B. J.; Wysocki, V. H.; Barondeau, D. P.; Clemmer, D. E.; Laganowsky, A.; Russell, D. H., Variable-Temperature Electrospray Ionization for Temperature-Dependent Folding/Refolding

Reactions of Proteins and Ligand Binding. *Analytical Chemistry* **2021**, *93* (18), 6924-6931.

282. Brabeck, G. F.; Chen, H.; Hoffman, N. M.; Wang, L.; Reilly, P. T. A., Development of MS_n in Digitally Operated Linear Ion Guides. *Analytical Chemistry* **2014**, *86* (15), 7757-7763.

283. Brabeck, G. F.; Koizumi, H.; Koizumi, E.; Reilly, P. T. A., Characterization of quadrupole mass filters operated with frequency-asymmetric and amplitude-asymmetric waveforms. *International Journal of Mass Spectrometry* **2016**, *404*, 8-13.

284. Brabeck, G. F.; Reilly, P. T. A., Mapping ion stability in digitally driven ion traps and guides. *International Journal of Mass Spectrometry* **2014**, *364*, 1-8.

285. Huntley, A. P.; Brabeck, G. F.; Reilly, P. T. A., Influence of the RF drive potential on the acceptance behavior of pure quadrupole mass filters operated in stability zones A and B. *International Journal of Mass Spectrometry* **2020**, *450*, 116303.

286. Huntley, A. P.; Opačić, B.; Brabeck, G. F.; Reilly, P. T. A., Simulation of instantaneous changes in ion motion with waveform duty cycle. *International Journal of Mass Spectrometry* **2019**, *441*, 8-13.

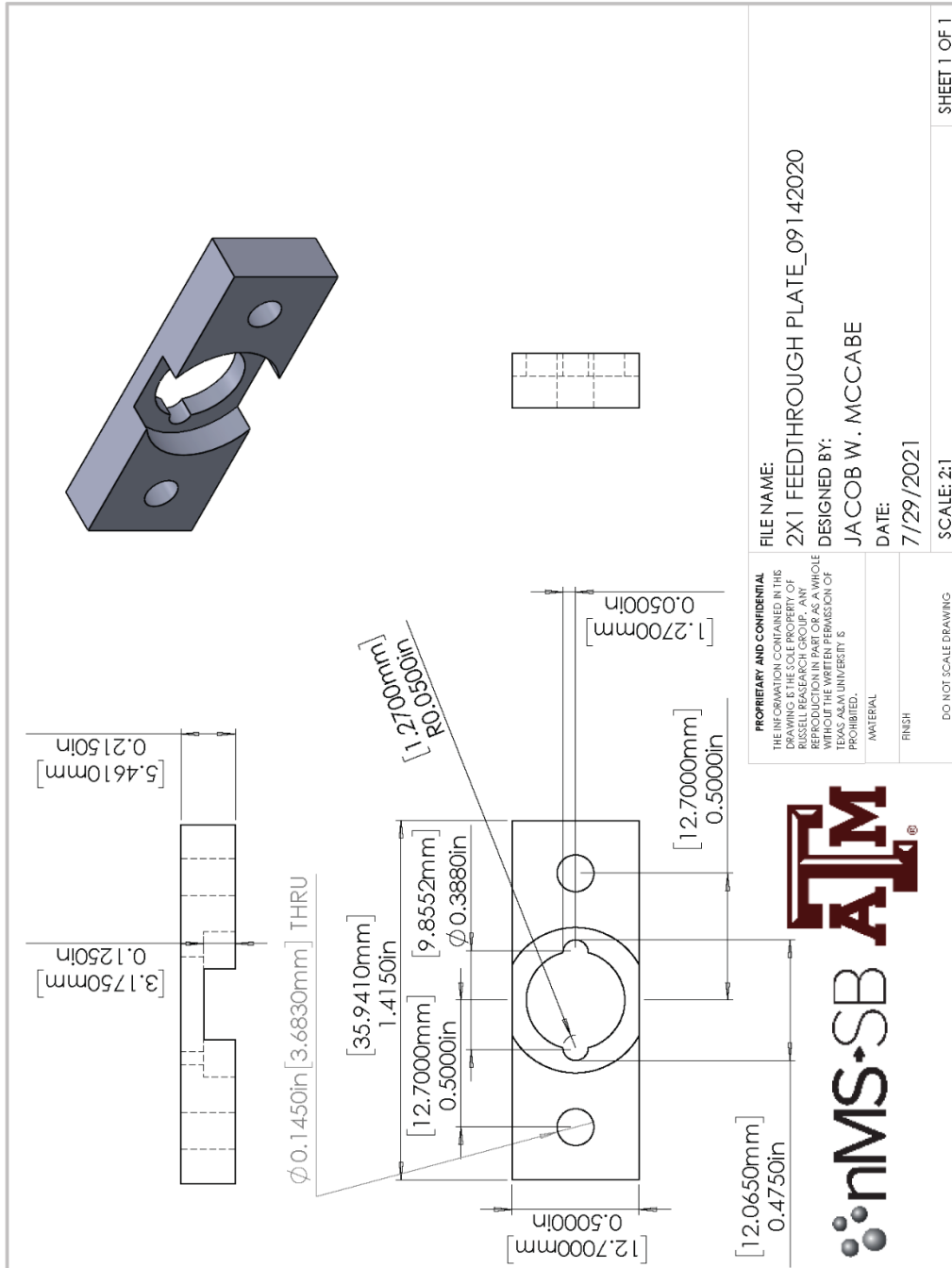
287. Opačić, B.; Huntley, A. P.; Clowers, B. H.; Reilly, P. T. A., Digital mass filter analysis in stability zones A and B. *Journal of Mass Spectrometry* **2018**, *53* (12), 1155-1168.

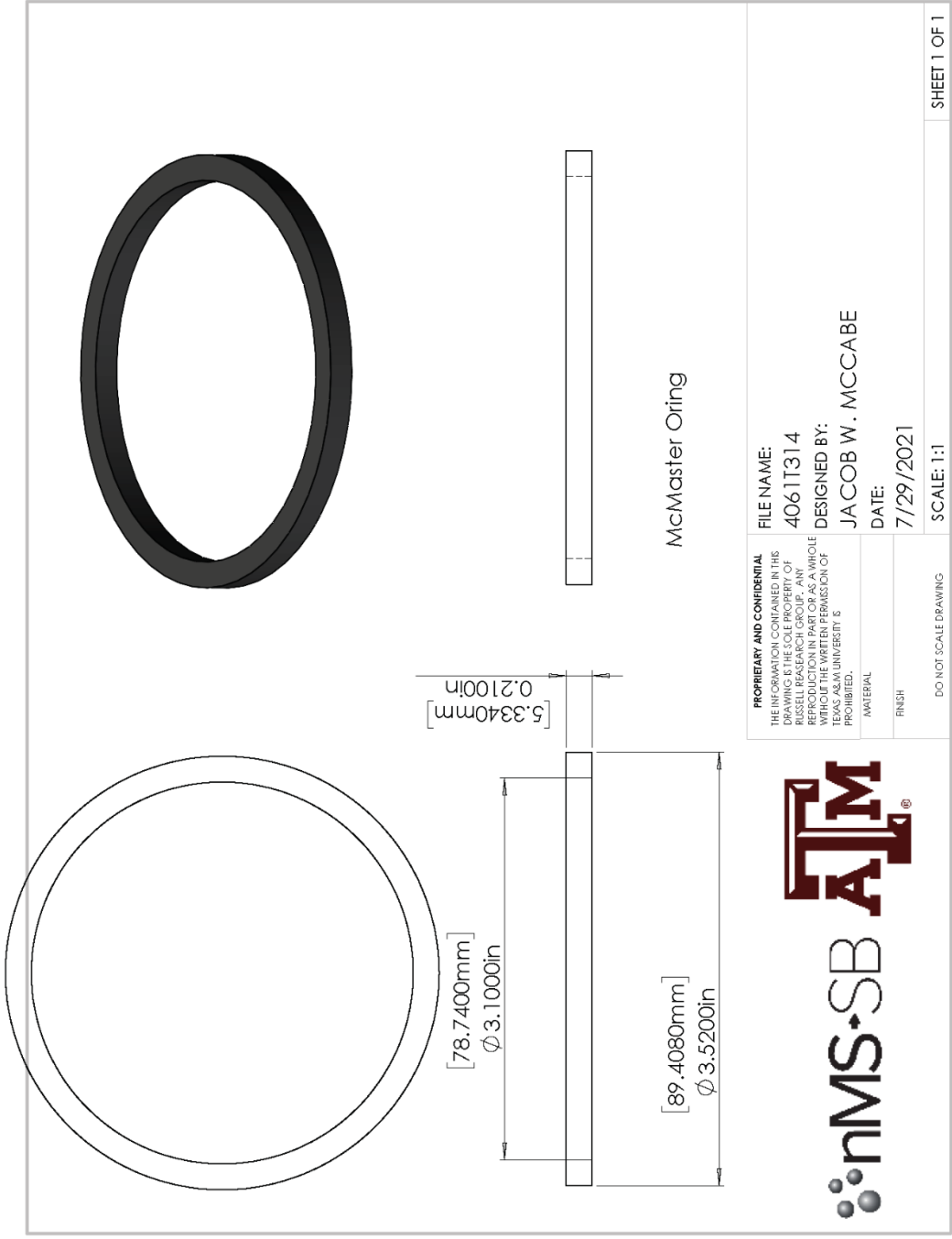
288. Reece, M. E.; Huntley, A. P.; Moon, A. M.; Reilly, P. T. A., Digital Mass Analysis in a Linear Ion Trap without Auxiliary Waveforms. *Journal of the American Society for Mass Spectrometry* **2020**, *31* (1), 103-108.
289. Singh, R.; Jayaram, V.; Reilly, P. T. A., Duty cycle-based isolation in linear quadrupole ion traps. *International Journal of Mass Spectrometry* **2013**, *343-344*, 45-49.
290. Snyder, D. T.; Panczyk, E.; Stiving, A. Q.; Gilbert, J. D.; Somogyi, A.; Kaplan, D.; Wysocki, V., Design and Performance of a Second-Generation Surface-Induced Dissociation Cell for Fourier Transform Ion Cyclotron Resonance Mass Spectrometry of Native Protein Complexes. *Analytical Chemistry* **2019**, *91* (21), 14049-14057.
291. Kwantwi-Barima, P.; Reinecke, T.; Clowers, B. H., Increased ion throughput using tristate ion-gate multiplexing. *Analyst* **2019**, *144* (22), 6660-6670.
292. Reinecke, T.; Davis, A. L.; Clowers, B. H., Determination of Gas-Phase Ion Mobility Coefficients Using Voltage Sweep Multiplexing. *Journal of the American Society for Mass Spectrometry* **2019**, *30* (6), 977-986.
293. Reinecke, T.; Naylor, C. N.; Clowers, B. H., Ion multiplexing: Maximizing throughput and signal to noise ratio for ion mobility spectrometry. *TrAC Trends in Analytical Chemistry* **2019**, *116*, 340-345.
294. Sanders, J. D.; Butalewicz, J. P.; Clowers, B. H.; Brodbelt, J. S., Absorption Mode Fourier Transform Ion Mobility Mass Spectrometry Multiplexing Combined with Half-Window Apodization Windows Improves Resolution and Shortens Acquisition Times. *Analytical Chemistry* **2021**, *93* (27), 9513-9520.

295. Schoen, A. E.; Amy, J. W.; Ciupek, J. D.; Cooks, R. G.; Dobberstein, P.; Jung, G., A hybrid BEQQ mass spectrometer. *International Journal of Mass Spectrometry and Ion Processes* **1985**, *65* (1), 125-140.
296. Keener, J. E.; Zhang, G.; Marty, M. T., Native Mass Spectrometry of Membrane Proteins. *Analytical Chemistry* **2021**, *93* (1), 583-597.
297. Fellers, R. T.; Greer, J. B.; Early, B. P.; Yu, X.; LeDuc, R. D.; Kelleher, N. L.; Thomas, P. M., ProSight Lite: Graphical software to analyze top-down mass spectrometry data. *PROTEOMICS* **2015**, *15* (7), 1235-1238.
298. Michalski, A.; Damoc, E.; Hauschild, J.-P.; Lange, O.; Wieghaus, A.; Makarov, A.; Nagaraj, N.; Cox, J.; Mann, M.; Horning, S., Mass Spectrometry-based Proteomics Using Q Exactive, a High-performance Benchtop Quadrupole Orbitrap Mass Spectrometer*. *Molecular & Cellular Proteomics* **2011**, *10* (9), M111.011015.

APPENDIX A

SOLIDWORKS DRAWINGS OF QQ-PF-DT-FT-IM ORBITRAP

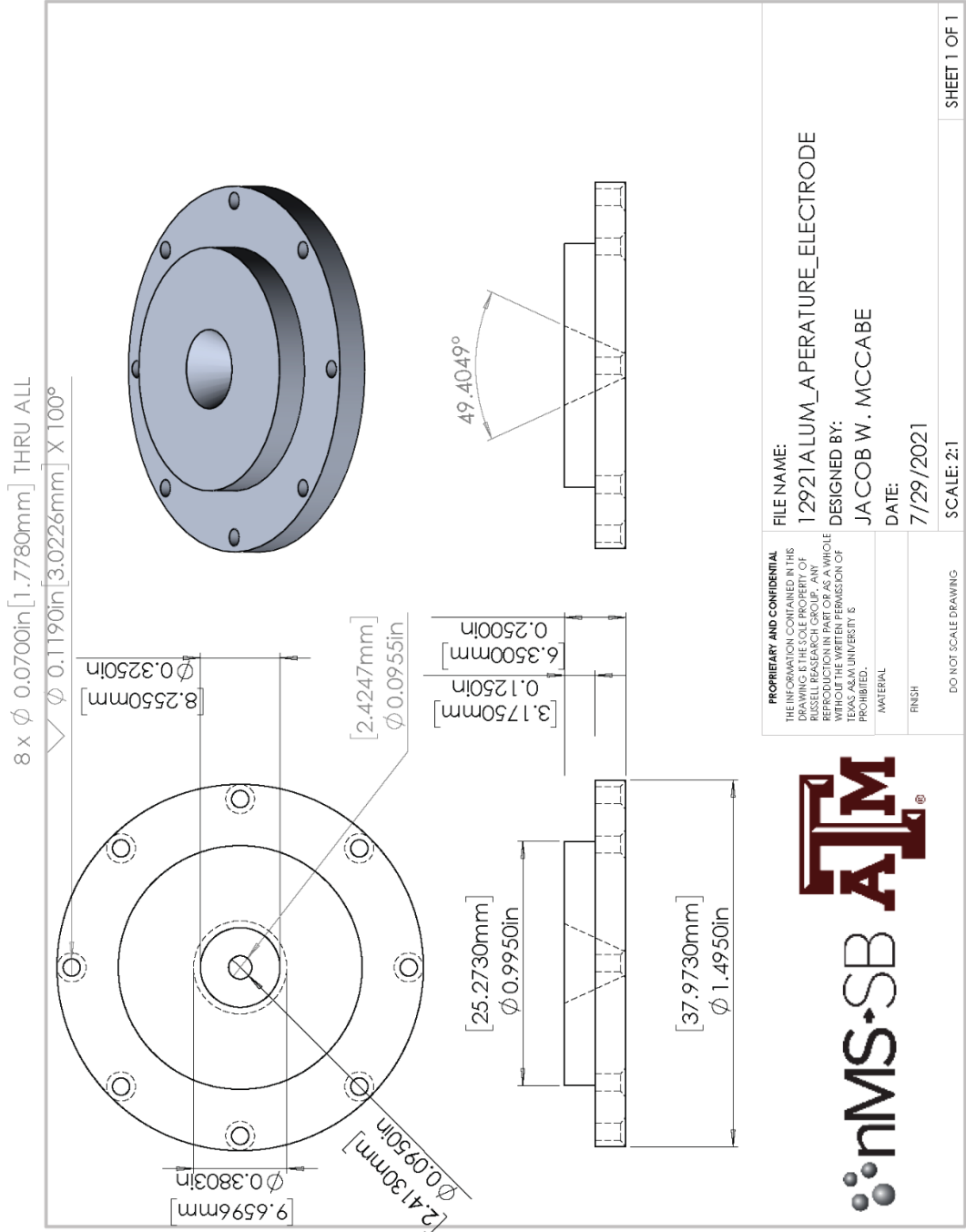




<p>PROPRIETARY AND CONFIDENTIAL THE INFORMATION CONTAINED IN THIS DRAWING IS THE SOLE PROPERTY OF RUSSELL RESEARCH GROUP. ANY REPRODUCTION IN PART OR AS A WHOLE WITHOUT THE WRITTEN PERMISSION OF TEXAS A&M UNIVERSITY IS PROHIBITED.</p>	<p>FILE NAME: 4061T314</p>	<p>DESIGNED BY: JACOB W. MCCABE</p>	<p>DATE: 7/29/2021</p>	<p>SCALE: 1:1</p>	<p>SHEET 1 OF 1</p>
	<p>MATERIAL</p>	<p>FINISH</p>	<p>DO NOT SCALE DRAWING</p>		



SOLIDWORKS Educational Product. For Instructional Use Only.



PROPRIETARY AND CONFIDENTIAL
 THE INFORMATION CONTAINED IN THIS DRAWING IS THE SOLE PROPERTY OF RUSSELL RESEARCH GROUP. ANY REPRODUCTION IN PART OR AS A WHOLE WITHOUT THE WRITTEN PERMISSION OF TEXAS A&M UNIVERSITY IS PROHIBITED.

MATERIAL: _____
 FINISH: _____

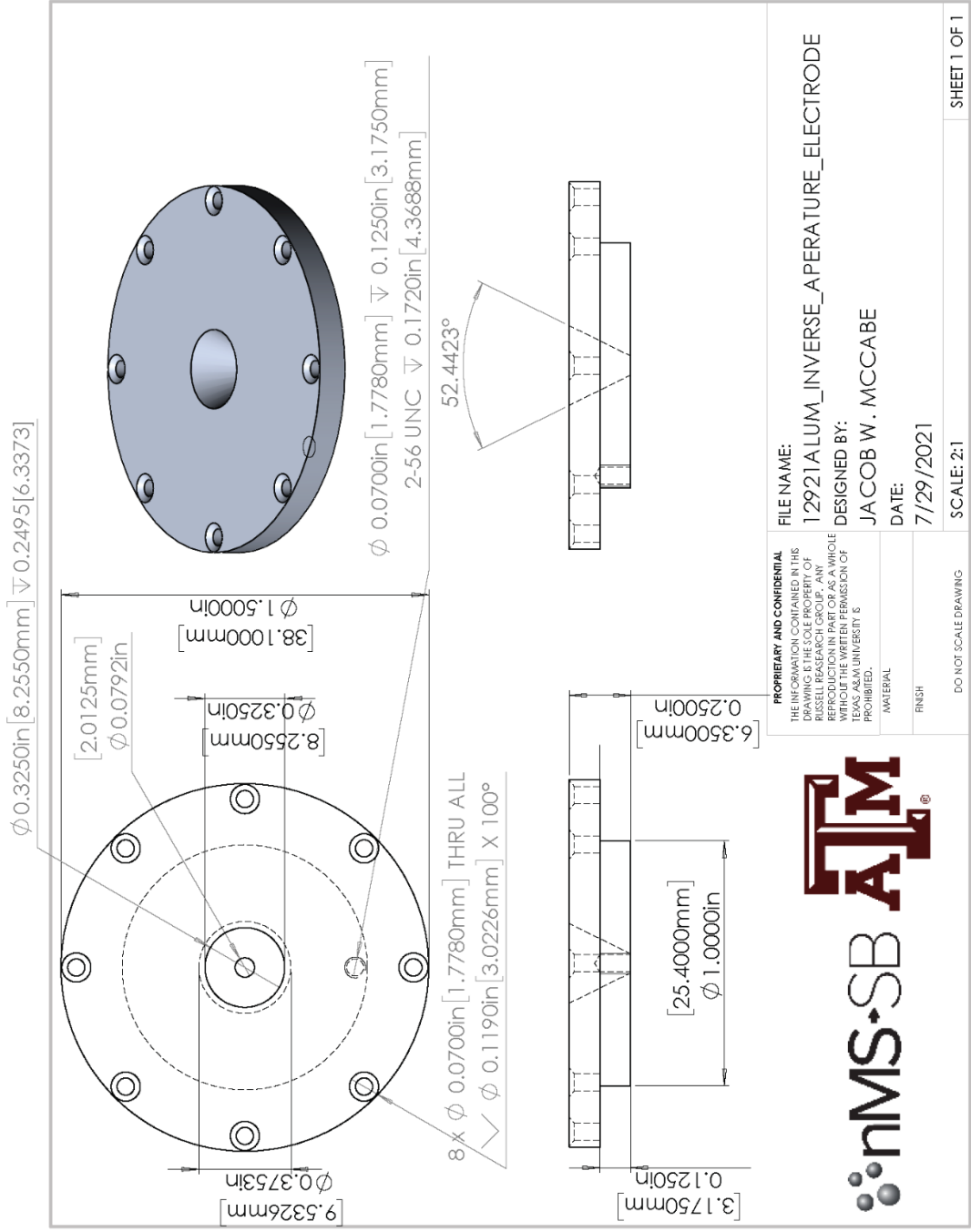
DO NOT SCALE DRAWING

FILE NAME: 12921A LUM_APERATURE_ELECTRODE
 DESIGNED BY: JACOB W. MCCABE
 DATE: 7/29/2021
 SCALE: 2:1



SHEET 1 OF 1

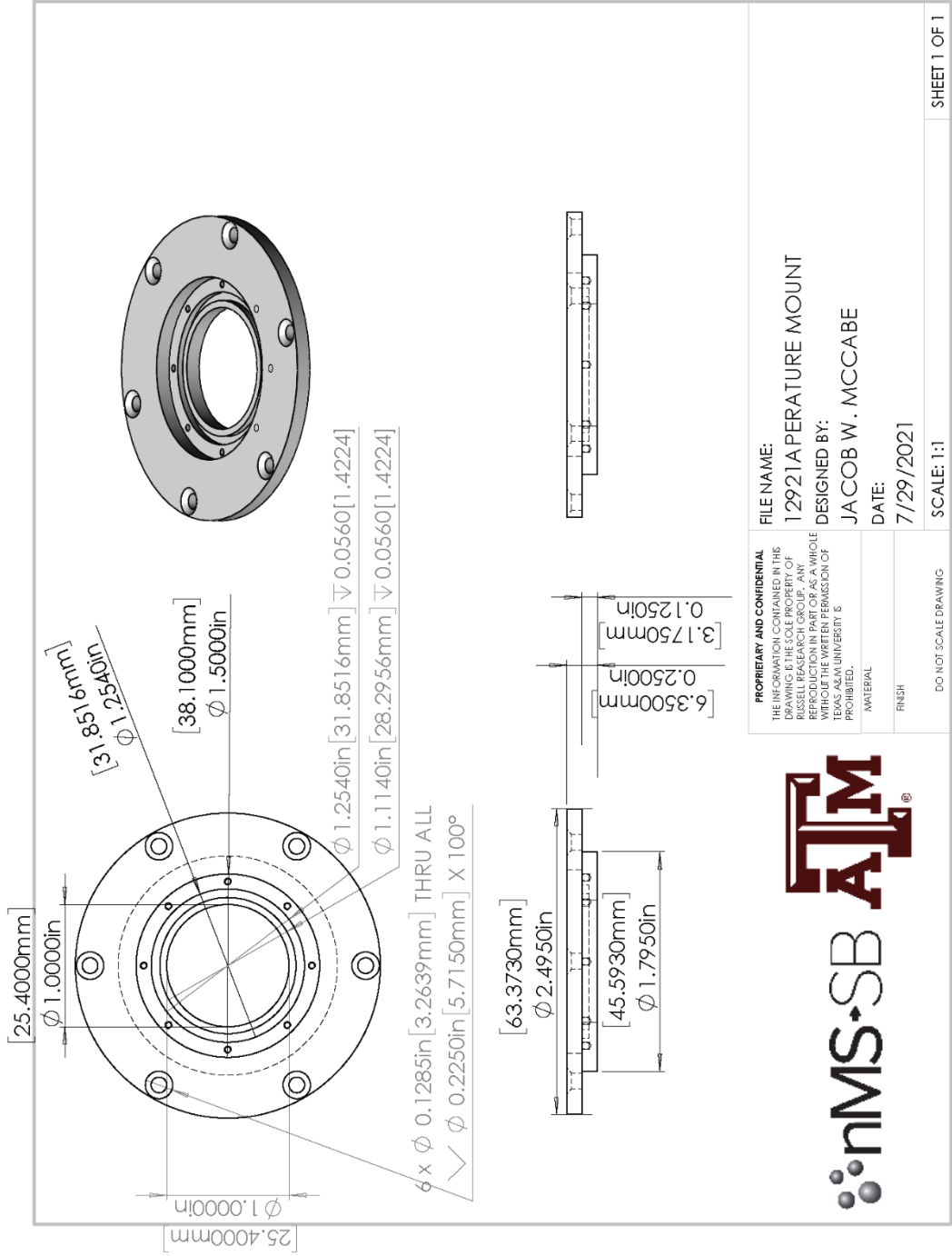
SOLIDWORKS Educational Product. For Instructional Use Only.



PROPRIETARY AND CONFIDENTIAL THE INFORMATION CONTAINED IN THIS DRAWING IS THE SOLE PROPERTY OF RUSSELL RESEARCH GROUP. ANY REPRODUCTION IN PART OR AS A WHOLE WITHOUT THE WRITTEN PERMISSION OF TEXAS A&M UNIVERSITY IS PROHIBITED. MATERIAL FINISH	FILE NAME: 12921A LUM_INVERSE_APERTURE_ELECTRODE	DESIGNED BY: JACOB W. MCCABE DATE: 7/29/2021	SCALE: 2:1 SHEET 1 OF 1
	DO NOT SCALE DRAWING		



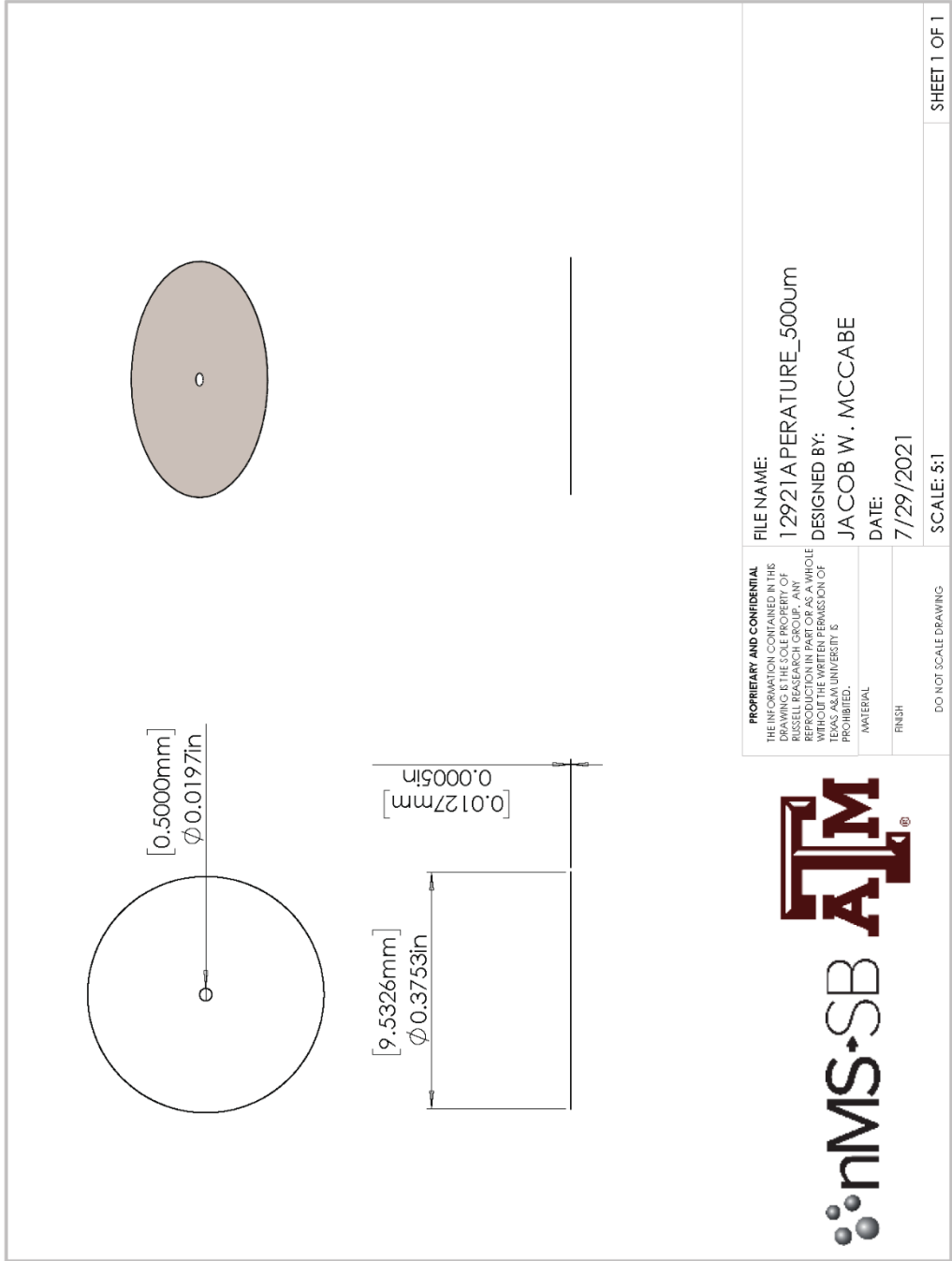
SOLIDWORKS Educational Product. For Instructional Use Only.



PROPRIETARY AND CONFIDENTIAL
 THE INFORMATION CONTAINED IN THIS
 DRAWING IS THE SOLE PROPERTY OF
 RUSSELL RESEARCH GROUP. ANY
 REPRODUCTION IN PART OR AS A WHOLE
 WITHOUT THE WRITTEN PERMISSION OF
 TEXAS A&M UNIVERSITY IS
 PROHIBITED.
 MATERIAL:
 FINISH:
 DO NOT SCALE DRAWING



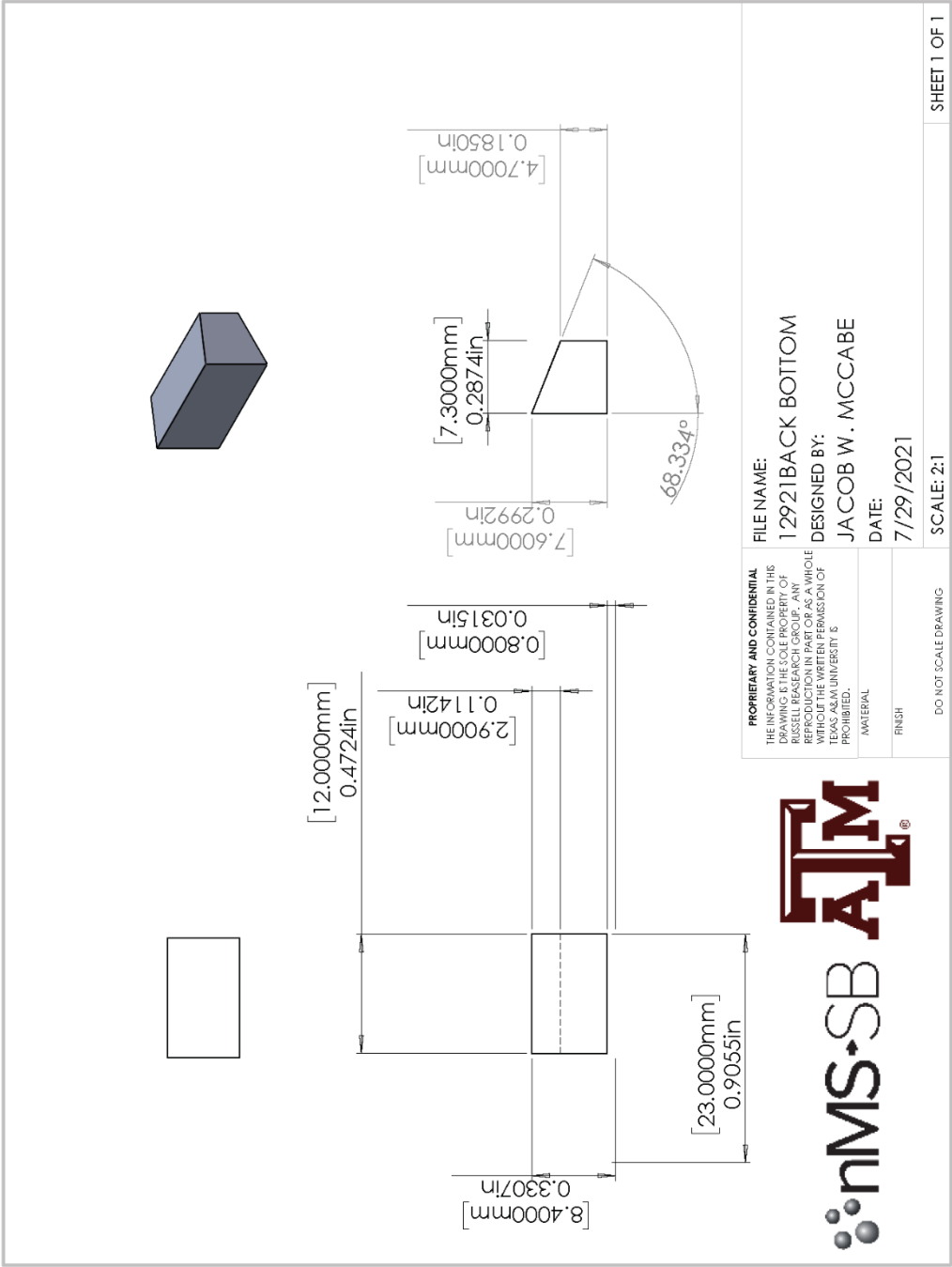
SOLIDWORKS Educational Product. For Instructional Use Only.

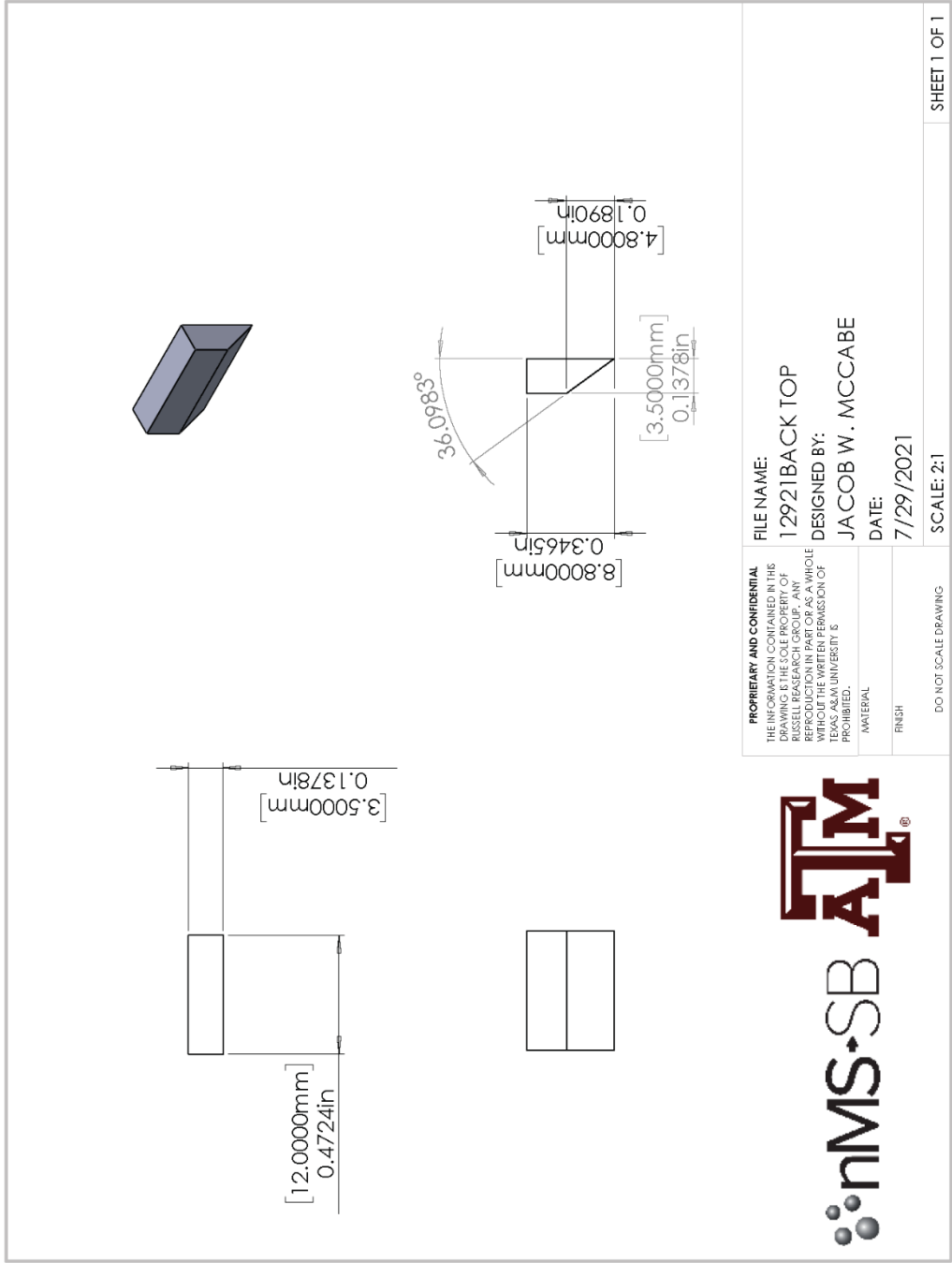


PROPRIETARY AND CONFIDENTIAL THE INFORMATION CONTAINED IN THIS DRAWING IS THE SOLE PROPERTY OF RUSSELL RESEARCH GROUP. ANY REPRODUCTION IN PART OR AS A WHOLE WITHOUT THE WRITTEN PERMISSION OF TEXAS A&M UNIVERSITY IS PROHIBITED.	FILE NAME: 12921A PERATURE_500um	DESIGNED BY: JACOB W. MCCABE	DATE: 7/29/2021	SCALE: 5:1	SHEET 1 OF 1
	MATERIAL FINISH				



SOLIDWORKS Educational Product. For Instructional Use Only.





PROPRIETARY AND CONFIDENTIAL
 THE INFORMATION CONTAINED IN THIS
 DRAWING IS THE SOLE PROPERTY OF
 RUSSELL RESEARCH GROUP. ANY
 REPRODUCTION IN PART OR AS A WHOLE
 WITHOUT THE WRITTEN PERMISSION OF
 TEXAS A&M UNIVERSITY IS
 PROHIBITED.



FILE NAME:
12921BACK TOP

DESIGNED BY:
JACOB W. MCCABE

DATE:
7/29/2021

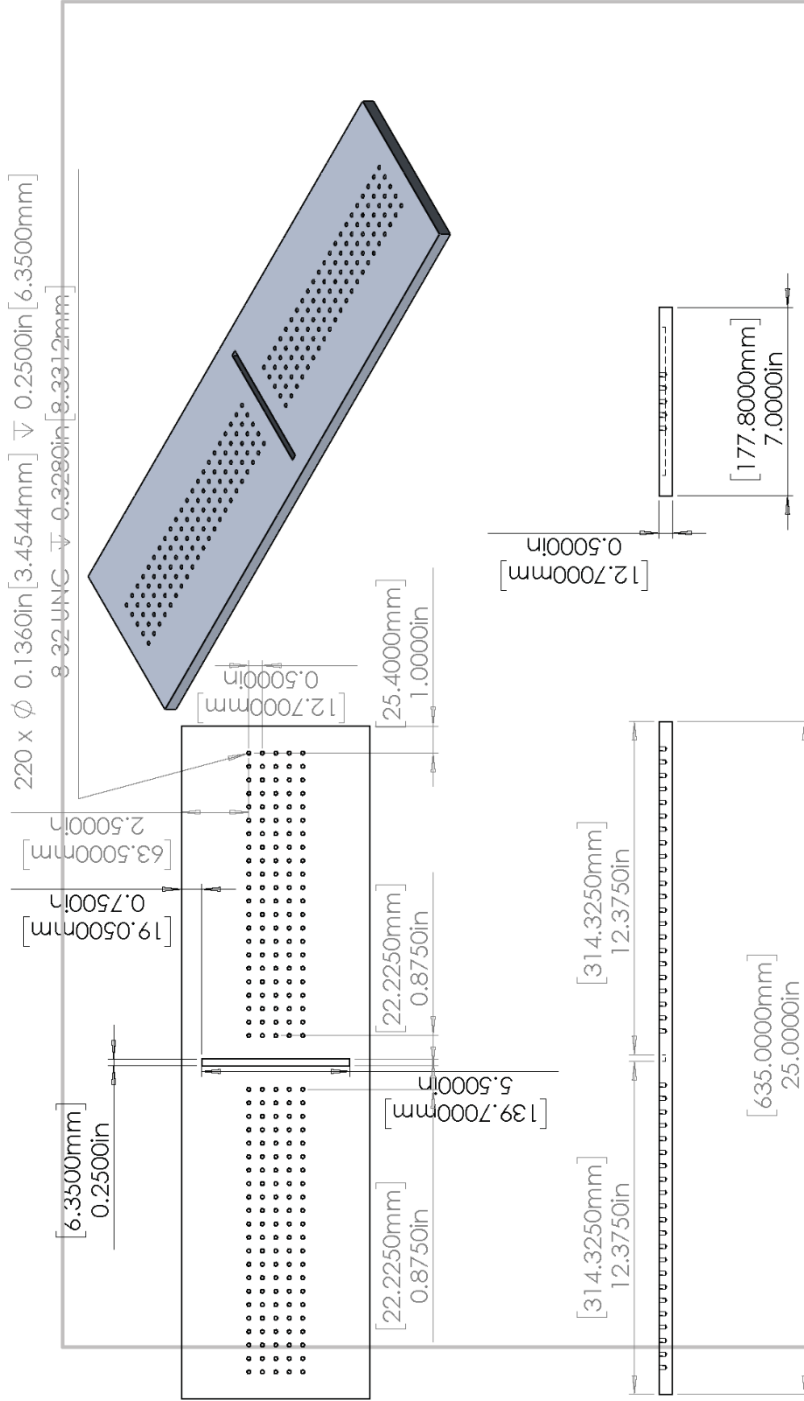
SCALE: 2:1

MATERIAL:

FINISH:

DO NOT SCALE DRAWING

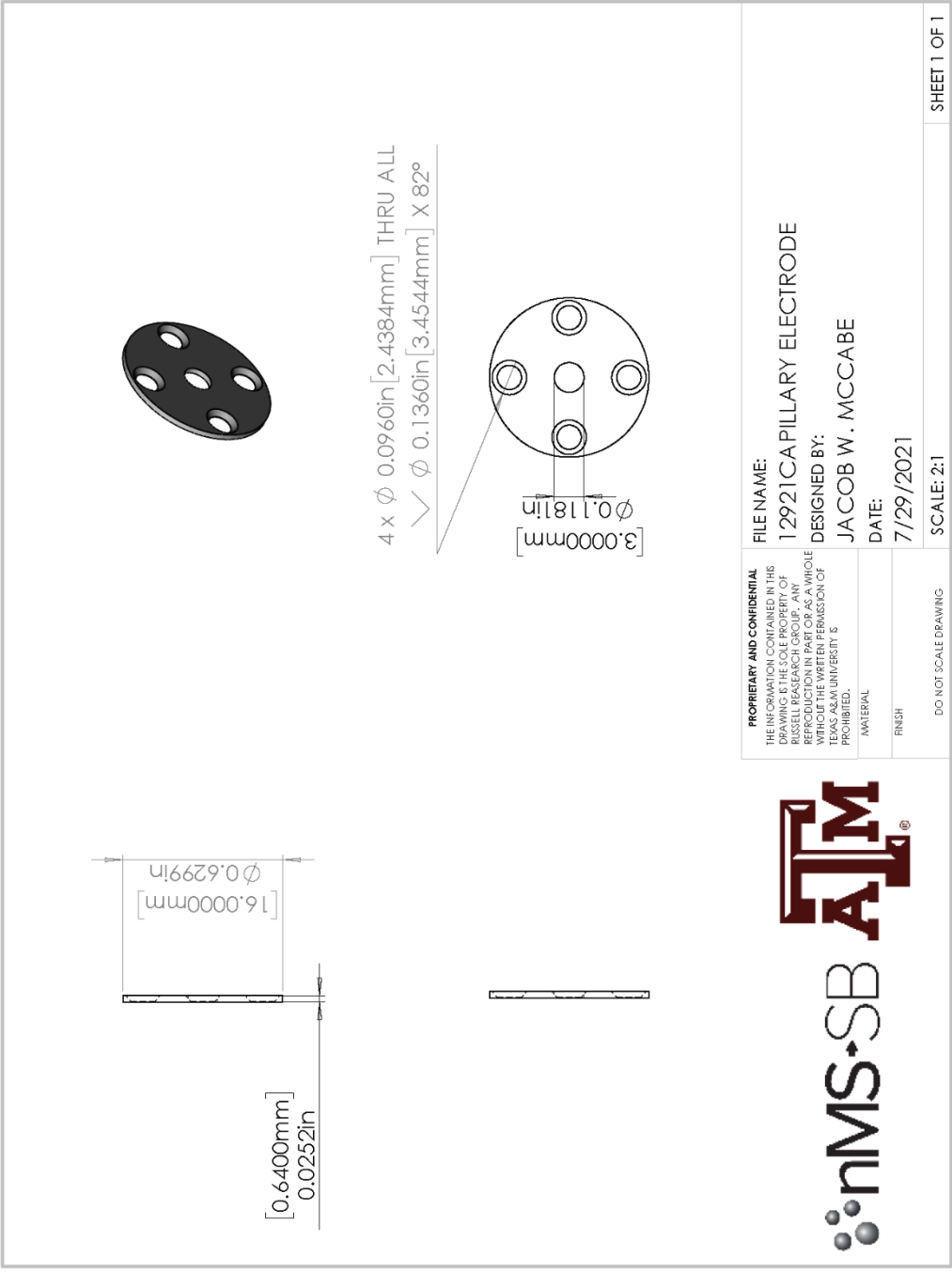
SHEET 1 OF 1

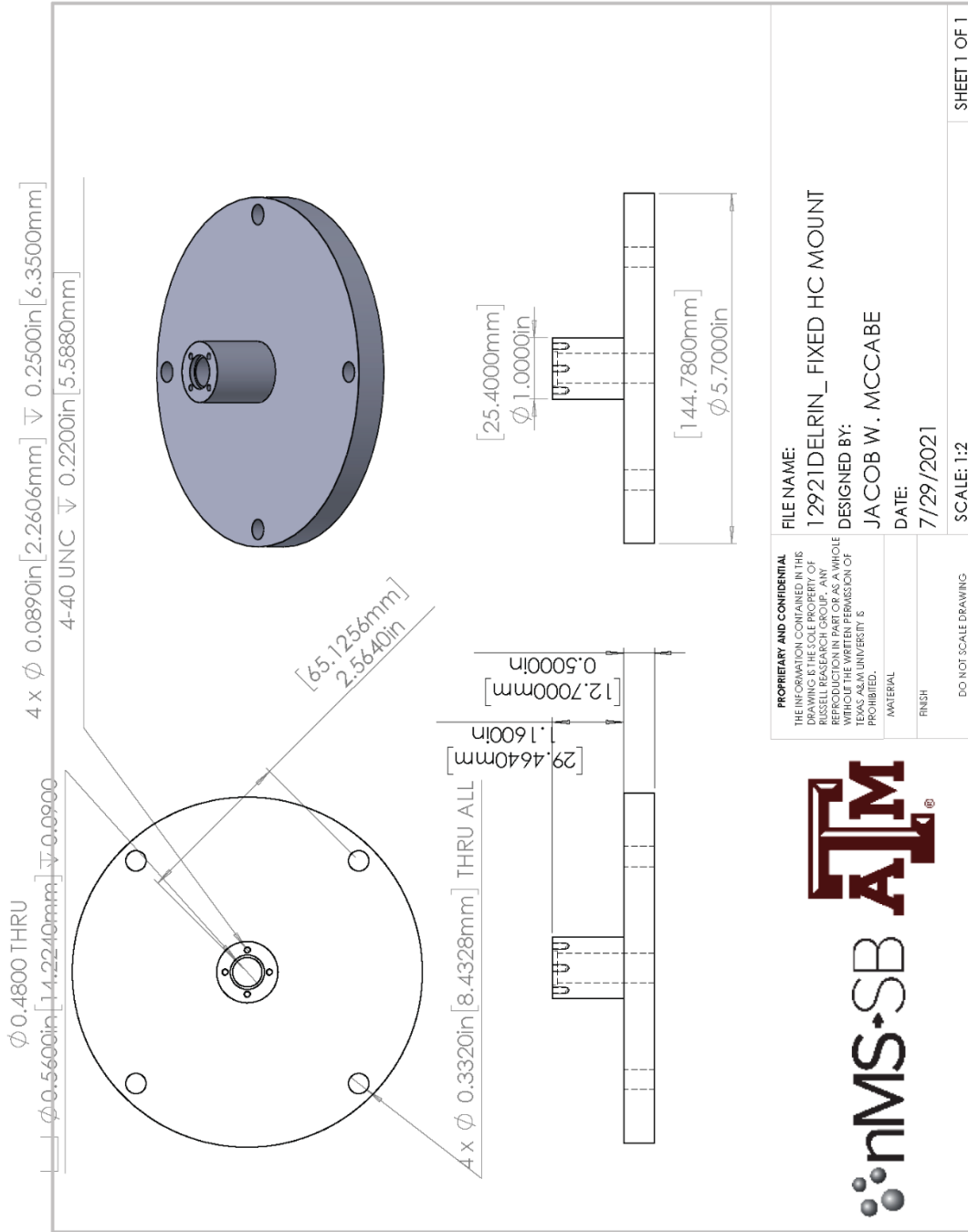


PROPRIETARY AND CONFIDENTIAL THE INFORMATION CONTAINED IN THIS DRAWING IS THE SOLE PROPERTY OF RUSSELL RESEARCH GROUP. ANY REPRODUCTION IN PART OR AS A WHOLE WITHOUT THE WRITTEN PERMISSION OF TEXAS A&M UNIVERSITY IS PROHIBITED.	MATERIAL
	FINISH
DO NOT SCALE DRAWING	
FILE NAME: 12921BOT DESIGNED BY: JACOB W. MCCABE DATE: 7/29/2021	SCALE: 1:5 SHEET 1 OF 1



SOLIDWORKS Educational Product. For Instructional Use Only.





PROPRIETARY AND CONFIDENTIAL
 THE INFORMATION CONTAINED IN THIS DRAWING IS THE SOLE PROPERTY OF RUSSELL RESEARCH GROUP. ANY REPRODUCTION IN PART OR AS A WHOLE WITHOUT THE WRITTEN PERMISSION OF TEXAS A&M UNIVERSITY IS PROHIBITED.



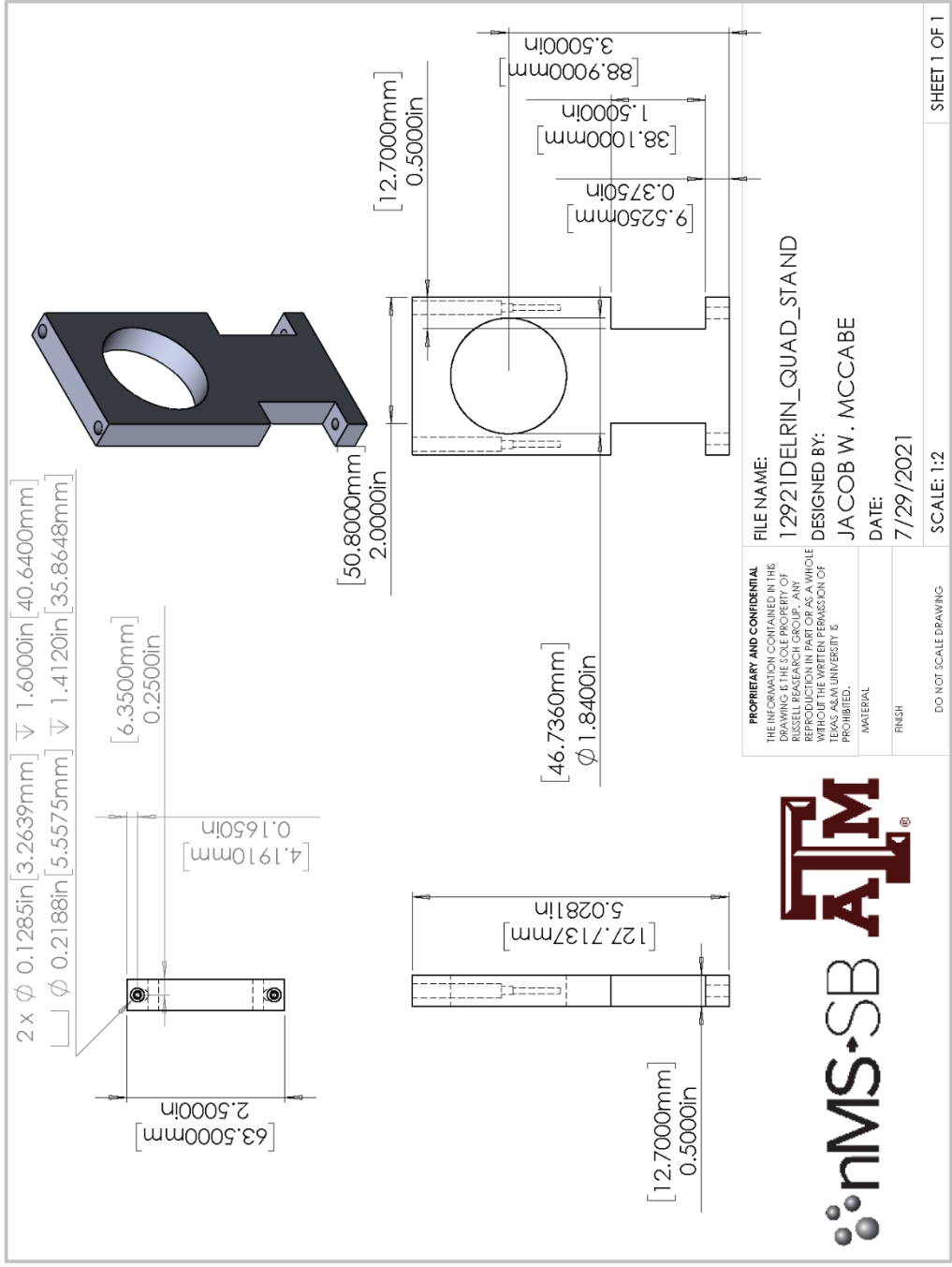
FILE NAME:
 12921DELIN_FIXED HC MOUNT
DESIGNED BY:
 JACOB W. MCCABE
DATE:
 7/29/2021

SCALE: 1:2

SHEET 1 OF 1

DO NOT SCALE DRAWING

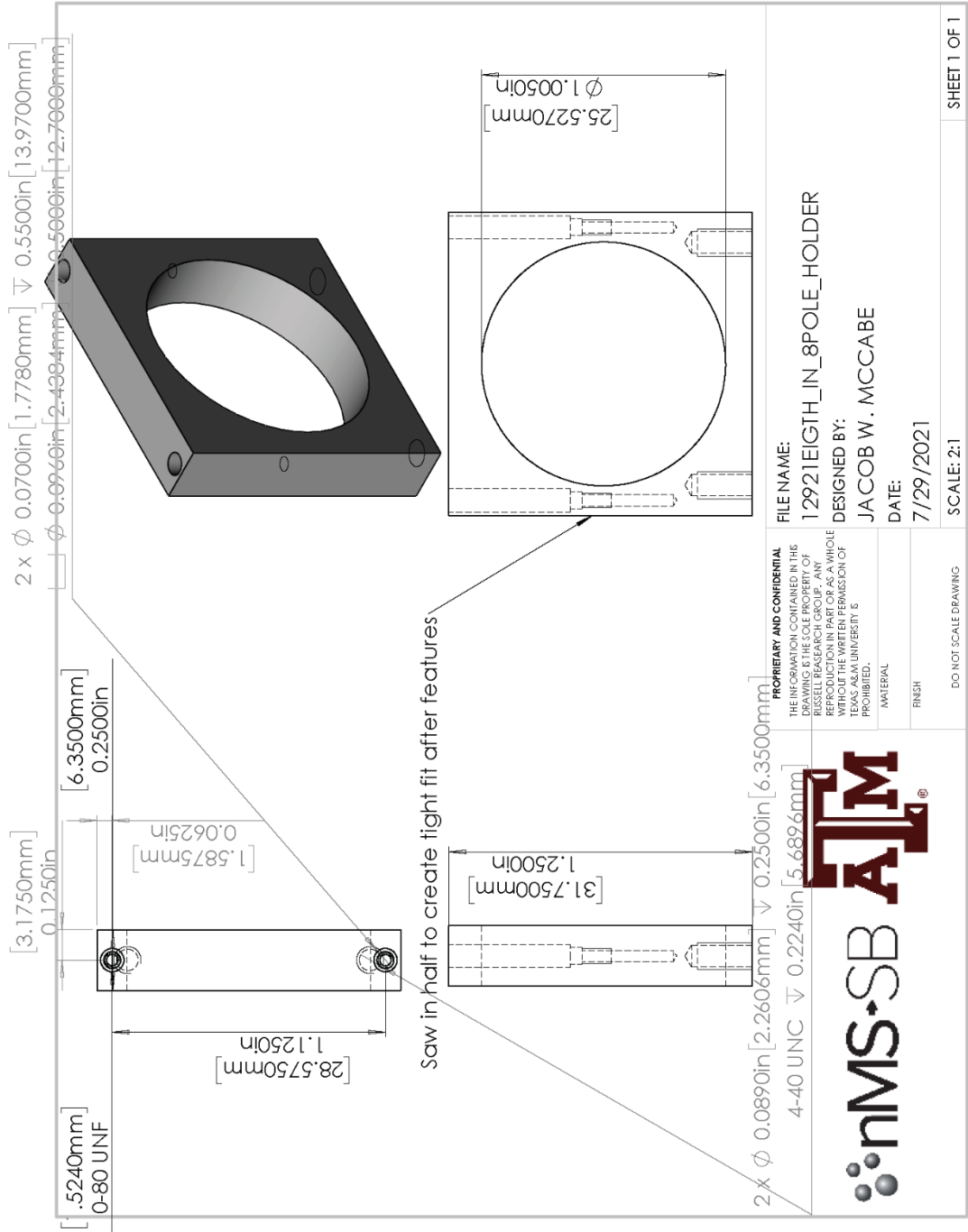
SOLIDWORKS Educational Product. For Instructional Use Only.

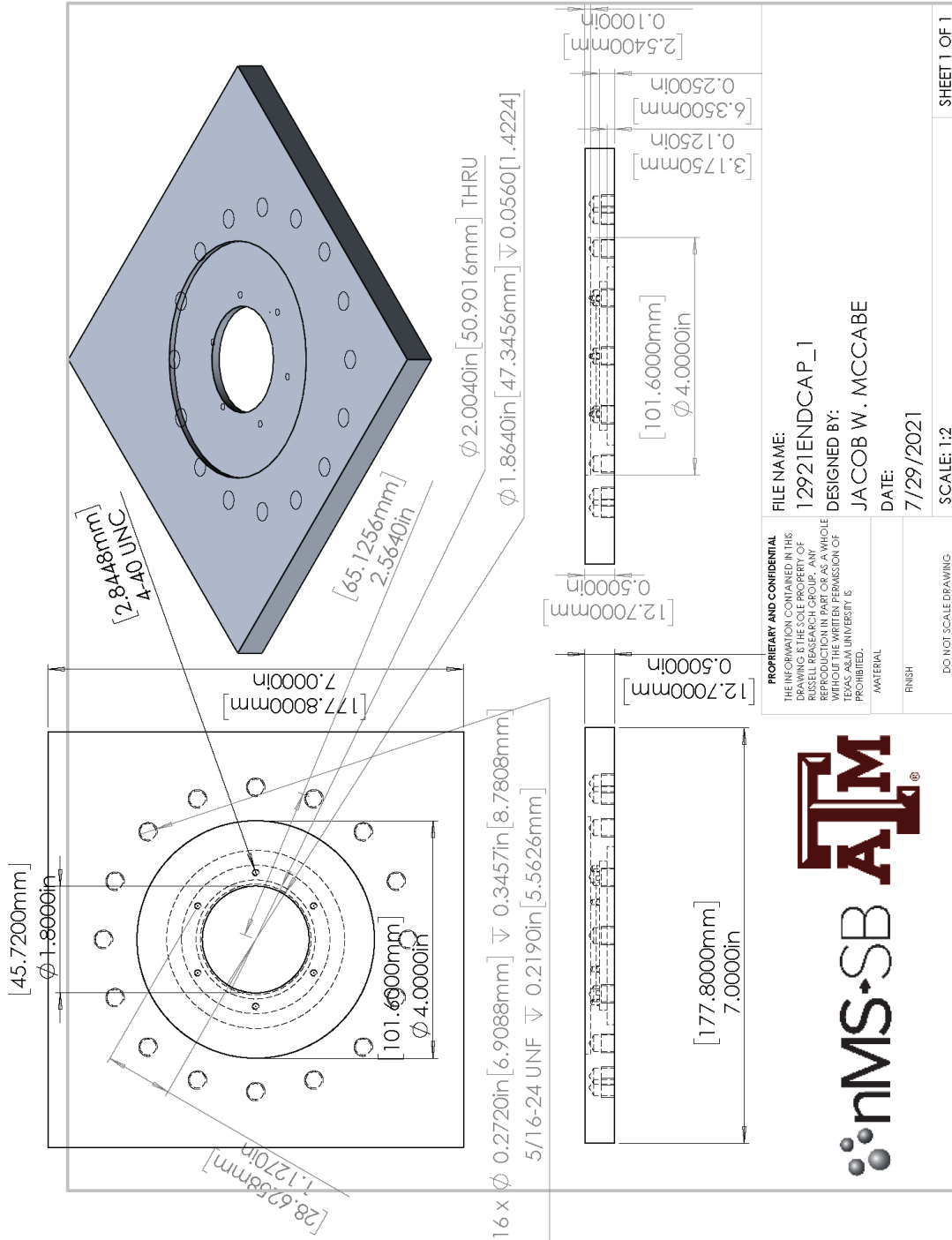




SHEET 1 OF 1

SOLIDWORKS Educational Product. For Instructional Use Only.





PROPRIETARY AND CONFIDENTIAL
 THE INFORMATION CONTAINED IN THIS DRAWING IS THE SOLE PROPERTY OF RUSSELL RESEARCH GROUP. ANY REPRODUCTION IN PART OR AS A WHOLE WITHOUT THE WRITTEN PERMISSION OF TEXAS A&M UNIVERSITY IS PROHIBITED.
 MATERIAL
 FINISH

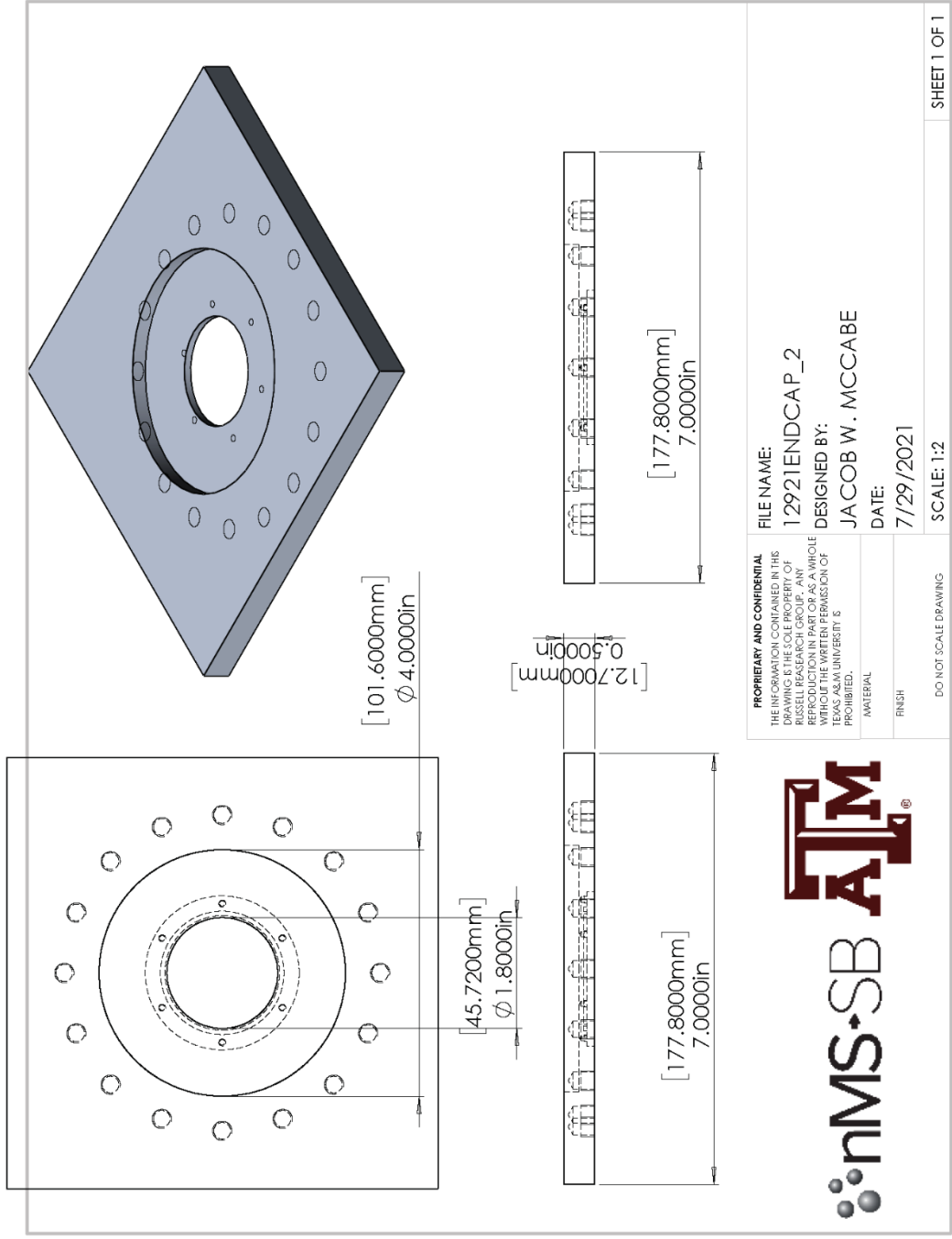
FILE NAME: 12921ENDCAP_1
 DESIGNED BY: JACOB W. MCCABE
 DATE: 7/29/2021

DO NOT SCALE DRAWING

SHEET 1 OF 1



SOLIDWORKS Educational Product. For Instructional Use Only.



PROPRIETARY AND CONFIDENTIAL
 THE INFORMATION CONTAINED IN THIS DRAWING IS THE SOLE PROPERTY OF RUSSELL RESEARCH GROUP. ANY REPRODUCTION IN PART OR AS A WHOLE WITHOUT THE WRITTEN PERMISSION OF TEXAS A&M UNIVERSITY IS PROHIBITED.



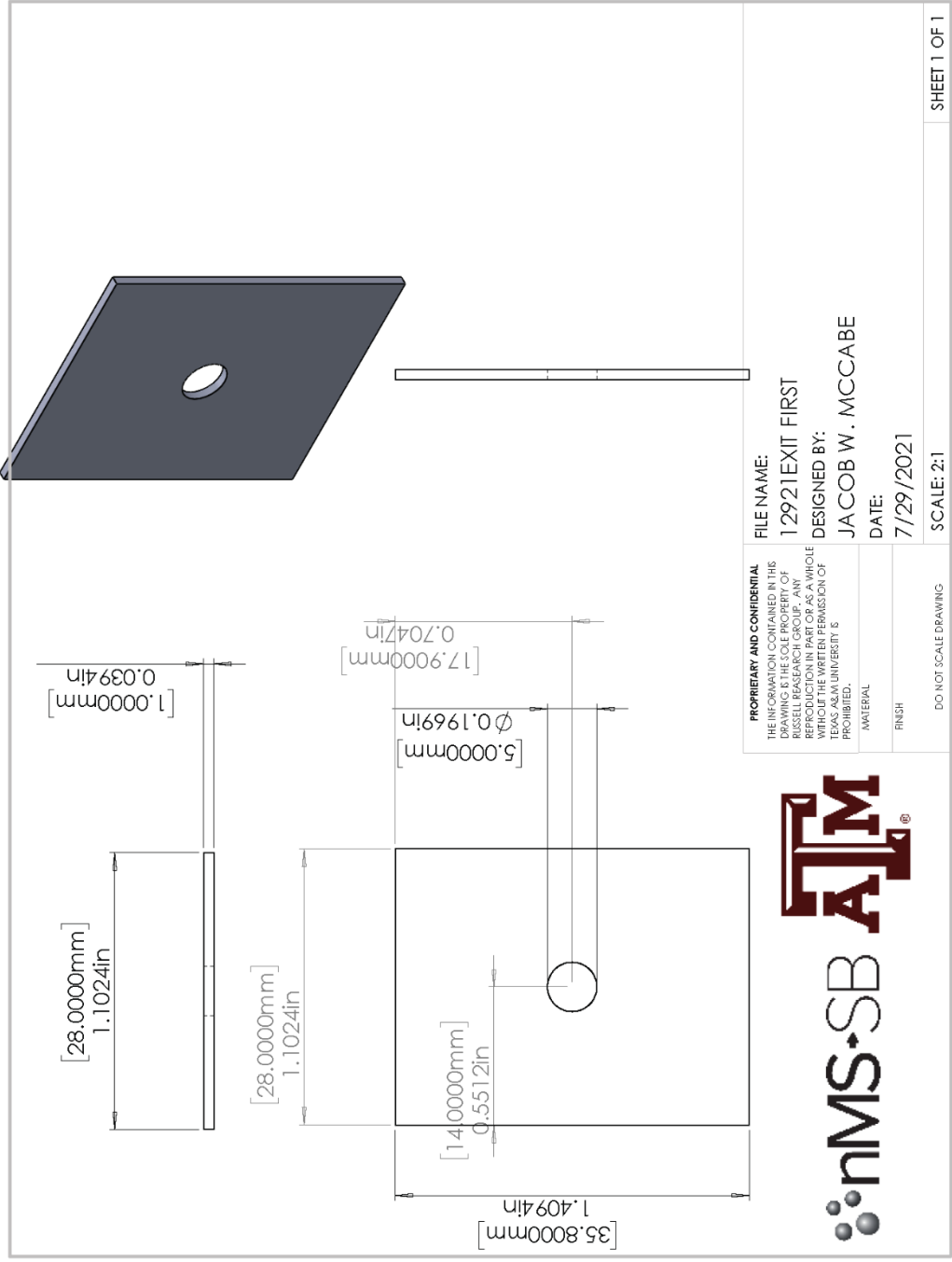
nMS-SB

FILE NAME: 12921ENDCAP_2
 DESIGNED BY: JACOB W. MCCABE
 DATE: 7/29/2021

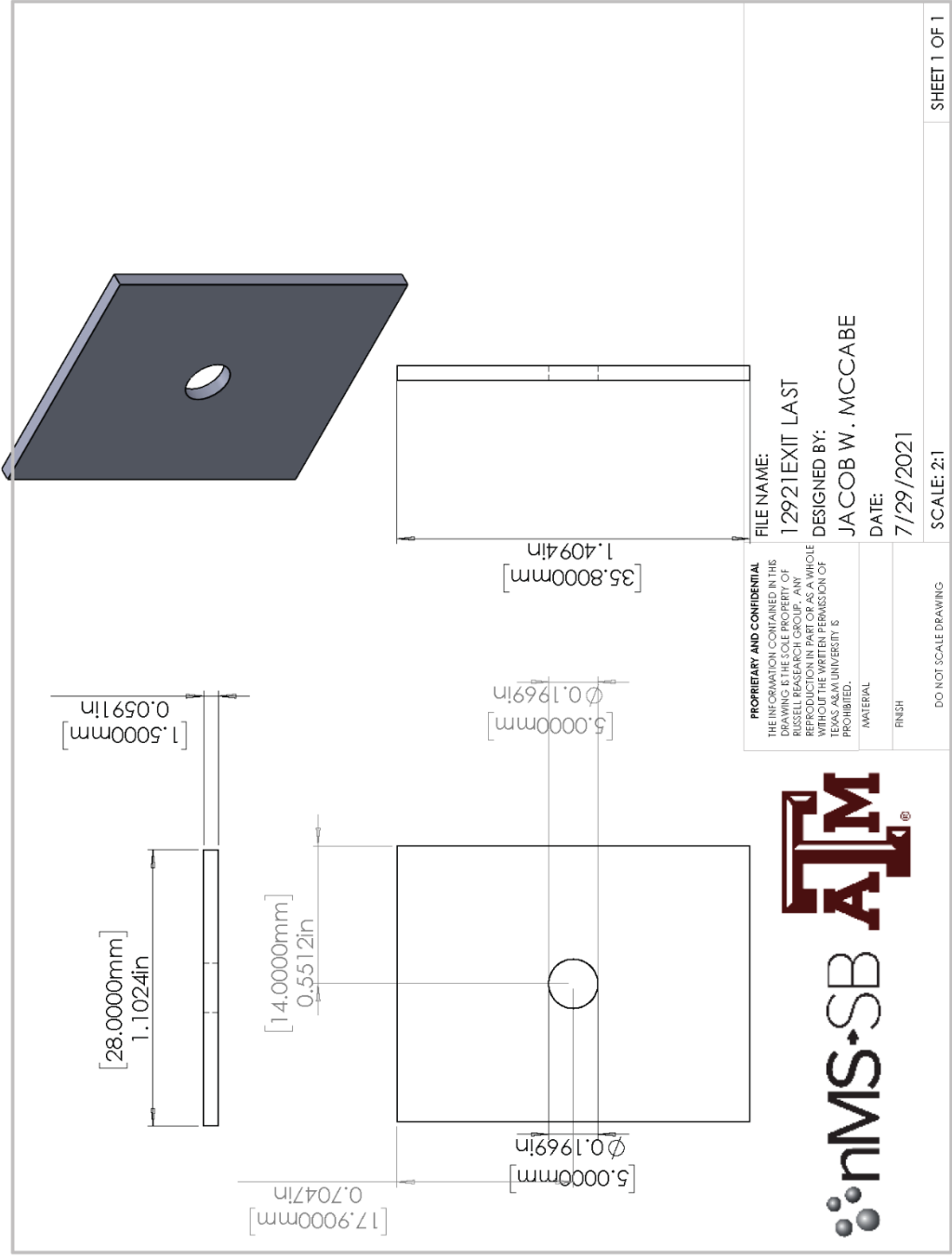
SHEET 1 OF 1

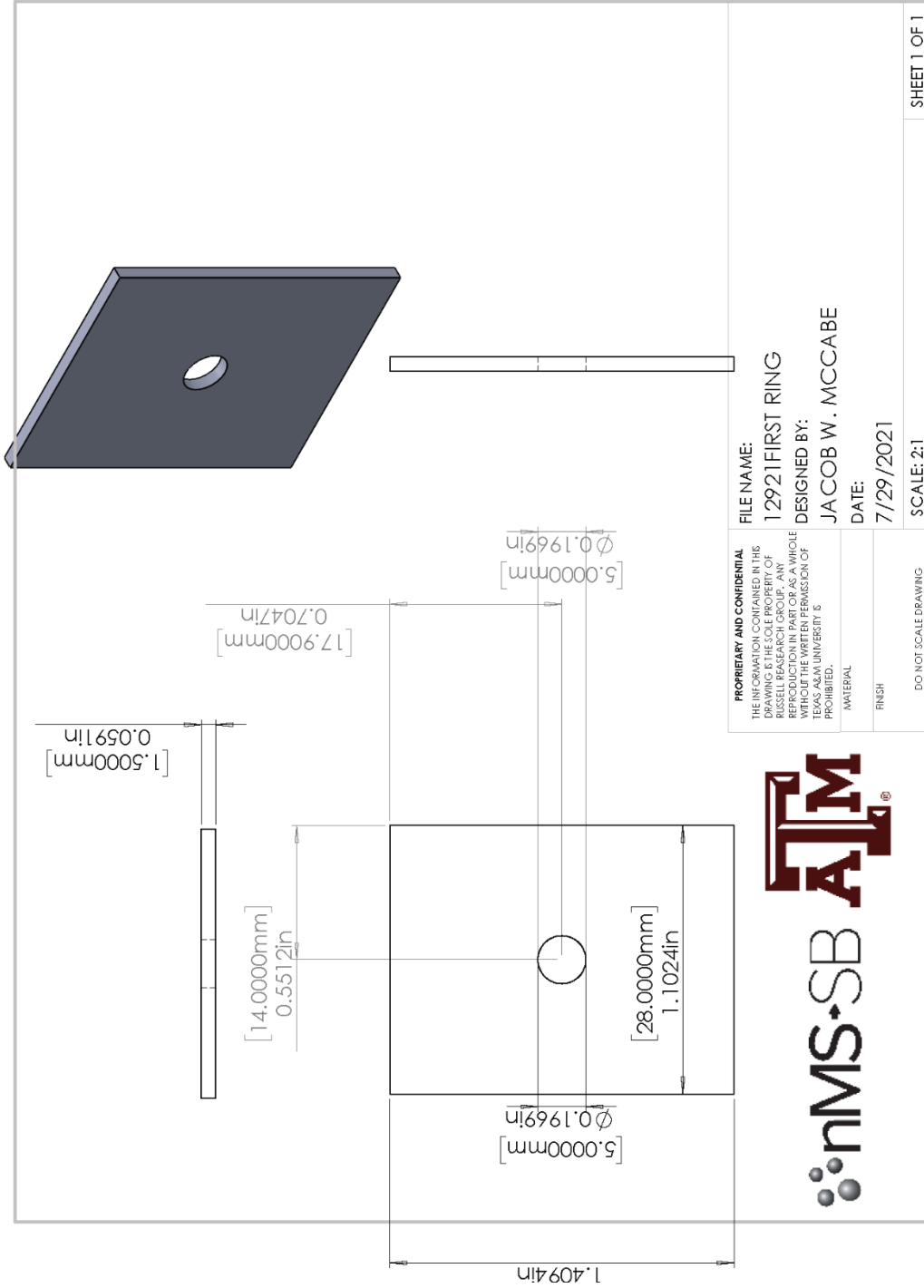
SCALE: 1:2

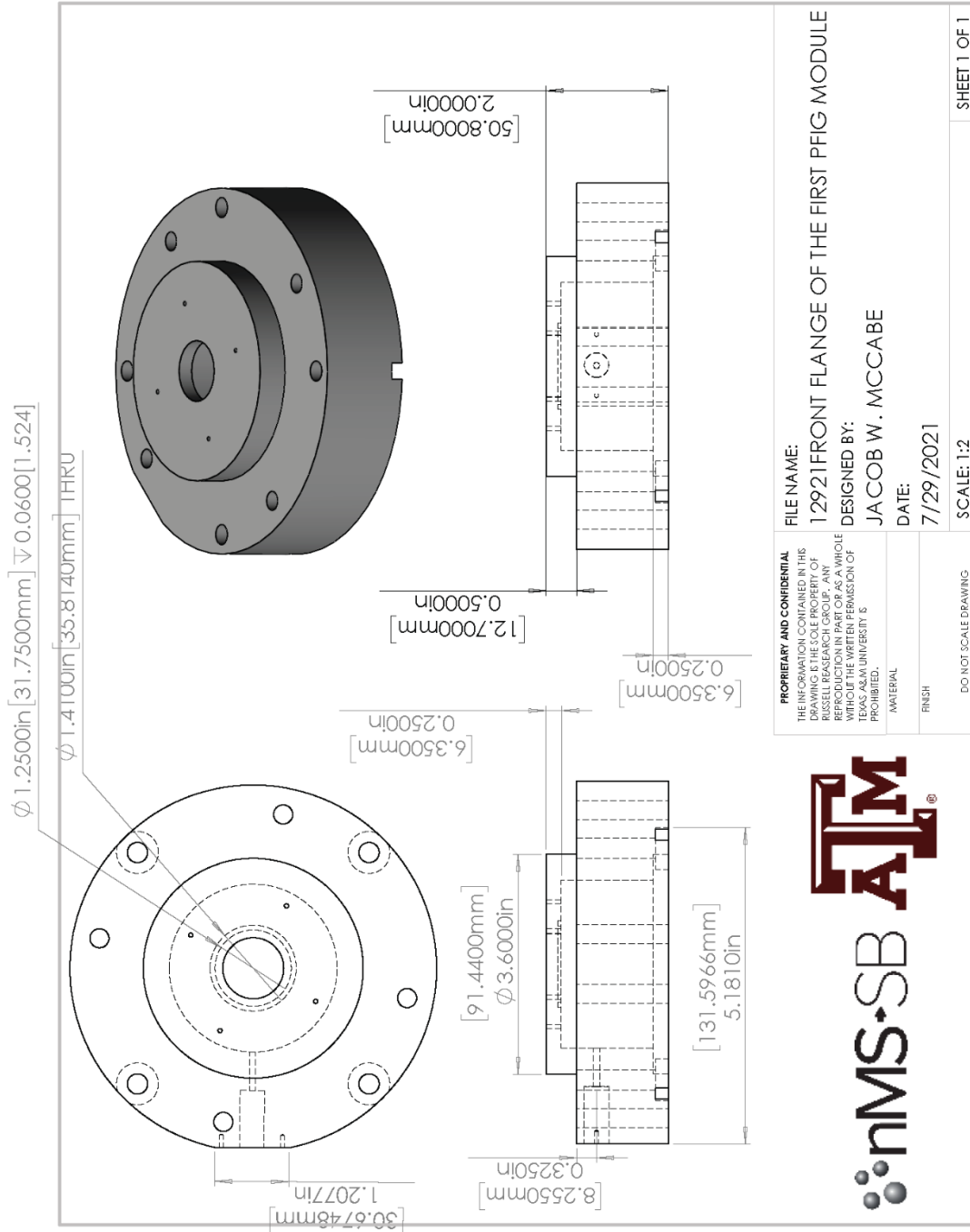
DO NOT SCALE DRAWING



SOLIDWORKS Educational Product. For Instructional Use Only.

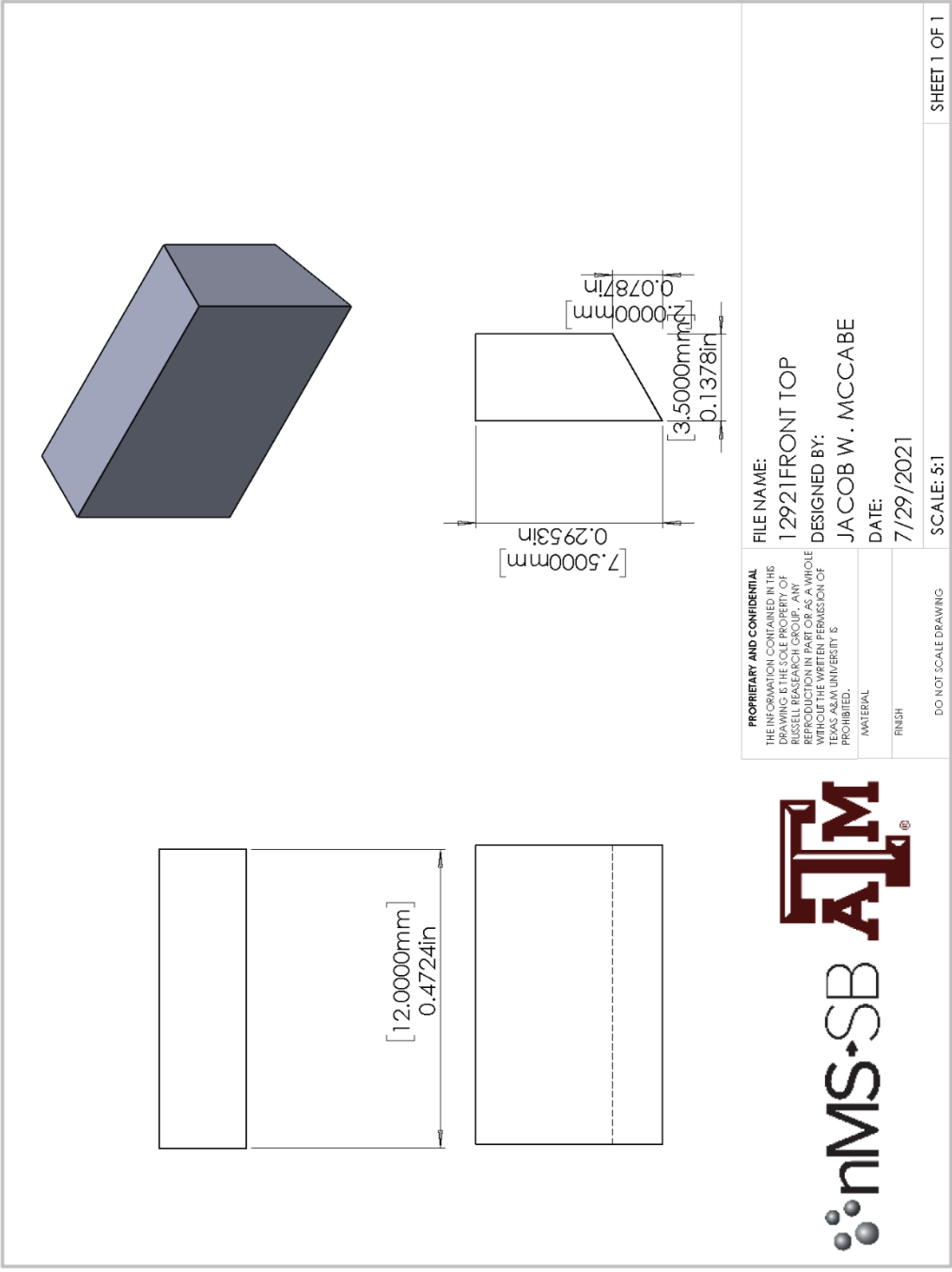


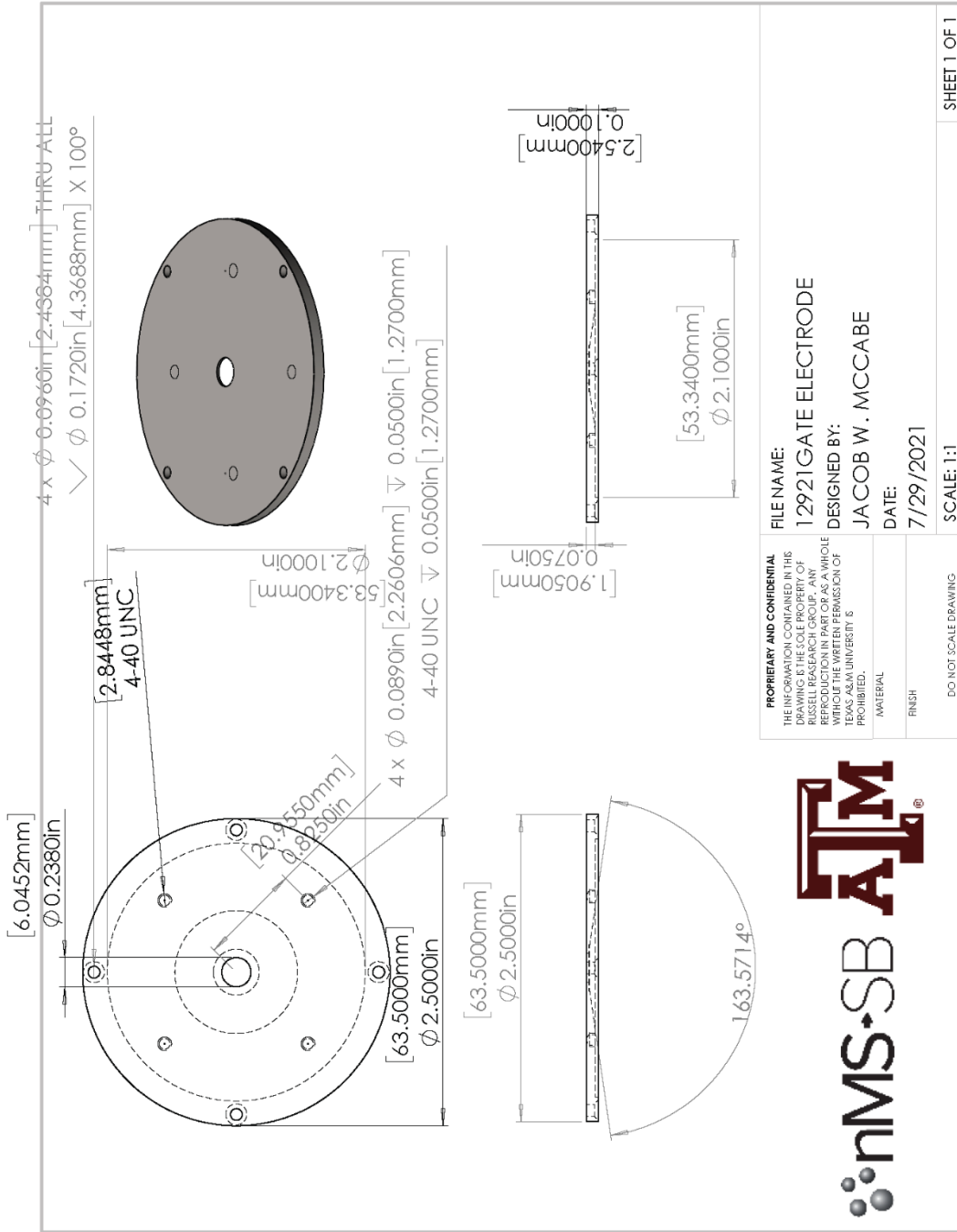


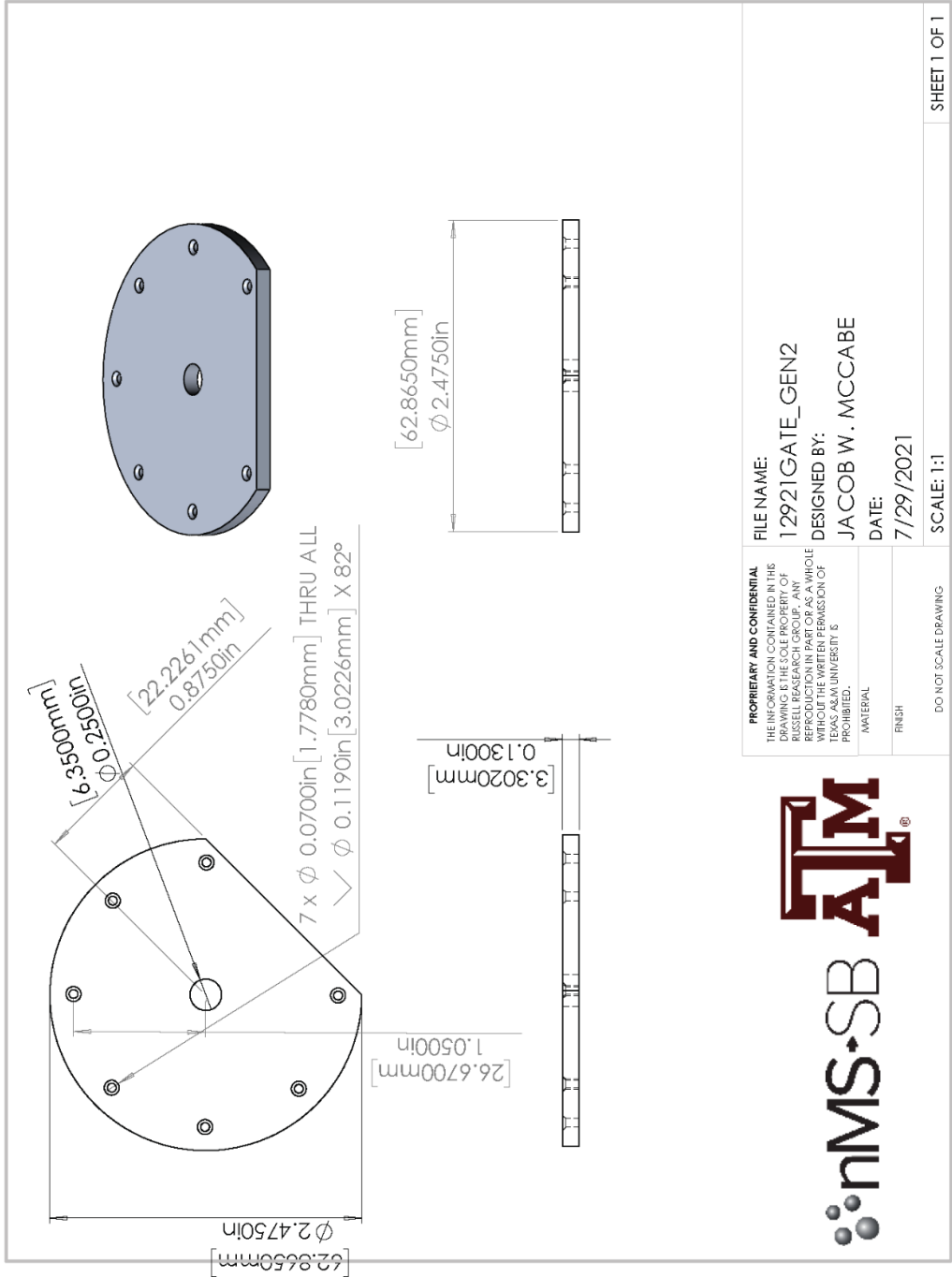


SHEET 1 OF 1

SOLIDWORKS Educational Product. For Instructional Use Only.







PROPRIETARY AND CONFIDENTIAL
 THE INFORMATION CONTAINED IN THIS
 DRAWING IS THE SOLE PROPERTY OF
 RUSSELL RESEARCH GROUP. ANY
 REPRODUCTION IN PART OR AS A WHOLE
 WITHOUT THE WRITTEN PERMISSION OF
 TEXAS A&M UNIVERSITY IS
 PROHIBITED.
 MATERIAL



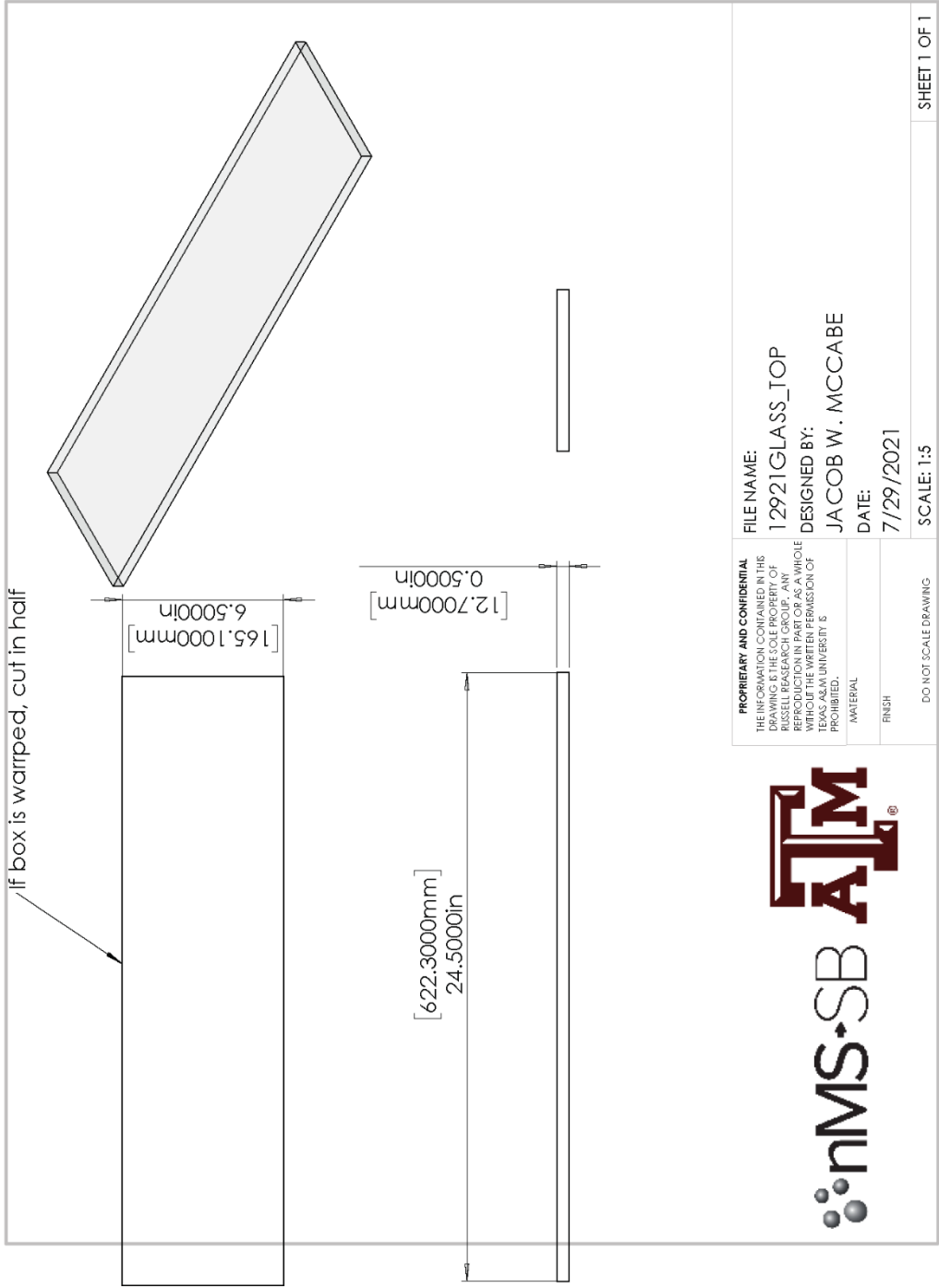
FILE NAME:
 12921GATE_GEN2
DESIGNED BY:
 JACOB W. MCCABE
DATE:
 7/29/2021

SCALE: 1:1

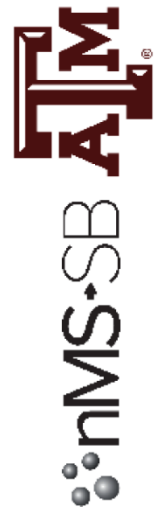
DO NOT SCALE DRAWING

SHEET 1 OF 1

SOLIDWORKS Educational Product. For Instructional Use Only.

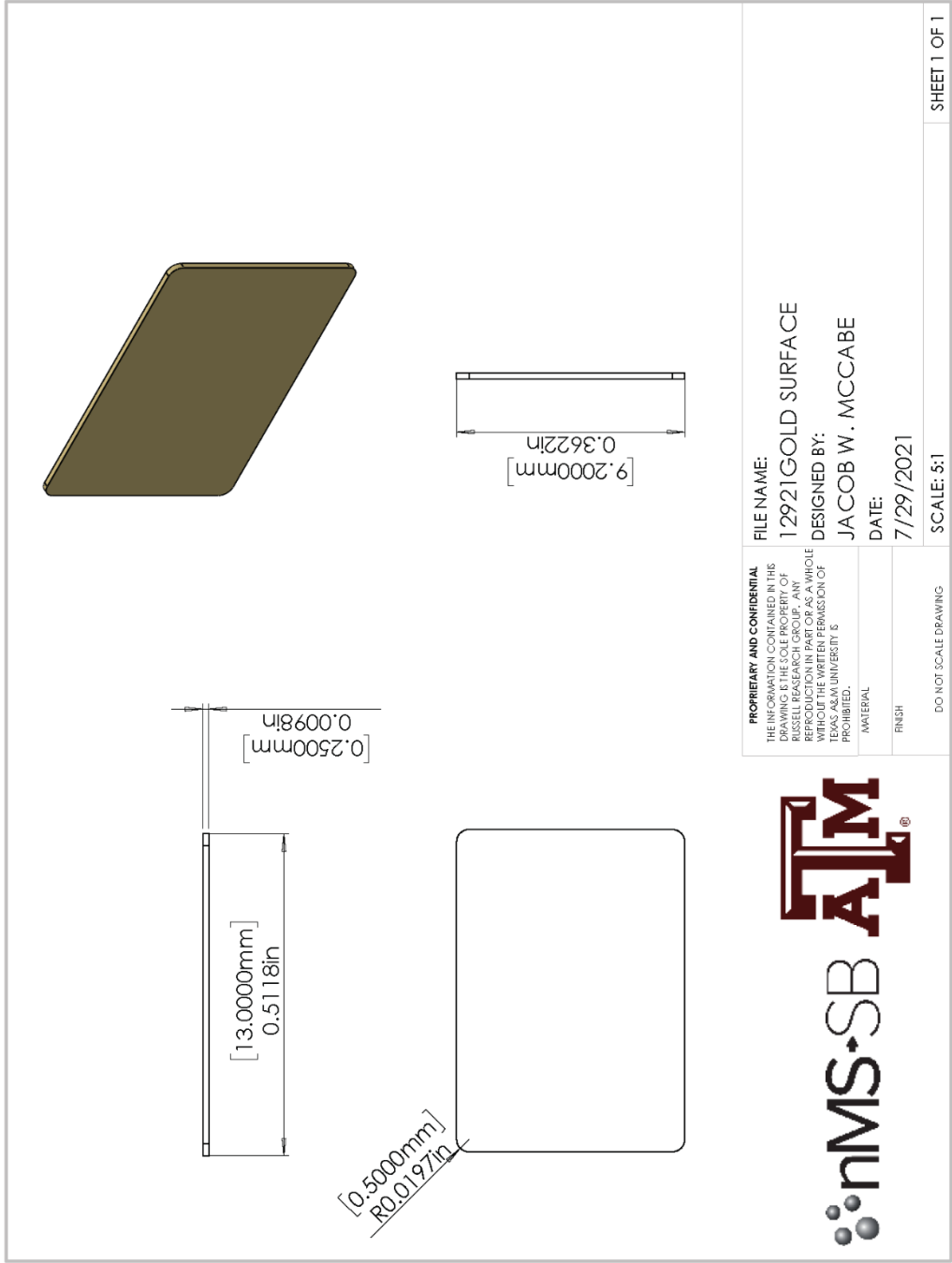


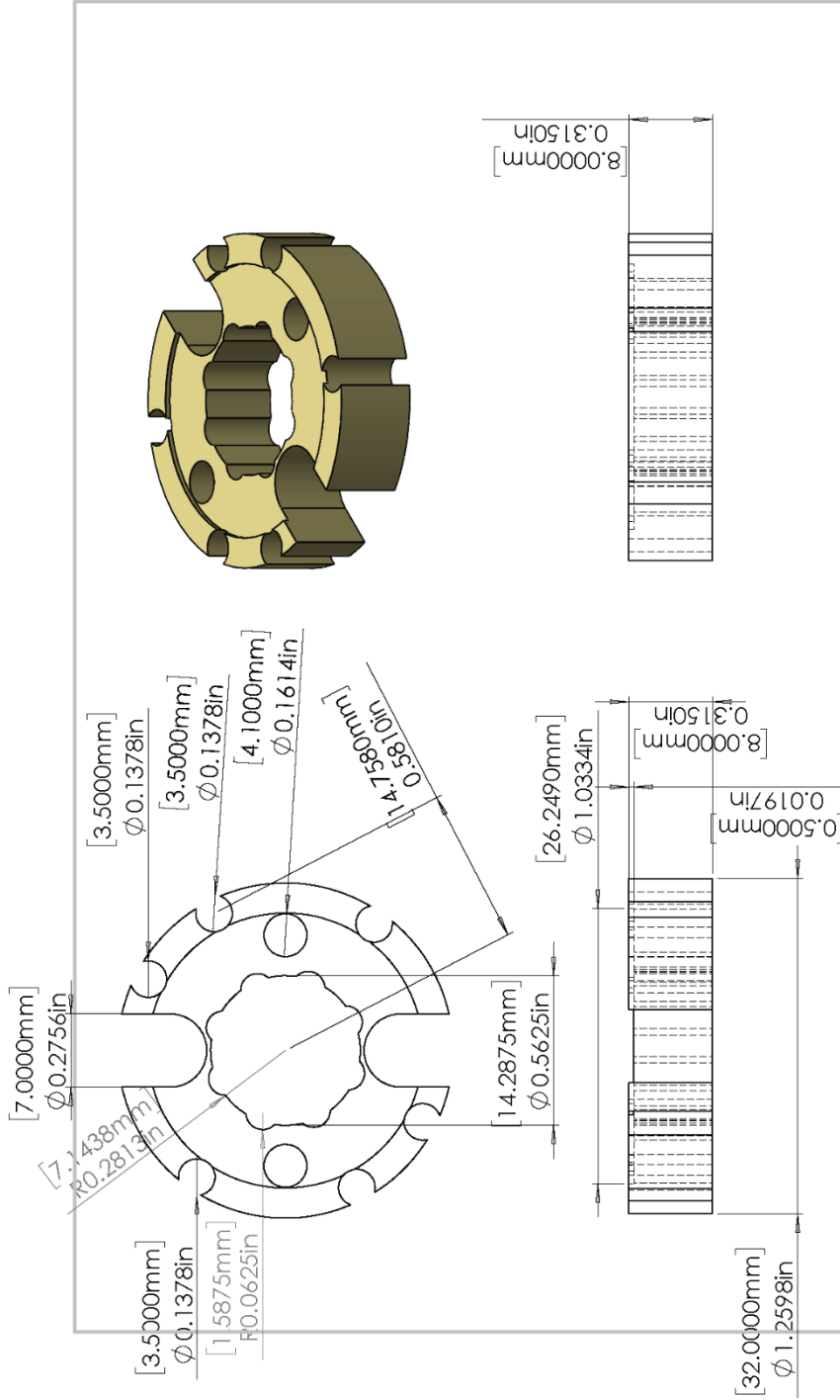
PROPRIETARY AND CONFIDENTIAL
 THE INFORMATION CONTAINED IN THIS
 DRAWING IS THE SOLE PROPERTY OF
 RUSSELL RESEARCH GROUP. ANY
 REPRODUCTION IN PART OR AS A WHOLE
 WITHOUT THE WRITTEN PERMISSION OF
 TEXAS A&M UNIVERSITY IS
 PROHIBITED.




DO NOT SCALE DRAWING

SHEET 1 OF 1





PROPRIETARY AND CONFIDENTIAL
 THE INFORMATION CONTAINED IN THIS DRAWING IS THE SOLE PROPERTY OF RUSSELL RESEARCH GROUP. ANY REPRODUCTION IN PART OR AS A WHOLE WITHOUT THE WRITTEN PERMISSION OF TEXAS A&M UNIVERSITY IS PROHIBITED.

nMS-SB  **ATM**®

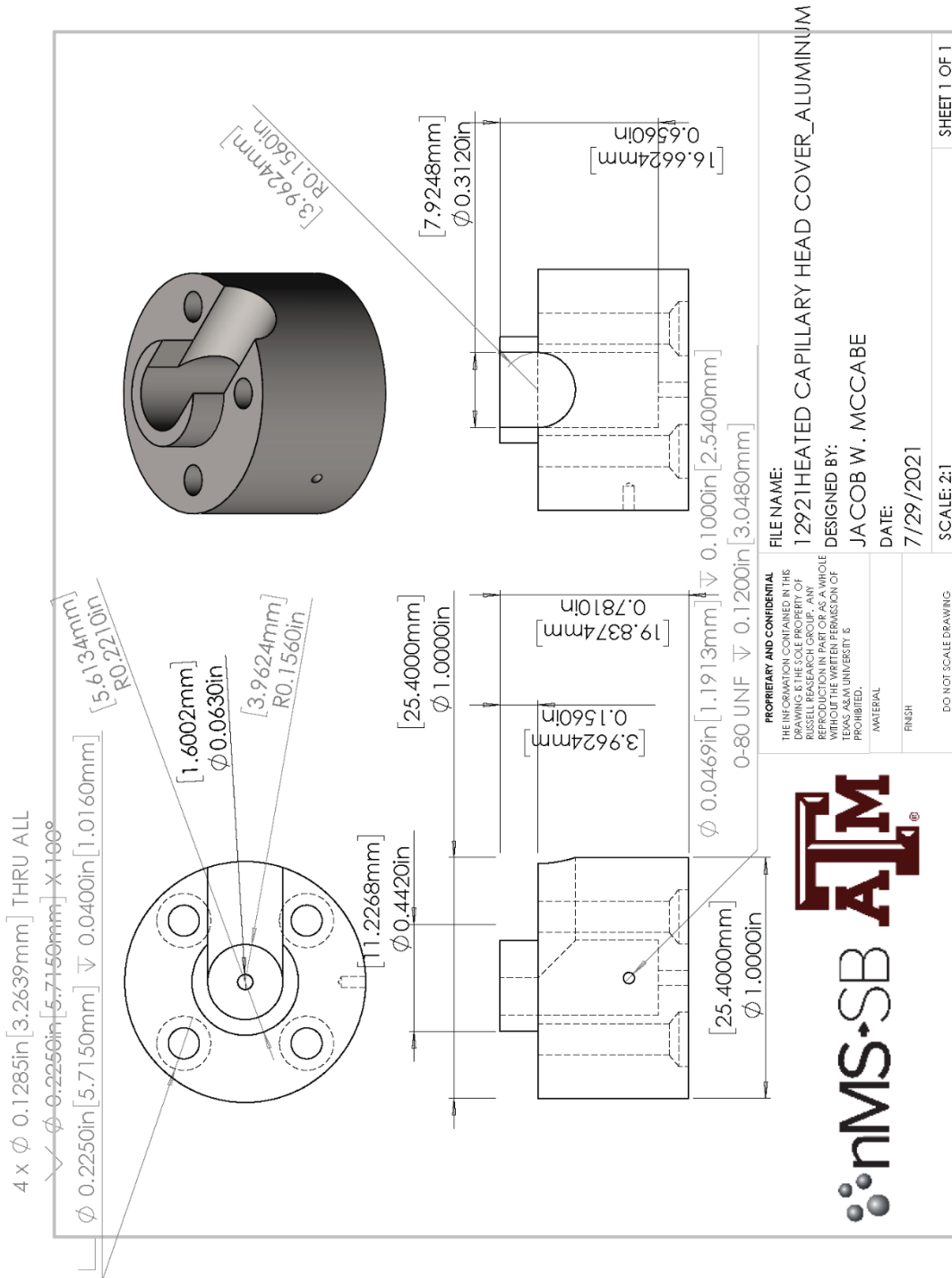
FILE NAME: 12921HCD CELL ENDCAP MOUNT_OCTAPOLE MOUNT_
DESIGNED BY: JACOB W. MCCABE
DATE: 7/29/2021

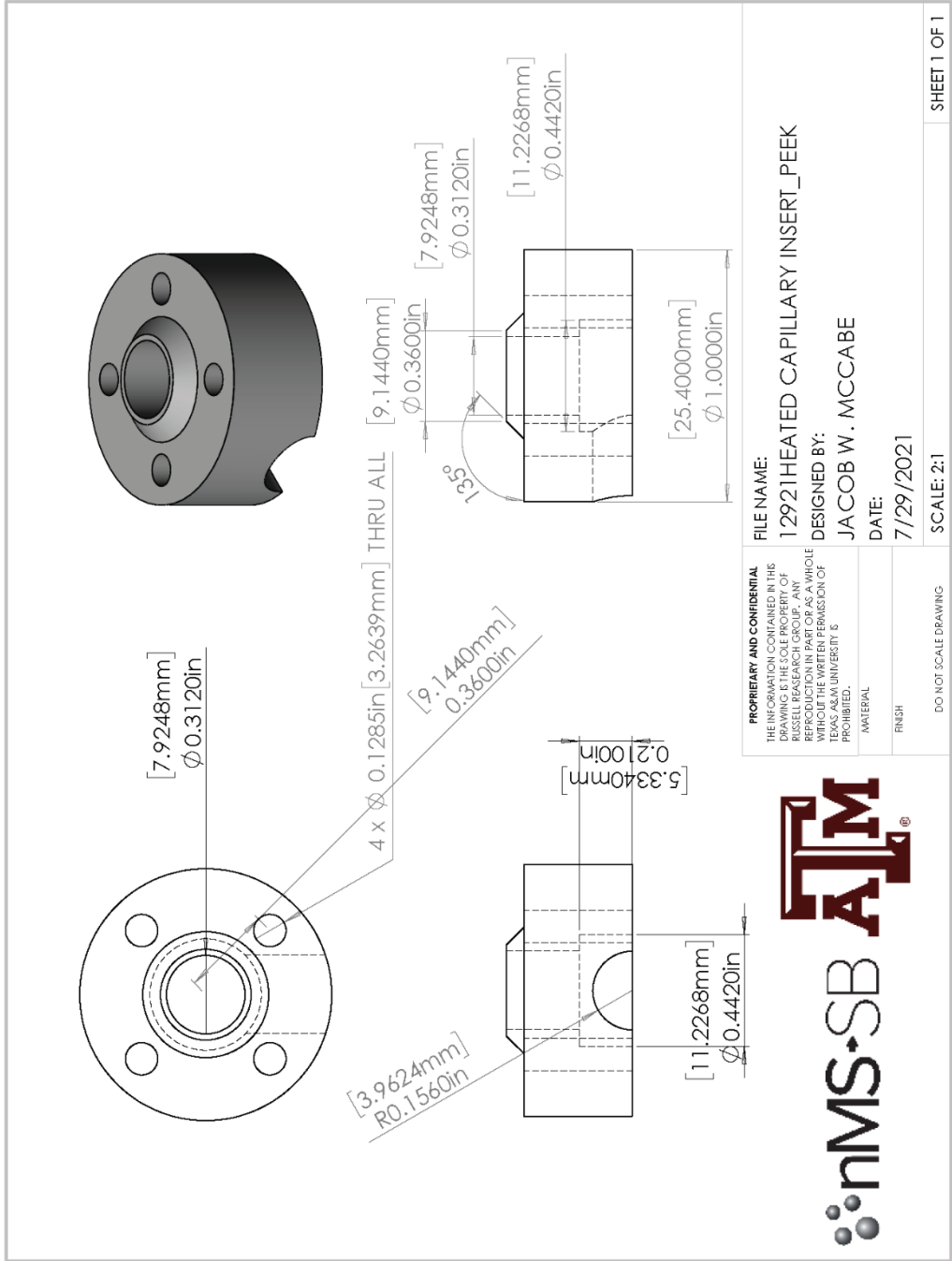
MATERIAL:
FINISH:
DO NOT SCALE DRAWING

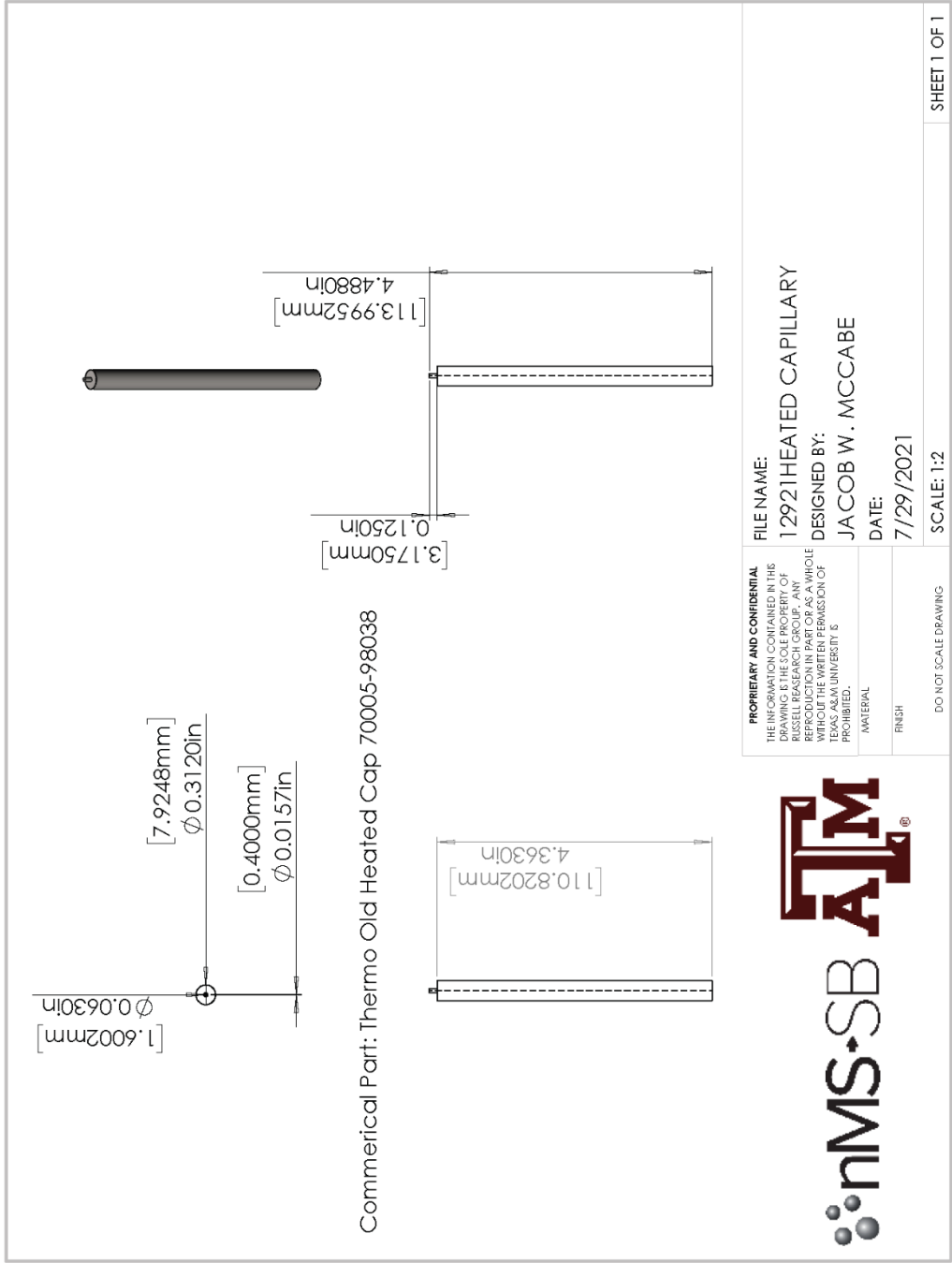
SCALE: 2:1

SHEET 1 OF 1

SOLIDWORKS Educational Product. For Instructional Use Only.







PROPRIETARY AND CONFIDENTIAL
 THE INFORMATION CONTAINED IN THIS
 DRAWING IS THE SOLE PROPERTY OF
 RUSSELL RESEARCH GROUP. ANY
 REPRODUCTION IN PART OR AS A WHOLE
 WITHOUT THE WRITTEN PERMISSION OF
 TEXAS A&M UNIVERSITY IS
 PROHIBITED.

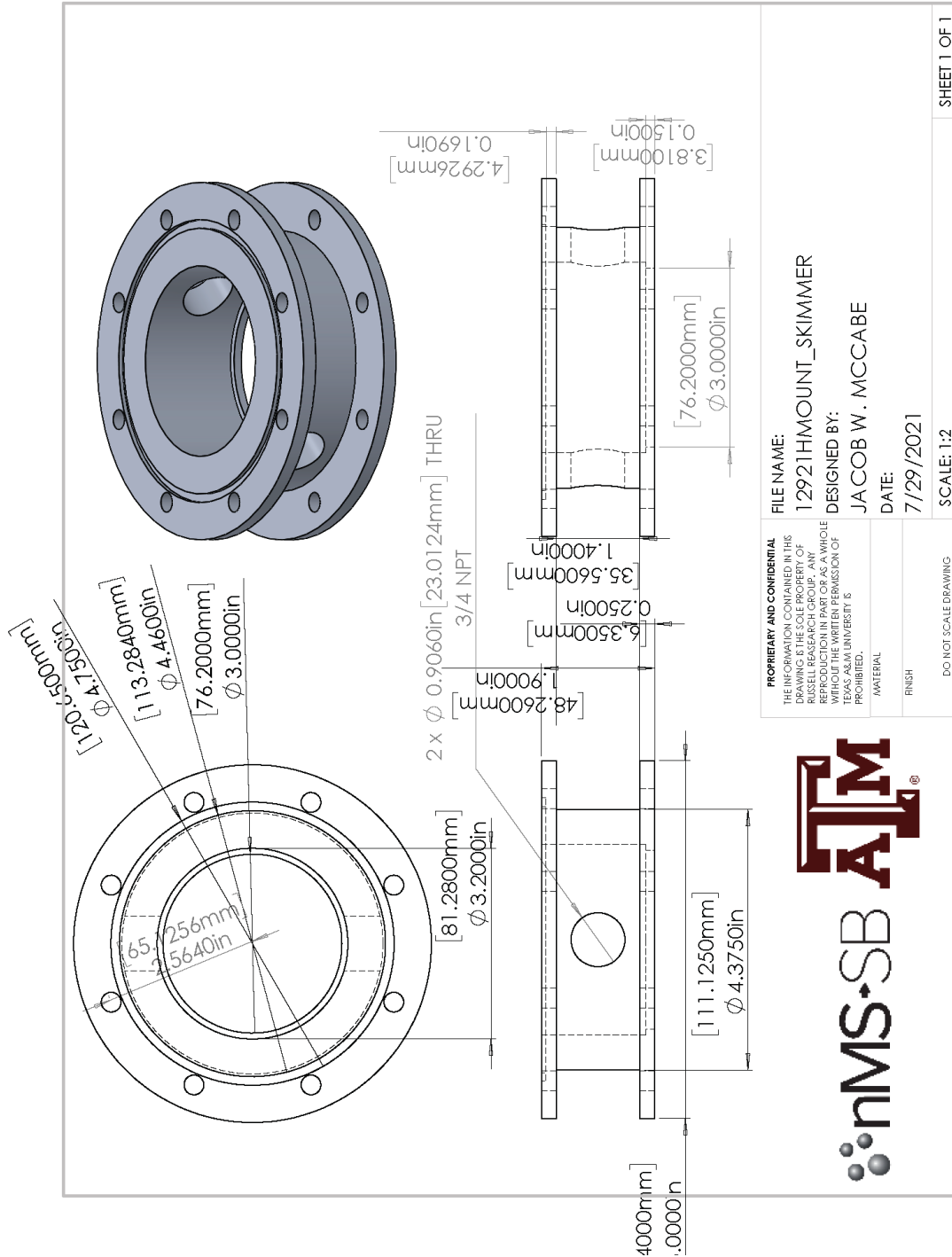


FILE NAME:
 12921HEATED CAPILLARY
DESIGNED BY:
 JACOB W. MCCABE
DATE:
 7/29/2021

MATERIAL:
FINISH:
 DO NOT SCALE DRAWING

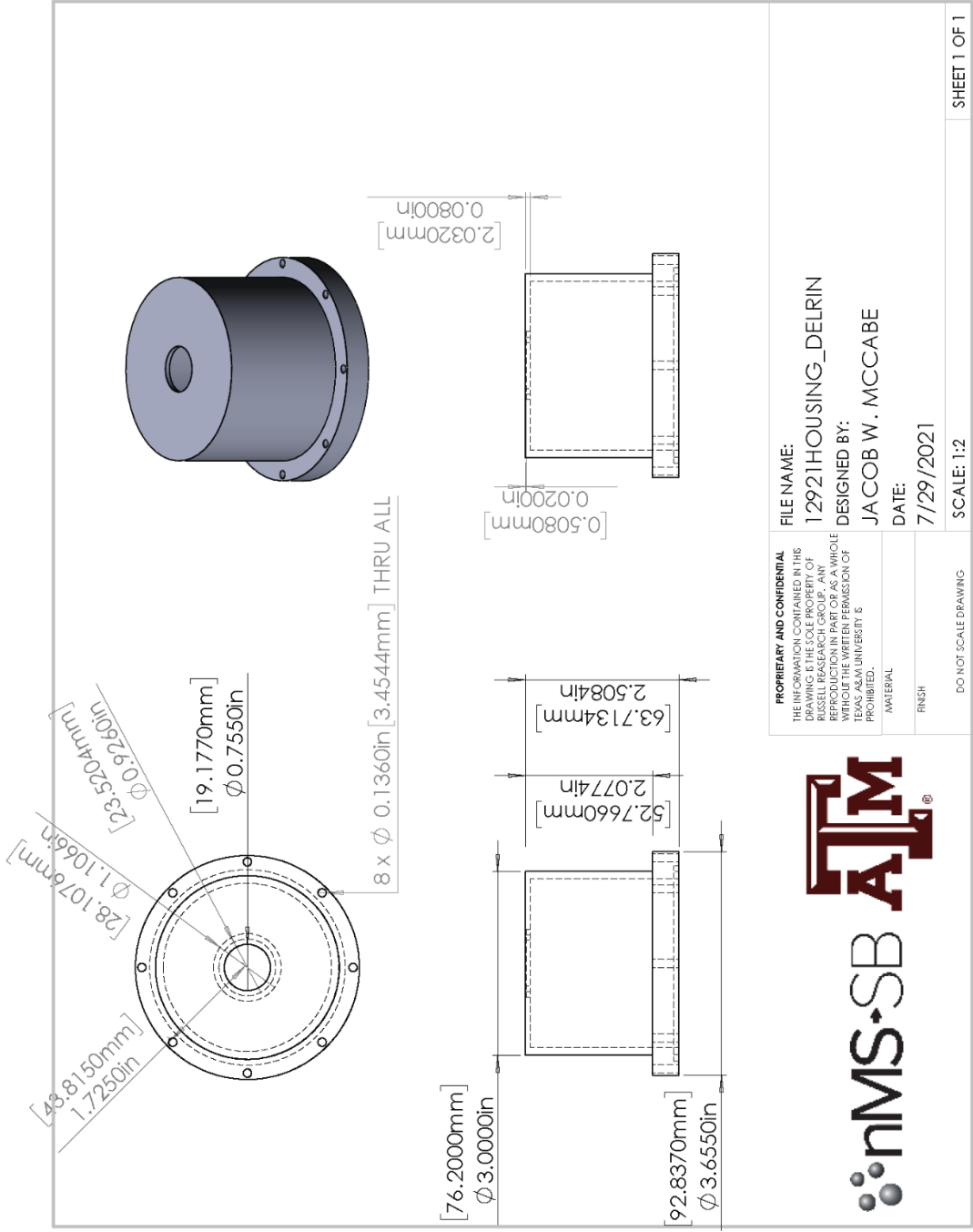
SHEET 1 OF 1

SOLIDWORKS Educational Product. For Instructional Use Only.



SHEET 1 OF 1

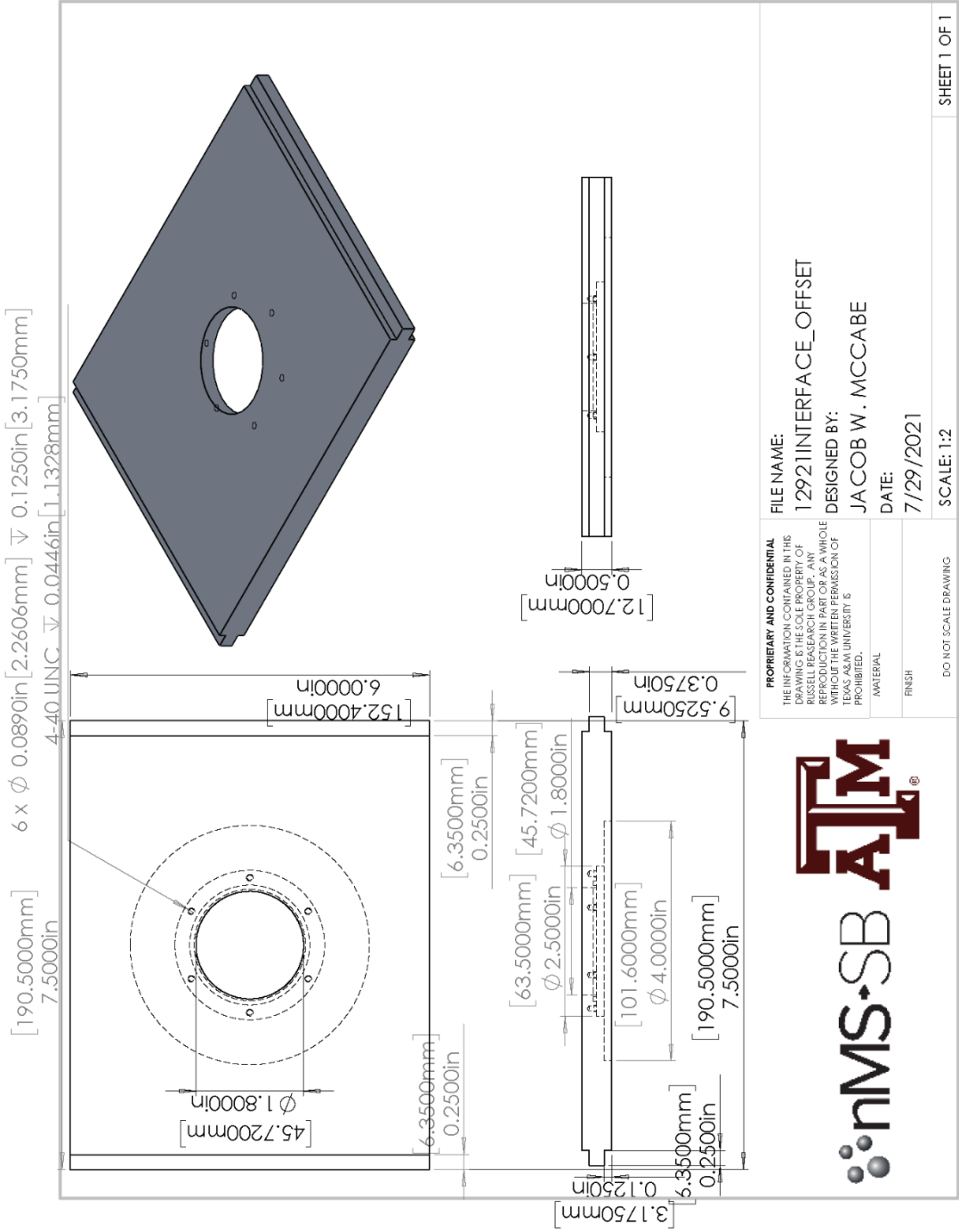
SOLIDWORKS Educational Product. For Instructional Use Only.



PROPRIETARY AND CONFIDENTIAL		FILE NAME:	12921HOUSING_DELRIN
THE INFORMATION CONTAINED IN THIS DRAWING IS THE SOLE PROPERTY OF RUSSELL RESEARCH GROUP. ANY REPRODUCTION IN PART OR AS A WHOLE WITHOUT THE WRITTEN PERMISSION OF TEXAS A&M UNIVERSITY IS PROHIBITED.		DESIGNED BY:	JACOB W. MCCABE
MATERIAL		DATE:	7/29/2021
FINISH		SCALE:	1:2
DO NOT SCALE DRAWING			SHEET 1 OF 1



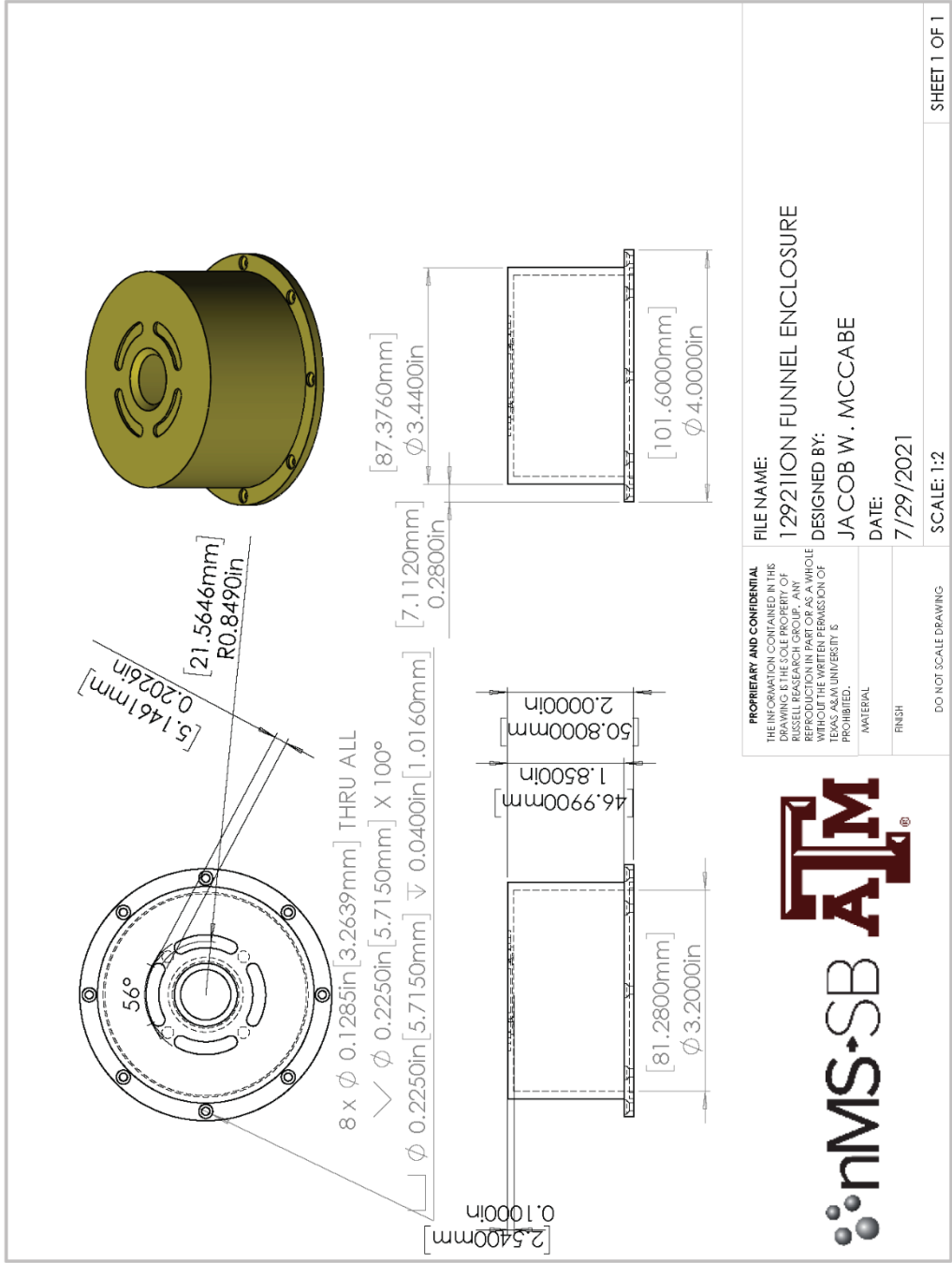
SOLIDWORKS Educational Product. For Instructional Use Only.



PROPRIETARY AND CONFIDENTIAL THE INFORMATION CONTAINED IN THIS DRAWING IS THE SOLE PROPERTY OF RUSSELL RESEARCH GROUP. ANY REPRODUCTION IN PART OR AS A WHOLE WITHOUT THE WRITTEN PERMISSION OF TEXAS A&M UNIVERSITY IS PROHIBITED.	FILE NAME: 12921INTERFACE_OFFSET
	DESIGNED BY: JACOB W. MCCABE
MATERIAL:	DATE: 7/29/2021
FINISH:	SCALE: 1:2
DO NOT SCALE DRAWING	
SHEET 1 OF 1	

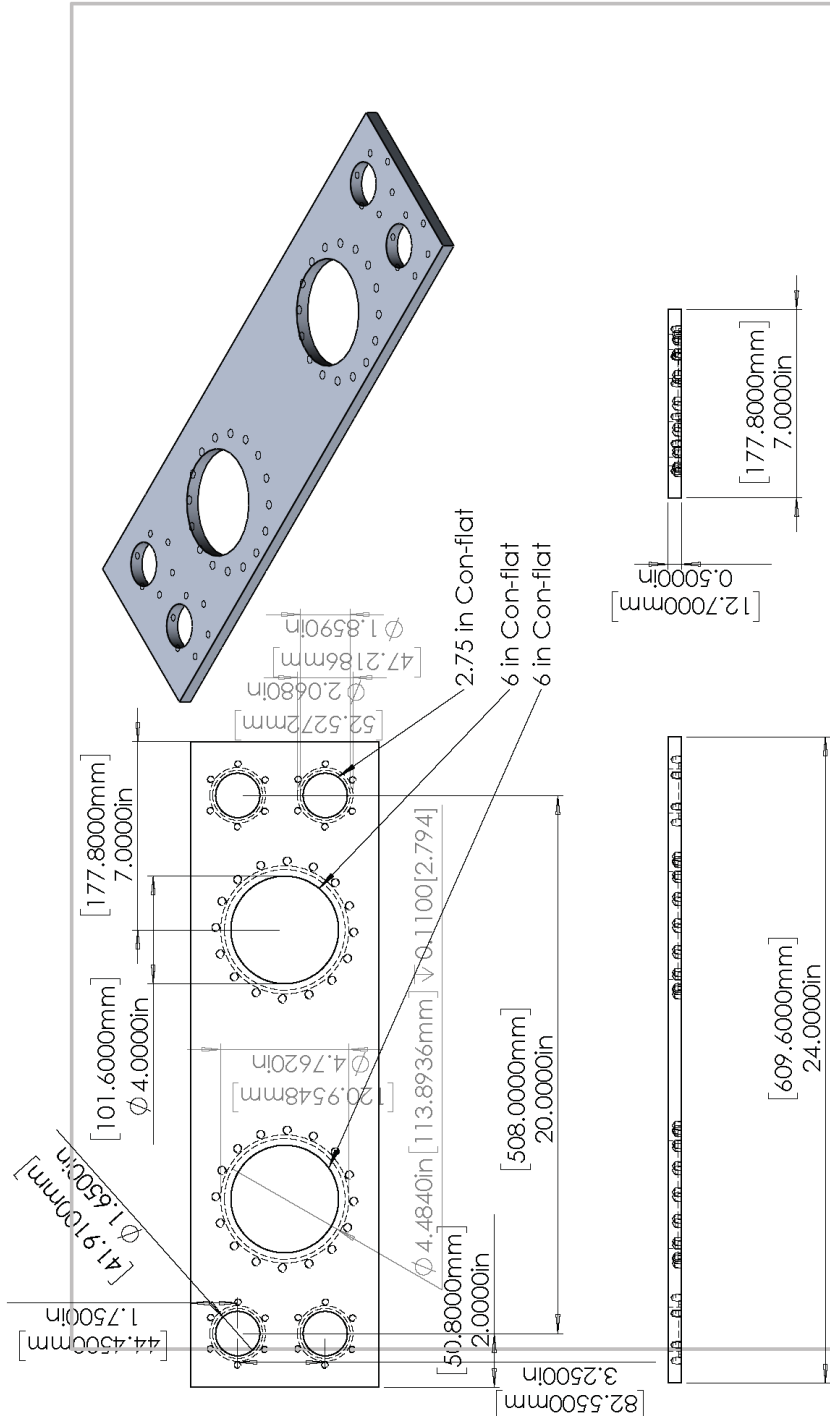


SOLIDWORKS Educational Product. For Instructional Use Only.



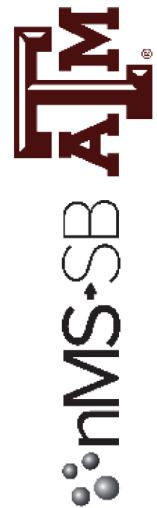
SHEET 1 OF 1

SOLIDWORKS Educational Product. For Instructional Use Only.

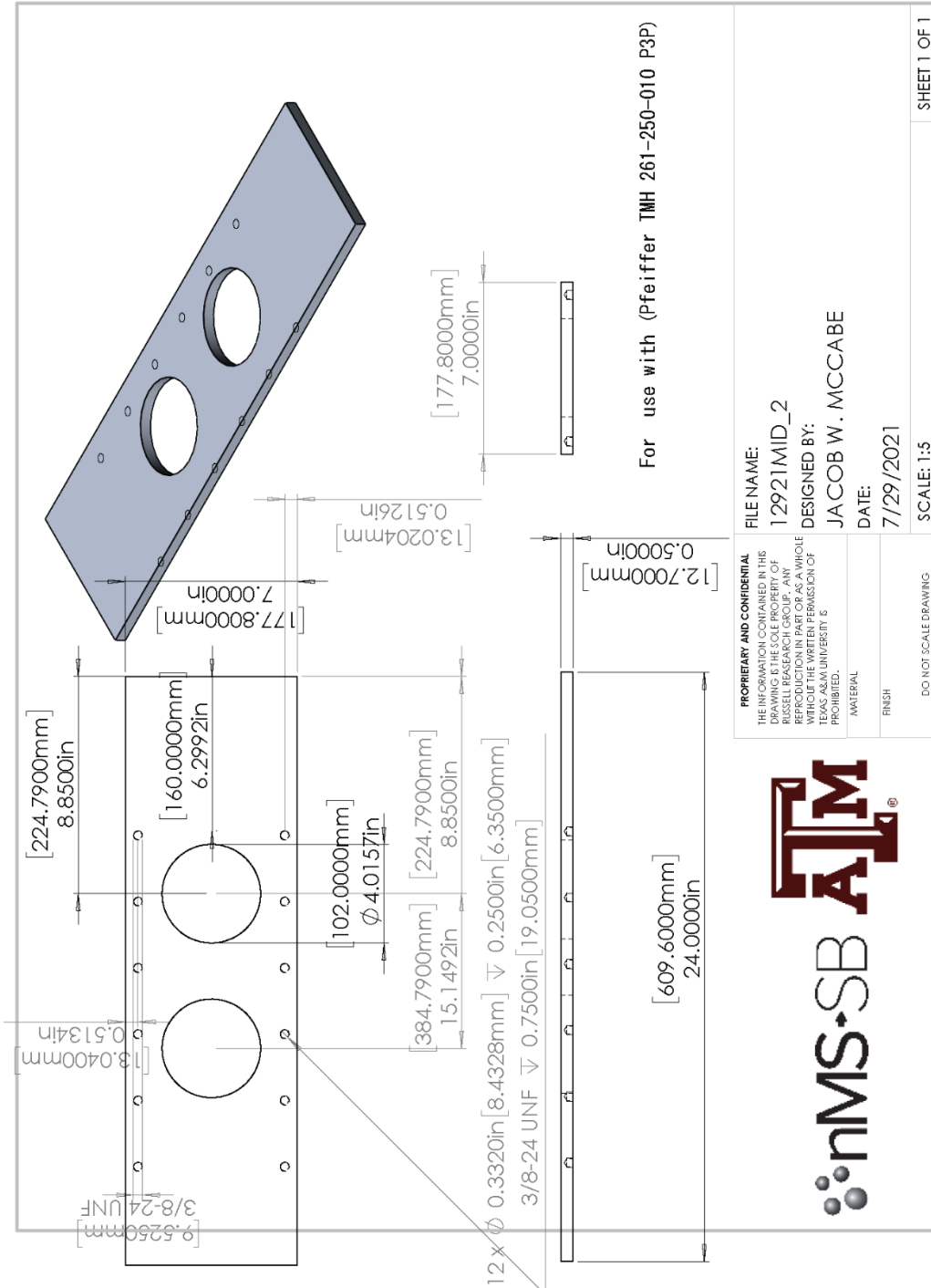


2.75 in Con-flat
 6 in Con-flat
 6 in Con-flat

PROPRIETARY AND CONFIDENTIAL THE INFORMATION CONTAINED IN THIS DRAWING IS THE SOLE PROPERTY OF RUSSELL RESEARCH GROUP. ANY REPRODUCTION IN PART OR AS A WHOLE WITHOUT THE WRITTEN PERMISSION OF TEXAS A&M UNIVERSITY IS PROHIBITED.		FILE NAME: 12921MID_1
MATERIAL		DESIGNED BY: JACOB W. MCCABE
FINISH		DATE: 7/29/2021
DO NOT SCALE DRAWING		SCALE: 1:5
		SHEET 1 OF 1



SOLIDWORKS Educational Product. For Instructional Use Only.



PROPRIETARY AND CONFIDENTIAL
 THE INFORMATION CONTAINED IN THIS
 DRAWING IS THE SOLE PROPERTY OF
 RUSSELL RESEARCH GROUP. ANY
 REPRODUCTION IN PART OR AS A WHOLE
 WITHOUT THE WRITTEN PERMISSION OF
 TEXAS A&M UNIVERSITY IS
 PROHIBITED.



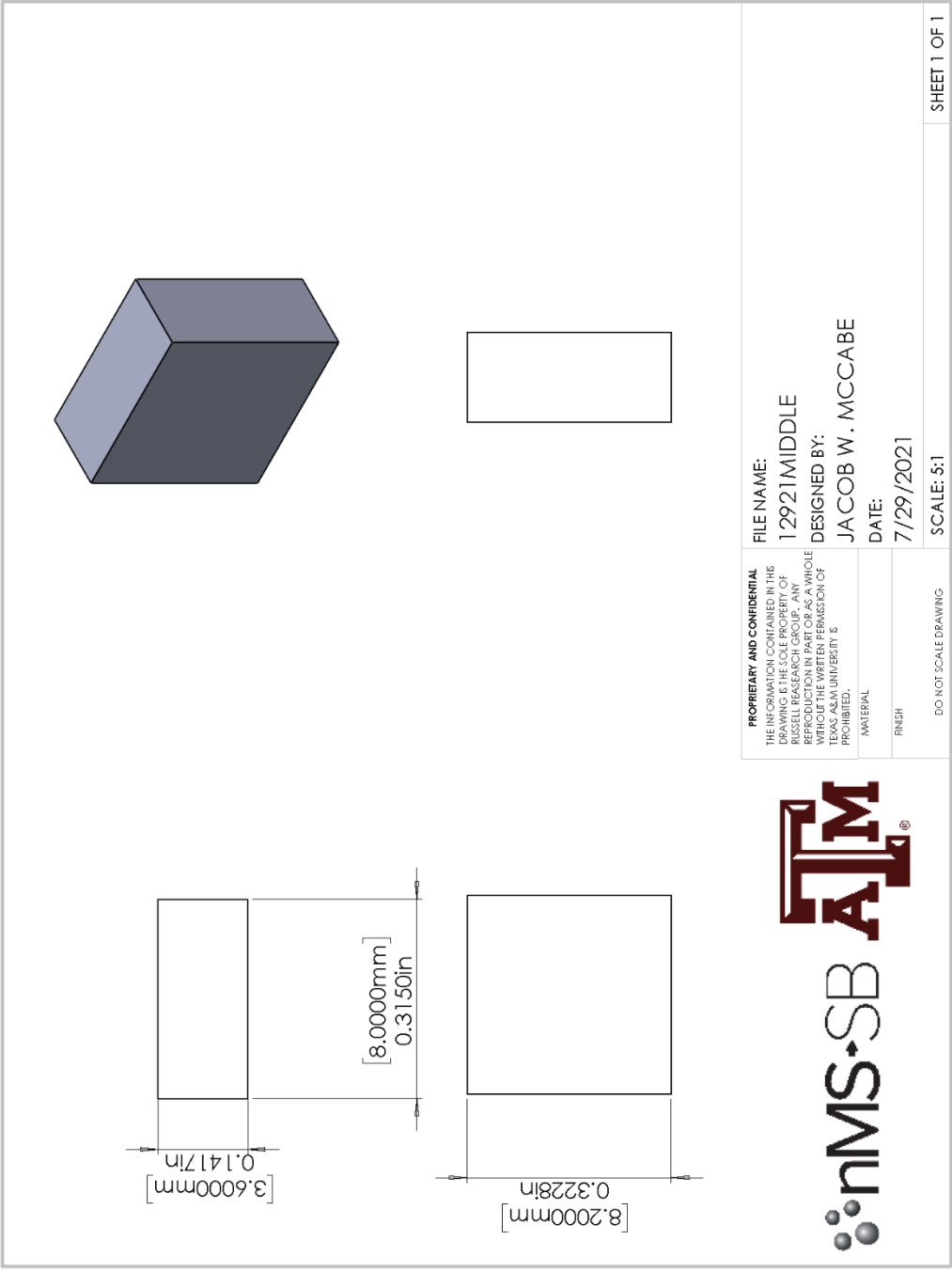
FILE NAME: 12921MID_2
 DESIGNED BY: JACOB W. MCCABE
 DATE: 7/29/2021

For use with Pfeiffer TMH 261-250-010 P3P

MATERIAL:
 FINISH:
 DO NOT SCALE DRAWING

SHEET 1 OF 1

SOLIDWORKS Educational Product. For Instructional Use Only.



PROPRIETARY AND CONFIDENTIAL
 THE INFORMATION CONTAINED IN THIS DRAWING IS THE SOLE PROPERTY OF RUSSELL RESEARCH GROUP. ANY REPRODUCTION IN PART OR AS A WHOLE WITHOUT THE WRITTEN PERMISSION OF TEXAS A&M UNIVERSITY IS PROHIBITED.



FILE NAME:
12921MIDDLE

DESIGNED BY:
JACOB W. MCCABE

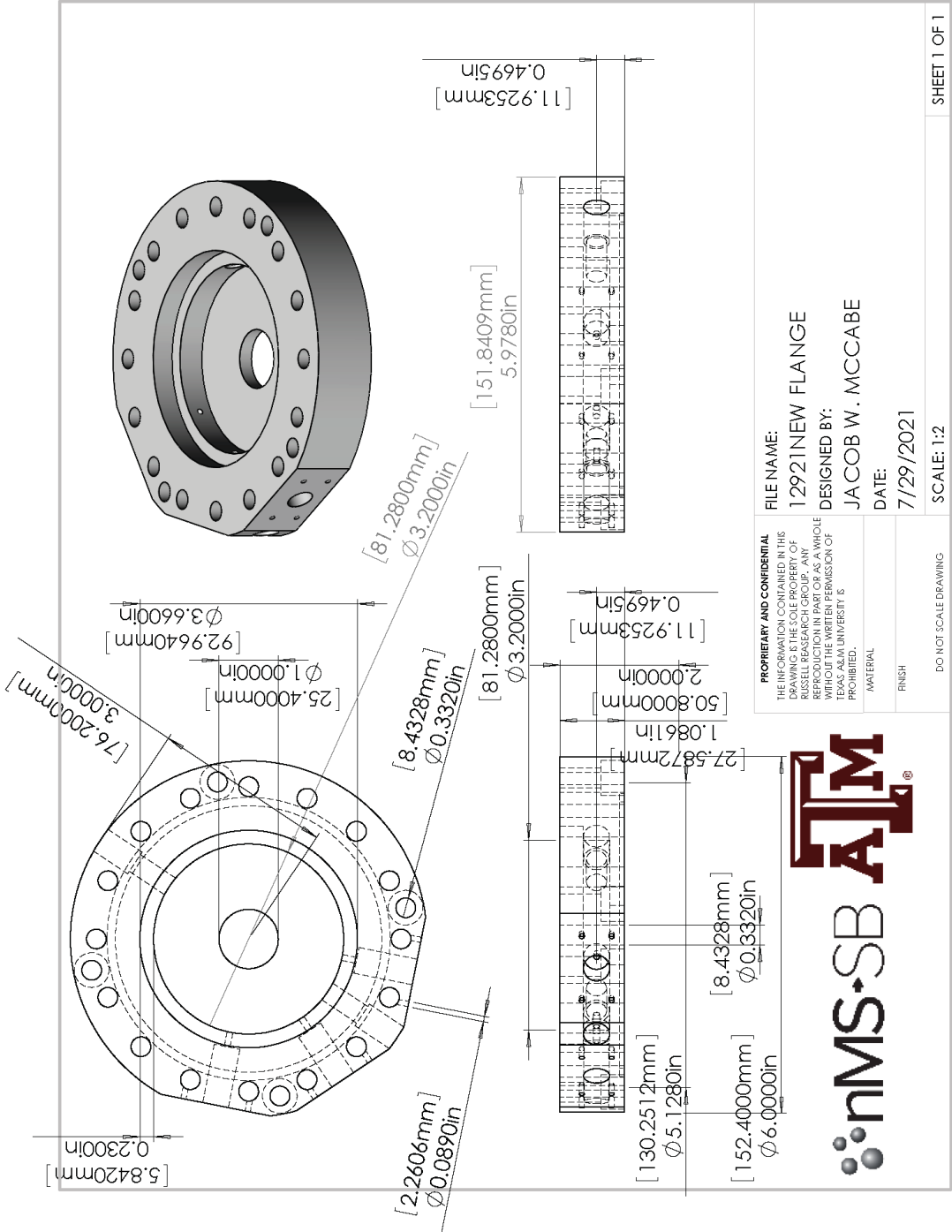
DATE:
7/29/2021

MATERIAL:
FINISH

SCALE: 5:1

DO NOT SCALE DRAWING

SHEET 1 OF 1



PROPRIETARY AND CONFIDENTIAL
 THE INFORMATION CONTAINED IN THIS DRAWING IS THE SOLE PROPERTY OF RUSSELL RESEARCH GROUP. ANY REPRODUCTION IN PART OR AS A WHOLE WITHOUT THE WRITTEN PERMISSION OF TEXAS A&M UNIVERSITY IS PROHIBITED.

nMS-SB **ATM**

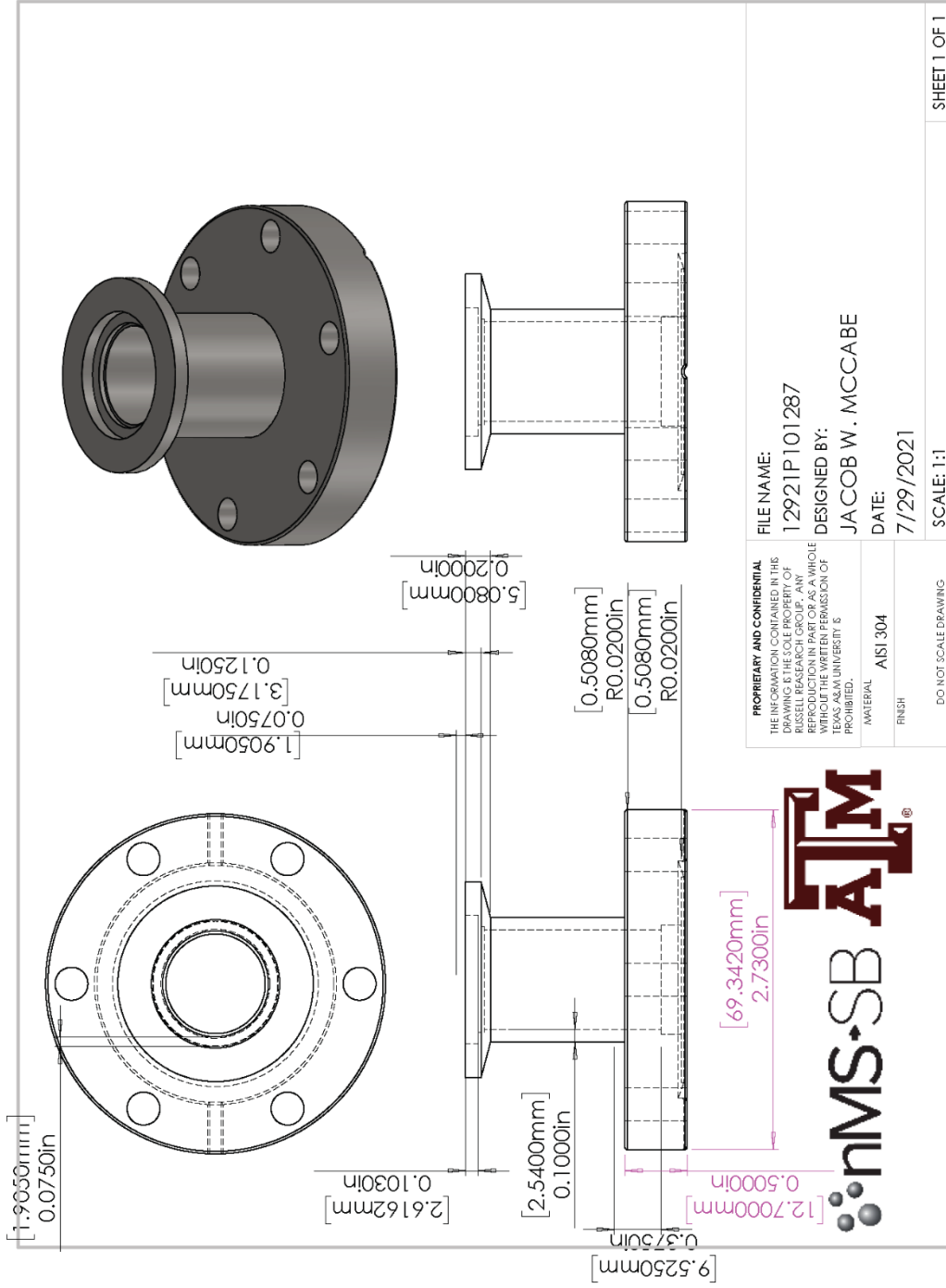
FILE NAME: 12921NEW FLANGE
DESIGNED BY: JACOB W. MCCABE
DATE: 7/29/2021

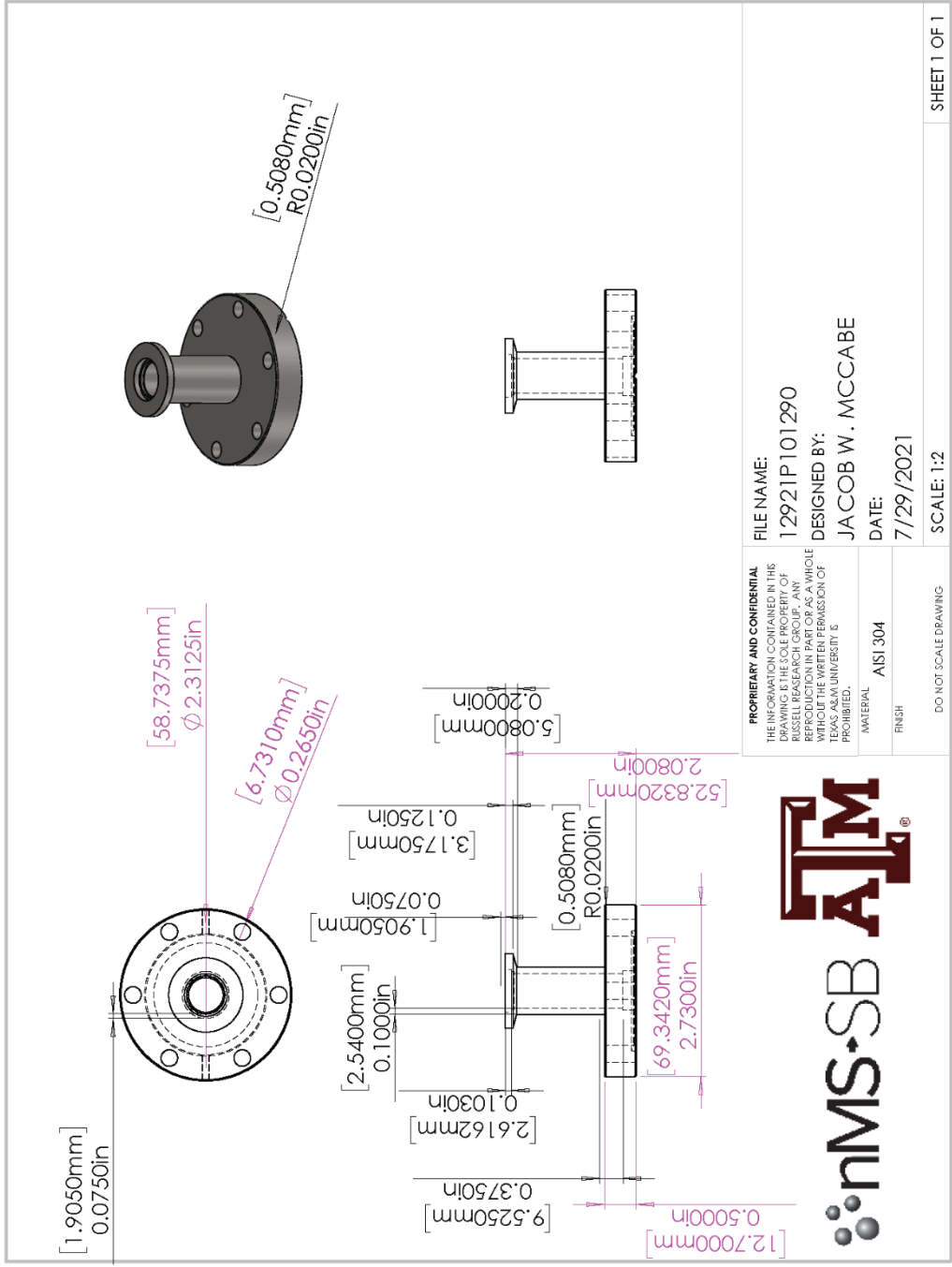
MATERIAL:
FINISH:

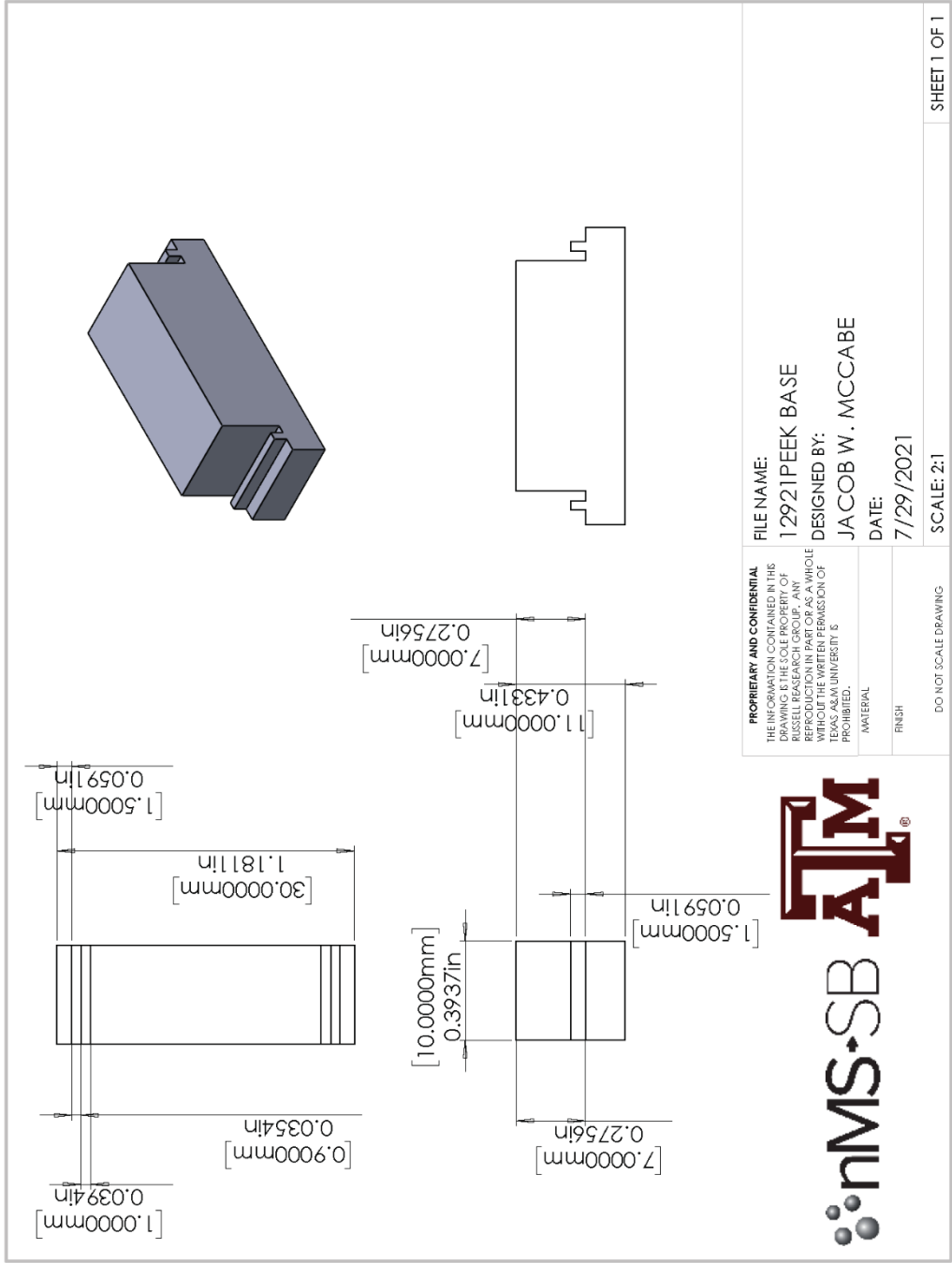
DO NOT SCALE DRAWING

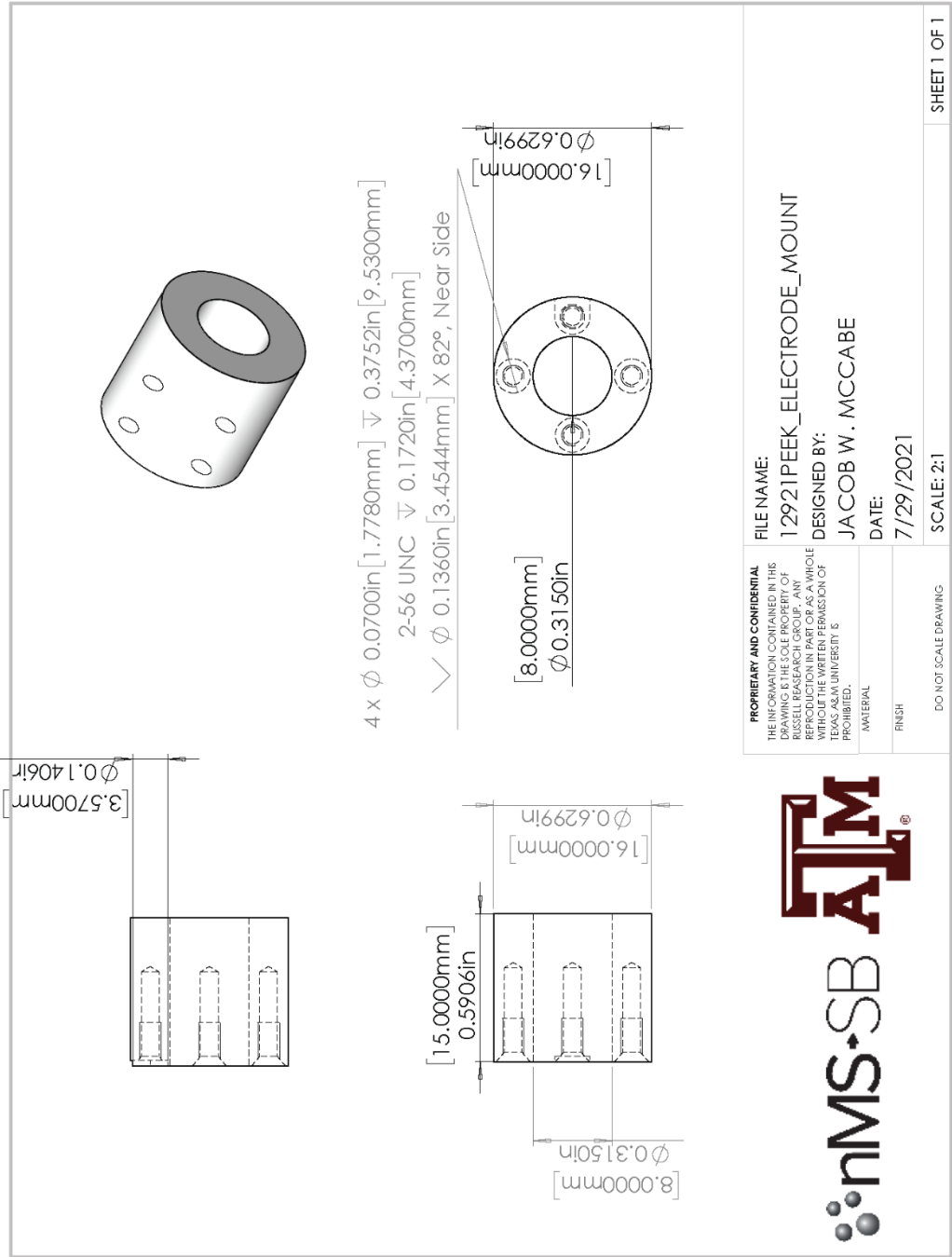
SCALE: 1:2

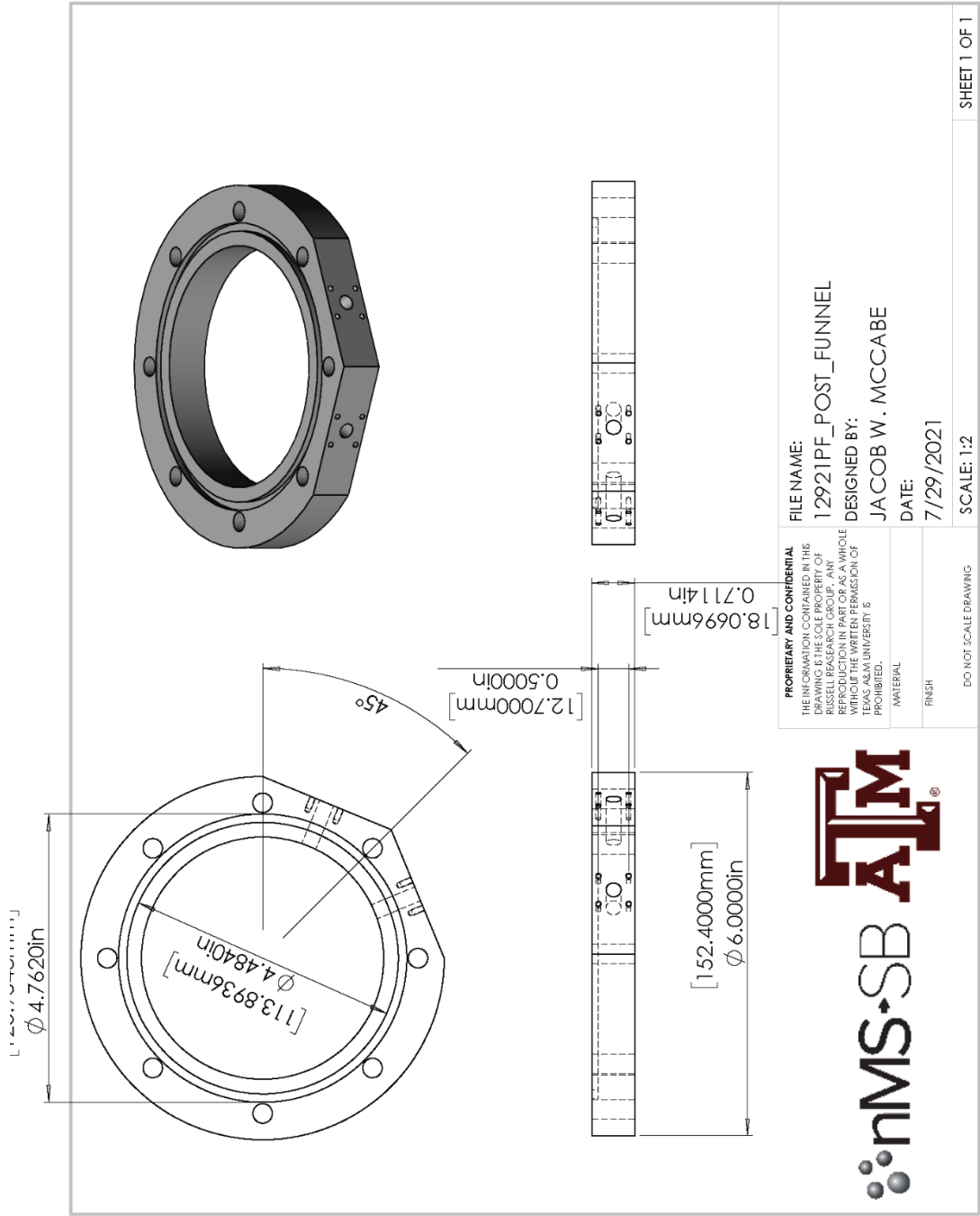
SHEET 1 OF 1











SHEET 1 OF 1



SOLIDWORKS Educational Product. For Instructional Use Only.

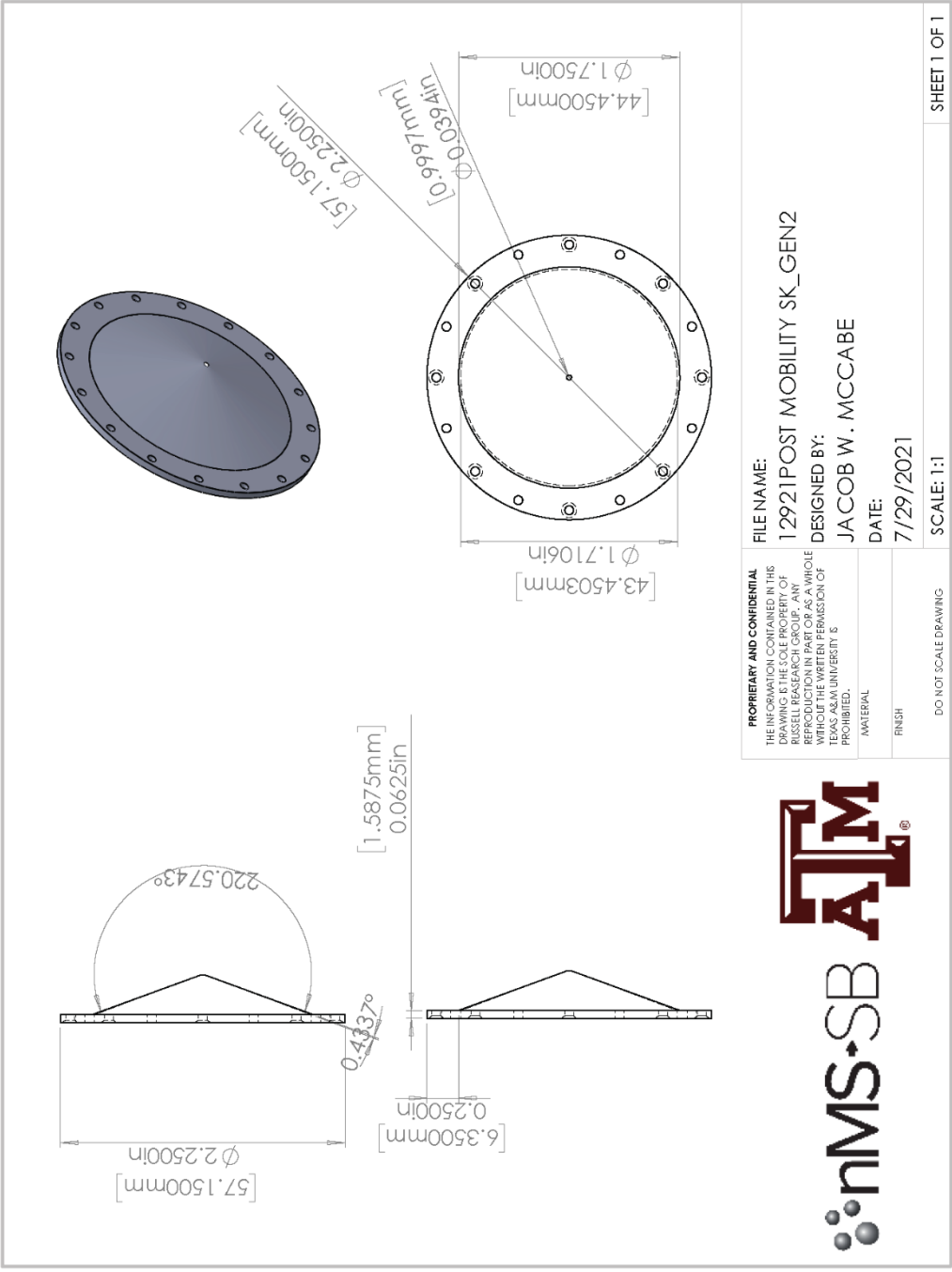


PROPRIETARY AND CONFIDENTIAL THE INFORMATION CONTAINED IN THIS DRAWING IS THE SOLE PROPERTY OF RUSSELL RESEARCH GROUP. ANY REPRODUCTION IN PART OR AS A WHOLE WITHOUT THE WRITTEN PERMISSION OF TEXAS A&M UNIVERSITY IS PROHIBITED.		FILE NAME: 12921PF_POST_FUNNEL_BIG
MATERIAL		DESIGNED BY: JACOB W. MCCABE
FINISH		DATE: 7/29/2021
DO NOT SCALE DRAWING		SCALE: 1:2
		SHEET 1 OF 1

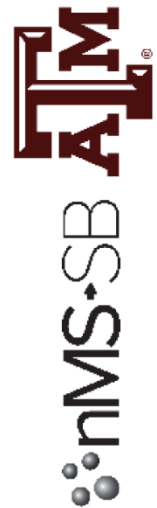


SOLIDWORKS Educational Product. For Instructional Use Only.

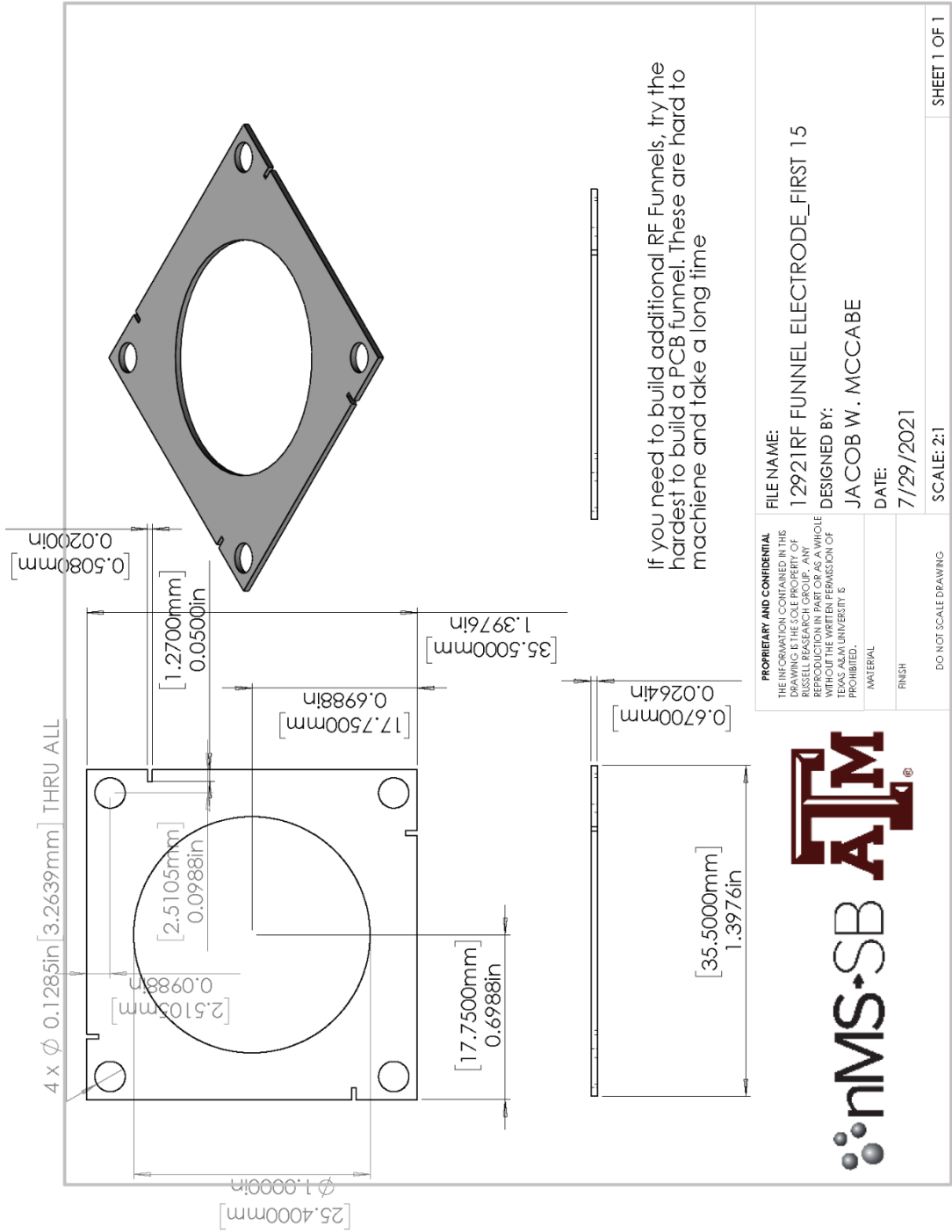




PROPRIETARY AND CONFIDENTIAL THE INFORMATION CONTAINED IN THIS DRAWING IS THE SOLE PROPERTY OF RUSSELL RESEARCH GROUP. ANY REPRODUCTION IN PART OR AS A WHOLE WITHOUT THE WRITTEN PERMISSION OF TEXAS A&M UNIVERSITY IS PROHIBITED.	MATERIAL
	FINISH
DO NOT SCALE DRAWING	
FILE NAME: 12921POST MOBILITY SK_GEN2 DESIGNED BY: JACOB W. MCCABE DATE: 7/29/2021	SCALE: 1:1 SHEET 1 OF 1



SOLIDWORKS Educational Product. For Instructional Use Only.

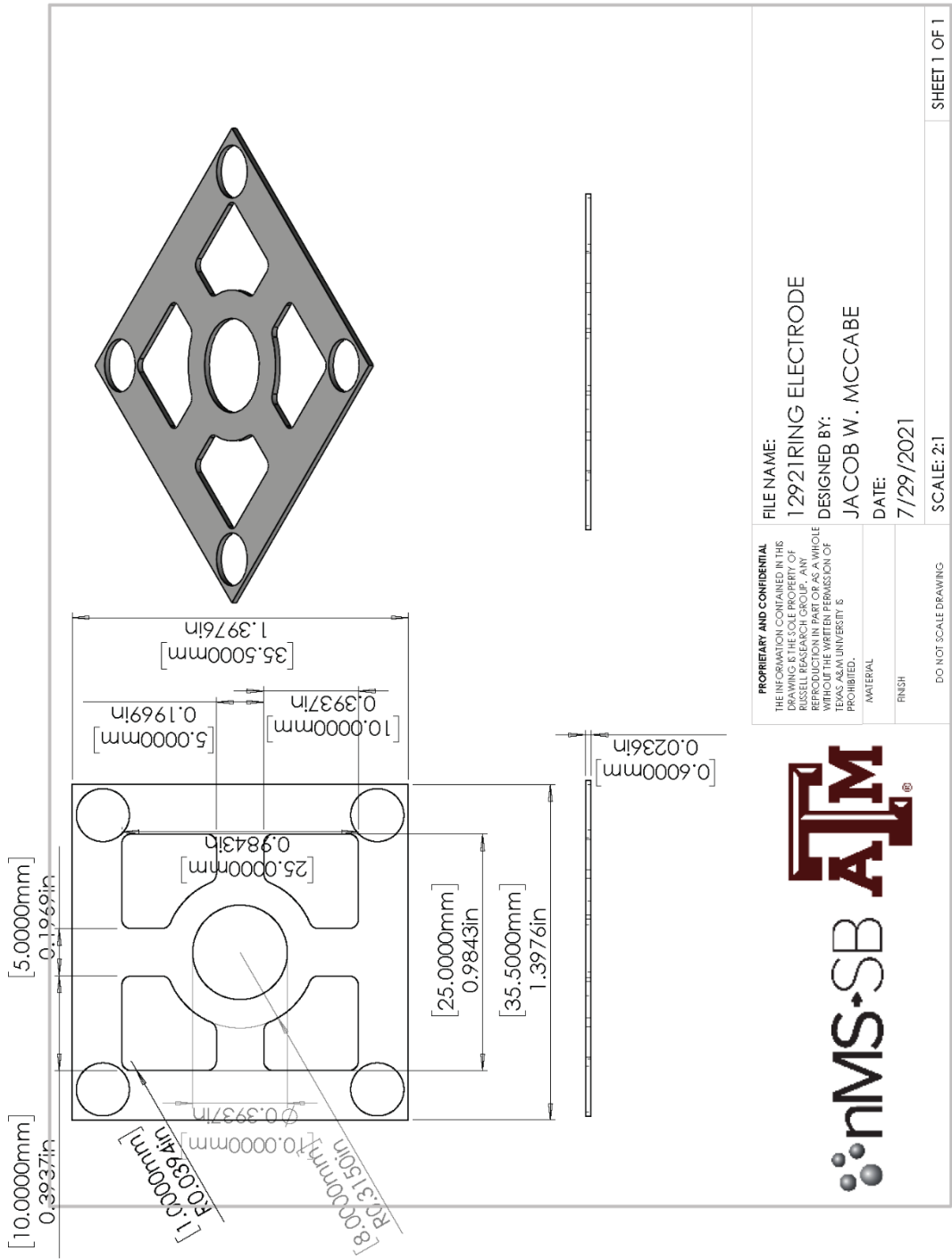


If you need to build additional RF Funnels, try the hardest to build a PCB funnel. These are hard to machine and take a long time

PROPRIETARY AND CONFIDENTIAL THE INFORMATION CONTAINED IN THIS DRAWING IS THE SOLE PROPERTY OF RUSSELL RESEARCH GROUP. ANY REPRODUCTION IN PART OR AS A WHOLE WITHOUT THE WRITTEN PERMISSION OF TEXAS A&M UNIVERSITY IS PROHIBITED.		FILE NAME: 12921RF FUNNEL ELECTRODE_FIRST 15
MATERIAL		DESIGNED BY: JACOB W. MCCABE
FINISH		DATE: 7/29/2021
DO NOT SCALE DRAWING		SCALE: 2:1
		SHEET 1 OF 1



SOLIDWORKS Educational Product. For Instructional Use Only.



PROPRIETARY AND CONFIDENTIAL
 THE INFORMATION CONTAINED IN THIS
 DRAWING IS THE SOLE PROPERTY OF
 RUSSELL RESEARCH GROUP. ANY
 REPRODUCTION IN PART OR AS A WHOLE
 WITHOUT THE WRITTEN PERMISSION OF
 TEXAS A&M UNIVERSITY IS
 PROHIBITED.



FILE NAME:
 12921RING ELECTRODE

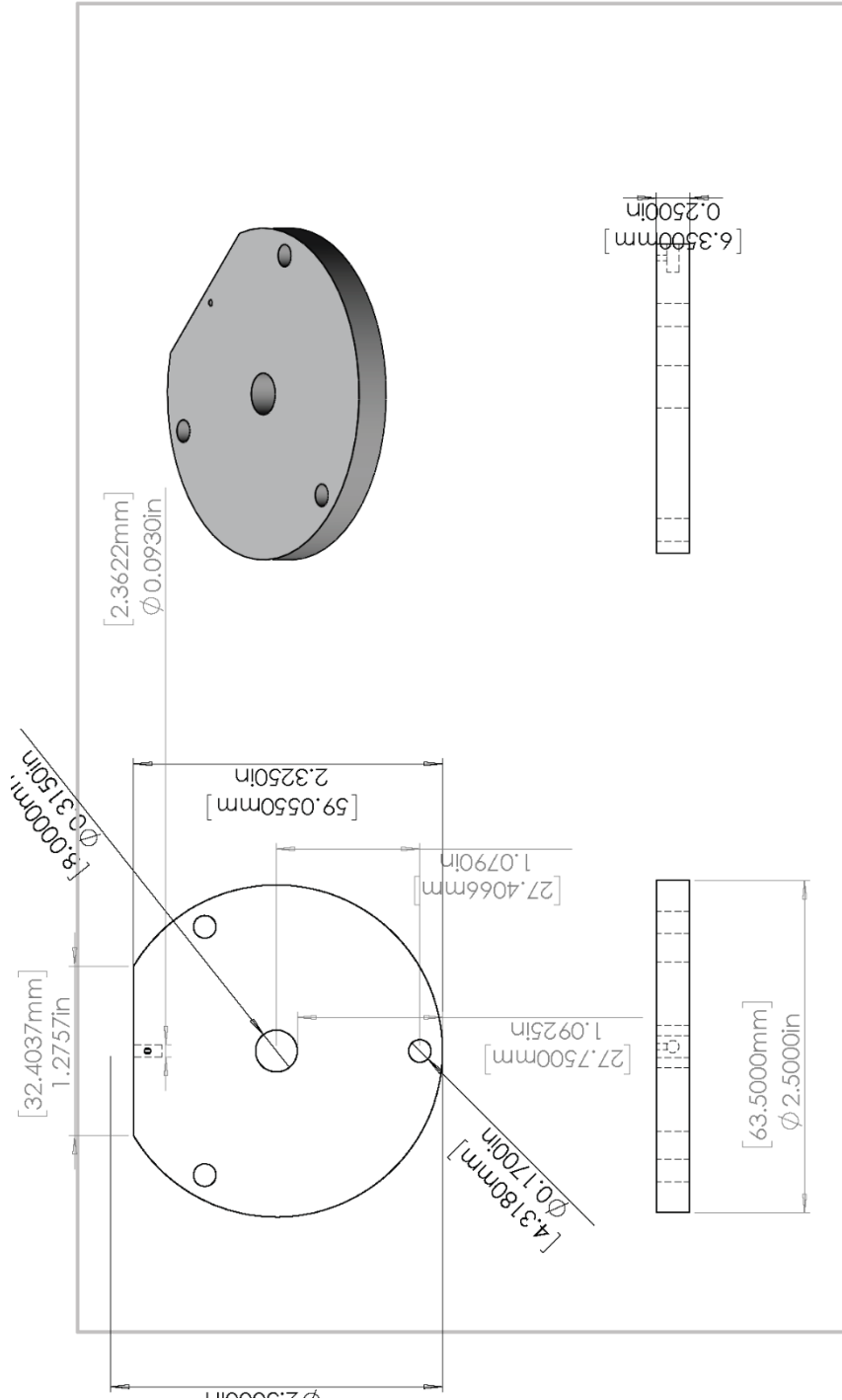
DESIGNED BY:
 JACOB W. MCCABE

DATE:
 7/29/2021

SCALE: 2:1

SHEET 1 OF 1

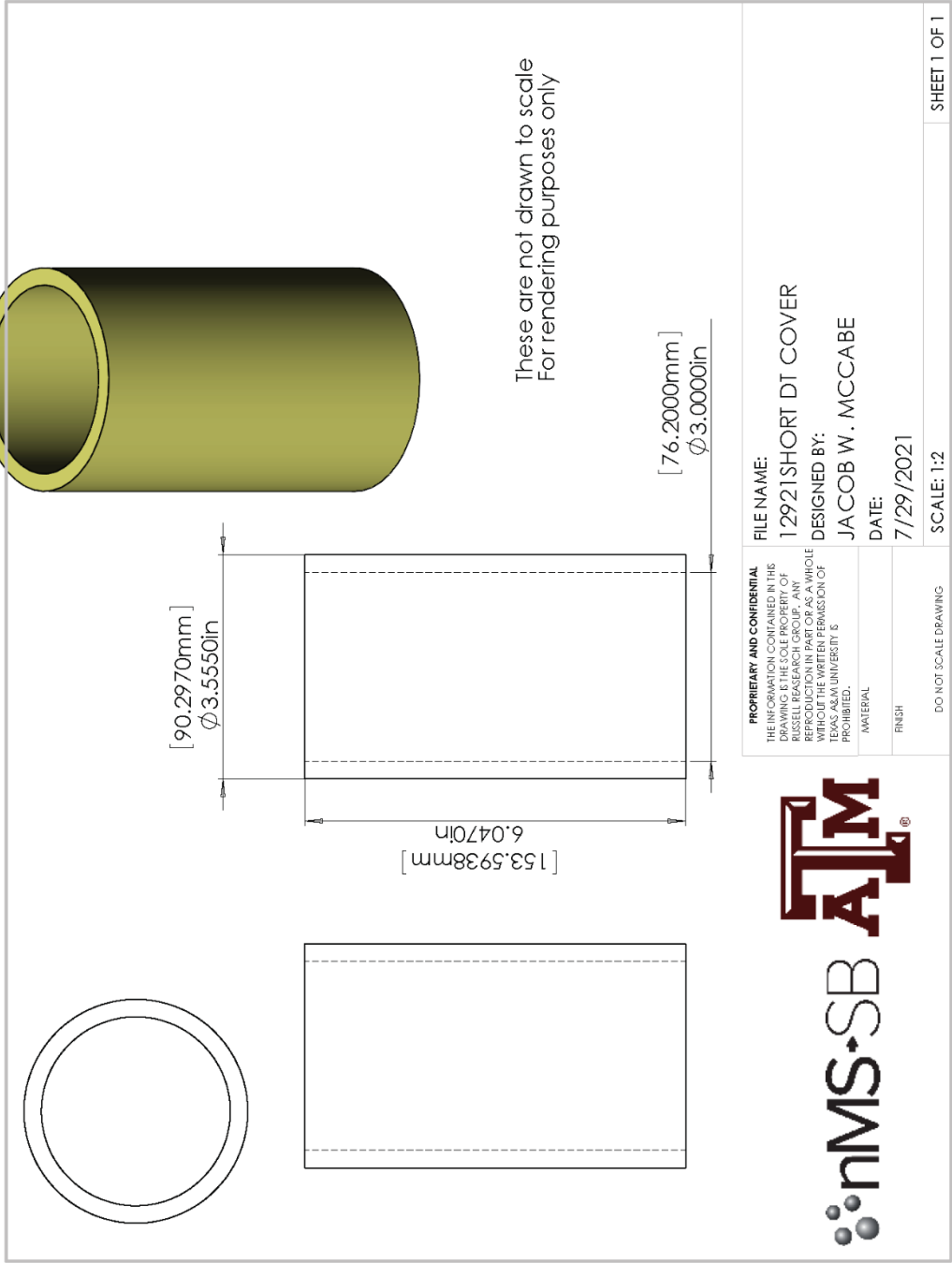
DO NOT SCALE DRAWING

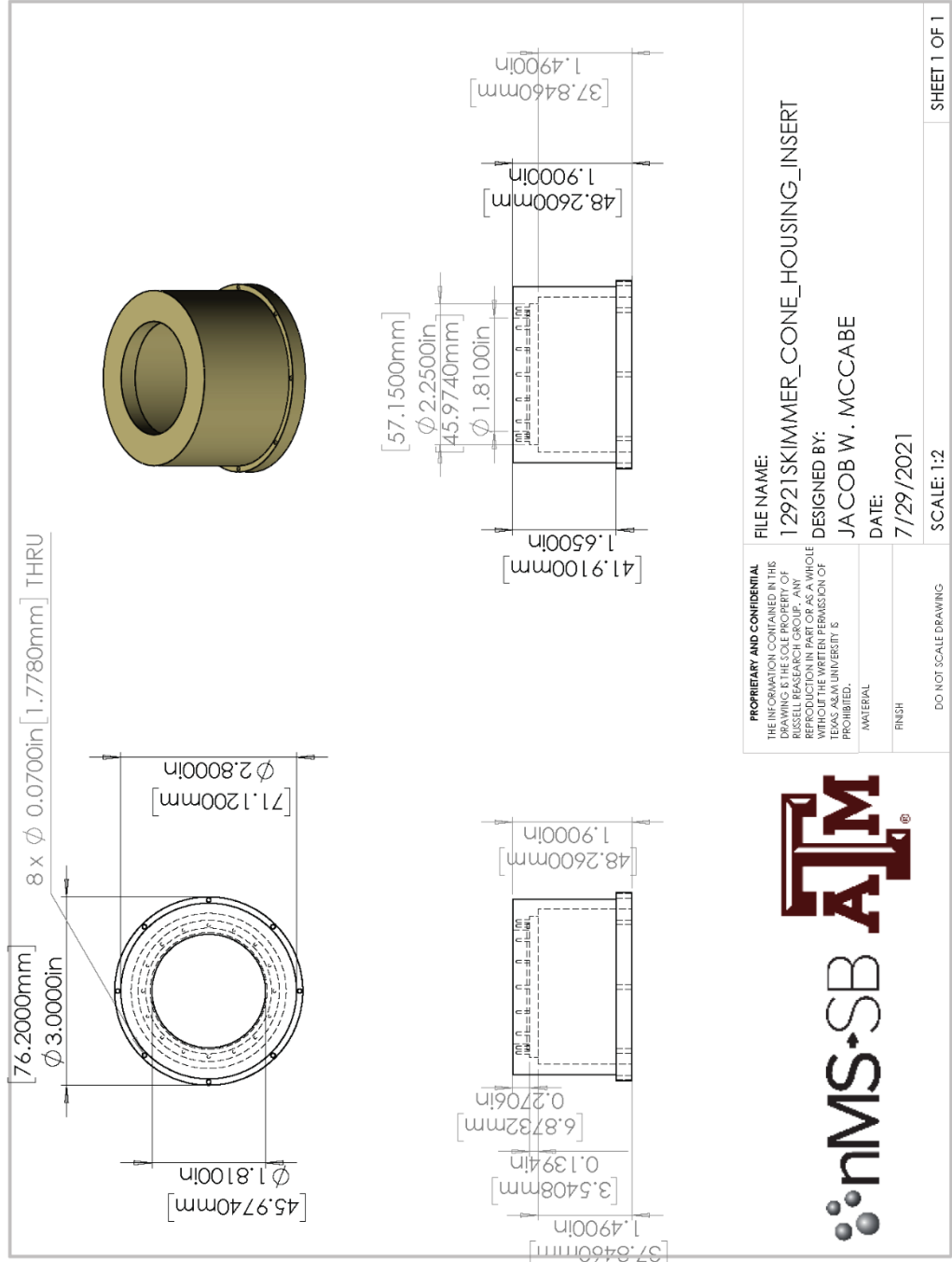


PROPRIETARY AND CONFIDENTIAL		FILE NAME:
THE INFORMATION CONTAINED IN THIS DRAWING IS THE SOLE PROPERTY OF RUSSELL RESEARCH GROUP. ANY REPRODUCTION IN PART OR AS A WHOLE WITHOUT THE WRITTEN PERMISSION OF TEXAS A&M UNIVERSITY IS PROHIBITED.		12921RYAN'S DRIFT TUBE ELECTRODE
MATERIAL		DESIGNED BY:
FINISH		JACOB W. MCCABE
DO NOT SCALE DRAWING		DATE:
		7/29/2021
		SCALE: 1:1
		SHEET 1 OF 1



SOLIDWORKS Educational Product. For Instructional Use Only.



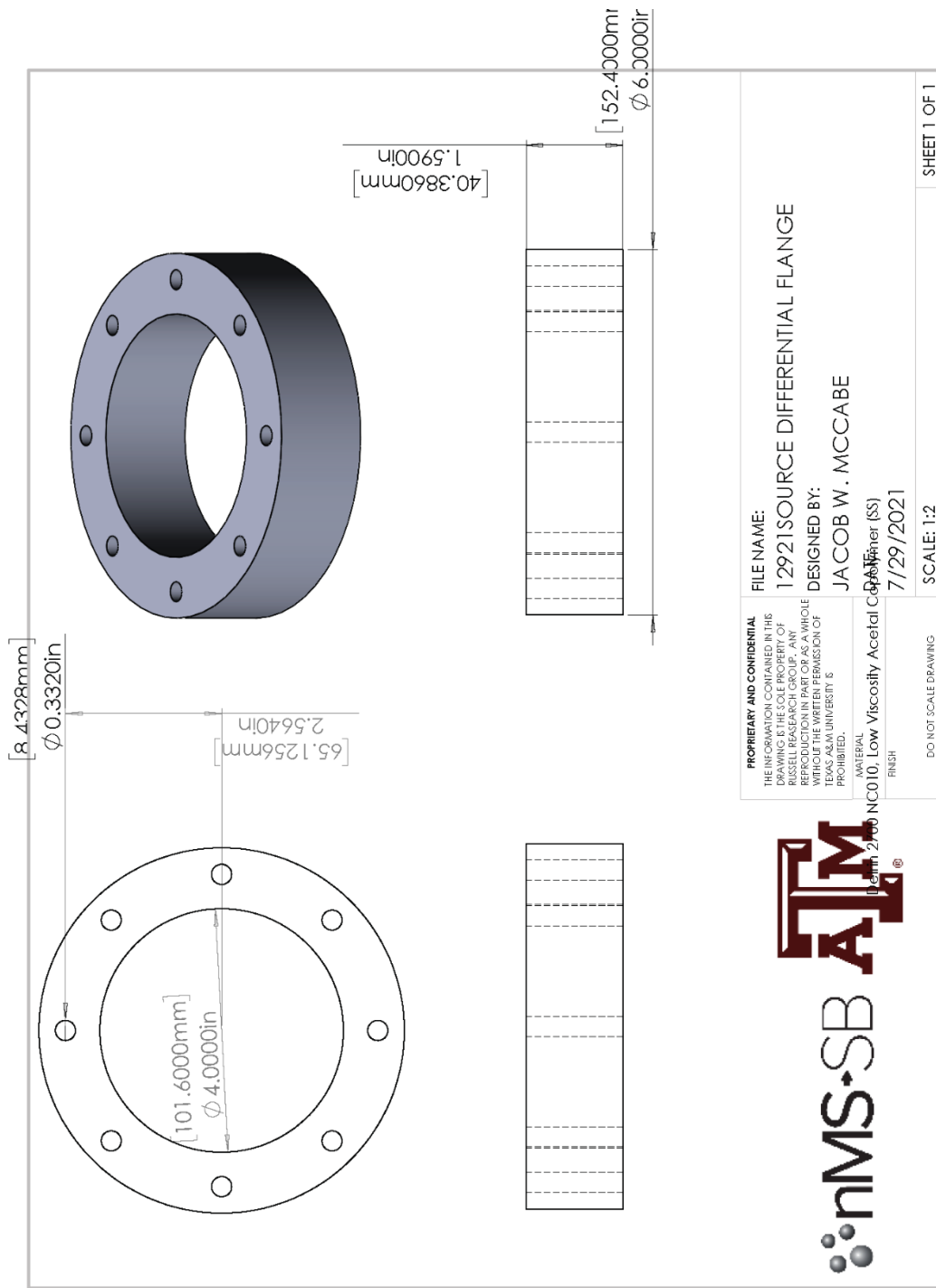


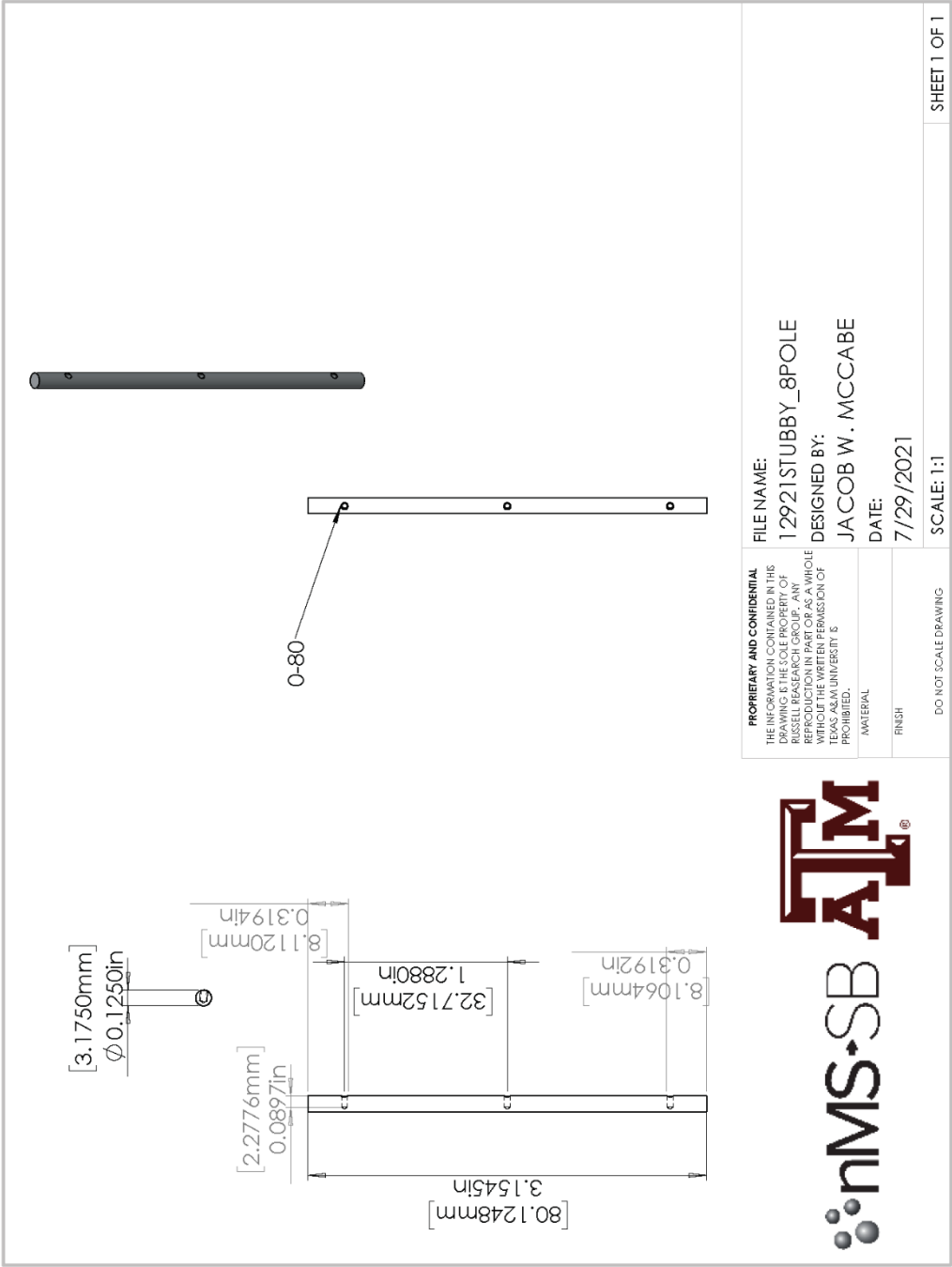
PROPRIETARY AND CONFIDENTIAL
 THE INFORMATION CONTAINED IN THIS DRAWING IS THE SOLE PROPERTY OF RUSSELL RESEARCH GROUP. ANY REPRODUCTION IN PART OR AS A WHOLE WITHOUT THE WRITTEN PERMISSION OF TEXAS A&M UNIVERSITY IS PROHIBITED.



FILE NAME: 12921SKIMMER_CONE_HOUSING_INSERT
DESIGNED BY: JACOB W. MCCABE
DATE: 7/29/2021

FINISH: DO NOT SCALE DRAWING
SCALE: 1:2
SHEET 1 OF 1

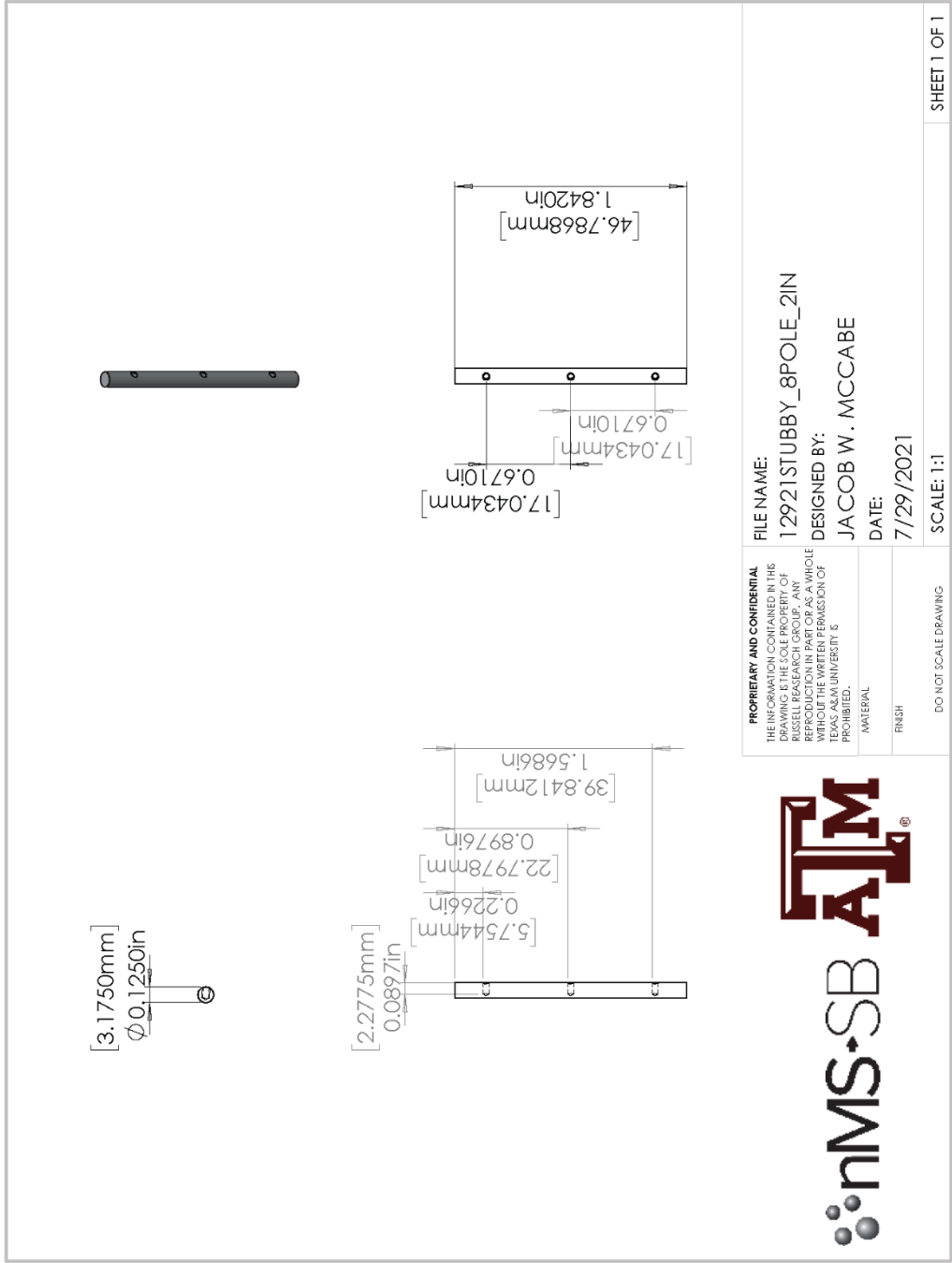


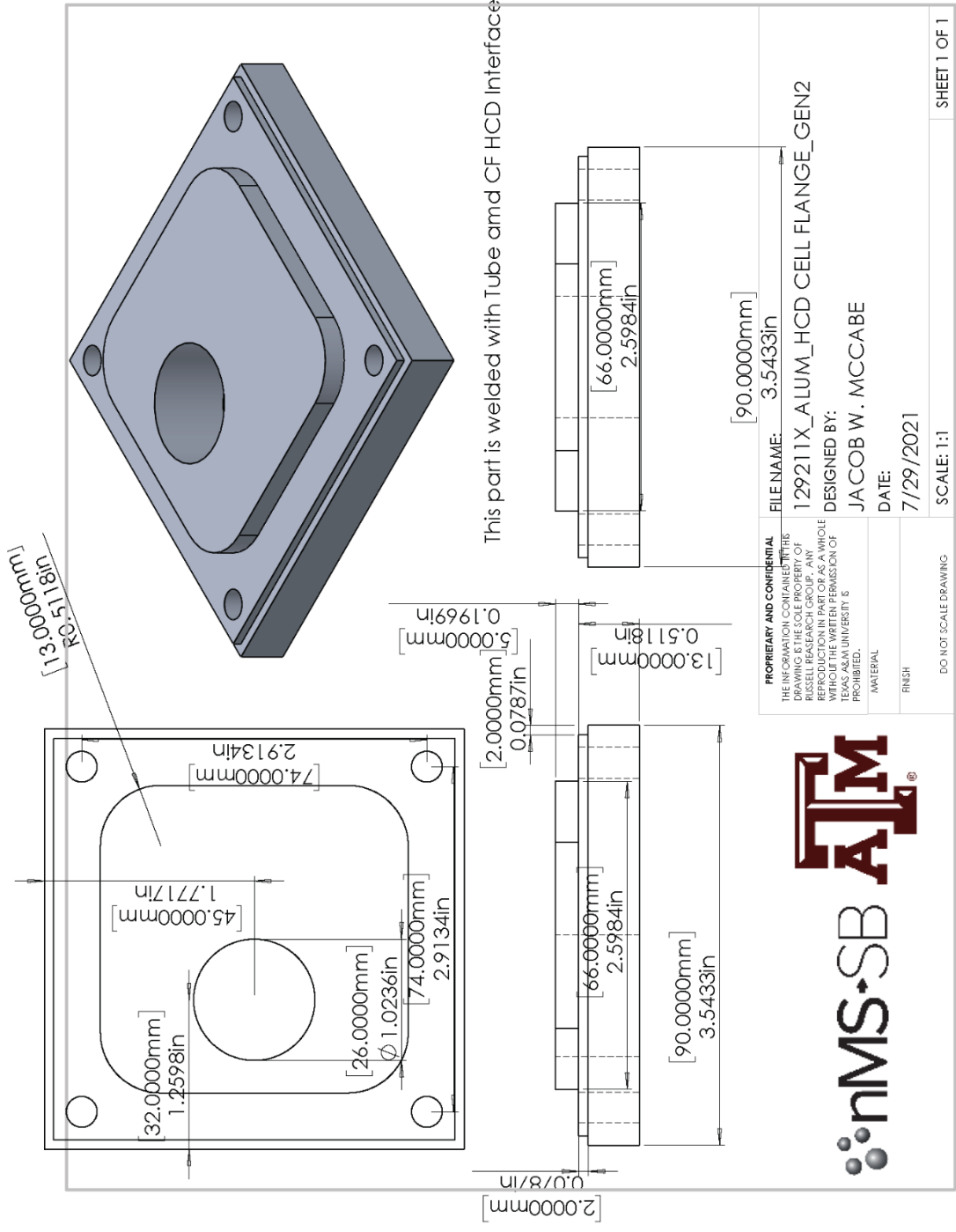


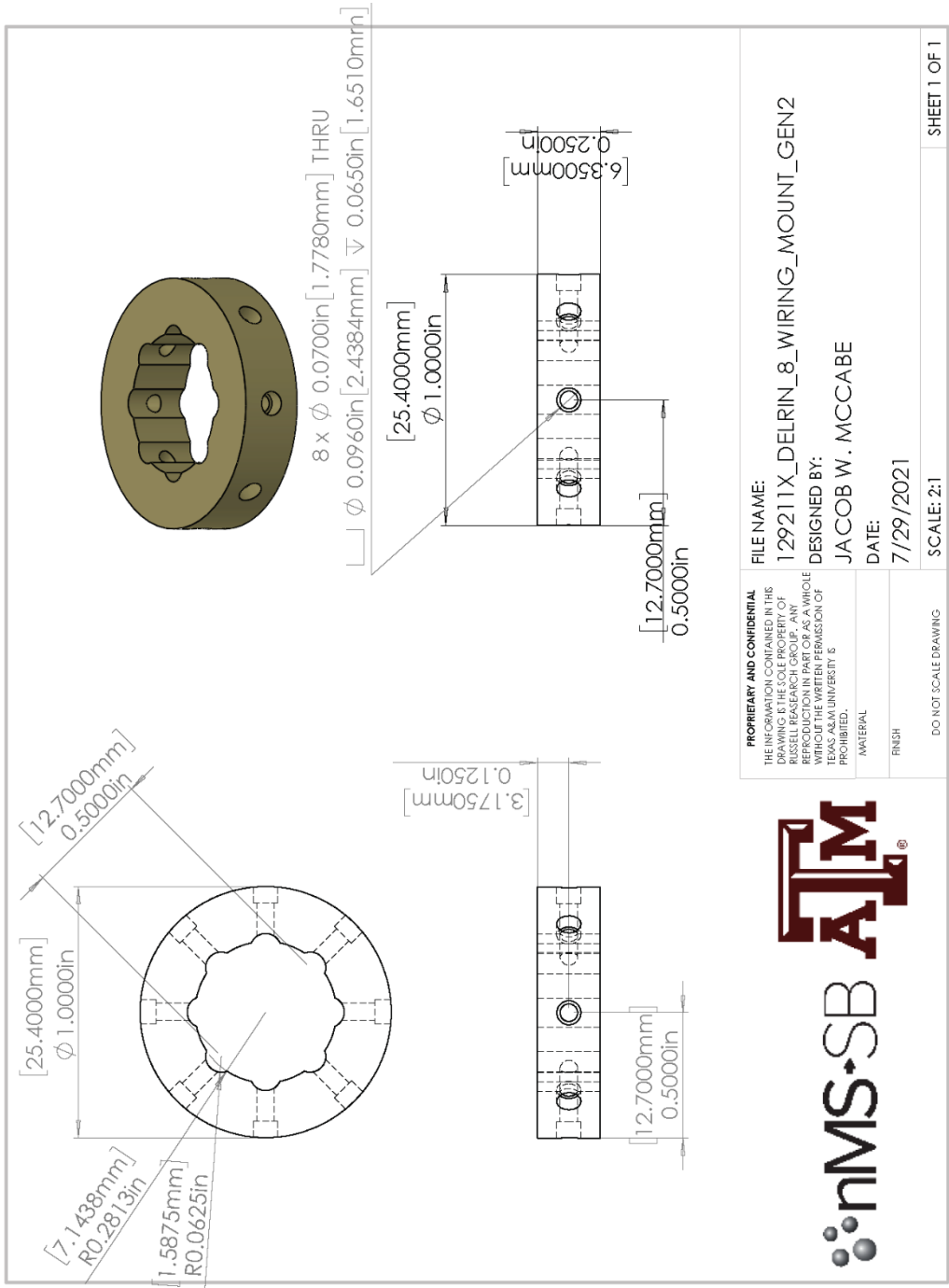
<p>PROPRIETARY AND CONFIDENTIAL THE INFORMATION CONTAINED IN THIS DRAWING IS THE SOLE PROPERTY OF RUSSELL RESEARCH GROUP. ANY REPRODUCTION IN PART OR AS A WHOLE WITHOUT THE WRITTEN PERMISSION OF TEXAS A&M UNIVERSITY IS PROHIBITED.</p>	<p>FILE NAME: 12921STUBBY_8POLE</p>
	<p>DESIGNED BY: JACOB W. MCCABE</p>
<p>MATERIAL:</p>	<p>DATE: 7/29/2021</p>
<p>FINISH:</p>	<p>SCALE: 1:1</p>
<p>DO NOT SCALE DRAWING</p>	<p>SHEET 1 OF 1</p>



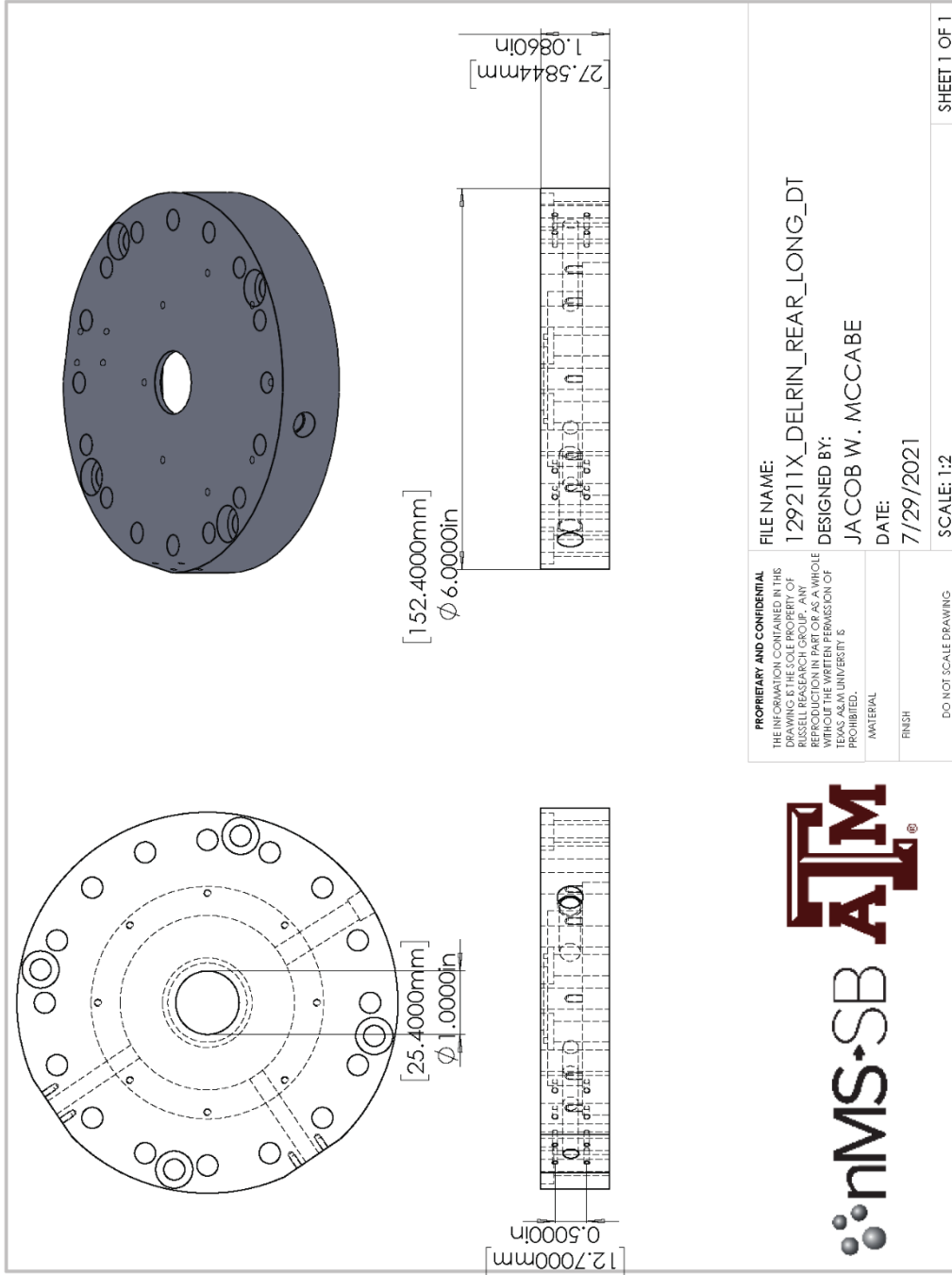
SOLIDWORKS Educational Product. For Instructional Use Only.



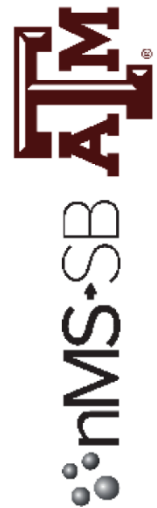




SOLIDWORKS Educational Product. For Instructional Use Only.



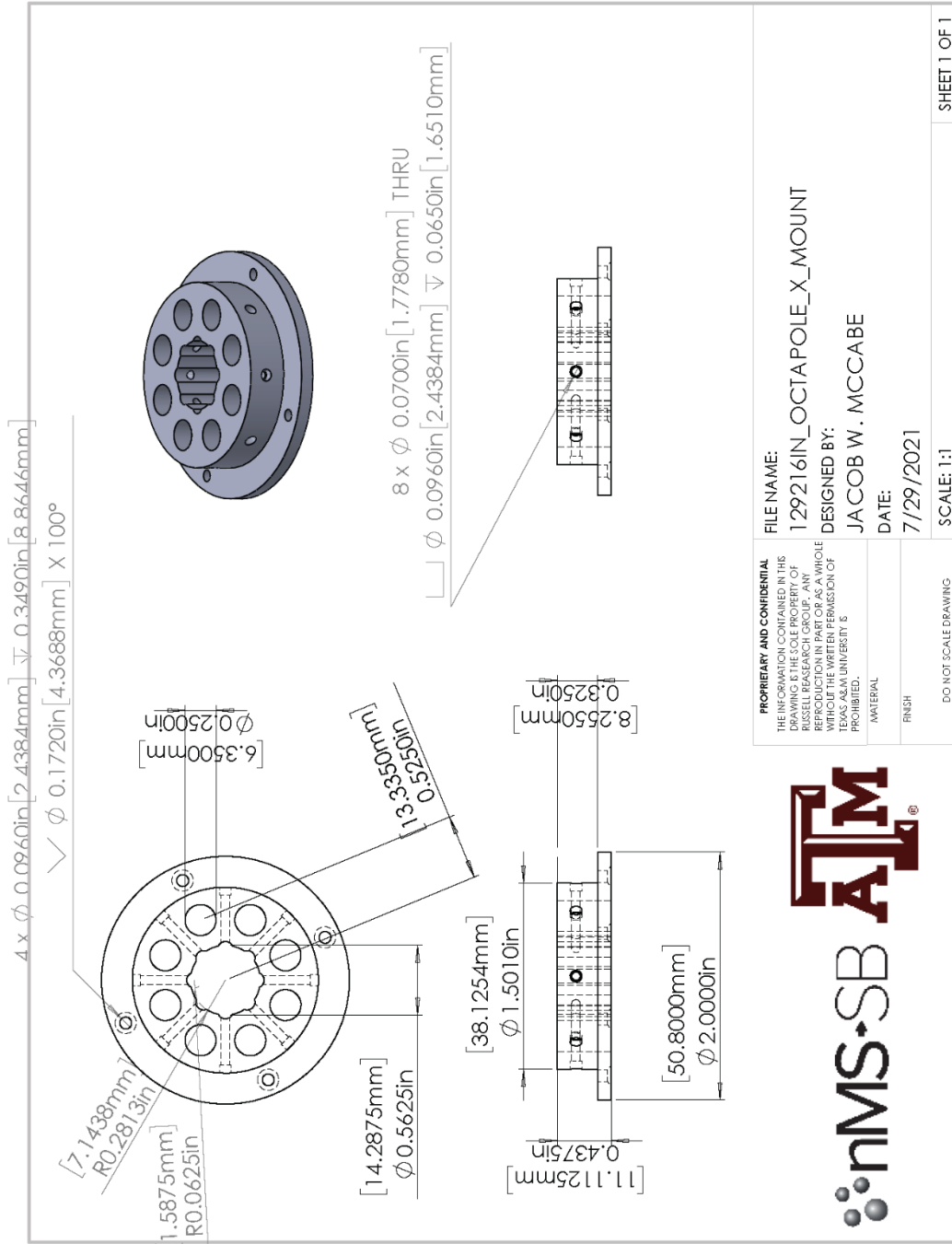
PROPRIETARY AND CONFIDENTIAL
 THE INFORMATION CONTAINED IN THIS DRAWING IS THE SOLE PROPERTY OF RUSSELL RESEARCH GROUP. ANY REPRODUCTION IN PART OR AS A WHOLE WITHOUT THE WRITTEN PERMISSION OF TEXAS A&M UNIVERSITY IS PROHIBITED.

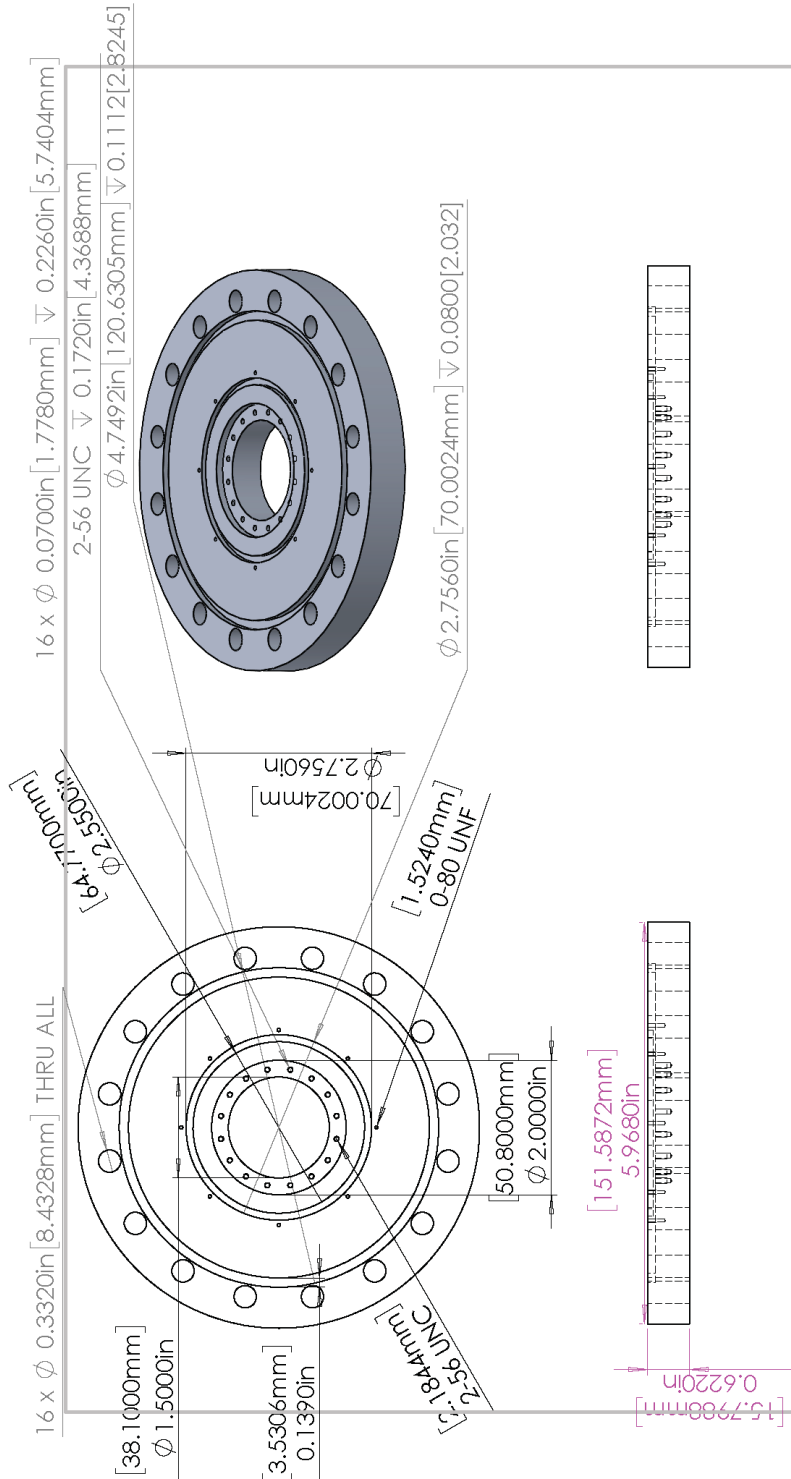


FILE NAME:
 129211X_DELRIN_REAR_LONG_DT
DESIGNED BY:
 JACOB W. MCCABE
DATE:
 7/29/2021

MATERIAL:
 FINISH:
 DO NOT SCALE DRAWING

SHEET 1 OF 1





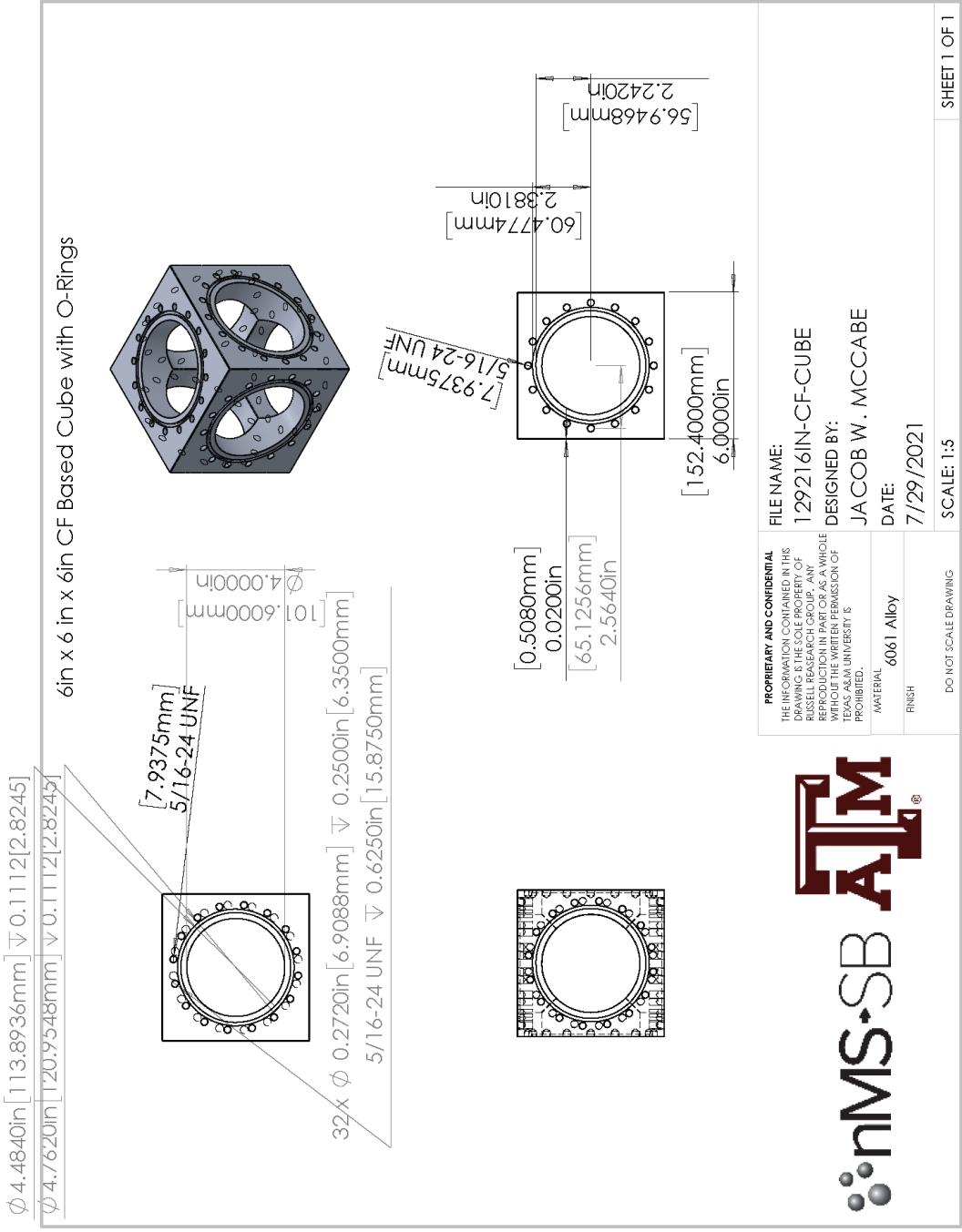
PROPRIETARY AND CONFIDENTIAL
 THE INFORMATION CONTAINED IN THIS DRAWING IS THE SOLE PROPERTY OF RUSSELL RESEARCH GROUP. ANY REPRODUCTION IN PART OR AS A WHOLE WITHOUT THE WRITTEN PERMISSION OF TEXAS A&M UNIVERSITY IS PROHIBITED.



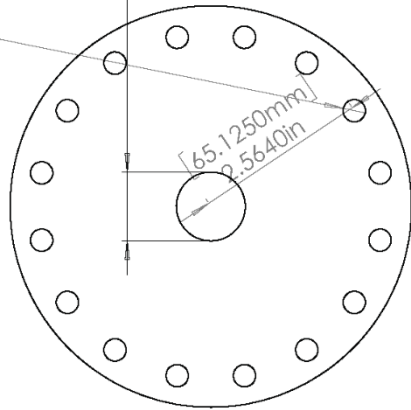
FILE NAME:
 129216IN-CF-8POLE-INTERFACE
DESIGNED BY:
 JACOB W. MCCABE
DATE:
 7/29/2021

MATERIAL:
FINISH:
 DO NOT SCALE DRAWING

SHEET 1 OF 1

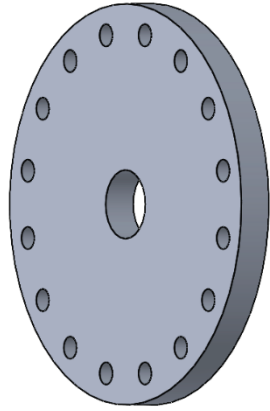


16 x ϕ 0.3320in [8.4328mm] THRU ALL



[26.0096mm]
 ϕ 1.0240in

[65.1250mm]
2.5640in



This part is welded with Tube and HCD Cell Flange

[12.700mm]
0.5000in

[151.5872mm]
5.9680in



PROPRIETARY AND CONFIDENTIAL
THE INFORMATION CONTAINED IN THIS DRAWING IS THE SOLE PROPERTY OF RUSSELL RESEARCH GROUP. ANY REPRODUCTION IN PART OR AS A WHOLE WITHOUT THE WRITTEN PERMISSION OF TEXAS A&M UNIVERSITY IS PROHIBITED.



FILE NAME:

129216IN-CF-HCD-INTERFACE

DESIGNED BY:

JACOB W. MCCABE

DATE:

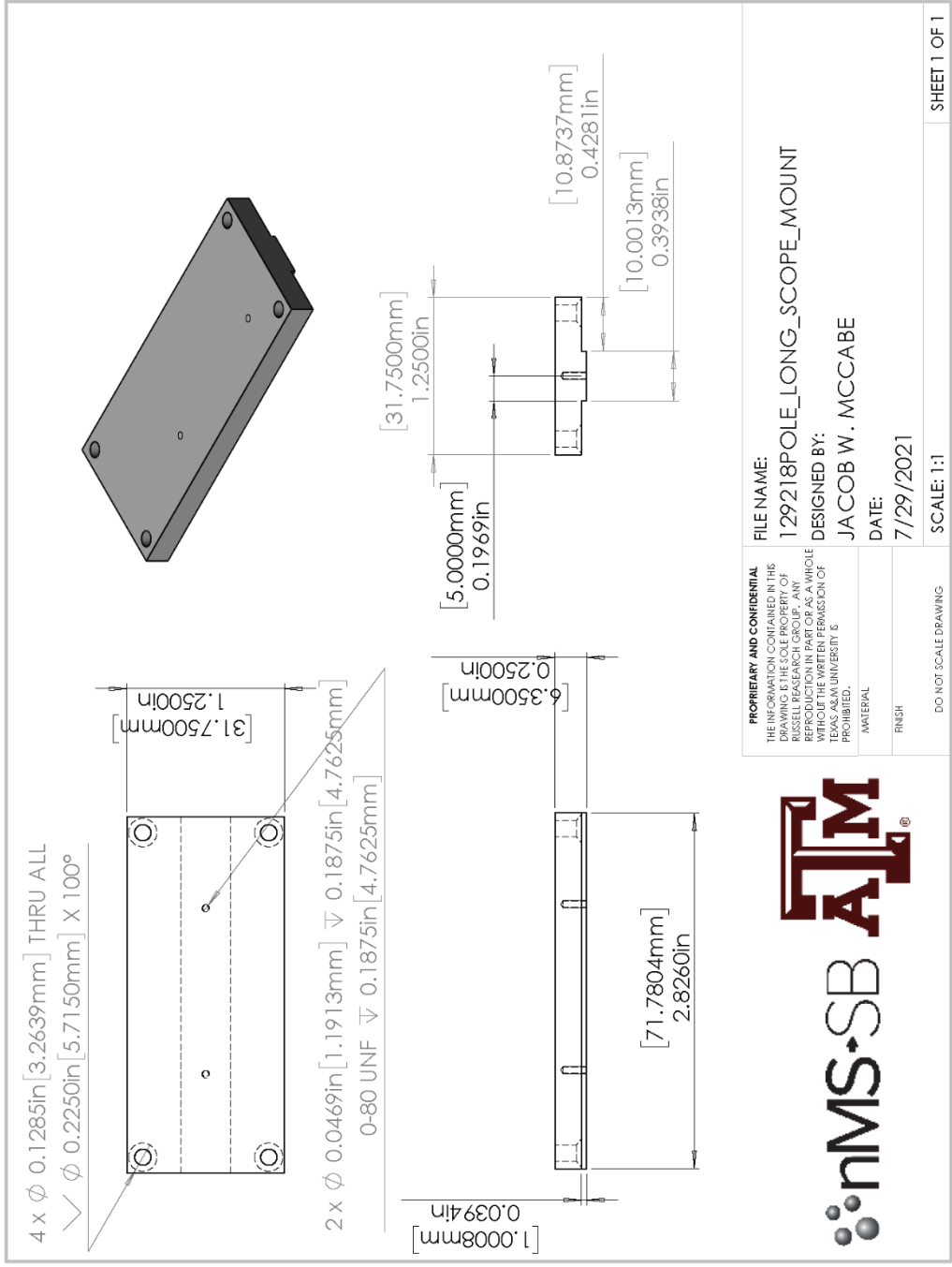
7/29/2021

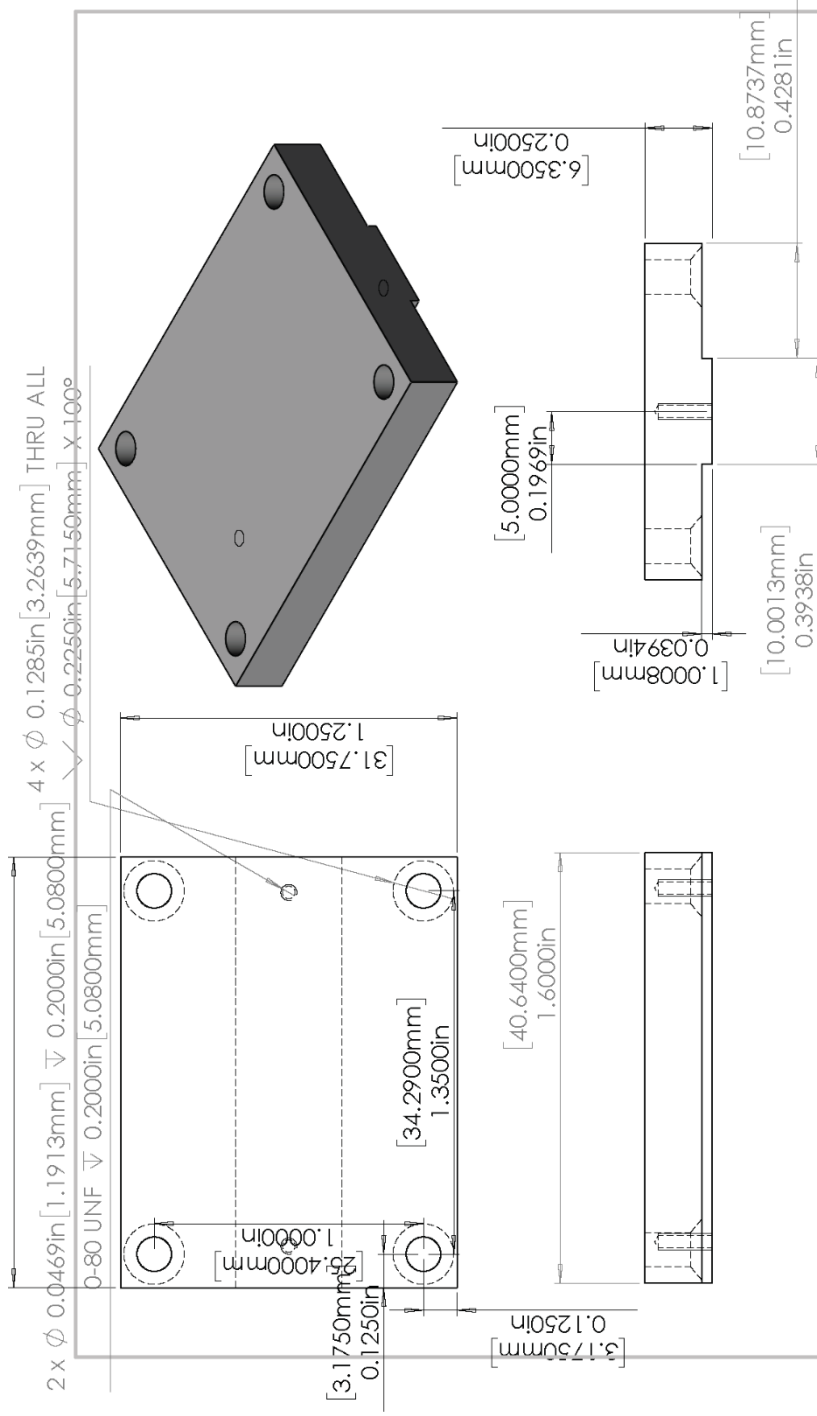
SCALE: 1:2

DO NOT SCALE DRAWING

SHEET 1 OF 1

SOLIDWORKS Educational Product. For Instructional Use Only.

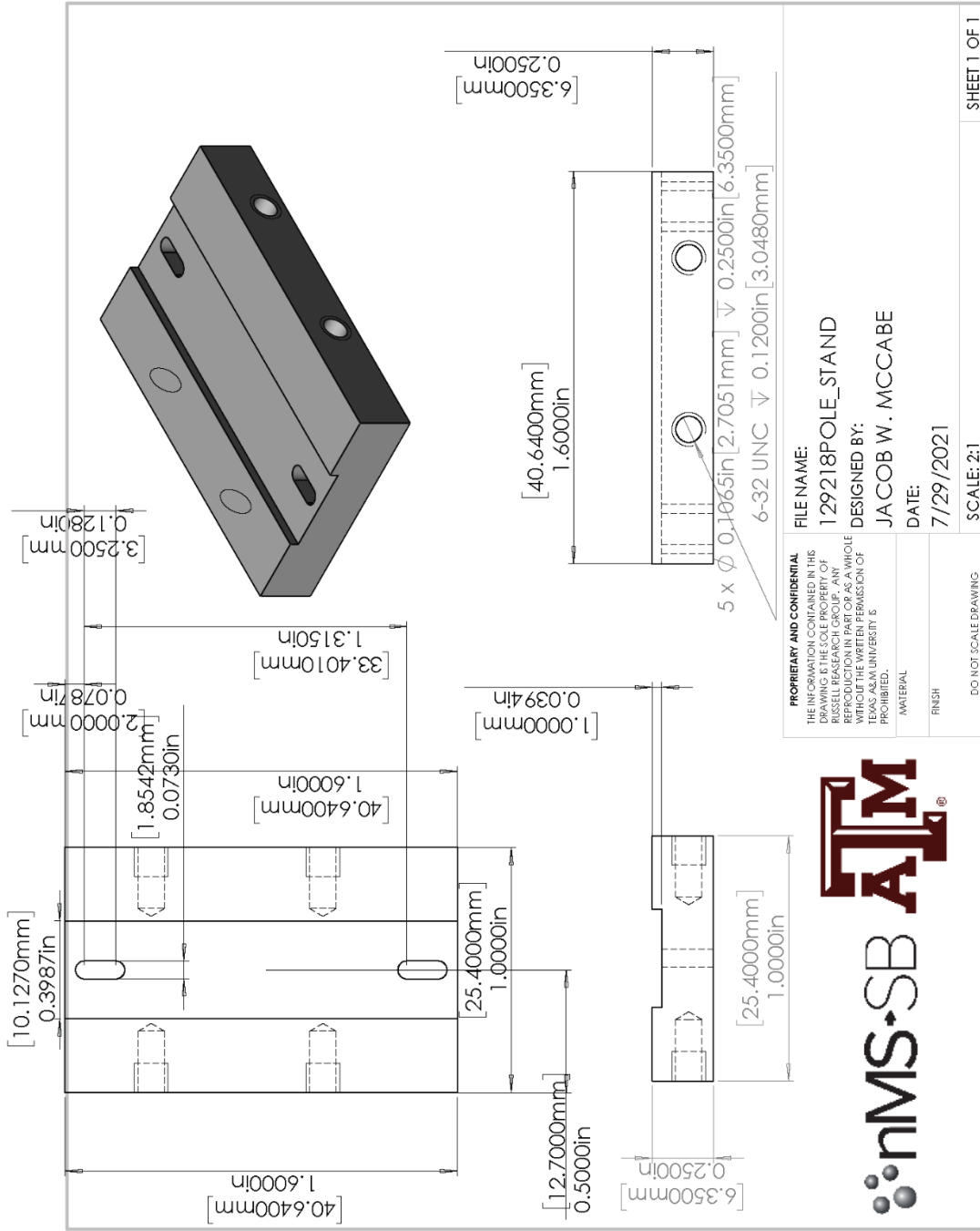


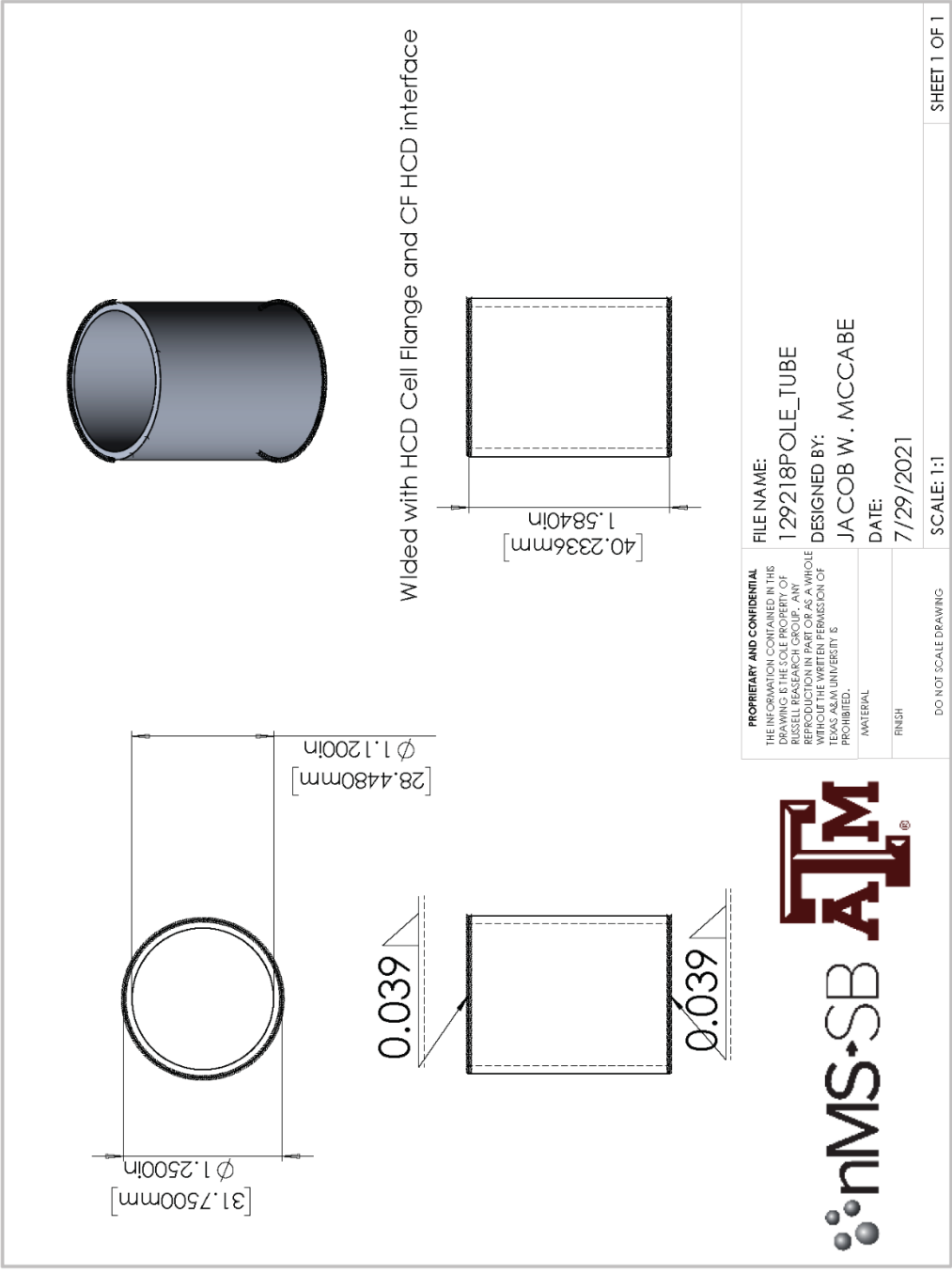


PROPRIETARY AND CONFIDENTIAL	
THE INFORMATION CONTAINED IN THIS DRAWING IS THE SOLE PROPERTY OF RUSSELL RESEARCH GROUP. ANY REPRODUCTION IN PART OR AS A WHOLE WITHOUT THE WRITTEN PERMISSION OF TEXAS A&M UNIVERSITY IS PROHIBITED.	
MATERIAL	
FINISH	
DO NOT SCALE DRAWING	
FILE NAME:	129218POLE_SCOPE_MOUNT
DESIGNED BY:	JACOB W. MCCABE
DATE:	7/29/2021
SCALE:	2:1
SHEET 1 OF 1	



SOLIDWORKS Educational Product. For Instructional Use Only.





PROPRIETARY AND CONFIDENTIAL
 THE INFORMATION CONTAINED IN THIS DRAWING IS THE SOLE PROPERTY OF RUSSELL RESEARCH GROUP. ANY REPRODUCTION IN PART OR AS A WHOLE WITHOUT THE WRITTEN PERMISSION OF TEXAS A&M UNIVERSITY IS PROHIBITED.

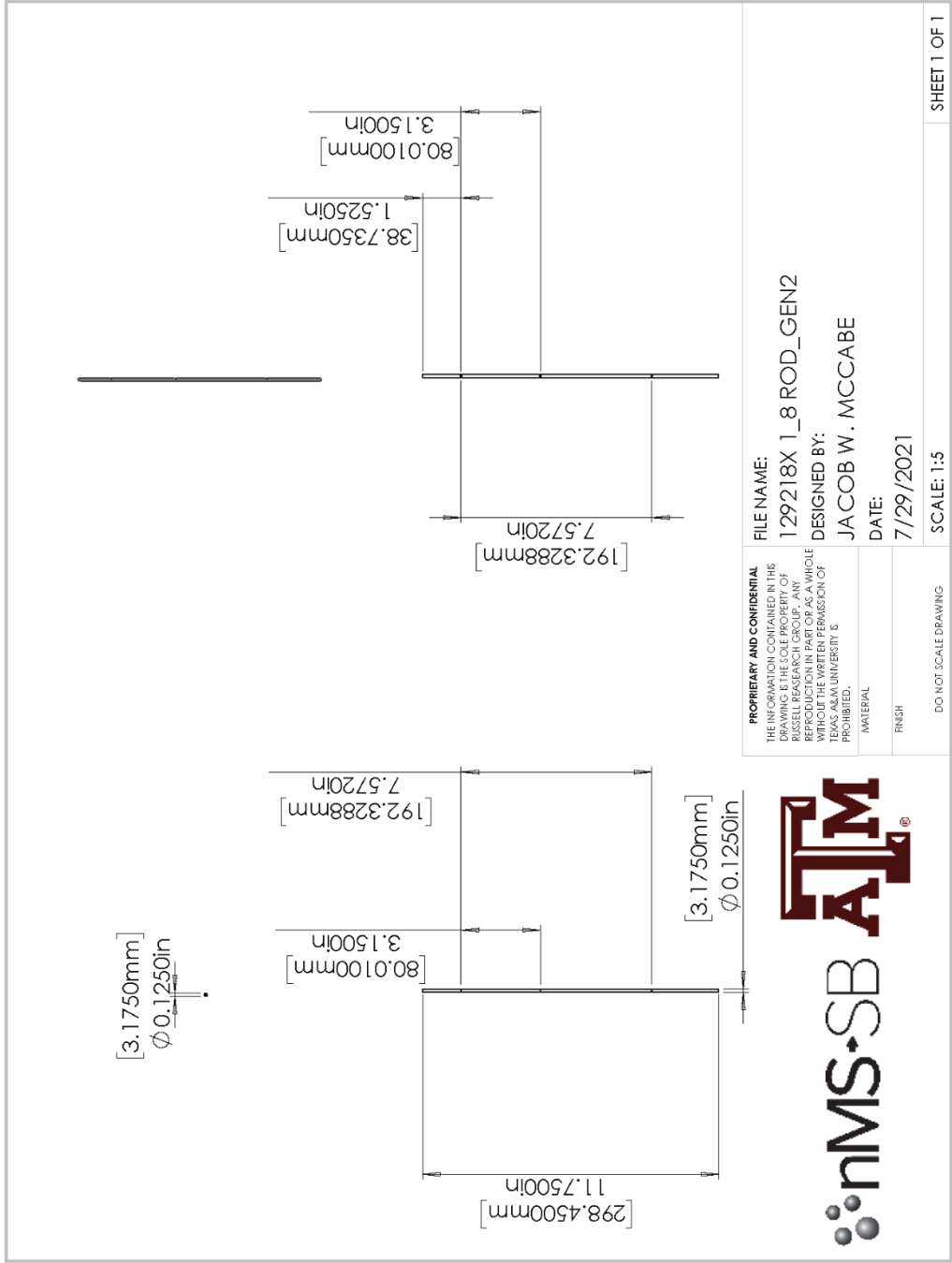
FILE NAME:
 129218POLE_TUBE

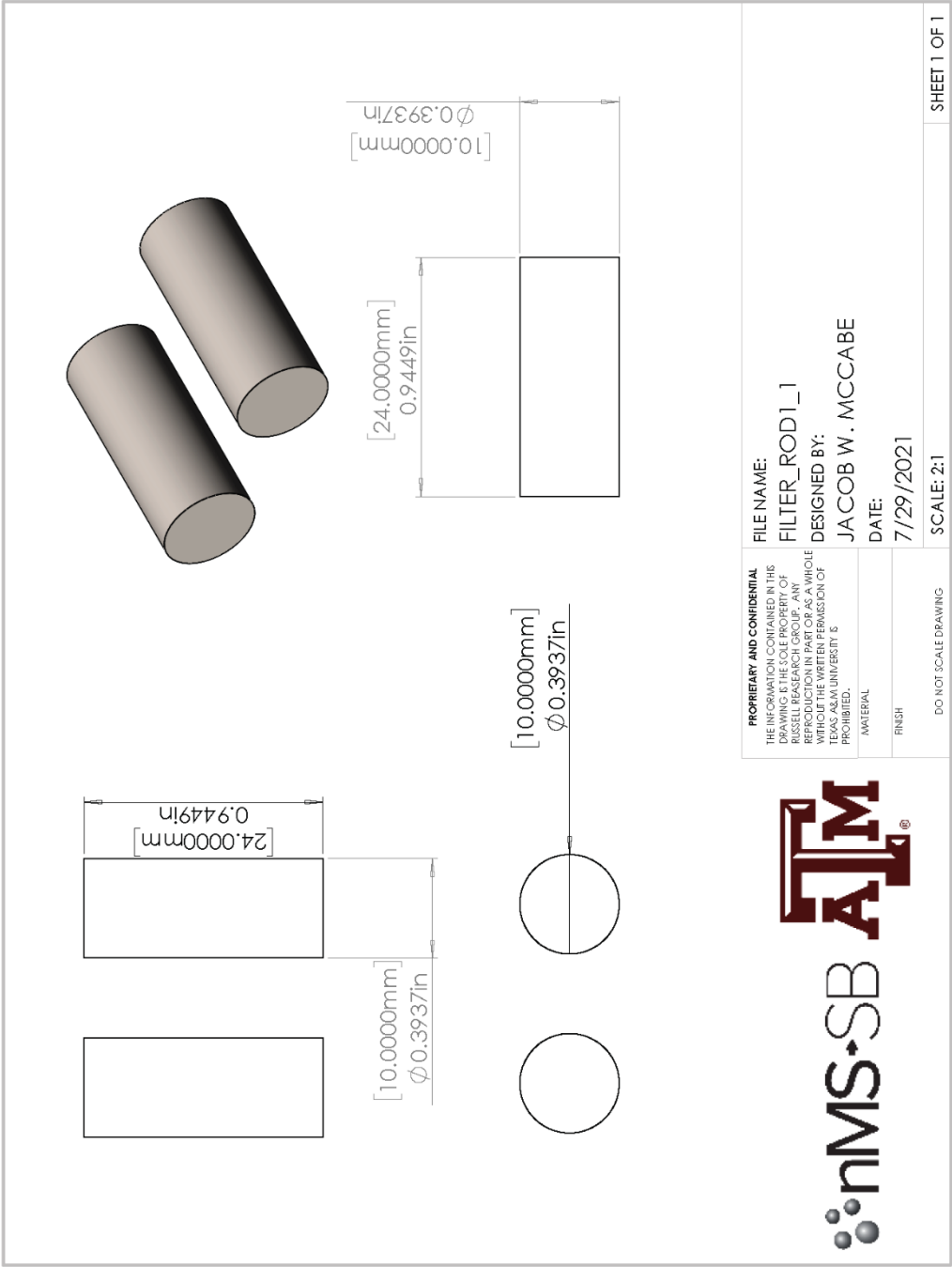
DESIGNED BY:
 JACOB W. MCCABE

DATE:
 7/29/2021

DO NOT SCALE DRAWING

SHEET 1 OF 1





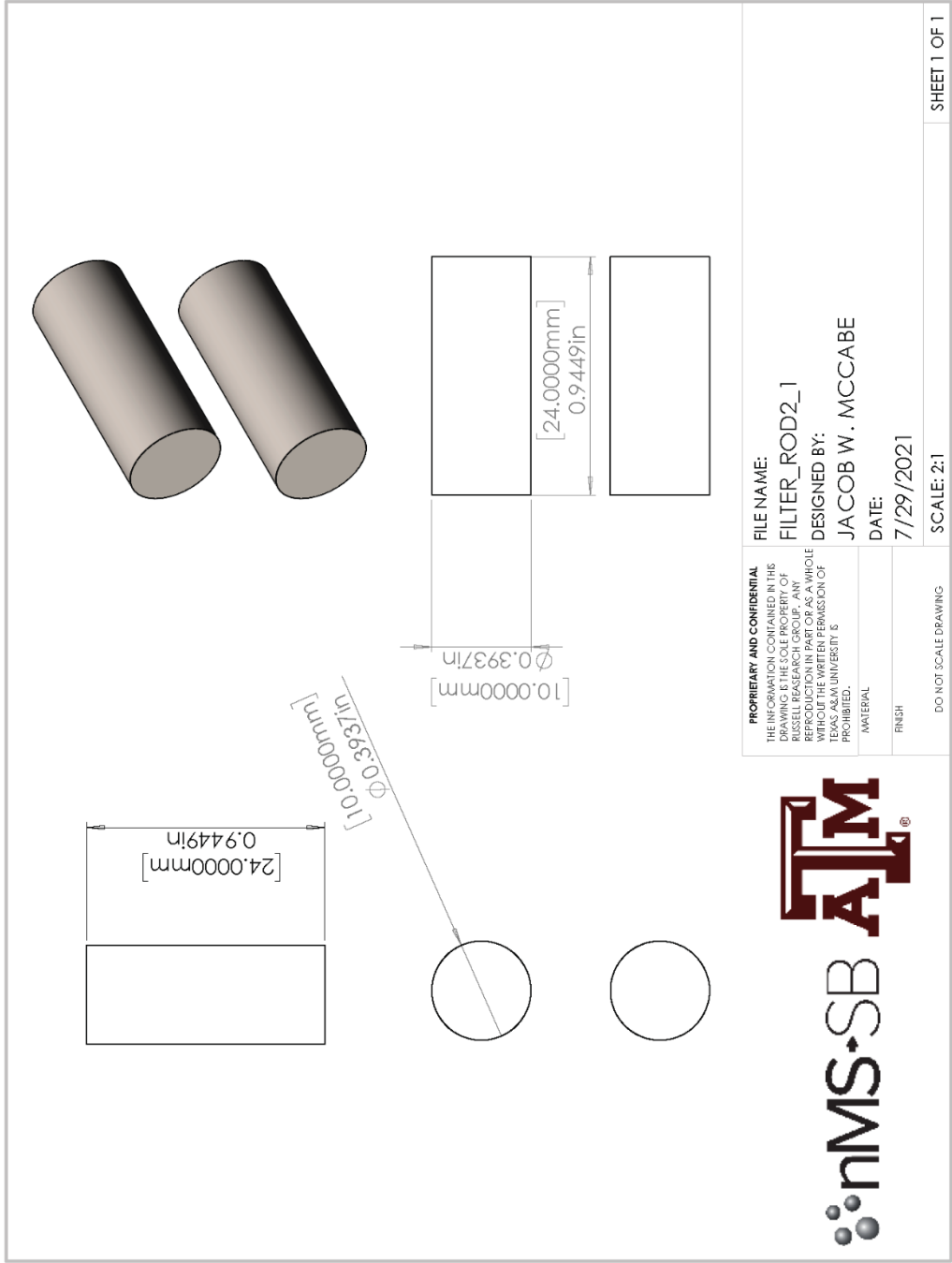
PROPRIETARY AND CONFIDENTIAL
 THE INFORMATION CONTAINED IN THIS DRAWING IS THE SOLE PROPERTY OF RUSSELL RESEARCH GROUP. ANY REPRODUCTION IN PART OR AS A WHOLE WITHOUT THE WRITTEN PERMISSION OF TEXAS A&M UNIVERSITY IS PROHIBITED.



FILE NAME: FILTER_ROD1_1
DESIGNED BY: JACOB W. MCCABE
DATE: 7/29/2021

MATERIAL:
FINISH:
 DO NOT SCALE DRAWING

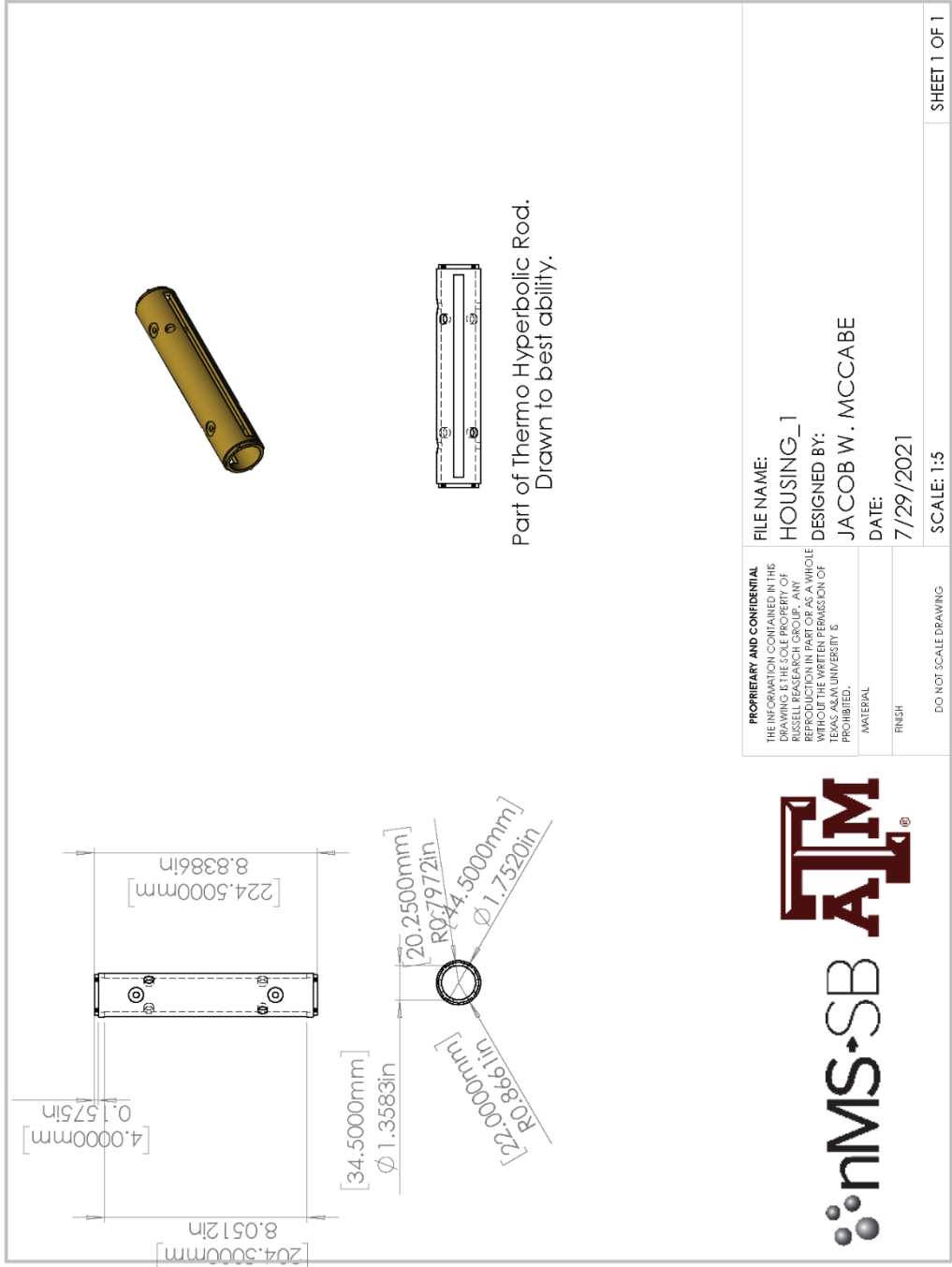
SCALE: 2:1
SHEET 1 OF 1



PROPRIETARY AND CONFIDENTIAL		FILE NAME:
THE INFORMATION CONTAINED IN THIS DRAWING IS THE SOLE PROPERTY OF RUSSELL RESEARCH GROUP. ANY REPRODUCTION IN PART OR AS A WHOLE WITHOUT THE WRITTEN PERMISSION OF TEXAS A&M UNIVERSITY IS PROHIBITED.		FILTER_ROD2_1
MATERIAL		DESIGNED BY:
FINISH		JACOB W. MCCABE
DO NOT SCALE DRAWING		DATE:
		7/29/2021
		SCALE: 2:1
		SHEET 1 OF 1

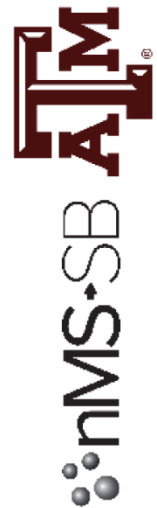


SOLIDWORKS Educational Product. For Instructional Use Only.

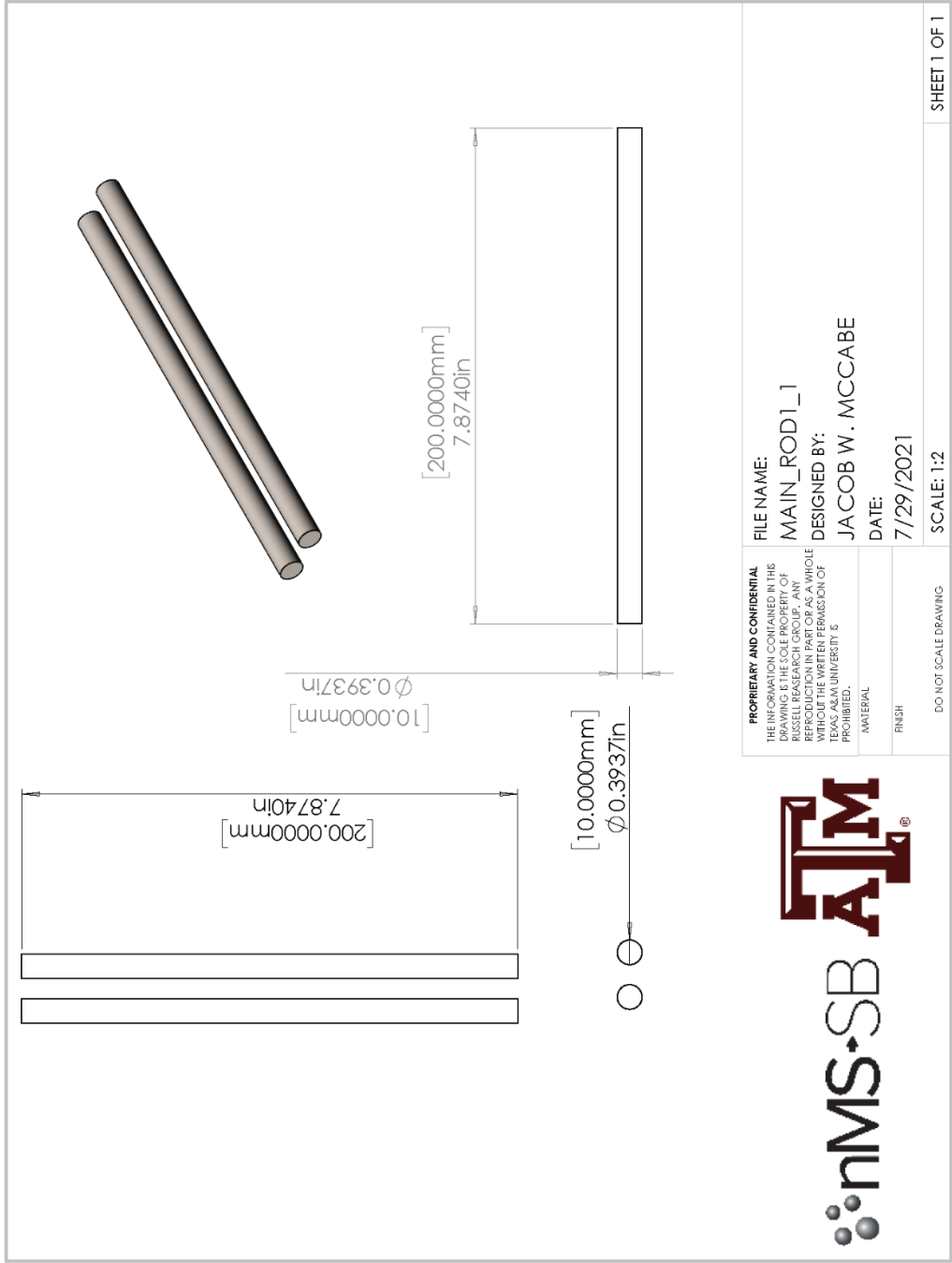


Part of Thermo Hyperbolic Rod.
Drawn to best ability.

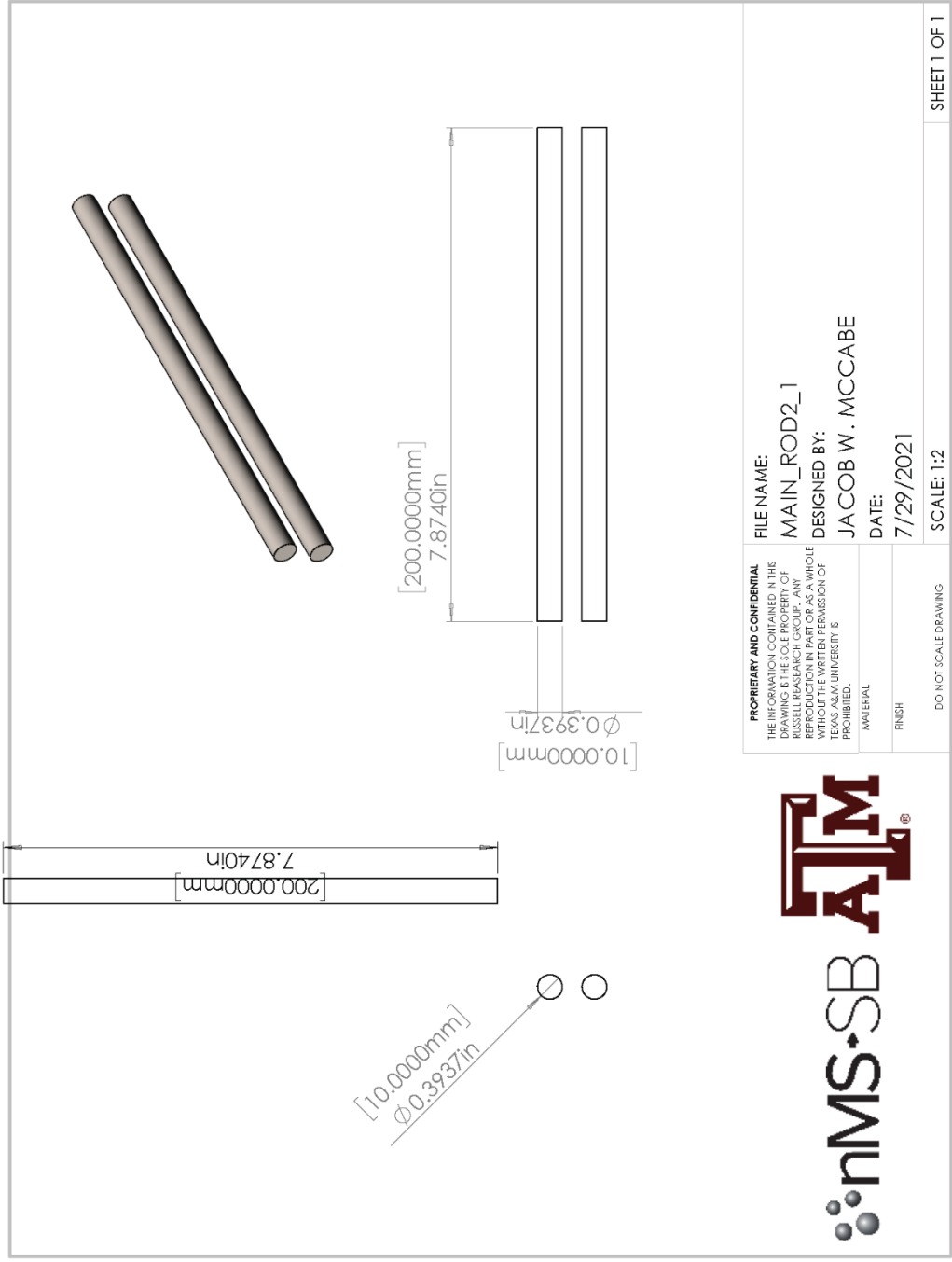
PROPRIETARY AND CONFIDENTIAL THE INFORMATION CONTAINED IN THIS DRAWING IS THE SOLE PROPERTY OF RUSSELL RESEARCH GROUP. ANY REPRODUCTION IN PART OR AS A WHOLE WITHOUT THE WRITTEN PERMISSION OF TEXAS A&M UNIVERSITY IS PROHIBITED.	FILE NAME: HOUSING_1
	DESIGNED BY: JACOB W. MCCABE
MATERIAL:	DATE: 7/29/2021
FINISH:	SCALE: 1:5
DO NOT SCALE DRAWING	
SHEET 1 OF 1	

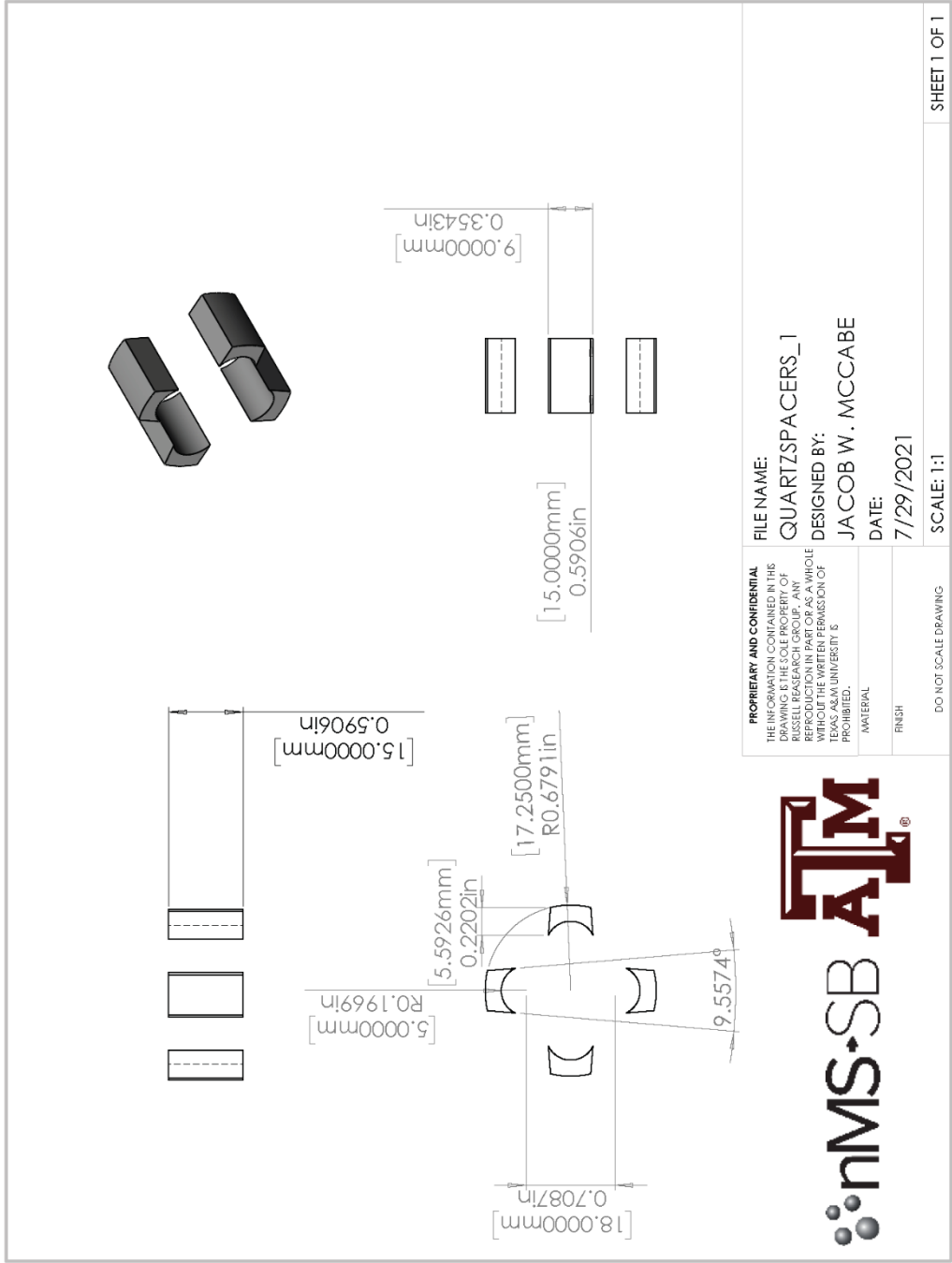


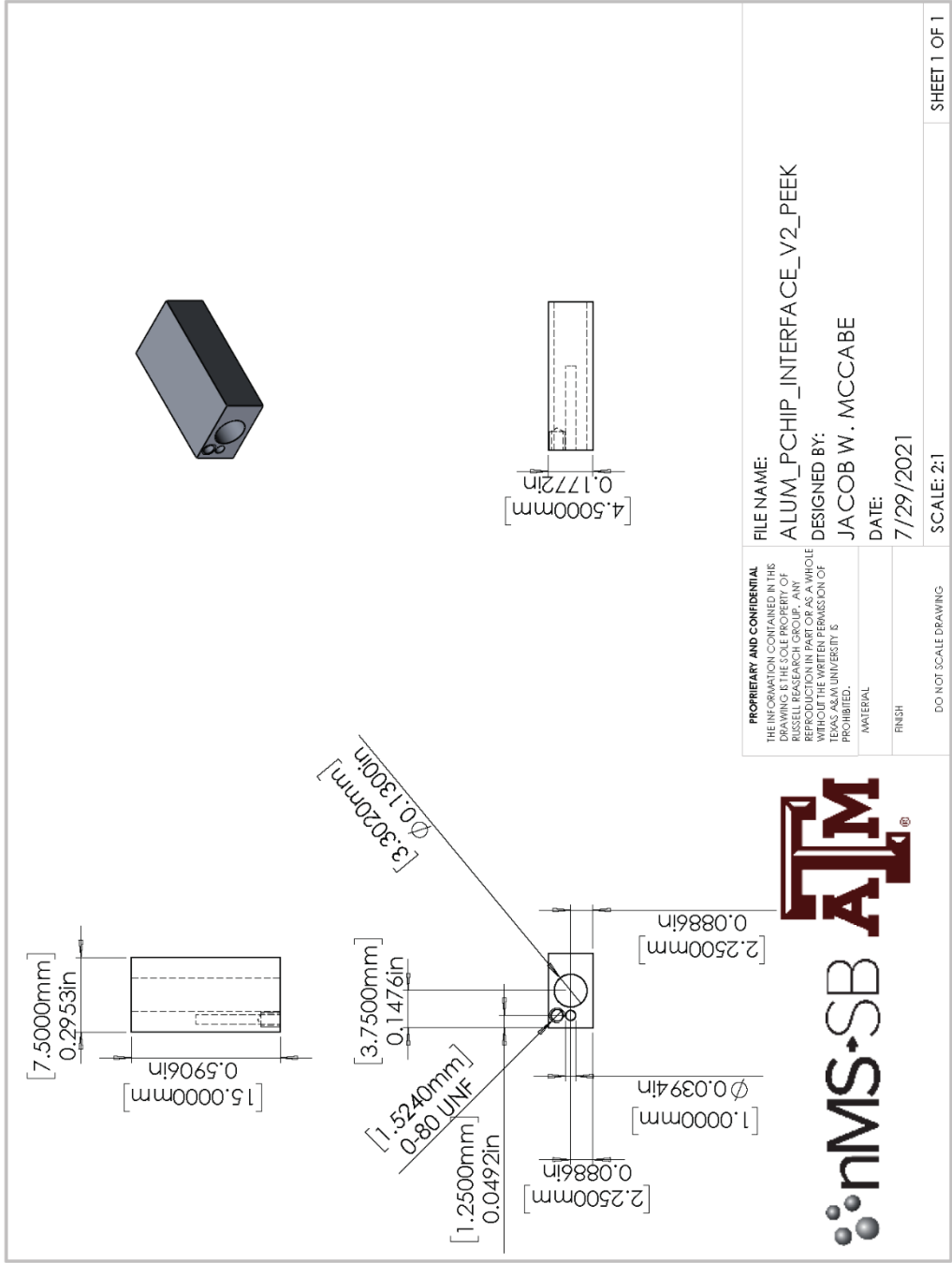
SOLIDWORKS Educational Product. For Instructional Use Only.

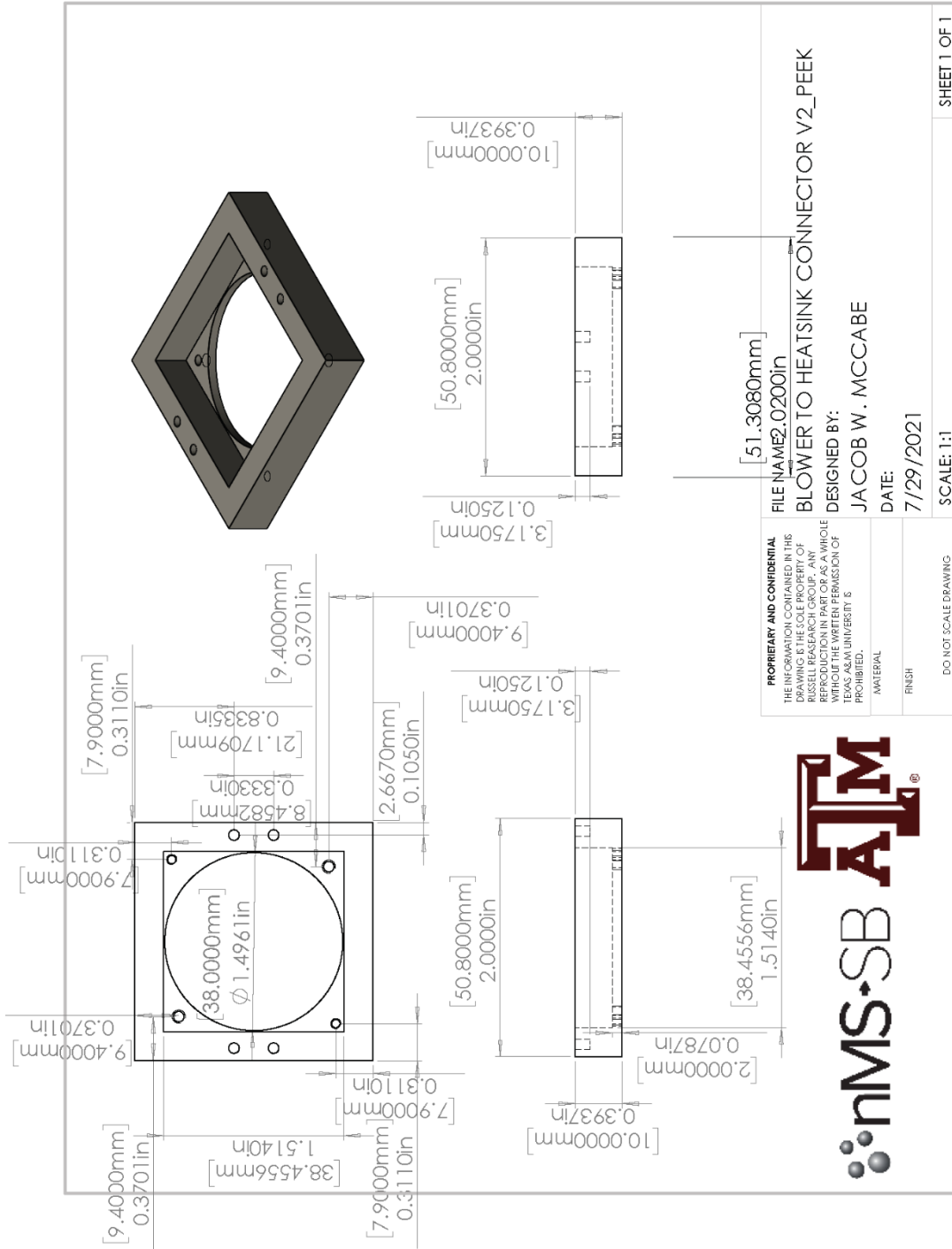


SOLIDWORKS Educational Product. For Instructional Use Only.

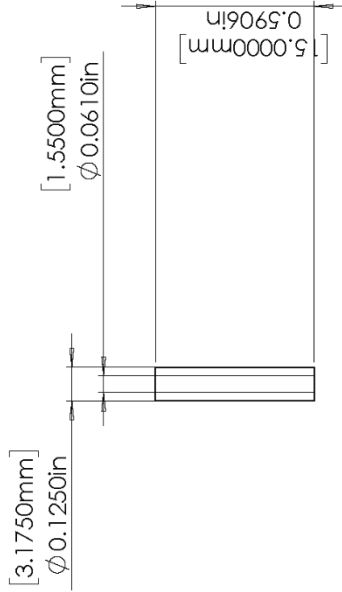
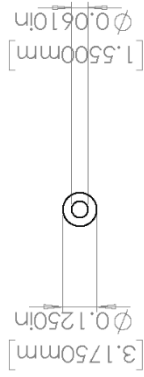








Purchased from Kimball Physics (PN# AL203-TU-C-500) and cut in glass shop



PROPRIETARY AND CONFIDENTIAL
 THE INFORMATION CONTAINED IN THIS
 DRAWING IS THE SOLE PROPERTY OF
 RUSSELL RESEARCH GROUP. ANY
 REPRODUCTION IN PART OR AS A WHOLE
 WITHOUT THE WRITTEN PERMISSION OF
 TEXAS A&M UNIVERSITY IS
 PROHIBITED.



FILE NAME:
 CERAMIC TUBE_PEEK
DESIGNED BY:
 JACOB W. MCCABE
DATE:
 7/29/2021

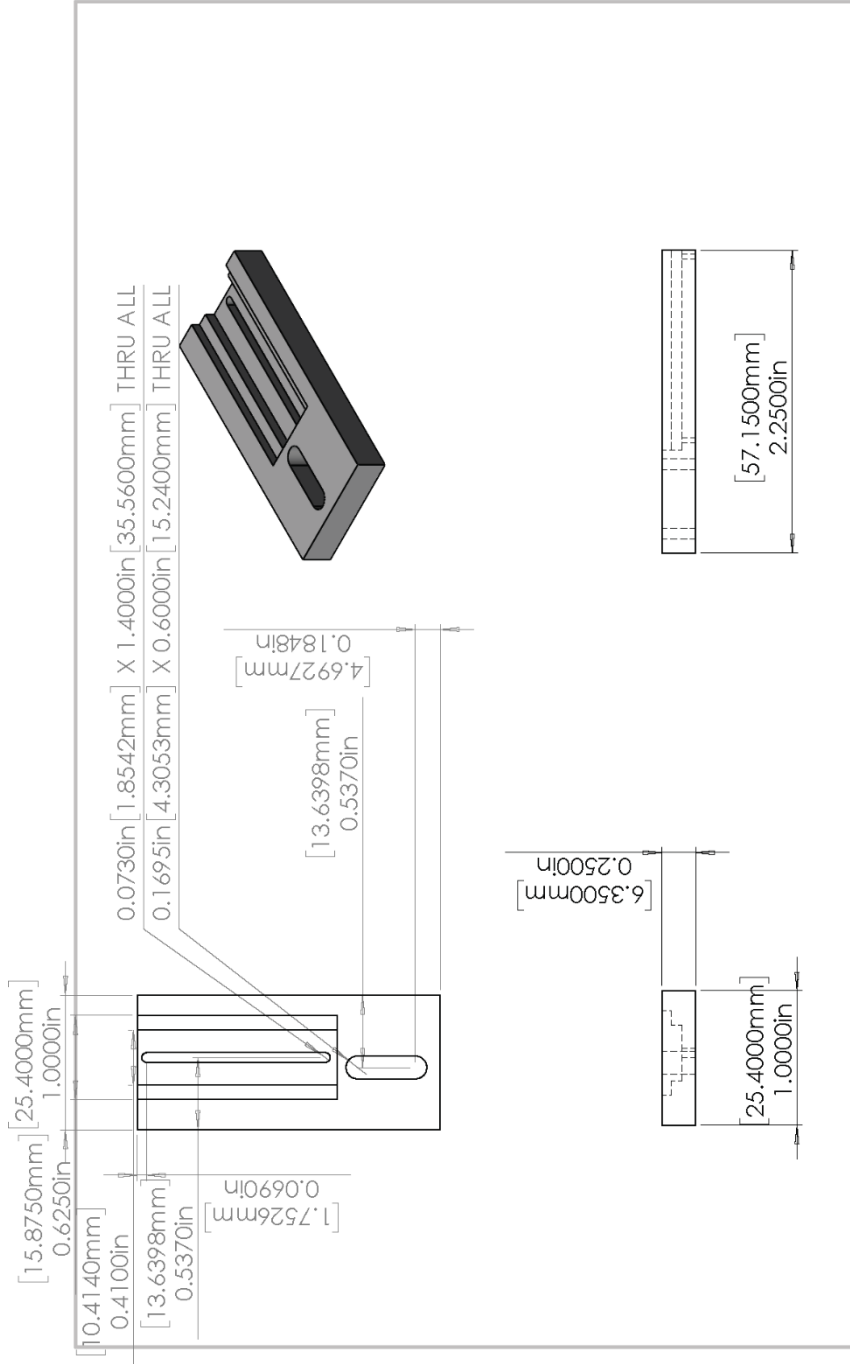
MATERIAL
 FINISH

SCALE: 2:1

DO NOT SCALE DRAWING

SHEET 1 OF 1

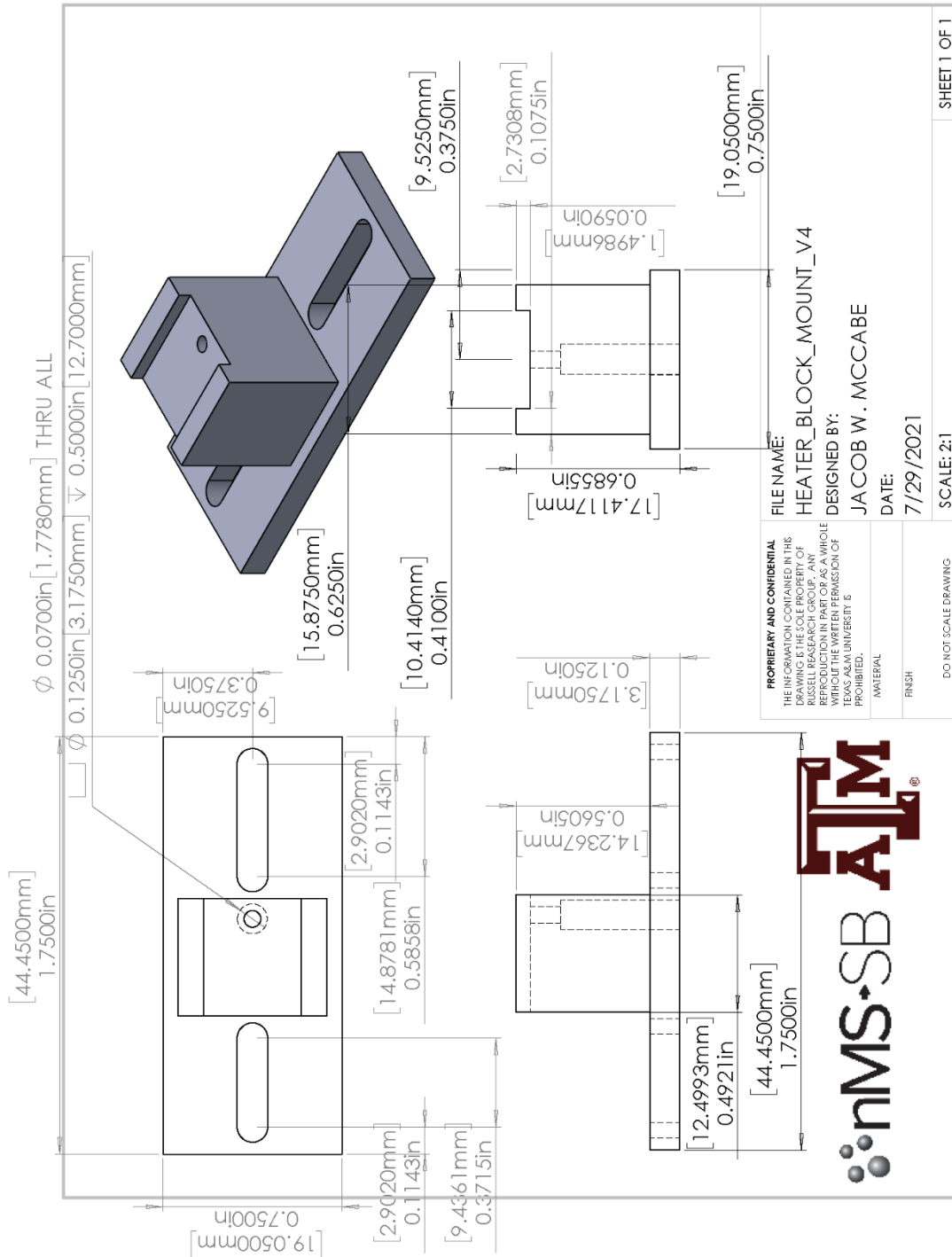
SOLIDWORKS Educational Product. For Instructional Use Only.

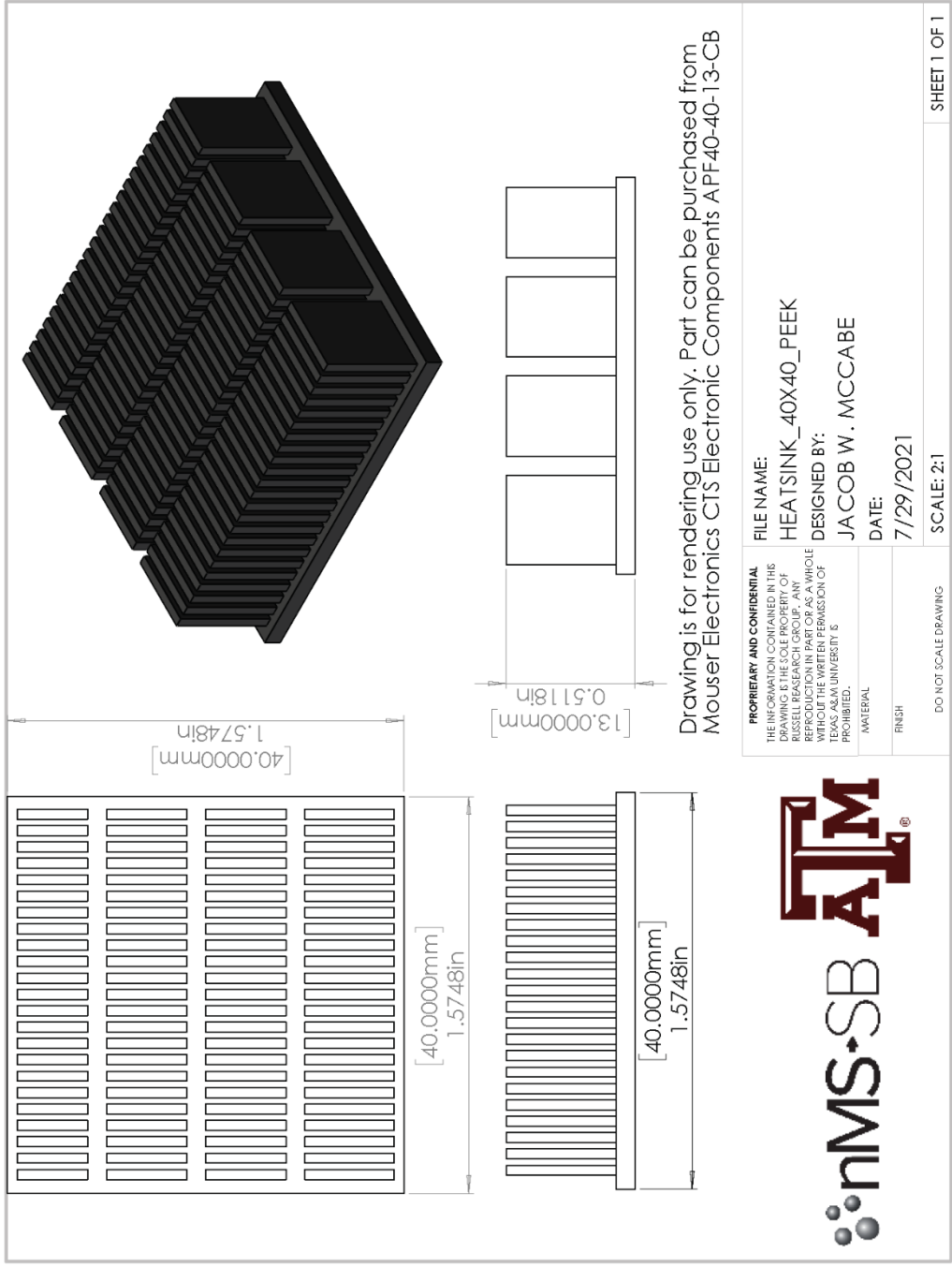


<p>PROPRIETARY AND CONFIDENTIAL</p> <p>THE INFORMATION CONTAINED IN THIS DRAWING IS THE SOLE PROPERTY OF RUSSELL RESEARCH GROUP. ANY REPRODUCTION IN PART OR AS A WHOLE WITHOUT THE WRITTEN PERMISSION OF TEXAS A&M UNIVERSITY IS PROHIBITED.</p> <p>MATERIAL</p> <p>FINISH</p> <p>DO NOT SCALE DRAWING</p>	<p>FILE NAME: HEATER_BLOCK_MOUNT_IM_V3_FLIPPED_LONGER_PEEK</p> <p>DESIGNED BY: JACOB W. MCCABE</p> <p>DATE: 7/29/2021</p> <p>SCALE: 1:1</p>
	<p>SHEET 1 OF 1</p>



SOLIDWORKS Educational Product. For Instructional Use Only.

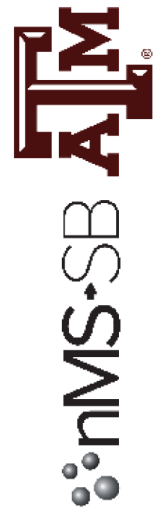
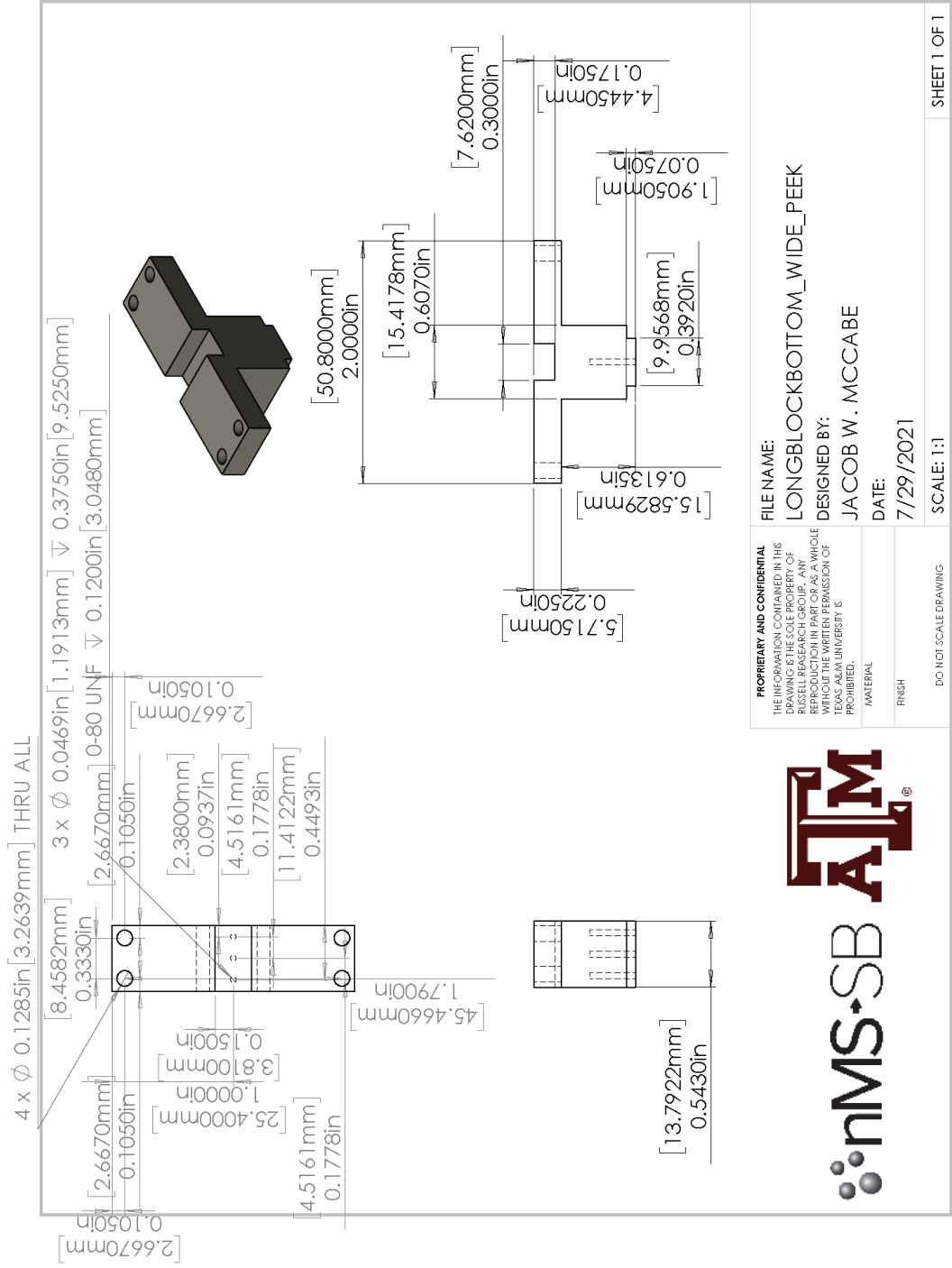




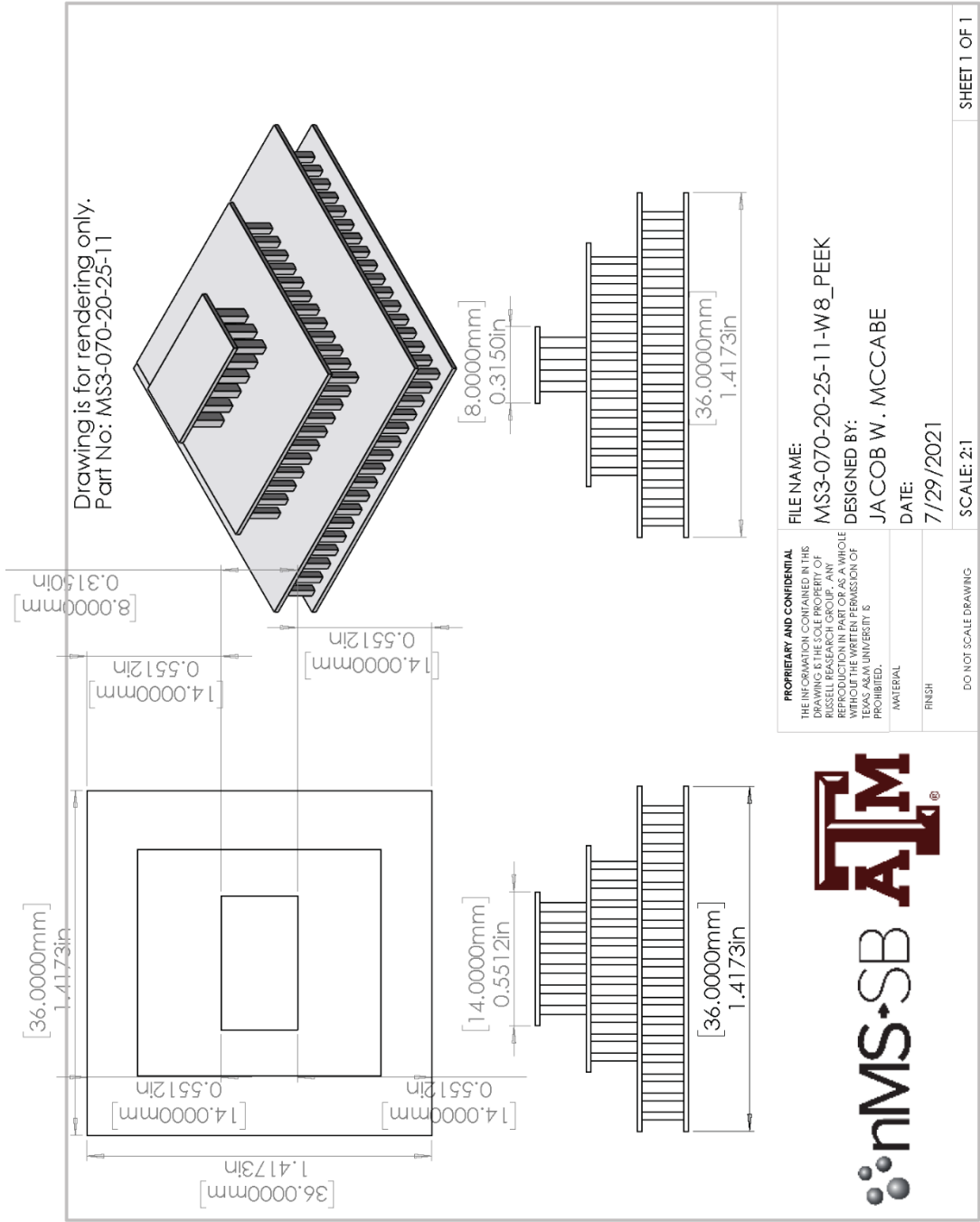
Drawing is for rendering use only. Part can be purchased from Mouser Electronics CTS Electronic Components APF40-40-13-CB



SOLIDWORKS Educational Product. For Instructional Use Only.



SOLIDWORKS Educational Product. For Instructional Use Only.



PROPRIETARY AND CONFIDENTIAL
 THE INFORMATION CONTAINED IN THIS
 DRAWING IS THE SOLE PROPERTY OF
 RUSSELL RESEARCH GROUP. ANY
 REPRODUCTION IN PART OR AS A WHOLE
 WITHOUT THE WRITTEN PERMISSION OF
 TEXAS A&M UNIVERSITY IS
 PROHIBITED.



FILE NAME:
MS3-070-20-25-11-W8_PEEK

DESIGNED BY:
JACOB W. MCCABE

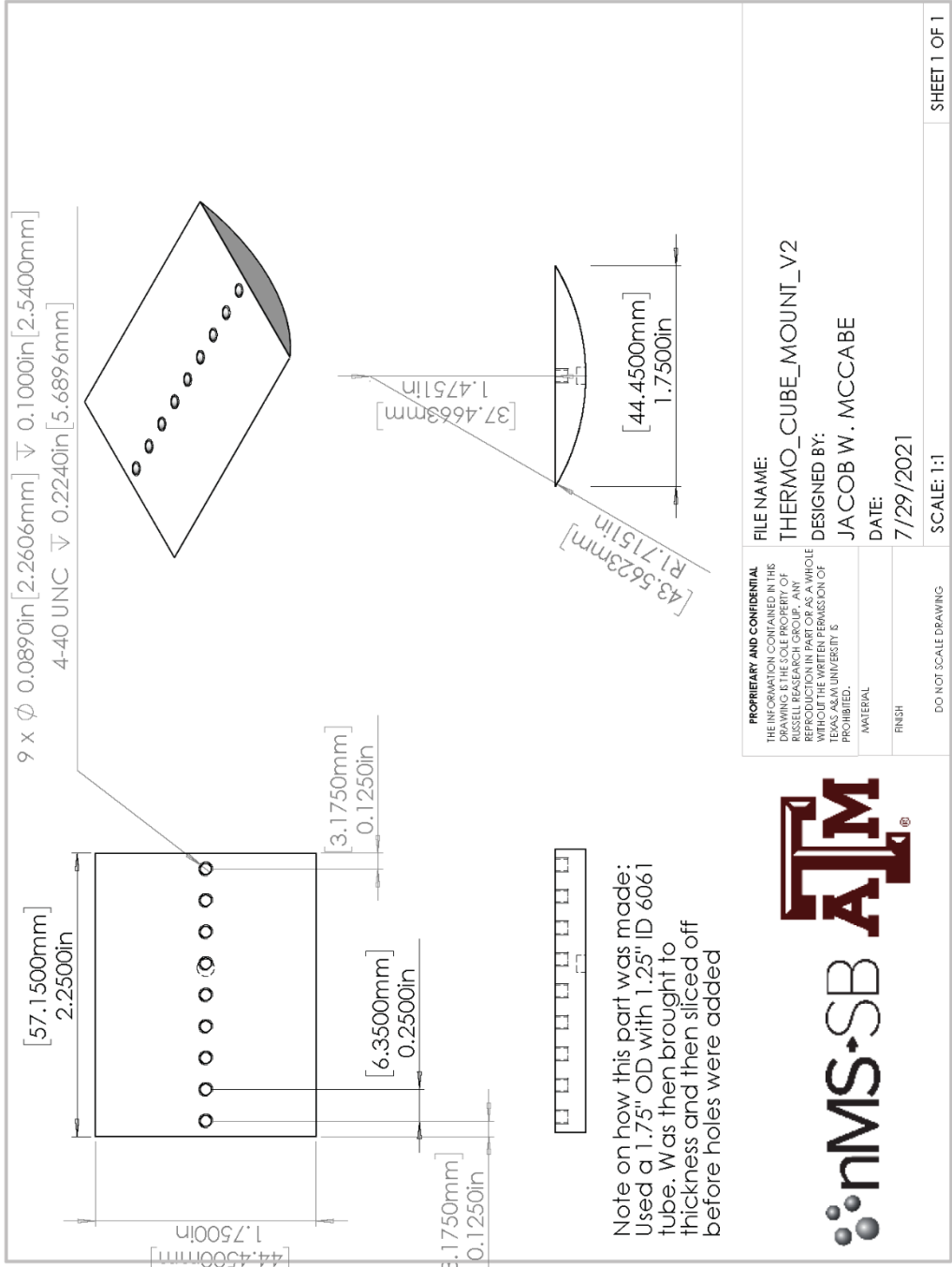
DATE:
7/29/2021

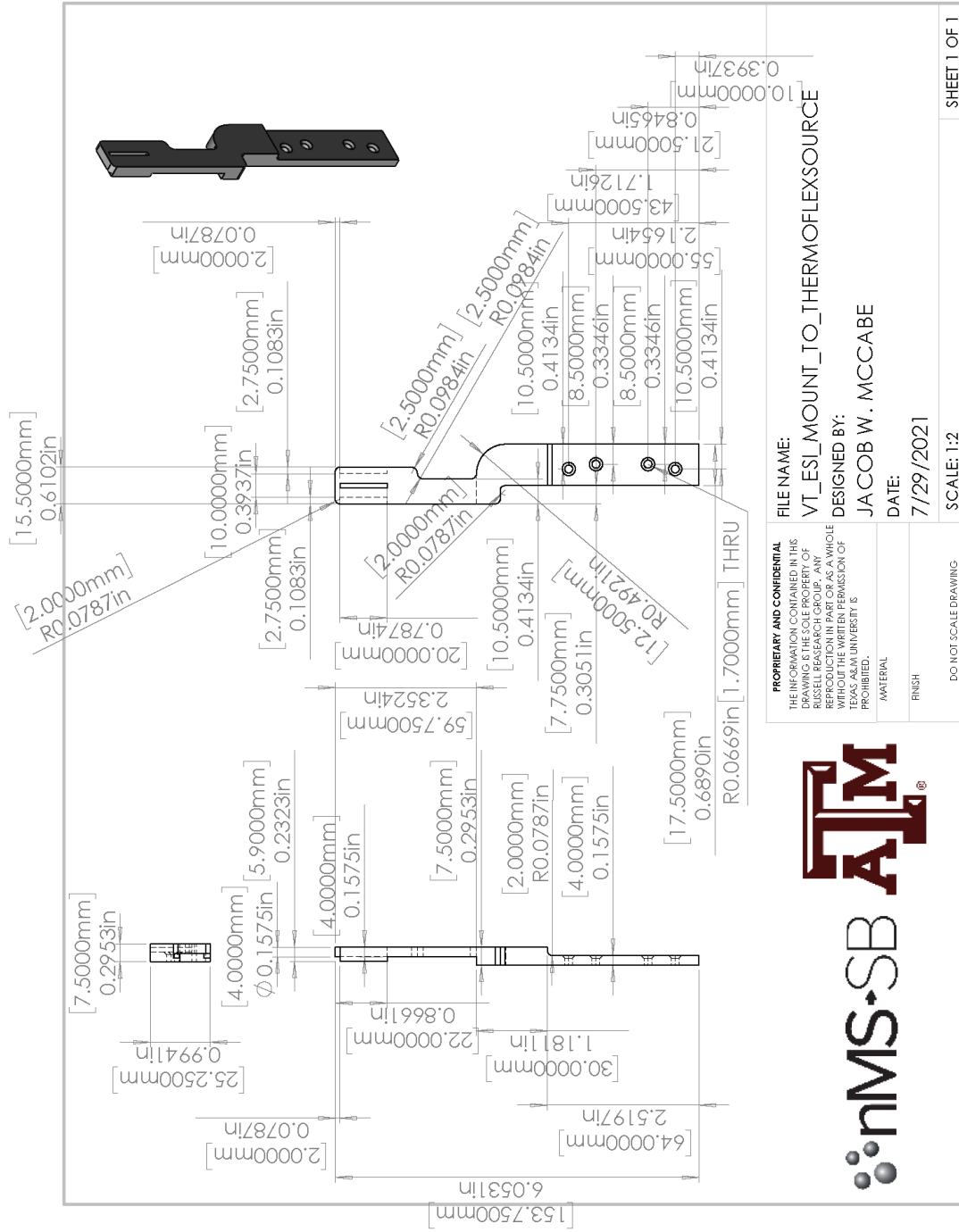
SHEET 1 OF 1

SCALE: 2:1

DO NOT SCALE DRAWING

SOLIDWORKS Educational Product. For Instructional Use Only.





PROPRIETARY AND CONFIDENTIAL
 THE INFORMATION CONTAINED IN THIS
 DRAWING IS THE SOLE PROPERTY OF
 RUSSELL RESEARCH GROUP. ANY
 REPRODUCTION IN PART OR AS A WHOLE
 WITHOUT THE WRITTEN PERMISSION OF
 TEXAS A&M UNIVERSITY IS
 PROHIBITED.



FILE NAME: VT_ESL_MOUNT_TO_THERMOFLEXSOURCE

DESIGNED BY: JACOB W. MCCABE

DATE: 7/29/2021

SCALE: 1:2

DO NOT SCALE DRAWING

SHEET 1 OF 1

SOLIDWORKS Educational Product. For Instructional Use Only.